Downloaded from orbit.dtu.dk on: Apr 24, 2024

DTU Library

Possible Power Estimation of Down-Regulated Offshore Wind Power Plants.

Gögmen, Tuhfe

Publication date:
2016

Document Version
Publisher's PDF, also known as Version of record

Link back to DTU Orbit

Citation (APA):
Gögmen, T. (2016). *Possible Power Estimation of Down-Regulated Offshore Wind Power Plants.* Technical University of Denmark.

General rights
Copyright and moral rights for the publications made accessible in the public portal are retained by the authors and/or other copyright owners and it is a condition of accessing publications that users recognise and abide by the legal requirements associated with these rights.

- Users may download and print one copy of any publication from the public portal for the purpose of private study or research.
- You may not further distribute the material or use it for any profit-making activity or commercial gain
- You may freely distribute the URL identifying the publication in the public portal

If you believe that this document breaches copyright please contact us providing details, and we will remove access to the work immediately and investigate your claim.

Author: Tuhfe Göçmen

Title: Possible Power Estimation of Down-Regulated Offshore Wind Power Plants

Division: Department of Wind Energy

Abstract:
The penetration of offshore wind power is continuously increasing in the Northern European grids. To assure safety in the operation of the power system, wind power plants are required to provide ancillary services, including reserve power attained through down-regulating the wind farm from its maximum possible power.

Currently, there is neither a standardised regulation by the TSOs nor a verified approach regarding the wind farm scale available power estimation. Here we describe an industrially applicable, validated method for the real-time estimation of the possible power of an offshore wind power plant. The developed procedure, the PossPOW algorithm, can also be used in the wind farm control as it yields a real-time wind farm power curve.

The modern wind turbines have a possible power signal at the turbine level and the current state of the art is to aggregate those signals to achieve the wind farm scale production capacity. However the summation of these individual signals is simply an over-estimation for the wind power plant, due to reduced wake losses during curtailment. The determination of the possible power with the PossPOW algorithm works as follows: firstly the second-wise upstream wind speed is estimated, since it is not affected by any wake. Then the upstream wind is introduced into the wake model, adjusted for the same time resolution, to simulate the power losses that would occur during nominal operation.

The PossPOW algorithm uses only 1 Hz turbine data as inputs, namely power, pitch angle, and rotational speed. The method is validated in Horns Rev-I, Lillgrund and Thanet offshore wind farms, together with NREL 5MW simulations. The reduced wake is replaced by the wake model which estimates the velocity deficit for nominal operation. An evaluation of the existing wake models show that the suitable models are tuned for 10-min averaged data. Therefore, the Larsen wake model is re-calibrated for real-time using Thanet data, validated in Horns Rev-I and then implemented in farm scale considering the local turbulence, time delay and meandering.

The validation of the algorithm is performed using experiments in Horns Rev-I where two of the upstream turbines are curtailed. The PossPOW algorithm is compared to the current practice and shown to perform significantly better, according to the error scores stipulated in the Danish grid code.

DTU Wind Energy PhD-0056
December 2015

ISBN: 978-87-93278-53-0

Project Period:
2012.12.15 – 2015.12.14

Education:
PhD

Division:
Wind Energy

Supervision:
Gregor Giebel
Poul Ejnar Sørensen
Niels Kjølstad Poulsen

Contract number:
2012-1-10763

Sponsorship:
Energinet.dk under the Public Service Obligation (PSO) scheme.

Project Website:
www.posspow.dtu.dk

Pages: 161
Tables: 4
References: 107

Technical University of Denmark
Department of Wind Energy
DTU Risø Campus Frederiksborgvej 399
Building 118
4000 Roskilde
Denmark

www.vindenergi.dtu.dk

1 Dansk Resumé 4

2 Introduction to Down-regulation and Available (Possible) Power 6
2.1 Global Regulations and Current Estimation of Available Power 6
2.2 Motivation of PossPOW and Project Flow 10

3 Local Wind Speed Estimation Using Turbine Data 12
3.1 Introduction 12
3.2 Rotor Effective Wind Speed Estimation 12
3.2.1 Effective Wind Speed in Horns Rev-I 13
3.2.2 Effective Wind Speed in Thanet 16
3.2.3 Effective Wind Speed in Lillgrund 16
3.2.4 NREL 5 MW Simulations 19

4 Wake Modelling 22
4.1 Wake Models Developed at the Technical University of Denmark: A Review 23
4.1.1 Infinite Wind Farm Boundary Layer Model 23
4.1.2 The Jensen Model 25
4.1.3 The Larsen Model 28
4.1.4 Dynamic Wake Meandering Model 31
4.1.5 FUGA 34
4.1.6 Ellipsys3D 35
4.2 Benchmarking Study 37
4.2.1 Sexbierum Wind Farm 37
4.2.2 Lillgrund Offshore Wind Farm 42
4.3 Application of the Models 47
4.3.1 Typical Usage 47
4.3.2 Accuracy 48
4.3.3 Computational costs 49

5 Re-calibration of the Larsen Model for Real Time Wake Modelling . . . 50
5.1 Estimation of Turbulence Intensity using Turbine Data 50
5.1.1 Atmospheric Turbulence Intensity 51
5.1.2 Turbulence Intensity in Wind Turbine Wakes 53
5.2 Single Wake Re-calibration 58
5.2.1 Time Delay Concept 59
5.2.2 Modelling of the Meandering inside the Wind Farm 59
5.2.3 Moving Average of the Time Series 60
5.2.4 Parametrisation and Curve Fitting 60

6 PossPOW Algorithm: Wind Farm Scale Available Power Estimation . . 63
6.1 Local Wind Direction inside the Wind Farm 64
6.2 Percentage Error in Wind Speed 65
6.3 Real-Time Wind Speed to Power 65

7 Full Scale Experiments at Horns Rev-I and Validation of the PossPOW Algorithm 69
7.1 Experimental Setup 69
7.2 Experimental Results and Validation under Down-regulation 72
7.2.1 Time series Analysis 73
7.2.2 Effects of Curtailment Further Downstream 76
7.2.3 PossPOW Validation in the frame of the TSO Regulations . . . 78

8 Conclusions & Future Work 82

Appendix A Calibration of Wind Direction SCADA Signal 88

Appendix B Journal Papers 90
Wind Speed Estimation and Parametrization of Wake Models for Down-regulated Offshore Wind Farms within the scope of PossPOW Project 91
Wind Turbine Wake Models Developed at the Technical University of Denmark: A Review 98
Estimation of Turbulence Intensity Using Rotor Effective Wind Speed in Lillgrund and Horns Rev Offshore Wind Farms 116
Possible (Available) Power of Down-regulated Offshore Wind Power Plants: The PossPOW Algorithm 133

Appendix C Conference Proceedings 151

Bibliography 152

1

Dansk Resumé

Udbygningen med offshore vindkraftværker har nu for alvor taget fart i de nordeuropæiske elsystemer. Som en konsekvens af den stadig stigende andel af vindkraftværker i elforsyningen stiller netselskaberne i dag krav til at vindkraftværker leverer systemydelser til nettet, herunder at et vindkraftværk kan nedreguleres til at producere mindre end hvad det ville gøre under normale driftsforhold, hvor vindkraftværket ellers ville producere så meget som muligt under de givne vindforhold.

Når et vindkraftværk nedreguleres opstår der et behov for at vide hvor meget vindkraftværket kunne have produceret under normale driftsforhold, dvs. hvis det ikke var nedreguleret. Oplysningen om denne mulige effektproduktion kan således enten bruges til at kompensere ejeren for tabt produktion eller til at styre vindkraftværket på en måde så det til enhver tid kan levere en systemydelse i form af en aftalt reserve.

I dag findes der hverken standardiserede eller verificerede metoder til bestemmelse af den mulige effektproduktion. Denne PhD-afhandling beskriver en ny industriel anvendelig og verificeret "PossPOW" algoritme til bestemmelse af den mulige effektproduktion. Metoden bygger på beregning af en realtids-effektkurve som ikke blot kan bruges til efterfølgende at beregne tabt produktion men også kan anvendes i realtid til at styre vindkraftværket så det sikrer tilstedeværelsen af en reserveeffekt som kan aktiveres hvis elsystemet får behov for det, f.eks. hvis et andet kraftværk falder ud pga. en fejl.

En moderne vindmølle beregner sin mulige produktion i realtid, og for et vindkraftværk med mange vindmøller er praksis i dag at beregne den mulige produktion fra vindkraftværket som summen af mulige produktioner fra de enkelte vindmøller. Denne metode overvurderer typisk den mulige produktion fra et vindkraftværk fordi den ikke tager hensyn til at skyggevirkningen fra foranstående vindmølle reduceres når denne nedreguleres, og den bagvedstående mølle derfor overvurderer den vindhastighed som den ville opleve hvis hele vindkraftværket var sat til at levere den mulige produktion. Den nye PossPOW algoritmen fjerner denne systematiske overvurdering af den mulige produktion fra de bagvedstående vindmøller ved først at estimere vindhastigheden i forreste række for derefter at bruge en skyggemodel til at beregne vindhastinghederne ved de bagvedstående møller.

Ovenstående PossPOW beregning opdateres i realtid baseret på opdaterede målinger af effekt, bladvinkel og omløbshastighed for hver enkelt vindmølle. Denne opdatering kan f.eks. ske for hvert sekund. Metoden er i første omgang evalueret baseret på målinger fra Horns Rev-I, Lillgrund and Thanet offshore vindkraftværker, og på simuleringer med NREL 5MW vindmøller. Efterfølgende er metoden valideret baseret på

eksperimenter med Horns Rev-I vindkraftværket, hvor to opstrøms vindmøller nedreguleres. PossPOW algoritmen viser sig at være en klar forbedring sammenlignet med nuværende praksis, både hvad angår nøjagtighed og hvad angår specifikke kriterier i danske krav til vindkraftværker.

2

Introduction to Down-regulation and Available (Possible) Power

In order to achieve the European climate and energy goals, the share of renewable energy as a proportion of final consumption has increased to 13% in 2012, and is expected to extend further to 21% in 2020 and 24% in 2030 [26]. The accelerated implementation of renewable energy implies many technical challenges particularly for the electricity system, which needs to adjust to the decentralised and highly variable production. Therefore, the modern offshore wind farms are designed as wind power plants required to contribute to the stability of the grid by offering grid services (also called ancillary services). One of those services is reserve power, which is achieved by down-regulating the wind farm from its maximum available power [25, 77, 12, 24].

The estimation of the available power, or eventually the reserve capacity, is essential as the balancing responsible parties (BRPs) are compensated for this service in terms of the level of reserves which can also be traded in the balancing market, depending on the national / local market schemes. Here in this chapter, the global regulations and current practices on the available power estimation are reviewed. Then accordingly, the objective and the added value of the PossPOW project together with a description of the developed technology is presented.

2.1 Global Regulations and Current Estimation of Available Power

The Transmission System Operators (TSOs) and the BRPs are required to know the amount of production capacity mainly for two reasons; 1) to be able to estimate what the power output will return to when the curtailment instruction is released, 2) to assess the amount of reserves within certain accuracy. The estimated reserves can either be used to calculate the compensation under mandatory down-regulation or can be traded in the balancing market. Most of the regulations are related to the compensation case. However, the reserves can be traded in the balancing market globally with flexible improvements where needed, and these regulations can be applied to assess the accuracy of the reserves as well. The qualification requirements of the estimated available power and relevant technical and market legislations differ regionally. In conformity with the European Network of Transmission System Operators for Electricity (ENTSO-E) poli-

cies [83], TSOs are held responsible within continental Europe for the quality of the reserves. The following section provides a brief summary of the existing regional / national regulations in Europe where the grid contains offshore wind power penetration.

Belgium

In Belgium, the majority of the reserves is delivered by the conventional power plants where the BRPs are responsible for balancing their portfolio on a 15-min level [70]. Belgian TSO Elia recently performed a pilot project including several tests conducted in Estinnes onshore wind farm [23]. It was investigated whether the design of the current balancing energy market facilitates the participation of wind farms and several changes were proposed. Although not concrete, the potential criteria to evaluate the estimated available power are specified as;

- Average available power calculation error must be close to zero,
- Most of the real-time available power calculation errors should be within a relatively small band around zero,
- Only a limited amount of real-time available power calculation errors can be outside a wider band around zero.

The final feasibility analysis of the required market changes and the targets for prequalification will be determined in close collaboration with all market parties in parallel with the developments on the European level.

The UK

By the end of 2014, the UK had the largest offshore wind capacity in Europe accounting for over 55% of all the installations [33]. Therefore, to allow better market participation of the renewable generators and enhance the system security, a Grid Code working group focusing solely on the wind farm scale available power provision was formed by the National Grid. It was concluded that [101] the SCADA available power from the individual turbines will be aggregated to the wind farm level, which will shown to be erroneous later in this study. The corresponding signal is to be fed over the existing SCADA data connections used to provide operational metering. No particular accuracy is specified as long as the data quality is in line with the ”Good Industry Practice” which will be described in Section 2.2. Additionally, the refresh rate of the potentially provided available power signal is 5-sec, although the actual reserve check is planned to be performed at 10-min intervals. The modification to the Grid Code was approved in early 2015 and is planned to go into operation on 1 April 2016 without any retrospective application.

Ireland

Both Northern Ireland as a part of the UK and the Republic of Ireland have been operating in the Single Electricity Market for the island since 2007. The Irish TSO EirGrid set the quality standard for the available power signal [21] based on the root mean square error, *RMS*, defined in Equation 2.1.

$$RMS = \sqrt{\frac{\sum_{h=1}^{h=p} (AP_h - MG_h)^2}{p}} \tag{2.1}$$

where AP_h is the available power and MG_h is the actual power output recorded by EirGrid averaged over the interval h within a period p. For the same period, the *RMS* is normalised using the maximum of the installed or maximum export capacity. The normalised *RMS* is calculated at 15-minutes intervals and has to be lower than 6% when calculated over a day. The standard in the available power estimation also fails when the estimation exceeds the greater of the installed or maximum export capacity by more than 6% in any quarter hour period.

Germany and the Netherlands

In Germany, the estimation of the reserve power during down-regulation is compulsory and data requirements from the BRPs during down-regulation are specified both at wind turbine and wind farm level [12]. At the turbine level; the operational state, produced power, wind speed and direction together with the source of the measurements (e.g. nacelle anemometers from the sites or FINO1 as a reference or farm average, etc.), theoretical possible power calculation (based on the certified power curve for the air density $1.225 kg/m^3$), a correction factor for the air density and the cost per kWh are to be delivered. For the wind farm level; the sum of the individual theoretical possible power calculations, wind speed and direction, the limitation in power and the power measured at the point of common coupling (PCC) are to be submitted. For the delivered wind speed data and the theoretical possible power calculations, the nacelle anemometers are encouraged to be used. In case they are not available, the reference FINO1 data are to be considered. The provision of the turbine level available power that is based on the nominal power curve with a resolution of $0.1 m/s$ should also include the wake losses at the turbine locations. The required time resolution for the data and the calculations are 15-minutes. The compensation and the reserve capacity claims are based on complex operational state descriptions [38].

The Dutch TSO TenneT in the Netherlands, which operates also in Germany, collects and stores the available power data in 15-minutes intervals. However, the reserved capacity is not compensated, even under mandatory curtailment.

Denmark

As a world record holder by getting 39.1% of its electricity consumption from wind in 2014 [33], it is only expected that the most detailed regulations regarding the available or reserve power are implemented in Denmark. Since the system is highly dependent on wind, the downward regulation is ordered rather frequently and the BRPs are compensated for their lost production according to the legislation set by the Danish TSO Energinet.dk [24]. The signals to be provided to settle non-supplied generation are: online active power measured both at the installation and the PCC, and online calculation of available and reserve power. Data is to be submitted as 5-minute time series and transferred to Energinet.dk once a day. In order for the settlement to be valid and the compensation to take place, the calculation of the available power must be verified. The error of the provided calculations are to be within $\pm 5\%$ span of the actual production for the wind farms ordered to produce in the range of 20 – 100% of the maximum power. Although the data is submitted in 5-minutes intervals, the error in the available power estimation is checked on 15-minutes average basis. If the deviations are outside of the $\pm 5\%$ span, Energinet.dk demands the calculation to be corrected and the model to be verified and approved. For consistent over-estimation cases, Energinet.dk calculates a correction factor to reduce the estimated non-supplied generation. Since an actual measurement of the available power is out of the question, the deviations are calculated for the most recent, entire day of normal operation on a site-specific basis. In the same dataset, if the 15-minutes averaged available power is over-estimated (i.e. $>5\%$ of the actual power) for more than 5% of the time, the correction factor is determined as the largest quarter-hourly deviation. This corresponds to a direct deduction from the compensation which seems to be experienced by the BRPs in Denmark rather commonly [38].

Not only in Denmark but also in other places, the risk of not being able to up-regulate to the approximated value is an important concern regarding the over-estimation. In order to make sure the estimated reserve is actually provided, the common practice is to down-regulate extra which might correspond to substantial reduction in profit at times. For example, Sorknæs et al. [97] demonstrated using Sund & Bælt's turbines in Denmark that, depending on the market structure and online prices, participation in the balancing market by providing downward regulation can increase the profit as significantly as 196%. Furthermore, the power balancing across the borders leads to market based shut-downs or down-regulations in the neighbouring country. For example, TenneT TSO GmbH in Germany paid Danish wind farm owners (or BRPs) to curtail 37 GWh of wind power in November 2015 to avoid cutting German output where for the first 11 months of the year, the total down-regulated wind power in Denmark is recorded as 237 GWh in 2015 [99].

The technical regulation and limitations (e.g. response time, duration, etc.) regarding mainly the primary and secondary frequency control are not considered in detail in this study but if interested a further reading is encouraged [25].

What is seen from the existing European regulations is that adequate and standardised regulations or technical requirements to help understanding the possible power or the amount of reserves for their system reliability is lacking. This research is critical not only for power stability but also for the business case for wind energy.

2.2 Motivation of PossPOW and Project Flow

The modern offshore wind turbines have a supervisory control and data acquisition system (SCADA) signal called available [49] or possible power [50]. Since the available power is the maximum power production capacity of the turbine(s) for that particular wind regime, that SCADA signal would be equal to the active power under nominal operation. "The Good Industry Practice" or the state of art in the wind farm scale available power estimation is to aggregate those turbine level SCADA signals. However during down-regulation, the upstream turbines are tuned to extract less power from the wind, leaving the downstream flow more energetic. Therefore, the sum of the individual SCADA signals is a clear over-estimation of the available power of a down-regulated wind farm simply because the wind speed is higher at the downstream turbine location(s) due to the decrease in wake losses under curtailment. As seen in the Section 2.1, the BRPs and the TSOs have no real way to determine exactly the available power of a whole wind farm under down-regulation. Therefore, PossPOW project aims to develop a verified, industrially applicable and internationally accepted way to determine the possible power of a down-regulated offshore wind farm. Along the way, it is intended to improve the use of wake models for real-time cases to obtain real-time wind farm power curves which can then be fed into a dynamic control system.

To correct the reduced wake effect during down-regulation is the conceptual basis of the PossPOW algorithm. In order to do that, first we have introduced a local effective wind speed estimation procedure based on the turbine data in Chapter 3 (the paper is attached on page 91). At every second, the effective wind speed is calculated using four different turbine types, three of which are located in operating offshore wind farms, and the model is validated under both nominal operation and down-regulation.

The next stage is to feed the effective wind speeds at the upstream turbines to a wake model to estimate the velocity deficit for normal operation and replace the down-regulated wake. A comprehensive and detailed literature review among the wake models developed at DTU Wind Energy is presented in Chapter 4 (paper is attached on page 98). The wake models are benchmarked using an onshore and an offshore wind farm and their targets of application are briefly described. It was seen that the wake models capable of resolving high fidelity data are computationally costly to perform real-time or to be implemented online. On the other hand, the robust models are tuned and validated using 10-min averaged conventional data to achieve long-term statistics rather than to investigate dynamics inside the wind farm. Therefore, as one of the most advanced readily-available engineering models, the Larsen model is re-calibrated for real-time

using a single wake case in Thanet and validated in Horns Rev-I offshore wind farms in Chapter 5. To further enhance the wake modelling, the local turbulence intensity is estimated using the effective wind speed and validated in Lillgrund offshore wind farm in Section 5.1 (the paper is attached on page 116).

The wind farm scale implementation of the developed real-time model and the final description of the large scale components of the PossPOW algorithm is represented in Chapter 5 (the paper is attached on page 133). The model is applied to Thanet and Horns Rev-I under nominal operation, hence the results are compared with the actual power production of the farms.

The test and validation of the algorithm is rather challenging since there is no actual measure of the available power on the wind farm scale. However, we can benefit from the similarity in power production between the neighbouring rows in a simple layout like the Horns Rev-I wind farm. The idea behind the validation, experimental set-up and the verification results are presented in Chapter 7.

The thesis mainly consists of relevant chapters directly taken from four manuscripts included in the appendices. Instead of attaching the papers as is, this configuration is selected in order to exclude side research, bring the compatible work together and avoid repetitions; essentially to provide a better representation of the project flow.

3

Local Wind Speed Estimation Using Turbine Data

3.1 Introduction

The first phase of PossPOW project is to estimate the rotor effective wind speed since the nacelle anemometers are known to have high uncertainties. The proposed method is to use power, pitch angle and rotational speed as inputs and combine it with a generic C_P model to estimate the wind speed, (related paper is attached on page 91).

The performance of the model has been evaluated for both normal operation and down-regulation periods using four different case studies: a dataset sampled at each second from the Horns Rev-I, Thanet and Lillgrund wind farms, respectively, together with the NREL 5MW single turbine simulations. The effective wind speed results in Horns Rev-I and Thanet wind farms, and NREL 5MW simulations are taken from the the paper included on page 91 where the Lillgrund results are from the paper starting on page 116.

3.2 Rotor Effective Wind Speed Estimation

Since the nacelle region is exposed to highly distorted flow [107], the anemometers mounted on that region have always been approached with suspicion. Especially for real time calculations, using nacelle wind speed values measured during relatively shorter period, may induce higher uncertainties and can even lead to faults [10]. Therefore, the idea is to use the general power expression given in Equation 3.1 with the turbine characteristics and second-wise SCADA signals namely the active power P, pitch angle θ and rotational speed ω.

$$P = \frac{1}{2}\,\rho\, C_P(\lambda,\theta)\,\pi R^2 U^3 \tag{3.1}$$

Since C_P during down-regulation does not follow the ideal curve and because generally very limited information is provided by the manufacturers, the generic C_P expression proposed by Heier [39] was used to simulate the pitch angle, θ, and tip speed ratio, λ, dependency of the power coefficient, C_P (Equation 3.2). Note that in an actual implementation, the manufacturer would have access to the actual C_P curve, e.g. ”Siemens WS” presented in the Lillgrund wind farm in Section 3.2.3.

Table 3.1: The coefficients used in the effective wind speed estimation

c_1	c_2	c_3	c_4	c_5	c_6	c_7	c_8	c_9
0.47	101	0.4	0.01	1.95	5	16.5	0.089	0.02

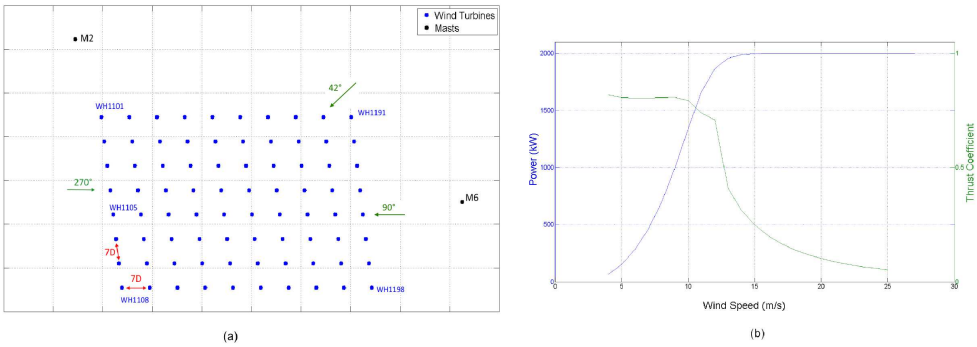

Figure 3.1: (a) Layout of the Horns Rev I offshore wind farm and (b) Vestas V80-2MW offshore turbine power, P, and thrust, C_T, curve

$$C_P(\lambda,\theta) = c_1\left(\frac{c_2}{\lambda_i} - c_3\theta - c_4\theta^{c_5} - c_6\right) exp\left(\frac{-c_7}{\lambda_i}\right)$$
$$\lambda_i = \left[\left(\frac{1}{\lambda + c_8\theta}\right) - \left(\frac{c_9}{\theta^3+1}\right)\right]^{-1} \tag{3.2}$$

The coefficients in Equation 3.2 are tabulated in Heier [39] but then modified by Ackermann [2] and Raiambal et al. [87] to fit for variable speed turbines and a specific turbine model, Vestas V-80, respectively. In this study, the latter version of coefficients with slight modifications (maximum change is less than 5%) is applied where all the modifications are determined by the agreement between the modelled and the provided ideal C_P curves. The final version of the coefficients is listed in Table 3.1 which is applied to all the turbines considered throughout this thesis.

In the following sections, we will try the rotor effective wind speed approach on three different offshore wind farms and a single turbine simulation.

3.2.1 Effective Wind Speed in Horns Rev-I

The Horns Rev-I offshore wind farm is located in western Denmark. It consists of 80 Vestas V-80, 2MW offshore wind turbines. The layout of the wind farm together with

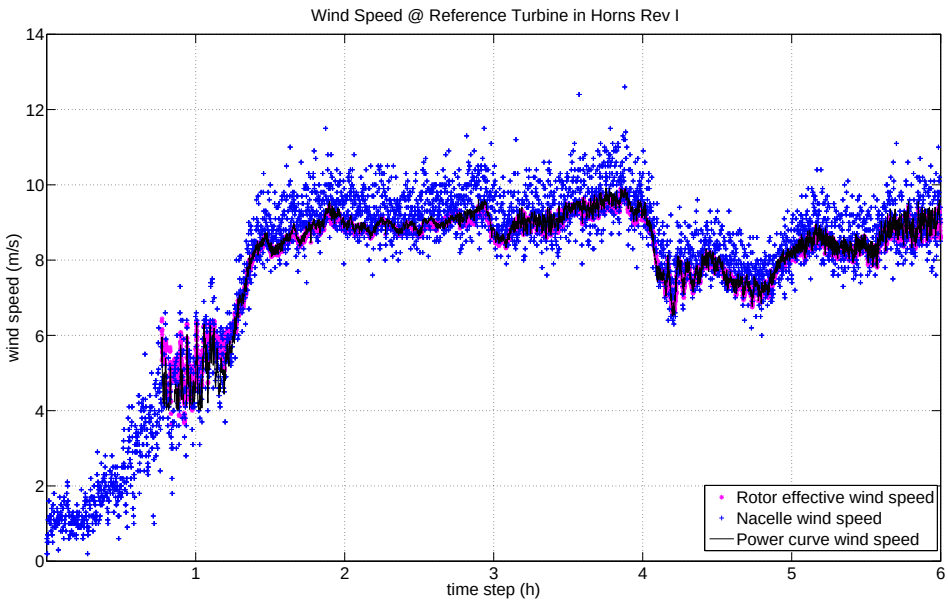

Figure 3.2: Wind Speed Comparison at the reference turbine located in Horns Rev-I Wind Farm, during normal (ideal) operation

the locations of two of the surrounding met masts ($M2, M6$) is shown in Figure 3.1(a). The wind speed was calculated for each turbine iteratively using two different datasets sampled at every second extracted from the wind farm. The first dataset presented is recorded under normal operational conditions and covers a 35-hour period whereas the other dataset is recorded when the wind farm is down-regulated for 2 hours. The provided channels are the active power, blade pitch angle, rotor rpm, averaged temperature, the nacelle anemometer wind speed measurements, wind direction and individual possible power signal for both of the datasets. The air density is corrected using the averaged temperature dataset which was sampled at every 10 minutes and standard atmospheric pressure together with the equation of state.

In Figure 3.2, *Rotor Effective wind speed* refers to the wind speed calculated iteratively where $U^3 = \left(\frac{\omega R}{\lambda}\right)^3$ and using the C_P model in Equation 3.2; the *Nacelle wind speed* is the wind speed measured using a nacelle anemometer and *Power Curve wind speed* is the wind speed calculated using the active power signal and the ideal power curve provided by the manufacturer, i.e. Figure 3.1(b).

It is seen in Figure 3.2 that the rotor effective wind speed is in a good agreement with

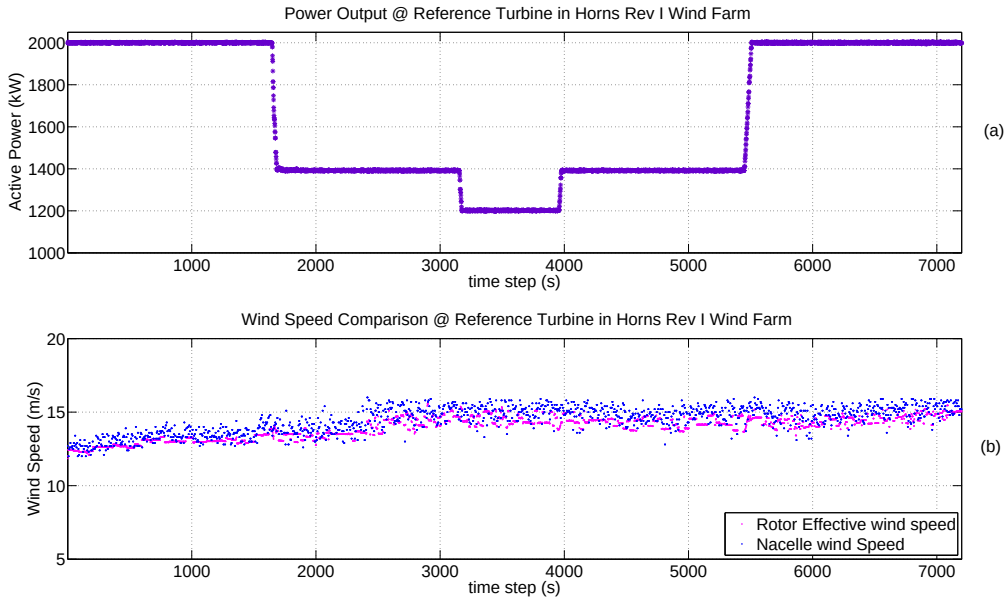

Figure 3.3: (a) Power output, (b) wind speed comparison of the reference turbine located in Horns Rev-I wind farm during down-regulation

the wind speed calculated using the power curve and also consistent with the nacelle anemometer measurements. Even though the nacelle anemometers are not favoured due to the reasons mentioned earlier, during the periods when the power curve methodology can no longer be applied (i.e. before cut-in and along rated region) the only available information regarding the wind speed is the nacelle anemometer measurements. Figure 3.3(b) includes a similar comparison this time performed for down-regulated conditions in which the high frequency noise in the nacelle wind speed is also clearly observed, particularly relative to the geometrically averaged rotor effective wind speed. Figure 3.3(a) schematically represents the active power signal, or in other words the down-regulation strategy.

If a comparative analysis is performed between Figure 3.2 and 3.3(b), it might be said that the deficit between the wind speed values obtained using the nacelle anemometer measurements and the Rotor Effective Wind Speed remained approximately the same under standard operation and down-regulated conditions. Under normal operation and below rated region, the common practice is to use the power curve approach when the meteorological mast is not available (e.g. [36, 37, 76]). Therefore, assuming the power curve approach in 3.2 is representative enough for the wind speed, the estimation of the

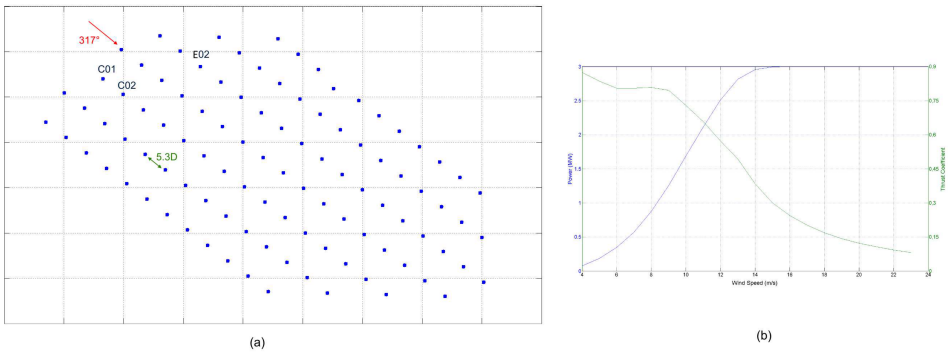

Figure 3.4: (a) Layout of the Thanet offshore wind farm and (b) Vestas – V90 3MW offshore turbine power, P, and thrust, C_T, curve

wind speed using the created algorithm for down-regulation periods can be justified.

3.2.2 Effective Wind Speed in Thanet

The Thanet offshore wind farm is located in the eastern UK, approximately 15 km away from the nearest shore. The wind farm consists of 100 Vestas – V90 3MW offshore turbines. The turbine diameters are 90 m and the hub is located at 70 m height. The distance between the turbines is 500 m corresponding to 5.3 diameters, D, for the perpendicular wind direction, 317°. The layout of the wind farm, together with the manufacturer's power and thrust curve is presented in Figure 3.4.

A large 1-sec dataset of 84 hours has been analysed. The provided SCADA signals are Active Power, P, Rotational Speed, ω, Pitch Angle, θ, Nacelle Wind Speed (measured by nacelle anemometers), NWS, averaged temperature, Wind Direction (yaw angles) and Possible Power (turbine level). The dataset includes a relatively short down-regulation period near hour 18, where the wind speed is slightly below rated.

From Figure 3.5, it can be seen that the rotor effective wind speed is in relatively good agreement with power curve wind speed along the region where it is applicable, i.e. during normal operation for incoming wind speeds above cut-in.

3.2.3 Effective Wind Speed in Lillgrund

The Lillgrund wind farm is located in Øresund area, between Sweden and Denmark, 6 – 8 km from the Swedish west coast; south of Malmö. It consists of 48 SWT – 2.3 – 93 wind turbines with a total rated capacity of 110 MW (power and thrust curves are

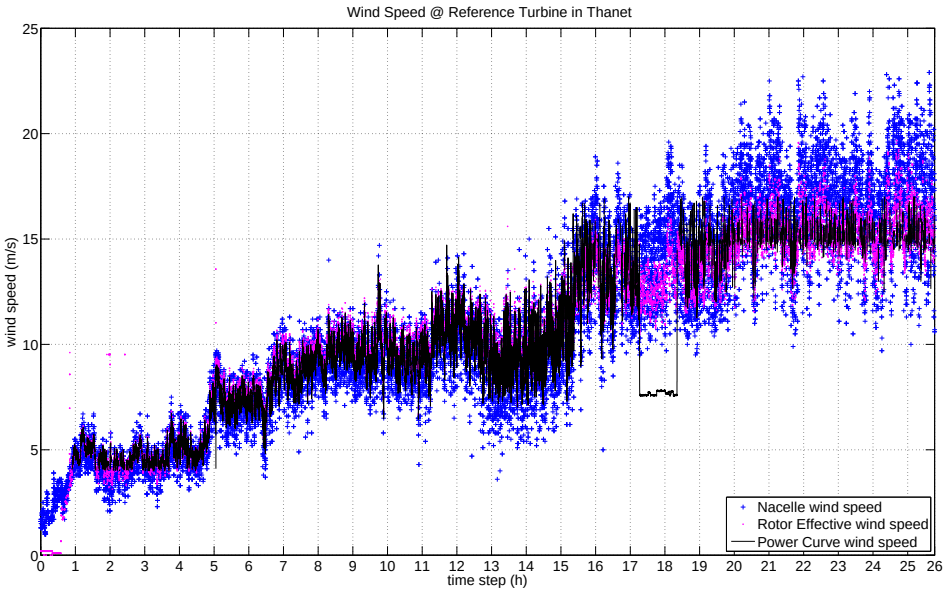

Figure 3.5: Wind Speed Comparison at the reference turbine located in Thanet Wind Farm, during normal (ideal) operation and down-regulation

shown in Figure 3.6(b)). The turbine diameters are 93 m and the hub is located at 65 m height. The layout of the Lillgrund is rather unusual due to a gap in the middle of the farm, and the quite small internal spacings of the turbines of 3.3 and 4.3 rotor diameters, D, as shown in Figure 3.6(a).

The data used in the calculations cover a period of 7 months, from 06/2012 to 01/2013, with a sampling rate of 1 Hz. On the met mast, the closest sensors to the hub height of the turbines are taken into account therefore the second-wise wind speed measurements are taken at 65 m while the wind direction and temperature are observed at 61 m. The second-wise extracted signals from the SCADA system are active power, pitch angle, rotational speed, and nacelle anemometer wind speed, where the first three are used to calculate the rotor effective wind speed. For the Lillgrund wind farm, an additional Siemens turbine SCADA signal called "WindEstimate" is extracted. The signal is called *SiemensWS* throughout this study and it was introduced to have a signal with smaller fluctuations, and one that is less sensitive to turbine curtailments than the anemometer signal. The signal is calculated by generating a look-up table for the produced power in terms of the rotor averaged wind speed, rotational speed and pitch angle together with the original rotor geometry. The look-up table is then used considering

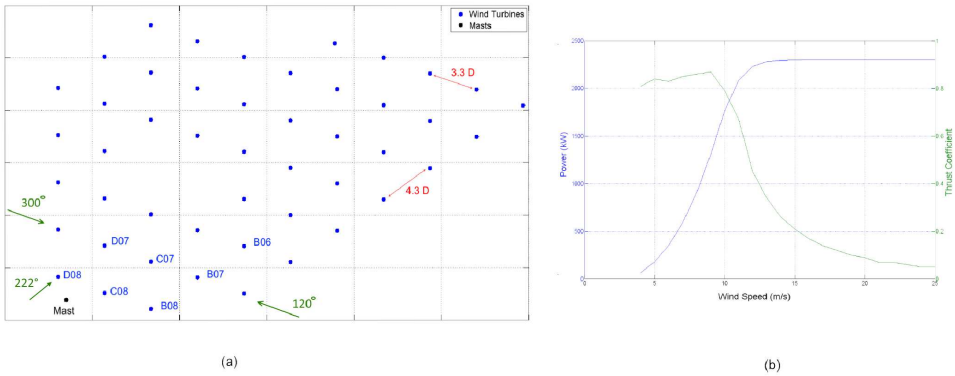

Figure 3.6: (a) Layout of the Lillgrund offshore wind farm and (b) Siemens SWT-2.3-93 turbine power, P, and thrust, C_T, curve

the operational power, rotational speed and pitch to interpolate the wind speed when the turbine is online.

In Figure 3.7, the rotor effective wind speed is implemented in Lillgrund and compared with the power curve, nacelle wind speed and SiemensWS as well as the high frequency (1 Hz) met mast wind speed observations.

Figure 3.7 shows that the fluctuations in point measurements (i.e. the nacelle and met mast wind speed) are a lot larger than the others. Since the power curve wind speed, Siemens estimated wind speed and rotor effective wind speed include the geometrical average over the rotor, the variation is smaller in general. Moreover, they all take produced power as an input, therefore seem inefficient to simulate lower wind speeds close to the cut-in. It is also seen that the power curve wind speed is not applicable for the wind speeds in the rated region, i.e. above 13 m/s. The geometrical average also explains the better agreement seen between the three local wind speed estimation methods. The developed rotor effective algorithm is seen to successively reproduce the wind speed estimated using the authentic $C_P(\lambda,\theta)$ table of the Siemens SWT – 2.3 – 93 turbine with a slight underestimation around the rated wind speed where the pitch peaks. The only significant deviation between those two outputs occurs where the pitch is around $\theta = -1^\circ$, due to the sensitivity in the developed algorithm, see Equation 3.2. It should be noted that the Siemens wind speed data is filtered for the turbine operational state so that the signal is not valid below cut-in and above cut-out. Therefore in comparison to the SiemensWS, the rotor effective wind speed is expected to have outliers in the transition region where the turbine is about to operate, around the cut-in wind speed as observed in the lower right corner Figure 3.7.

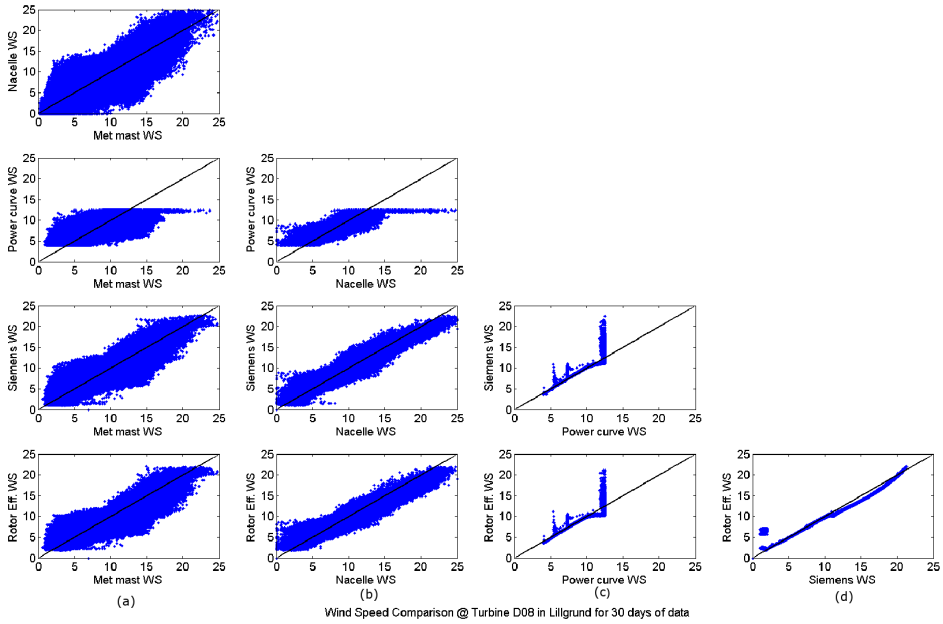

Figure 3.7: Second-wise Wind speed comparison of the measurements taken at the **(a)** met mast *Met mast WS*, **(b)** the nacelle anemometer *Nacelle WS*; and the estimations using **(c)** the turbine power curve *Power curve WS*, **(d)** the manufacturer $C_P(\lambda,\theta)$ *Siemens WS* and **(d)** the approximated $C_P(\lambda,\theta)$ as in Equation 3.2 *Rotor eff. WS*

3.2.4 NREL 5 MW Simulations

Since NREL 5MW is an artificial turbine with public features [94], the developed wind speed algorithm can easily be tested using different scenarios. The simulations were performed by Mahmood Mirzaei from DTU Wind Energy for NREL 5 MW wind turbine [71] which include two different scenarios: normal operation with a mean wind speed of 9 m/s and 50 % down-regulation with a mean wind speed of 13 m/s. For the first scenario, the simulated wind speed (dataset) was compared with the power curve and the rotor effective wind speed - see Figure 3.8(a). The second simulation of wind speed was compared with the model estimation only since the power curve wind speed is not available for down-regulation periods - see Figure 3.8(b). The air density was taken as $1.225\,kg/m^3$.

In Figure 3.8(a), a very good agreement is observed between the simulated, power curve and effective wind speed values. It is also seen, especially between 2000-2750s

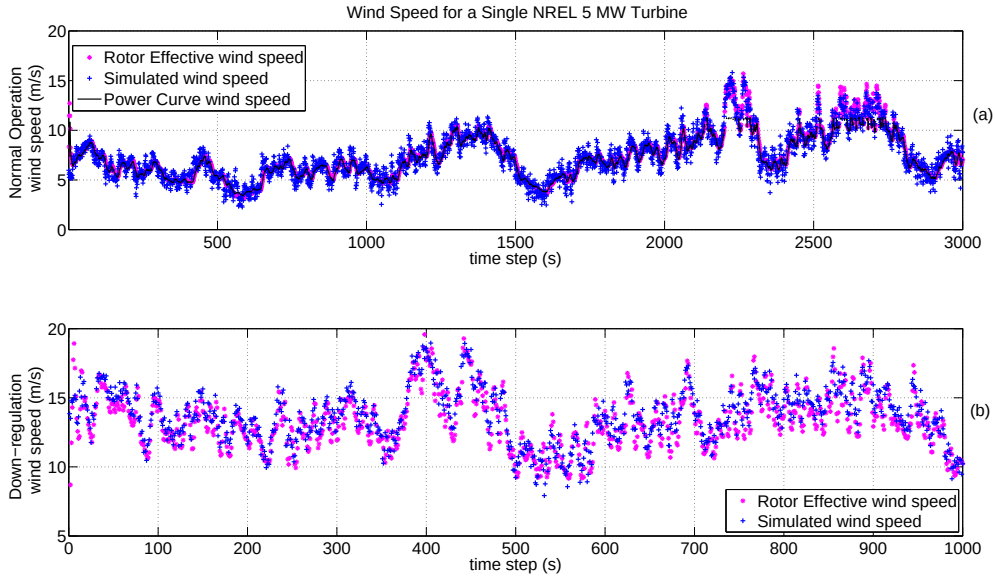

Figure 3.8: Wind Speed Comparison of a single NREL 5MW turbine during (a) normal operation (b) 50% down-regulation

time steps, that the power curve method is not applicable where the inflow velocity has exceeded the rated wind speed which is around 12 m/s for NREL 5 MW turbine. Figure 3(b) presents the agreement between the simulated (dataset) and the rotor effective wind speed also during down-regulation period.

Summary

In order to assess the wind speed under down-regulated conditions at the turbine locations, we introduced a real-time rotor effective wind speed estimation method using SCADA data such as active power, pitch angle and rotational speed together with a generic C_P model (Equation 3.2). We have evaluated the performance of the method for both normal operation and down-regulation using Horns Rev-I, Thanet and Lillgrund offshore wind farms and the NREL 5MW single turbine simulations. The second-wise rotor effective wind speed calculations are shown to be in a good agreement with the power curve wind speed when available, i.e. during normal operation between cut-in and rated wind speed. Furthermore, the approach is compared with the 7-months, also second-wise, met-mast data from Lillgrund wind farm. Due to the fact that the met-

mast provides point-wise measurements while the effective wind speed is geometrically averaged over the rotor, the correlation is observed to be scattered. In fact, considering Taylor's frozen turbulence hypothesis, the eddies smaller than the rotor area are automatically filtered out. Accordingly, a back-of-the-envelope calculation would indicate the time scale of the smoothing effect would be the ratio of the rotor diameter to the mean inflow wind speed, upstream or in the wake depending on the turbine location. Thus, for an incoming wind speed of 8 m/s, the time scale threshold the investigated wind farms would be in the order of 10-seconds. On the other hand, for the Lillgrund case, the effective wind speed is seen to be capable of reproducing the SiemensWS signal, which is estimated with the same principle but considering the actual tabulated $C_P(\theta,\lambda)$ values instead of Equation 3.2.

The estimated 1-sec rotor effective wind speed at the upstream location(s) are to be input to a wake model simulating the normal operating conditions to achieve the available power at the wind farm scale.

4

Wake Modelling

The estimated second-wise wind speed at the upstream turbine locations are to be input to a wake model optimized for the same time resolution. Since a number of approaches exist in the literature to assess the flow characteristics behind a turbine [19, 91, 103], see also Section 4.1, it is not planned to develop another wake model in the PossPOW project. To calculate the available power and provide a real-time power curve on the wind farm scale, the wake model to implement is required to be fast and robust, representing most of the physical properties and maintaining a certain degree of accuracy. To evaluate the current in-house options in terms of the project needs, a comprehensive survey among the wake models developed in DTU Wind Energy is presented here in this chapter. Note that, the model descriptions and the benchmark cases are taken from the relevant journal paper starting from page 98.

Wind turbine wake modelling concentrates on characterizing the flow behind wind turbines. There are two main physical phenomena of interest in the wake: 1) the momentum (or velocity) deficit, which causes a reduction in the power output of the downstream turbines, and 2) the increased level of turbulence, which gives rise to unsteady loading on downstream turbines.

The wake-induced power losses and blade loadings are studied in two regions within the wake, referred to as near and far wake. The near wake starts right after the turbine and extends to approximately 2 – 4 rotor diameters (D) downstream [28, 64]. In this region, the flow is highly influenced by the rotor geometry, which leads to the formation of the blade tip vortices. In addition, there are steep gradients of pressure and axial velocity, and wake expansion. In the far wake, the effects of the rotor geometry are limited to the reduced wind speeds and increased turbulence intensities. Furthermore, the turbulence is the dominating physical property in the far wake [18]. In addition to the rotor induced turbulence, the region further downstream is influenced by the large scale (or atmospheric) turbulence. The turbulence mixing accelerates the wake recovery in terms of both the velocity deficit and the turbulence intensity. In the far wake, the velocity deficit approaches to a Gaussian profile, which is axisymmetric and self-similar [8]. Moreover, the meandering of the wake might also contribute to the recovery of the velocity deficit although it significantly increases the unsteady loading on the downstream turbine(s). All these elements lead to different approaches for the development of wind turbine wake models.

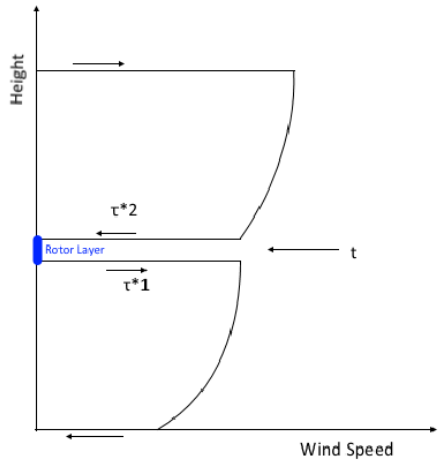

Figure 4.1: Illustration of the vertical flow shear, shear forces and external forces in the IWFBL model

4.1 Wake Models Developed at the Technical University of Denmark: A Review

In order to evaluate the existing selection of wake models developed at the DTU to decide which model to implement in the real-time PossPOW algorithm, an extensive conceptual review is presented in this section. The consequences of the main assumptions and simplifications considered in the models together with their targets of application are investigated through two benchmark cases constructed for Sexbierum and Lillgrund offshore wind farms.

4.1.1 Infinite Wind Farm Boundary Layer Model

An infinite wind farm boundary layer (IWFBL) model was developed by Frandsen [28]. In the model, around the turbine rotors, i.e. the "rotor layer", the velocity profile is reduced compared to that above hub height and both profiles are logarithmic as shown in Figure 4.1.

Inside the wind farm the turbines are assumed to be evenly spaced at a distance x and a dimensionless separation between the turbines is defined as; $s = x/R$, the term R being the radius of the turbine.

As shown in Figure 4.1, the difference in shear stresses around the turbine hub height is

$$t = -\rho C_T' u_h^2, \tag{4.1}$$

where u_h is the asymptotic spatial average wind speed at hub height, and C_T' is the simplified thrust coefficient with $C_T' = C_T\pi/(8s^2)$. Therefore the relation between the friction velocities and u_h can be calculated using

$$\rho u_{*2}^2 = \rho u_{*1}^2 + \rho C_T' u_h^2, \tag{4.2}$$

where u_{*2} is the friction velocity above and u_{*1} below hub height.

Note that, under the rotor layer, the logarithmic wind profile is valid and can be used to relate u_h to u_{*1} using logarithmic law. For the region above that layer, the simplified geostrophic law [41] is applied and the resulting expression is found as;

$$\frac{G-u_h}{u_{*2}} = \frac{1}{\kappa}\ln\left(\frac{G}{hf_p}\right), \tag{4.3}$$

h is the hub height, $f_p = f_c exp(A_*)$ where f_c is the Coriolis parameter, A_* is the modified A parameter from the resistance-law constants, and G the geostrophic wind speed. The friction velocities are parametrized as;

$$\begin{aligned} u_{*1} &= \frac{u_h}{K_1}, \qquad \text{where} \qquad K_1 = \frac{1}{\kappa}\ln\left(\frac{h}{z_0}\right), \\ u_{*2} &= \frac{G-u_h}{K_2}, \qquad \text{where} \qquad K_2 = \frac{1}{\kappa}\ln\left(\frac{G}{hf_p}\right). \end{aligned} \tag{4.4}$$

Substituting them into Equation 4.2 and solving for u_h yields

$$u_h = \frac{G}{1 + K_2\sqrt{K_1^{-2} + C_T'}} \tag{4.5}$$

After solving for u_h, the friction velocities, u_{*1} and u_{*2}, can also be calculated.

Additionally, Frandsen [28] approximated the wind speed reduction at hub height, $R_u = u_h/u_0$, where u_0 is the undisturbed wind speed at the same height, as

$$R_u \approx \ln\left(\frac{1}{e^{-1/\gamma} + C_T'}\right)^{\gamma}, \tag{4.6}$$

where $\gamma = 0.025/\ln(h/z_0)^{1/3}$, z_0 being the surface roughness.

Atmospheric stability correction

Peña and Rathmann [81] added atmospheric stability effects to the IWFBL model extending the logarithmic wind profile using a correction term depending on the dimensionless wind shear. The wind speed reduction has a similar form as that of Frandsen [28] where u_{*free} is the undisturbed friction velocity,

$$R_u = \frac{1 + K_2\left(u_{*free}\right)\sqrt{K_1^{-2}}}{1 + K_2\left(u_{*2}\right)\sqrt{K_1^{-2} + C_T'}}, \tag{4.7}$$

but both K_1 and K_2 are modified to include atmospheric stability by adding/subtracting the stability function, $\Psi_m(z/L_s)$,

$$K_1(u_*) = 1/\kappa\left[\ln\left(\frac{h}{z_0}\right) - \Psi_m(h/L_s)\right], \tag{4.8}$$

$$K_2(u_*) = 1/\kappa\left[ln\left(\frac{G}{hf}\right) - A_*(\mu_0) + \psi(h/L_s)\right], \tag{4.9}$$

where $A_* = ln\left(\frac{G}{fz_0}\right) - \frac{\kappa G}{u_*}$ and $\mu_0 = \kappa u_*/f_c L_s$,where u_{*2} for the section above rotor layer is formulated as

$$u_{*2} = \frac{u_h \kappa}{\ln(h/z_{00}) - \Psi_m(h/L_s)}. \tag{4.10}$$

z_{00} is the effective roughness length of the wind farm,

$$z_{00} = \left[\frac{-\kappa}{C_T + K_1^{-2}} - \Psi_m(h/L_s)\right]. \tag{4.11}$$

4.1.2 The Jensen Model

The Jensen wake model is one of the most popular models among engineering applications due to its simplicity, practicality and robustness. The description is based on the studies of Jensen [42] and Katic et al. [45].

Using the control volume presented in Figure 4.2, where $D = D_r$ is the rotor diameter, and assuming a top-hat inflow profile the mass balance between the rotor plane and the downstream flow yields,

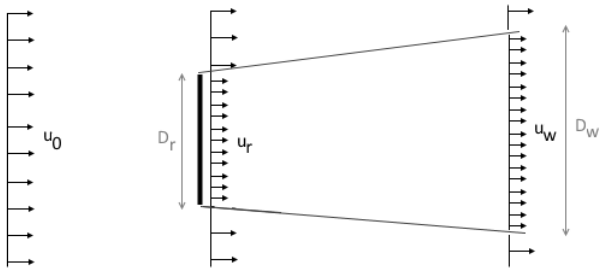

Figure 4.2: The control volume of the Jensen wake model

$$\left(\frac{D_r}{2}\right)^2 u_r + \left[\left(\frac{D_w}{2}\right)^2 - \left(\frac{D_r}{2}\right)^2\right] u_0 = \left(\frac{D_w}{2}\right)^2 u_w, \tag{4.12}$$

Also, the wake is assumed to be expanded linearly as a function of the downstream distance x at a rate α, $D_w = D_r + 2\alpha x$ and $u_r/u_0 = 1-2a$ using the axial induction factor, the fractional decrease in wind speed, $a = \frac{u_0 - u_r}{u_0}$. Putting them into 4.12, the normalized velocity can be found as

$$\frac{u_w}{u_0} = 1 - \frac{2a}{(1+2\alpha x/D_r)^2}, \tag{4.13}$$

Assuming ideal axially symmetric flow, no rotation, no turbulence and conic shape wake profile, the axial induction factor can also be written as

$$a = \frac{1-\sqrt{1-C_T}}{2}. \tag{4.14}$$

Interpretations of the Jensen Model

The Park Model The Park model implemented in WAsP [73] is based on the Jensen wake model and accounts for the effect of multiple wakes on the velocity. In the original version of Katic et al. [45], the ground interaction of the wake is taken into account by assuming an "underground rotor", which is a reflection of the original one. To derive the efficiency of a wind farm, the combination of the effects of four different overlapping mechanisms is considered:

1. Directly upwind rotor wakes
2. Reflected upwind "underground rotors"
3. Shading upwind rotors, located left or right of the directly upwind rotor
4. Reflected shading upwind rotors, located left or right of the wind direction

The local wakes are superposed to estimate the velocity deficit at the n^{th} turbine $\delta_n = \left(\sum_{i=1}^{n} \delta_i^2\right)^{1/2}$ where $\delta_n = 1 - \frac{u_n}{u_0}$

Infinite Row of Turbines Jensen [42] already estimated a model for the velocity deficit of an infinite row of turbines based on his wake model. If the velocity at the last partition of the infinite row of turbines is defined as u_{inf} then

$$\frac{u_{inf}}{u_0} = 1 - \left(\frac{2a}{1-2a}\right)\left(\frac{f}{1-f}\right), \tag{4.15}$$

where

$$f = \left[\frac{1}{1+2\alpha D_r x}\right]^2. \tag{4.16}$$

Infinite Park Wake Model Considering the effects of four overlapping of wakes in the Park wake model the total wake deficit δ_T is estimated as the quadratic sum of four types of wakes [79],

$$\delta_T^2 = \delta_i^2 + \delta_{ii}^2 + \delta_{iii}^2 + \delta_{iv}^2 \tag{4.17}$$

Rathmann et al. [88] has solved those effects analytically and Peña and Rathmann proposed [81],

$$\begin{aligned}
\delta_i^2 &\approx \frac{\delta_0^2}{(1+2\alpha s_r)^3}\left[\frac{1}{2(1+2\alpha s_r)} + \frac{1}{6\alpha s_r}\right], \\
\delta_{ii}^2 &\approx \frac{\delta_0^2}{128(h/D)^3}\left[\frac{1}{4(h/D)} + \frac{1}{3\alpha s_r}\right], \\
\delta_{iii}^2 &\approx \frac{\delta_0^2}{16 s_f^4}\left(1 + \frac{s_f/s_r}{\alpha}\right), \\
\delta_{iv}^2 &\approx \frac{\delta_0^2}{16 s_f^4}\left[\left(1+4\left[(h/D)/s_f\right]^2\right)^{-2} + \left(\frac{s_f/s_r}{\alpha}\right)\left(\frac{1-\left[1+4([h/D]s_f)^2\right]^{-3/2}}{6[(h/D)/s_f]^2}\right)\right],
\end{aligned} \tag{4.18}$$

where δ_0 is the initial wake deficit, $\delta_0 = \left(1-\sqrt{1-C_T}\right)$, s_r is the dimensionless stream-wise separation between turbines, i.e. $s_r = x/D$ and $s_f = y/D$ with y being the cross-wind turbine-turbine distance.

Wake Decay Coefficient When using the Park model in WAsP, the wake decay coefficient term α is by default $\alpha = 0.075$. In the study of Peña and Rathmann [81], the wake decay coefficient was shown to be a function of height roughness, atmospheric stability and turbulence separation. For practical purposes, the below expression is recommended.

$$\alpha = \alpha\left[\ln\left(h/z_0\right) - \Psi_m\left(h/L_s\right)\right]^{-1}, \tag{4.19}$$

which showed very good agreement with data from the Sexbierum [80] and the Horns Rev-I wind farms [82]. Using the similarity theory, α can be related to the turbulence intensity, TI, as $\alpha \approx 0.4TI$.

4.1.3 The Larsen Model

1988 (Early) Version

Larsen [55] has introduced a simple wake calculation procedure which was implemented in the commercial software WindPRO [75]. In the model, the axis-symmetric form of the RANS equations with the thin shear layer approximation is used. The pressure term appearing in the parabolic equations was also neglected and the turbulence closure, ν_T, was represented using Prandtl's mixing-length theory as

$$\nu_T = l^2\sqrt{S_{ij}S_{ij}}, \tag{4.20}$$

where l is the mixing length and S_{ij} is the strain rate tensor. The problem is assumed to be steady, axisymmetric and self-similar along the perpendicular direction to the flow.

Larsen considered the solution of the RANS equations using first and second order approximations. In the first order approximation, the expression to be solved together with continuity equation is simplified as:

$$U_\infty \frac{\partial u_x}{\partial x} = \frac{1}{r}\frac{\partial}{\partial r}\left[l^2 r\left(\frac{\partial u_x}{\partial r}\right)^2\right], \tag{4.21}$$

u_x is the wake perturbation of the inflow along the axial direction and r is the radial direction and x is the axis of symmetry.

In order to solve Equation 4.21, two boundary conditions are defined: 1) $u_x = 0$ on the boundary of the wake, and 2) $U_\infty \gg u_x$, which is obtained by writing the momentum balance assuming the inflow velocity to be much higher than the axial wake perturbations. Using those conditions, the radius of the wake, r_w, and the axial (u_x) and radial (u_r) wake perturbations are found as:

$$r_w(x,r) = (35/2\pi)^{1/5}(3c_1^2)^{1/5}(C_T A x)^{1/3}, \tag{4.22}$$

$$u_x(x,r) = -\frac{U_\infty}{9}(C_T A x^{-2})^{1/3}\left\{r^{3/2}(3c_1^2 C_T A x)^{-1/2} - (35/2\pi)^{3/10}(3c_1^2)^{-1/5}\right\}^2, \tag{4.23}$$

$$u_r(x,r) = -\frac{U_\infty}{3}(C_T A)^{1/3}x^{-5/3}r\left\{r^{3/2}(3c_1^2 C_T A x)^{-1/2} - (35/2\pi)^{3/10}(3c_1^2)^{-1/5}\right\}^2, \tag{4.24}$$

where C_T is the thrust coefficient, A is the rotor swept area, and c_1 is a constant that is defined empirically [55].

The second order system uses the full form of the RANS equations, which were later found to be negligible for most engineering applications [55].

2009 (Later) Version

The main improvements in the 2009 version of the Larsen model [53] compared to the 1988 one are the boundary condition(s) and the wind farm approach because the early version was derived considering the single wake case only and provided no solution for multiple wake situations.

The later version of the model defines the boundary conditions using the results of the analysis of full scale experiments. The first boundary condition is defined at the rotor plane and the second one is defined at a fixed frame of reference placed at a distance $9.6D$ downstream.

The second order approximation is neglected in the later version as well, and the wake radius and velocity deficit resulting from the updated boundary conditions are

$$r_w(x,r) = (35/2\pi)^{1/5}(3c_1^2)^{1/5}(C_T A(x+x_0))^{1/3}, \tag{4.25}$$

$$u_x(x,r) = -\frac{U_\infty}{9}\left(C_T A(x+x_0)^{-2}\right)^{1/3}\left\{r^{3/2}(3c_1^2 C_T A(x+x_0))^{-1/2} - (35/2\pi)^{3/10}(3c_1^2 f)^{-1/5}\right\}^2, \tag{4.26}$$

where

$$c_1 = (105/2\pi)^{-1/2} \left(\frac{d_1 D}{2}\right)^{5/2} (C_T A x_0)^{-5/6}, \tag{4.27}$$

$$x_0 = \frac{9.6D}{\left(\frac{2R_{9.6D}}{d_1 D}\right)^3 - 1}, \tag{4.28}$$

$$d_1 = \sqrt{\frac{1+1/\sqrt{1-C_T}}{2}}, \tag{4.29}$$

with $R_{9.6D}$ being the wake radius at $9.6D$, which is empirically calculated using the analysis performed for the Vindeby offshore wind farm, and expressed using atmospheric turbulence intensity, I_a as,

$$R_{9.6D} = a_1 \exp(a_2 C_T^2 + a_3 C_T + a_4)(b_1 I_a + 1)D, \tag{4.30}$$

where the constants a_1, a_2, a_3, a_4 and b_1 are defined in Larsen [53].

The wind farm approach is considered using two different methodologies to calculate the inflow speed: the geometric (or linear) averaging and momentum balance, which are respectively,

$$U_\infty = \bar{U} = \frac{1}{A}\int_A U dA, \tag{4.31}$$

$$\bar{U} = \sqrt{\frac{1}{A}\int_A U^2 dA}, \tag{4.32}$$

where U is the incoming ambient velocity modelled by logarithmic wind profile. The velocity inside the wind farm is calculated using the linear averaging as:

$$\bar{U}_m = \bar{U} - \sum_{\substack{i=1 \\ R_i \leq r_{0_i}+R}}^{M} u_{x_i}, \tag{4.33}$$

where M is the number of upstream rotors that generate wakes affecting the rotor m.

For the non-linear approach, the decomposition of U_m cannot be performed linearly, thus, the velocity profile imposed on rotor m may be described as;

$$\bar{U}_m = \sqrt{\frac{1}{A}\int_A \left(\bar{U} - \sum_{\substack{i=1 \\ R_i \leq r_{0_i}+R}}^{M} u_{x_i}\right)^2 dA}. \tag{4.34}$$

Equations 4.33 and 4.34 are solved using a 4-point Gauss integration method, which is explained in detail in Larsen [53]. Additionally, in both of those equations it can be seen that the multiple wake effects are superposed using the linear sum.

4.1.4 Dynamic Wake Meandering Model

The dynamic wake meandering (DWM) model describes the wake as a passive tracer driven by the large-scale turbulence structures in the atmospheric boundary layer. The model may be further investigated using the studies performed by Larsen et al. [56, 54] and Madsen et al. [63]. The recent improvements to the model and the validation cases are presented in [58, 46, 47, 48].

The DWM model consists of three elements, which together describe the essential flow characteristics behind a turbine: 1) Velocity or wake deficit; 2) Meandering of the wake and; 3) Rotor added turbulence. Here they will be considered separately.

Velocity Deficit

In the DWM model, the velocity deficit is initialised by the pressure gradient and formulated in the meandering frame of reference. The profile behind the turbine is assumed to be axisymmetric and steady. Parabolic Navier-Stokes equations with neglected pressure terms are used and the resulting equations are

$$U\frac{\partial U}{\partial x} + V_r\frac{\partial U}{\partial r} = \left(\frac{\nu_T}{r}\right)\frac{\partial}{\partial r}\left[r\frac{\partial U}{\partial r}\right], \tag{4.35}$$

$$\frac{1}{r}\frac{\partial}{\partial r}(rV_r) + \frac{\partial U}{\partial x} = 0, \tag{4.36}$$

where V_r denote the mean velocity along the radial direction. The eddy viscosity ν_T is mainly described by the methodology proposed by Ainslie [3] and manipulated to include ambient turbulence intensity,

$$\nu_T = F_2 k_2 \left(\frac{b}{r}\right)\left(1 - \frac{U_{def,min}}{U_H}\right) + F_1 k_{amb} I_{amb}, \tag{4.37}$$

where k_2 is an empirical constant for the flow field, b is the instantaneous wake half width, $U_{def,min}$ is the minimum wake wind speed, U_H is the wind speed at hub height, I_{amb} is the ambient turbulence intensity at hub height, k_{amb} is a calibration constant, and F_1 and F_2 are filter functions depending on the downstream distance x only.

Meandering of the Wake

As mentioned earlier, the DWM model assumes the wake to behave as a passive tracer transported in a large-scale turbulence field, where eddies larger than two rotor diameters. Therefore, the large-scale transversal and vertical velocities, v and w respectively, are important.

The displacement of the wake is defined by the characteristic velocities,

$$v_c(x^b, y^b, z^b) = \frac{1}{A_f}\iint_{A_f} v(x^b, y^b, z^b) dy^b dz^b, \tag{4.38}$$

$$w_c(x^b, y^b, z^b) = \frac{1}{A_f}\iint_{A_f} w(x^b, y^b, z^b) dy^b dz^b, \tag{4.39}$$

where (x^b, y^b, z^b) are the inertial coordinate system fixed to the turbulence box introduced, and A_f is the averaging area most logically selected as a circle in which the origin is assigned as (y^b, z^b) with a diameter D_w.

The transversal and vertical wake displacements are described as,

$$\frac{dy^g}{dt} = v_c(U[T - t_i], y^b, z^b), \tag{4.40}$$

$$\frac{dz^g}{dt} = w_c(U[T - t_i], y^b, z^b), \tag{4.41}$$

where T is the time interval considered in the "snapshot" associated with the Pseudo – Lagrangian approach formulated by $T = L/U$ with L being the along-width length of the turbulence box considered, and t_i is the time when the velocity deficit is released.

Additionally, the initial conditions at the time t_i are given as,

$$y^g(t_i) = 0; \qquad \frac{dy^g}{dt}|_{t=t_i} = v_c(U[T-t_i],0,0), \tag{4.42}$$

$$z^g(t_i) = 0; \qquad \frac{dz^g}{dt}|_{t=t_i} = w_c(U[T-t_i],0,0), \tag{4.43}$$

The solution to Equations 4.38 and 4.39 together with Equations 4.40 – 4.43 are presented in detail in Larsen [54] including methodologies for their simplification and a numerical algorithm. Finally, it should be noted that the wake deficit is not affected by the meandering progress.

Rotor Induced Turbulence

The rotor induced turbulence, or wake added turbulence, in the meandering frame of reference corresponds to the small scale turbulence, namely the tip, root and blade bound vortices, as well as the wake shear layer. In the DWM model, the wake added turbulence at a particular downstream position is modelled using an isotropic Mann turbulence box [65, 66], with cross sections corresponding to one rotor diameter. The Mann model looks at the spectral tensor of atmospheric turbulence at neutral stability state. The spectral tensor contains all information on spectra, cross-spectra and coherences that are required for engineering applications in wind energy. In the model, the Rapid Distortion Theory (RDT) [84] is combined with the "eddy lifetime" to describe the amount of shear, which gives the turbulence an anisotropic character. The model involves three adjustable parameters which can roughly be described as 1) a length scale that defines the size of the turbulent eddies, 2) a non-dimensional parameter to estimate the eddy lifetime, and 3) a parameter related to the energy.

Additionally, the added wake turbulence intensity is assumed to be rotationally symmetric and does not influence the meandering or velocity deficit processes.

In summary, the resulting turbulence in the DWM model includes components from meandering, added wake turbulence and ambient turbulence. The resulting velocity field may be expressed as

$$U_{res} = U_m + u_{aw} + u_{amb}, \tag{4.44}$$

$$v_{res} = v_{aw} + v_{amb}, \tag{4.45}$$

$$w_{res} = w_{aw} + w_{amb}, \tag{4.46}$$

where U_{res}, v_{res} and w_{res} are the axial, lateral and vertical velocity components of the resulting velocity field, respectively. The subscript *aw* represents the added wake component, and the subscript *amb* is the ambient contribution. Finally, U_m denotes the unsteady velocity component obtained from the meandering of the velocity deficit, which is determined as

$$U_m = U(x_m, r_m), \tag{4.47}$$

with x_m and r_m being the downstream axial and radial coordinates, respectively, updated at each time step.

4.1.5 FUGA

Fuga is a fast engineering tool based on the linearised RANS equations. It uses a system of look-up tables to construct the velocity field behind a turbine, and it uses linear summation to consider multiple wake cases. Due to its simplicity in wake modelling, Fuga is one the most robust computational fluid dynamics (CFD) based models established for wake effects calculations. The methodology presented in this study is based on the works by Ott et al. [78].

The Cartesian form of the RANS equations are used with a simple closure, where the eddy viscosity is equal to that usually used within the atmospheric surface layer.

$$\nu_T = \kappa u_* z. \tag{4.48}$$

Since the equations are not parabolised, there is no need to artificially induce the rotor velocity where the atmospheric inflow is modelled using the logarithmic wind profile including the stability effects. The drag forcing term, is modelled using an actuator disk model with a layered control volume as,

$$\bar{f_i} = f_x = -\frac{1}{2} C_T U_{free}^2 \delta(x - x_h)\Theta(R^2 - (y - y_h)^2 - (z - z_h)^2) \tag{4.49}$$

where δ is the Dirac delta function and Θ is a step function, which is equal to zero for negative and 1 for positive arguments. Due to the fluctuations related to the existence of a step function, the drag calculations are smeared out.

The simplified RANS equations are linearised using Taylor expansion and only the terms with order zero and one are considered. The zeroth order equations correspond to the case without any perturbations to the flow, meaning that there are no turbines. The drag force of order one, f_x^1, is defined by fitting the first order equations to a chapeau function. The resulting equations are further simplified using Fourier transformation

in which two mixed spectral variables are defined along x and y directions. A new numerical scheme is implemented to overcome the difficulties of solving a linearised model for flows over small values of z_0 which is the case for offshore sites with low roughness lengths and where the wakes are more pronounced. The scheme is described in detail in Ott et al. [78] together with the validation of the model for certain test cases.

4.1.6 Ellipsys3D

Ellipsys3D [69, 96] is a 3D general purpose CFD solver with a block-structured finite volume approach. Both RANS and LES models are available in EllipSys3D and can be further examined in Sanderse et al. [91].

RANS

In the RANS version of Ellipsys3D, the rotor is modelled as an actuator disk, the elliptic form of the Navier-Stokes equations are used thus no external induction is introduced, and the non-linear terms, $u_j\left(\frac{\partial u_i}{\partial x_j}\right)$, are discretised using the QUICK scheme [104].

Ellipsys3D can use a number of turbulence models. One of the latest development is the k-ε-f_P model [51], which is a modified version of the widely used k-ε model from Launder and Spalding [60]. Where the standard k-ε model fails to predict the velocity deficit in the near wind turbine wake [51, 13, 89, 22, 86], the k-ε-f_P model has shown good agreement with LES and measurements for single [51], double wake cases [102], and complete wind farms [52]. In the turbulence models, the turbulent eddy-viscosity is defined as:

$$\nu_T = C_\mu f_P \frac{k^2}{\varepsilon} \tag{4.50}$$

where C_μ is a constant, k the turbulent kinetic energy, and ε the turbulent dissipation. In the standard k-ε, $f_P = 1$ and the effective eddy-viscosity coefficient $C_\mu f_P$ is a constant. In the k-ε-f_P model, f_P is a scalar function that depends on the local shear parameter $\sigma \equiv \frac{k}{\varepsilon}\sqrt{(u_{i,j})^2}$.

The scalar function f_P in the k-ε-f_P model is defined as

$$f_P(\sigma/\tilde{\sigma}) = \frac{2f_0}{1+\sqrt{1+4f_0(f_0-1)\left(\frac{\sigma}{\tilde{\sigma}}\right)^2}},\ f_0 = \frac{C_R}{C_R-1}, \tag{4.51}$$

where $\tilde{\sigma}$ is the shear parameter in an idealized (logarithmic) neutral atmospheric surface layer and C_R is a calibration parameter. In the neutral stability solution, $f_P = 1$

because $\sigma = \tilde{\sigma}$. In regions with a high shear parameter, i.e. $\sigma > \tilde{\sigma}$, $f_P < 1$ and the turbulent eddy viscosity from Equation (4.50) is decreased.

The near wind turbine wake is characterized by high velocity gradients, where $\sigma >> \tilde{\sigma}$. As a result, the k-ε-f_P eddy viscosity model delays the wake recovery compared to the standard k-ε. It should be noted that C_R controls the magnitude of the delayed wake recovery. The constant C_R is calibrated against LES for eight different single wind turbine cases [51]. The same transport equations for k and ε are used in both turbulence models,

$$\frac{Dk}{Dt} = \nabla \cdot \left[\left(\nu + \frac{\nu_T}{\sigma_k} \right) \nabla k \right] + \mathscr{P} - \varepsilon, \tag{4.52}$$

$$\frac{D\varepsilon}{Dt} = \nabla \cdot \left[\left(\nu + \frac{\nu_T}{\sigma_\varepsilon} \right) \nabla \varepsilon \right] + \left(C_{\varepsilon,1} \mathscr{P} - C_{\varepsilon,2} \varepsilon \right) \frac{\varepsilon}{k}, \tag{4.53}$$

where $\mathscr{P} \equiv \overline{u_i' u_j'} U_{i,j}$ is the turbulent production, ν is the kinematic molecular viscosity and $C_{\varepsilon,1}, C_{\varepsilon,2}$, σ_k, σ_ε are constants. The values of the constants are listed in Table 4.1.

Table 4.1: Model constants.

C_R	C_μ	$C_{\varepsilon,1}$	$C_{\varepsilon,2}$	σ_k	σ_ε	κ
4.5	0.03	1.21	1.92	1.00	1.30	0.40

When the standard k-ε is applied to atmospheric flows, it is common to control the ambient turbulence intensity at a reference height $I_{H,\infty}$ with C_μ using

$$I_{H,\infty} \equiv \frac{\sqrt{\frac{2}{3}k}}{U_\infty} = \frac{\kappa \sqrt{\frac{2}{3}}}{\ln\left(\frac{z_{ref}}{z_0}\right) \sqrt[4]{C_\mu}}, \tag{4.54}$$

Subsequently, one of the model constants from Table 4.1 is adjusted to maintain the logarithmic solution [90]

$$\sqrt{C_\mu} \sigma_\varepsilon \left(C_{\varepsilon,1} - C_{\varepsilon,2} \right) + \kappa^2 = 0. \tag{4.55}$$

However, the behaviour of the f_P function changes when C_μ is altered, which is not desired. Therefore, the ambient turbulence intensity is set with z_0, and the friction velocity u_* is adapted to set the free-stream velocity. As a result, the velocity inflow profile differs from the measured profile, although the difference in the rotor area is only in the order of a few percent.

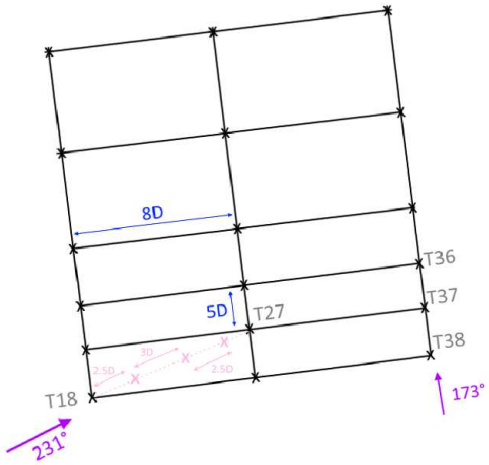

Figure 4.3: Sexbierum Wind Farm Layout

LES

In the EllipSys3D LES, the non-linear terms are discretised using a hybrid scheme formed of QUICK and fourth order central differencing schemes and the empirical constants are chosen based on the studies of Troldborg related with the actuator line [100]. There, the rotor is modelled as an actuator line, and the axial force is defined using BEM, which requires sectional aerodynamic characteristics of the blades but increases the efficiency of the calculations. The inflow velocity profile is defined considering the surface shear and the Mann Turbulence box [65, 66] is used as inflow turbulence, where neutral atmospheric conditions are assumed.

4.2 Benchmarking Study

4.2.1 Sexbierum Wind Farm

Introduction

Sexbierum is an onshore wind farm located in the Northern part of the Netherlands at approximately 4 km from the shore on homogeneous flat terrain, mainly grassland. It consists of 18 turbines with a total installed capacity of 5.4 MW. The layout of the wind farm is presented in Figure 4.3.

The turbines in the farm are HOLEC WPS 30–3 [27] with a rated power of 310 kW, a rotor diameter of 30.1 m and 35 m hub height. These turbines are pitch regulated with

a cut-in wind speed of 5 m/s, a rated wind speed of 14 m/s, and a cut-out wind speed of 20 m/s.

For Sexbierum case, two benchmarks were defined; the single and double wake cases by Cleijne [16, 15].

B1 - Single Wake In the single wake test case, the comparison between the simulations and the measurements is performed in the wake of the turbine T18. The met masts are placed 2.5, 5.5 and 8 diameters downstream of T18, and the wind speed measurements during 6 months provided in Cleijne [16] are considered in the benchmark. The observed wind speeds are between 5–10 m/s, where for the simulations 8 ± 1 m/s incoming wind speed is considered as this is the most frequent wind speed bin observed. The roughness length and the turbulence intensity at hub height are estimated to be 0.049 m and 9.5%, respectively. Neutral atmospheric stability is assumed for the wake computations but discussed afterwards.

In this benchmark, the results of the Jensen model, Larsen model (2009 version), Fuga, and Ellipsys3D RANS and LES solvers are presented. Two RANS turbulence models are tested: the standard $k-\varepsilon$ model and the $k-\varepsilon-f_P$ model. The RANS computations are performed with a domain size of $25D \times 16D \times 8D$. The inlet is defined at $5D$ upstream of T18 and the refinement of the mesh in the wake region is performed in such a way that there are 10 cells per rotor diameter as proposed by van der Laan et al. [51] to obtain good resolution in the near wake region with Ellipsys3D RANS. The high resolution area starts at $3D$ downstream from the inlet with a width and length of $4D$ and $14D$, respectively. Vertically, it starts from $0.5D$ below hub height and goes up to $1.5D$ above the rotor. The mesh has a maximum expansion ratio of 1.2 with an initial height of z_0 on the ground. The computational domain for Ellipsys3D RANS includes 1.57 million cells, and the boundary conditions for that domain are: 1) rough wall condition at the ground surface, 2) symmetric boundary conditions on the sides, 3) inlet velocity condition at the inlet and top, and 4) far field outlet boundary conditions.

The time required to run Ellipsys3D RANS for the single wake case with a convergence criterion of 10^{-5}, i.e. the iteration is terminated when the difference between two calculation steps falls below 10^{-5}, is 3-minutes and 3-sec with a time step of 0.008-sec and 48 CPUs.

The computational domain used for Ellipsys3D LES is the same for both the single and double wake cases and its dimensions are $15D \times 15D \times 23.25D$. The inlet boundary is located at $7.35D$ from the first upstream turbine (T18 for single wake, T38 for double wake case). The grid points are distributed uniformly in such a way that there are 30 points corresponding to each rotor, and two refined regions to resolve the inflow and wake turbulence. The first high resolution region is located at $0.35D$ upstream of the first turbine and extends to $10.3D$ downstream with a height and width of $1.8D$. The second highly resolved area is located at $1.8D$ upstream of the first turbine where the inflow turbulence is introduced. It has the same height and width of $1.8D$ and it extends to $1.9D$.

The computational domain has 19.7 million grid points and the boundary conditions for that domain are: 1) no slip condition at the ground surface, 2) periodic boundary conditions on the sides, 3) far – field velocity on the top, 4) inlet velocity and turbulence as described in Section 4.1.6, and 5) unsteady convective outlet conditions.

The computational time required to run the single wake case using the Ellipsys3D LES for 12-minutes real-time with a time step of 0.008-sec and 150 CPUs is approximately 4 days and 4 hours. However, it should be noted that the computational domain used for the single wake case was actually optimized for the double wake case. Therefore it should be expected that the performance of the simulation in terms of the computational costs can be enhanced by simplifying the mesh according to the single wake requirements.

B2 - Double Wake In this benchmark, the power measurements of turbine T36 in the wake of T38 and T37 (see Figure 4.3), covering a period of 3 months are studied. Similar to the single wake case, the wind speed interval is 5 – 10 m/s for the dataset. The model simulations are performed at 8 m/s and the roughness length and turbulence intensity are 0.045 m and 9.5%, respectively, as recommended by Cleijne [15].

For the double wake case, the results of the Jensen model, Larsen model, Fuga, and Ellipsys3D RANS (using the same two turbulence models) and LES solvers are presented. Four relative different wind directions [0°, +7°, +14°, +21°] are simulated in LES, and 22 min of data with a time step of 0.008-sec and 150 CPUs took over a week to run, which corresponds to approximately 27500 CPU hours.

Sexbierum Results and Discussion

B1 - Single Wake In the Sexbierum single wake case two different wind direction averaging techniques are applied to both the Jensen (with wake decay coefficient, $\alpha = 0.04$) and the Larsen results; a wind direction sectoral averaging (BinAve) and a Gaussian averaging considering the wind direction uncertainty [30] (GauAve). For these two models, the bin averaging is performed for a 30° wind direction span where 2.5° simulations are run and averaged over 5° bins. The Gaussian averaging method was applied with a standard deviation of 5° in the wind direction, although no information about the wind direction uncertainty is provided in the corresponding report [16]. Note that, the free stream wind direction is measured via the meteorological mast and given relative to the line connecting turbines $T18$ and $T27$, denoted as 0°.

The wake model performance in the near wake region is compared in Figure 4.4. All the model and solver results, independently from the post-processing method, considerably deviate from the measurements. The data were collected approximately for only 43 hours, therefore they are not statistically representative.

The deviation might be due to the atmospheric conditions. However, the atmosphere is very likely to be stable during the measured period [80]. With a low turbulent mixing

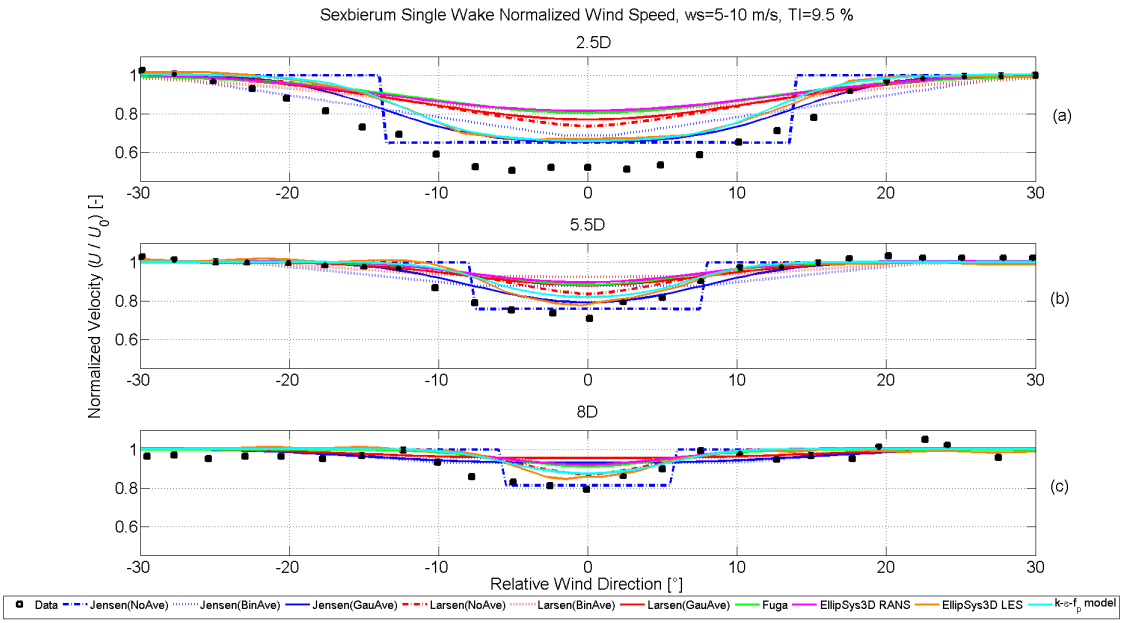

Figure 4.4: Sexbierum single wake normalized wind speed at (a) 2.5D downstream, (b) 5.5D downstream, and (c) at 8D downstream

of the stable atmosphere, the wake takes longer to recover, which explains the depth of the measured wake together with the under-estimation of the models, which are valid for neutral conditions, especially in the near wake region – see Figure 4.4(a).

Looking at the performance of the models, Fuga, the Larsen and the standard $k-\varepsilon$ RANS underestimate the velocity deficit, and the $k-\varepsilon-f_P$ compares well with the LES (note that the LES results are not Gaussian averaged though). The Jensen model, the simplest of all, with Gaussian averaging provides very similar results to those of LES at $2.5D$ and $5.5D$ downstream distances. The Jensen model outperforms the others because of the wake decay coefficient used in the simulations. For onshore sites the recommended value is $\alpha = 0.075$, whereas in our case $\alpha = 0.04$ but as shown in Peña et al. [80] α could be even lower.

B2 - Double Wake Figure 4.5 is a combination of the results of the Jensen (with a wake decay coefficient of $\alpha = 0.04$), the Larsen and Fuga models, EllipSys3D RANS $k-\varepsilon-f_P$ and Ellipsys3D LES solvers where the runs were performed in a similar manner as in the single wake case using a 5°bin and a wind direction step size of 2.5°.

Similar to the single wake case, the models generally under-predict the wake losses

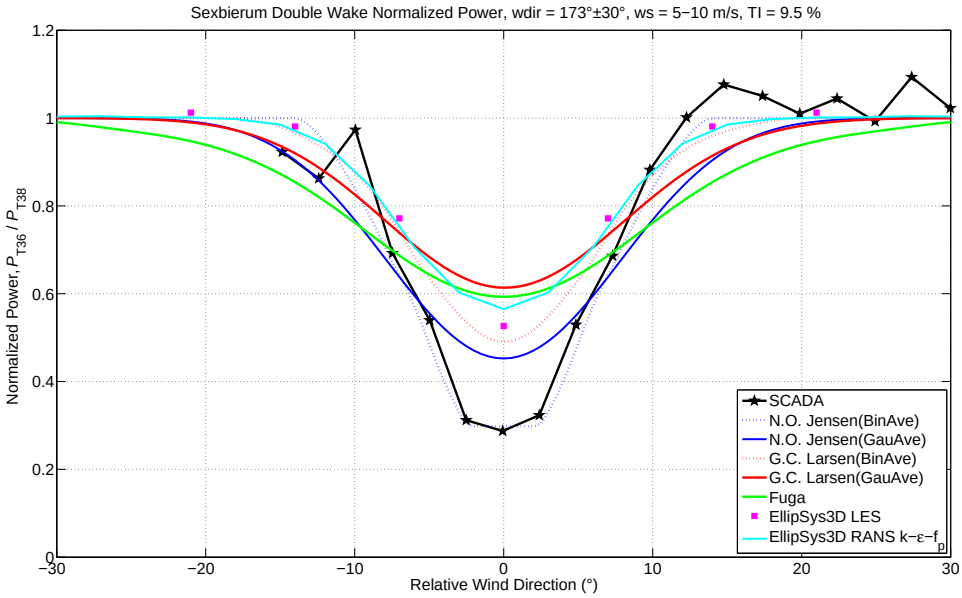

Figure 4.5: Sexbierum Double Wake Normalized Power flow direction = 173°±30°

which might be due to the stable atmospheric conditions (9.5% turbulence intensity for a 0.045 m roughness length).

Apart from the performance of the Jensen model, especially the bin averaged version, the Larsen model with bin average seems to perform very well compared to the LES results. This might be due to the turbine spacing for the double wake case $(10D)$ which is very close to the distance that the model is calibrated $(9.6D)$. On the other hand, the Gaussian averaged version of the Larsen, Fuga and RANS $k-\varepsilon-f_P$ turbulence model results seem to deviate from the measurements. Note that the Gaussian averaging takes into account the wind directions that might highly differ from the mean value during the averaging time period. However, for less turbulent cases, the deviation of the wind direction from the mean value is small. In that case, the wake deficit profile is over-smeared and the details are lost.

Notes and Remarks about the Sexbierum Wind Farm case The benchmarks included in the Sexbierum case were constructed using the reports of Cleijne [16, 15] and all the models except for DWM were used for the simulations. In general, the models seem to deviate from the measurements significantly, which may be a consequence of

the probable stable characteristic of the atmosphere. The Jensen model with a low wake decay seems to provide very good results although it is the simplest model used. It is concluded that the post processing approach for stable cases should be revised and differ from the one developed for the neutral atmospheric conditions.

Note that in all the cases, the measured wake deficit profile is far from being symmetric which may occur due to the onshore effects such as terrain complexity, etc. However, it is not easy to tell since the dataset covers only a short period of time and the observations might be biased in terms of the atmospheric stability by the seasonal variation of the atmospheric stability. The wind farm wake modelling, especially for onshore sites, requires more inputs to model the inflow and the Sexbierum case is another example of data issues encountered in wind farm simulations.

4.2.2 Lillgrund Offshore Wind Farm

In the EERA-DTOC report for the Lillgrund wind farm test case, Figure 3.6, four benchmarks were specified as listed below [35].

B1 - Sector Variation The power deficit along complete rows with internal spacing of $3.3D$ and $4.3D$ is simulated to test the sensitivity of the models to the flow direction. The roughness length is 0.0001 m, the inflow mean velocity at hub height is 9 m/s and the inflow turbulence intensity at hub height is 6 %, which is estimated based on sector wise-long term measurements of the met mast.

Two different rows that do not have a missing turbine are used and for the $3.3D$ case the wind direction is in the interval $120^\circ \pm 15^\circ$, whereas for the $4.3D$ case it is $222^\circ \pm 15^\circ$. Note that, the runs are performed at every 2.5° step for both arrays.

B2 - Speed Recovery The power deficit along a row with missing turbine(s) and internal spacing of $3.3D$ and $4.3D$ are observed. In addition, the sensitivity of the models to the flow direction together with the speed recovery due to the missing turbines is tested. The input data and the characteristics of the runs to be performed are the same as in the previous benchmark, B1.

B3 - Power Deficit as a function of Turbulence Intensity The calculations are performed for different inflow turbulence intensity levels at hub height (2-12%) with the same inflow conditions as in the previous benchmarks. Two different runs are performed for both $3.3D$ and $4.3D$ spacings using only the first two turbines in the row and the wind direction sectors are $120^\circ \pm 2.5^\circ$ and $222^\circ \pm 2.5^\circ$, respectively.

B4 - Park efficiency The wind farm park efficiency is defined as the ratio between the wind farm total output power and the power of the wind farm assuming undisturbed

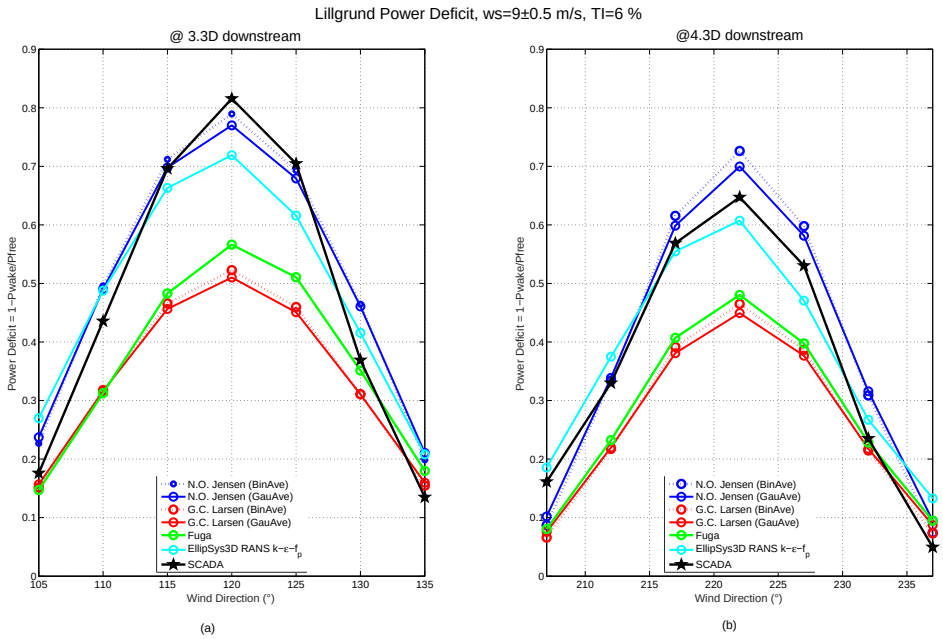

Figure 4.6: Lillgrund power deficit at (a) 3.3D for $120^\circ \pm 15^\circ$ and (b) 4.3D for $222^\circ \pm 15^\circ$

inflow for each turbine. Similar input data as in the previous benchmarks is considered and the inflow sector is taken as $0-360^\circ$ with a span of 3°.

Results and Discussion

We use a wake decay coefficient of 0.04 for the Jensen model with a quadratic sum for the wake summation, whereas for the Larsen model a linear summation is applied. Additionally, the thrust coefficients in both models are those provided by the turbine manufacturer.

B1 - Sector Variation In Figure 4.6, two different wind direction averaging techniques with 3 different models are run for this case with 3.3D and 4.3D spacings. The simulations are run at 2.5° step wind directions and averaged over 5° bins. The Gaussian averaging is applied for a 5° standard deviation in wind direction. Additionally, the same technique is applied to Fuga where the uncertainties in wind direction are taken into account using a Gaussian distribution of 4.9°. The Larsen model and Fuga under predict the wake losses for the second turbine placed at 3.3D and 4.3D. Both models

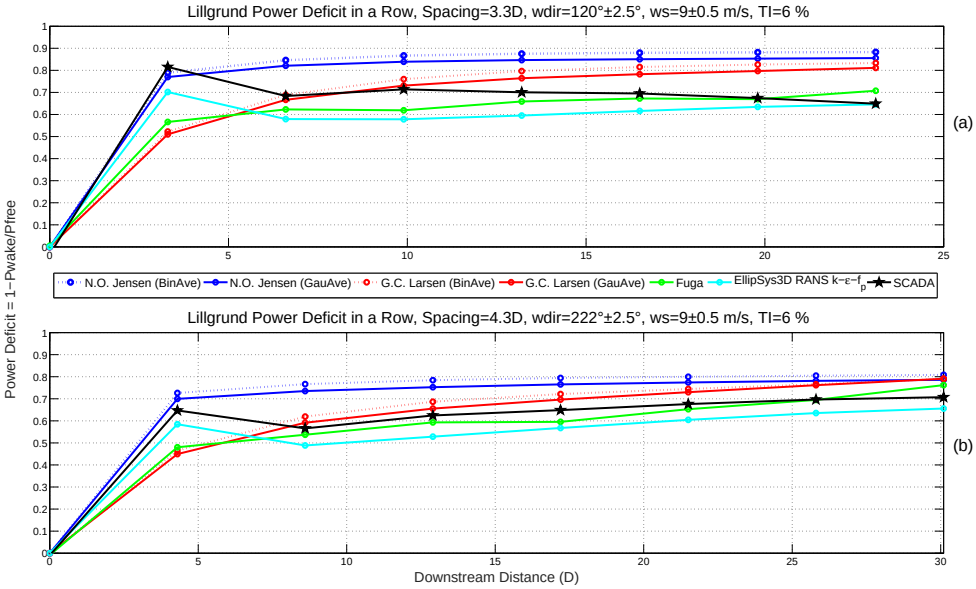

Figure 4.7: Lillgrund power deficit in a row with (a) 3.3D spacing and $120^\circ \pm 2.5^\circ$ and (b) 4.3D spacing and $222^\circ \pm 2.5^\circ$

are however designed to simulate the flow behaviour at much larger downstream distances. On the other hand, as shown in Figure 4.7(a), the wake deficit under-prediction is compensated with a good prediction for the following rows, especially for the Larsen model.

The models are shown to perform better for wider wind direction sectors in Lillgrund by Gaumond et al. [31]. In our case, the EllipSys3D RANS $k-\varepsilon-f_P$ model over-performs to estimate the power deficit at the second wind turbine, because the f_P function delays the wake recovery compared to the standard $k-\varepsilon$ model.

B2 - Speed Recovery In Figure 4.8, the recovery point is clearly seen at 16.5D for $120^\circ \pm 2.5^\circ$ and 17.2D for $222^\circ \pm 2.5^\circ$. All the models capture the recovery and for this particular case the Larsen and the $k-\varepsilon-f_P$ model seem to estimate the power production reasonably well, especially after the second turbine. Both the Jensen and the Larsen models produce better results with the post processing of the wind direction uncertainty using a Gaussian distribution, which was also the case in previous benchmark, B1. Fuga seems to over-predict the power production for the first downstream turbine and then

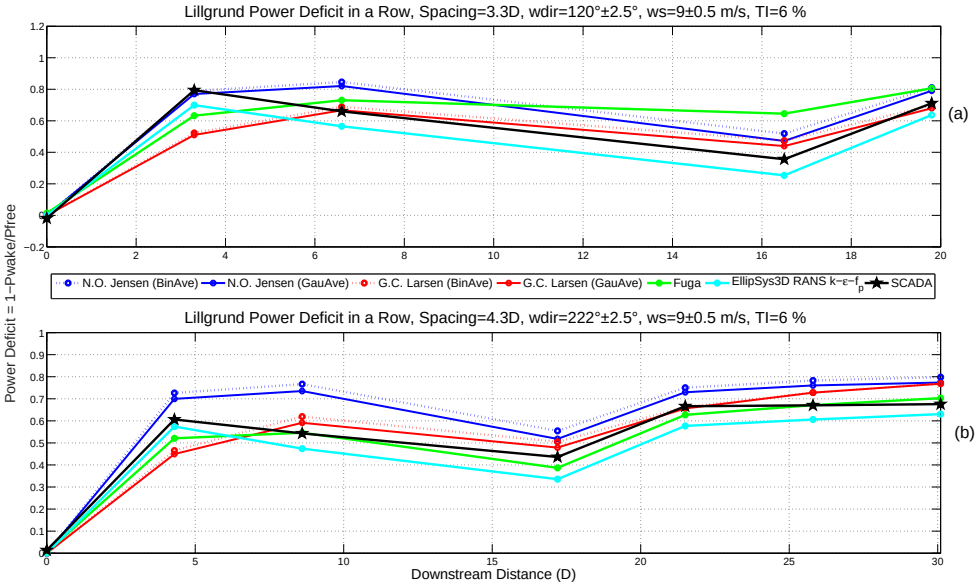

Figure 4.8: Lillgrund power deficit in a row with (a) 3.3D spacing, 2 missing turbines and 120° ± 2.5° and (b) 4.3D spacing, 1 missing turbine and 222° ± 2.5°

under-predicts the power production for the following turbines including the recovery point in the 3.3D spacing case. However, for the 4.3D spacing case, and similar to the previous benchmark, agreement between Fuga and the measurements is improved.

B3 - Power deficit as a function of turbulence intensity The standard uncertainty of the power deficit for the turbulence case is represented by the error bars in Figure 4.9 with a confidence level of 68% for the SCADA results [37].

Since the original Jensen model does not consider the variations in turbulence, it remains constant. Both the Larsen model and Fuga significantly deviate from the measurements, especially for high turbulence levels. Increasing turbulence intensity levels show larger lateral wind components. That results in greater wind direction variations. Due to those large variations and narrow sectors, both models might fail to reproduce the observations well. The necessity to use the local turbulence intensity in simulations is addressed later in this study. Furthermore, a pragmatic approach to introduce dynamic effects to the engineering wake model is developed and presented in the following chapter.

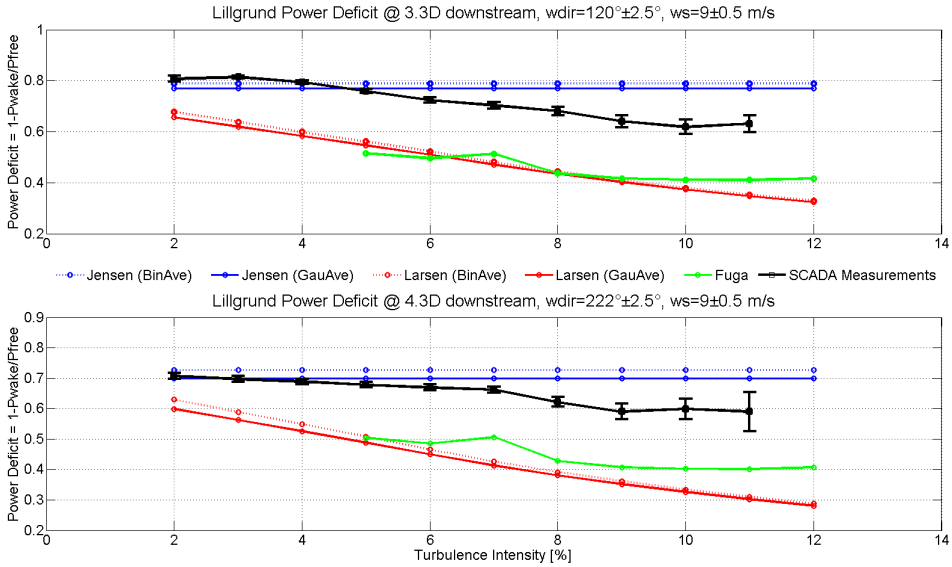

Figure 4.9: Lillgrund power deficit in a row at (a) 3.3D with $120^\circ \pm 2.5^\circ$ and (b) 4.3D with $222^\circ \pm 2.5^\circ$

B4 - Park efficiency The error bars indicated in Figure 4.10 corresponds to the uncertainty of power deficit with a 68% confidence level for the SCADA results [37]. The improvement of the model results by post-processing the wind direction uncertainty using a Gaussian distribution is considerable. Those Gaussian averaged versions of the Jensen and the Larsen model show a fair agreement with measurements. However, significant differences around maxima and minima, which are critical wind direction sectors are observed.

Remarks about Lillgrund Wind Farm case Especially for the first three benchmark cases, the narrow wind sector of 5° ($\pm 2.5^\circ$) is the major source of uncertainty since the data is 10-min averaged and most probably includes wind directions outside of that range.

Overall, the Larsen model and Fuga performed in a similar manner when considering a Gaussian distribution for the direction uncertainty, in agreement with the results obtained for Horns Rev Wind Farm [30]. In such a layout with small turbine spacings, the k-ε-f_P closure of the Ellipsys3D RANS is seen to capture well the wind speed at the closest turbines through downstream. It can be said that even though the direction bins

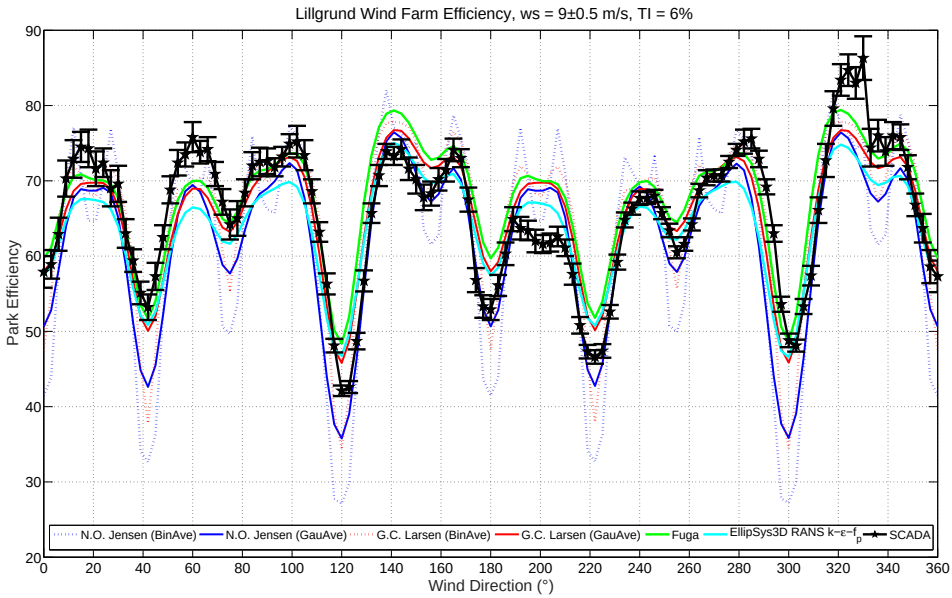

Figure 4.10: Lillgrund wind farm efficiency for inflow sector $0-360^\circ$ with 3° increment and 1.5° sector

are narrow $(\pm 2.5^\circ)$ for 10-min averaged data, the performances of all the models were considerably good in all benchmarks in general.

4.3 Application of the Models

In this section, the application of the wake models developed in DTU will be discussed in terms of their typical usage, validity, accuracy, complexity, the uncertainty of the required inputs and computational costs.

4.3.1 Typical Usage

The WAsP version of the Park model based on the Jensen model is targeted for wind farm planning and annual energy production (AEP) estimates. Due to its simplicity and practicality, it is often used to perform preliminary studies which are then improved with more sophisticated models.

Similarly, the Larsen model, also implemented in WindPro, is used for both single wind turbine and wind farm design and development stages. Fuga is a relatively new model. However, its robustness, speed, and promising results have already made it popular in the wind energy industry, and it is recently implemented in WAsP. The results showed that especially for the Lillgrund offshore wind farm case, Fuga and the Larsen model provide good results and are comparable to those of the more sophisticated models in offshore.

The DWM model is not only developed to be able to estimate the power production losses due to wake effects but it can also calculate the loading caused by the wake effects. It is implemented in the aeroelastic code HAWC2 and calibrated accordingly but unfortunately it was not available for the present work.

The LES version of Ellipsys3D, due to its complexity and computational cost, is run by a limited number of users and mainly for academic purposes. Additionally, both RANS and LES simulations are conventionally performed for small number of turbines rather than large scale wind farms for the same practicality reasons.

4.3.2 Accuracy

Most of the models proposed show a fair agreement with the observations especially when they are post-processed to take into account the wind direction uncertainty or the atmospheric stability conditions. Physically, the models with more realistic considerations, or in other words less simplifying assumptions are more successful in simulating wake characteristics in detail. Thus, in general, the more complicated models are more likely to be more accurate. However, the Sexbierum test case in Section 4.2.1 showed that even the most sophisticated models can fail to reproduce the flow characteristics when the inputs are erroneous or deficient.

Complexity and uncertainty of inputs

The quantity and quality of the modelling inputs are crucial for wakes. In general, all models regarding their complexity require measurements of the turbulence level and the atmospheric stability condition. Additionally the wind speed and direction should contain information about their distribution so that a proper post-processing can be performed and the results are fairly compared with the observations. Particularly for Ellipsys3D LES, when modelling the wind turbine, the tabulated values of the airfoil aerodynamic properties are required, which are calculated using the airfoil geometry. Such information is hard to obtain from the manufacturers. In addition, the methodologies used to obtain the lift and drag coefficients of a given geometry have their own inaccuracies and limitations.

In the two field validation test cases for the existing wake models developed at the DTU Wind Energy presented in this chapter, it was seen that even the most representative LES models fail to reproduce the flow behind the turbine(s) when the inflow wind

conditions are not properly described. On the other part, even the simplest Jensen wake model was observed to perform satisfactorily for the corrected inputs. Having that in mind, here in the rest of the study, the data to be introduced to the real-time wake modelling (both in re-calibration and validation studies) is to be handled with care where the extensive uncertainty analysis is left as a future work.

4.3.3 Computational costs

In general, the computational expenses of the wake models increase with the complexity of the model. Therefore, the Jensen model is the fastest to produce results, followed by the Larsen model and Fuga. The DWM model needs a relatively highly resolved turbulence field to feed back the aeroelastic code in the current version, but yet the computational cost is not implied as a main issue. Ellipsys3D on the other hand, suffers a lot from high CPU usage especially for the LES version, which eventually limits its application to the super-computers or clusters. There are a lot of studies regarding the hybrid RANS and LES methods which are more accurate and representative than RANS simulations but still more affordable than LES alone. A comprehensive review of various approaches to couple RANS with LES may be found in the study of Fröhlich and von Terzi [29].

Concluding Remarks & Model Selection for the PossPOW Algorithm

Since the PossPOW algorithm is designed to perform real-time and is constructed based on operational data, the fast and robust wake models were of particular interest throughout the benchmarks. Especially for the Lillgrund offshore wind farm, both the Larsen and the Fuga models are observed to accomplish good results, particularly when the uncertainty in the wind direction is taken into account. Comparing the two, the parametrisation setup of the Larsen model is found to be much more straightforward and flexible. Additionally, the real-time application of the look-up tables might affect the processing time of Fuga and the required input of atmospheric stability is difficult to get from many of the operating wind farms. Therefore, the Larsen model was decided to be used in order to clear the reduced wake effects inside the down-regulated wind farms throughout the PossPOW algorithm.

5

Re-calibration of the Larsen Model for Real Time Wake Modelling

As discussed in the previous chapter, most of the existing computationally affordable wake models are tuned and validated for 10-minutes data to simulate steady-state, long term behaviour. However, in order to observe the wind farm operations on-line and develop active control strategies accordingly, dynamic simulations that are capable to represent short term performance are required. Instead of developing yet another wake model, here we choose to re-calibrate the Larsen wake model, described in detail in Section 4.1.3, as it is robust and shown to perform relatively well also on offshore, see Section 4.2.2 and [31].

The re-calibration process requires the formulation of the parameters to be adjusted inside the Larsen model which includes the variables of the turbine thrust coefficient, C_T, and the local turbulence intensity, TI. In this chapter, the TI estimation procedure using the SCADA signals is described before the details of the actual parameter fitting are presented. The re-calibrated model, together with the estimated effective wind speeds constitute the PossPOW algorithm which will be applied to operating offshore wind farms to provide a real-time power curve and available power during curtailment.

5.1 Estimation of Turbulence Intensity using Turbine Data

In wind farm calculations, the best possible way to estimate the TI is to use the standard deviation and the mean of the wind speed over 10 minute intervals measured by a meteorological mast (met mast). However, those measurements do not provide the accurate TI at the turbine position since they are located elsewhere and, depending on the wind direction, the measurements might be in the wake of the wind farm or any other obstacle. Also in some cases, often after the turbines started operating, the met mast measurements are not available or they can not be used due to data issues [36, 6]. On the other hand, to estimate the turbulence in the wake either advanced, computationally expensive numerical simulations or parametrised correlations fitted to the experimental data are in use, depending on the distance from the upstream turbine [103]. Here we propose another method to estimate the TI using the turbine data which is applied to the Lillgrund and Horns Rev I offshore wind farms. The results are compared with the TI

derived from the met mast measurements as well as the standard deviation of the nacelle anemometer wind speed and the power fluctuations. Both the atmospheric and wake added TI are calculated using the local rotor effective wind speeds described in Chapter 3.

5.1.1 Atmospheric Turbulence Intensity

The atmospheric turbulence levels are generally lower offshore than over land and the typical TI values offshore are 6 – 8% [6]. Low atmospheric turbulence, together with stable conditions, tends to delay the wake recovery and does not necessarily mean less structural loading on the turbines since the wake added turbulence plays an important role. Therefore, also in the offshore wind farm calculations the TI is considered to be an important parameter [95].

The TI calculated using the 1 Hz met mast measurements for a period of 7 months is compared to the upstream turbine data in Lillgrund, for details of the dataset see Section 3.2.3. Using 1 Hz SCADA data, the atmospheric TI is computed using; 1) the nacelle anemometer measurements, 2) Siemens estimated wind speed, 3) rotor effective wind speed as described in Chapter 3, and 4) the standard deviation of the active power signal from the most upstream turbine(s) in Equation 5.3. The implementation of the first three methods is fairly straight-forward. In the last approach, the standard deviation of the active power is correlated to the standard deviation of the wind speed using the method developed by Jørgensen et al. [44] based on Thomsen and Petersen [68], as

$$\sigma_P = B\sigma_U \left(\frac{dP}{dU}\right)_{U_{pow}}, \tag{5.1}$$

where σ_P is the 10-min standard deviation of the active power signal sampled at 1 Hz, B is a constant typically ranges between $0.8 - 0.9$, depending on the mean wind speed, P is the active power and U is the wind speed. The slope $\left(\frac{dP}{dU}\right)_{U_{pow}}$ is calculated using the manufacturer's power curve and the mean power curve wind speed. Therefore, it is important to note that the difference between the operational power curve and the manufacturer's power curve affects the results. Additionally, the method is only applicable where the slope, $\left(\frac{dP}{dU}\right)_{U_{pow}}$ is other than zero and the turbine is operational, i.e. between the cut-in and rated wind speeds, 4 – 13 m/s for SWT – 2.3 – 93 offshore wind turbine.

In order to approximate the constant B, the methodology proposed by Barthelmie et al. [7] is implemented as

$$B = \frac{\sigma_P}{\left(\frac{dP}{dU}\right)_{U_{pow}} U_{pow} TI_{metmast}}, \tag{5.2}$$

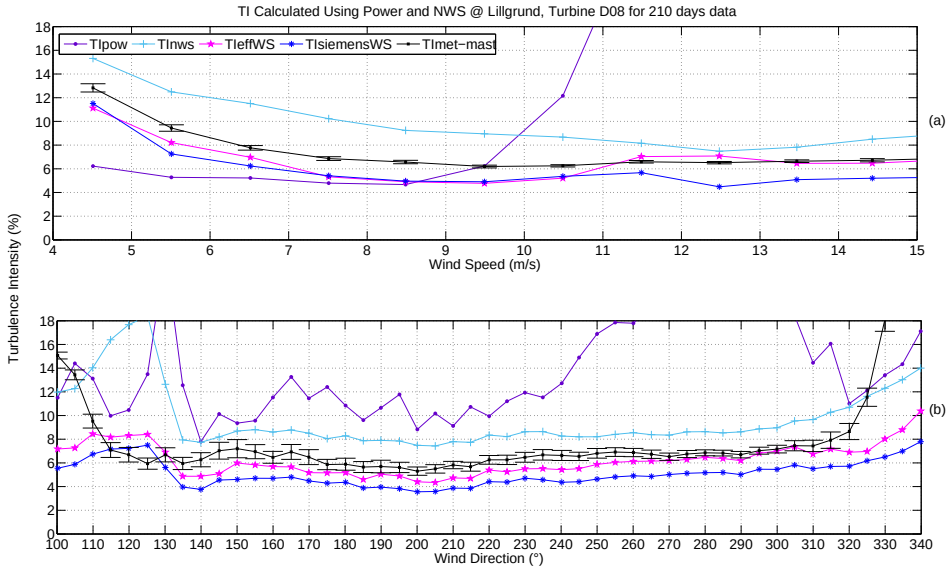

Figure 5.1: Ambient Turbulence Intensity in Lillgrund, presented in terms of (a) the wind speed (b) the wind direction, errorbars indicating 95% normalized confidence intervals

where the TI calculated by the power fluctuations (TI_{pow}) is assumed to be equal to the TI calculated using the met mast measurements ($TI_{metmast}$). Averaging results between 5 and 12 m/s, using another dataset from Lillgrund covering 3 years period (from 01/2012 to 01/2015), gives $B = 0.744$ which is considered in both the atmospheric and the wake induced turbulence calculations.

In Figure 5.1, the ambient TI is calculated using the met mast together with the power measurements, nacelle anemometer (TI_{nws}), Siemens estimated wind speed ($TI_{SiemensWS}$), and rotor effective wind speed (TI_{effWS}) at turbine $D08$. The results are averaged over 1 m/s bins between 4.5 - 15.5 m/s for all the wind directions in the top figure and; over 5° wind direction bins for all the wind speeds in the bottom figure where $TI_{metmast}$ is presented with 95% confidence level normalized with respect to the number of data points in the interval.

It can be seen from both Figure 5.1(a) and (b) that the TI_{nws} is higher than the $TI_{metmast}$ for all the wind speed and directions, as expected due to the high levels of noise in the signal. Although the TI_{pow} is in a good agreement with the met mast for low speed flows, around the rated wind speed it rapidly increases due to the behaviour of the power curve. The TI_{effWS} on the other hand, seems to be successfully representing the

characteristics of the $TI_{metmast}$ with a consistent bias similar to the Siemens estimated wind speed. That difference can be explained by the fact that the $TI_{metmast}$ is calculated using the point measurements whereas the TI_{effWS} and $TI_{SiemensWS}$ are considering the wind speed seen by the whole rotor. That automatically includes the geometrical averaging between 21.5 m – 114.5 m, which smooths out the fluctuations in wind speed.

Where the wind direction is between $100-120^{\circ}$ and $320-340^{\circ}$ in Figure 5.1(b), the results of the TI_{effWS} and $TI_{metmast}$ are diverse due to the location of the turbine $D08$ and the met mast, where the met mast is affected by the wake - see Figure 3.6(a). Note that the TI measured by the met mast in the wake is much higher than the atmospheric TI which will be discussed later in detail.

5.1.2 Turbulence Intensity in Wind Turbine Wakes

Downstream of a turbine, in addition to the atmospheric turbulence the wake induced turbulence should also be taken into account. While increasing TI corresponds to higher mixing and therefore reduced wake losses, its impact on the fatigue loading of the downstream turbine(s) is significant mainly due to the partial wakes [14].

Since the atmospheric TI calculations show that the rotor estimated wind speed gives the best TI estimate, the other TI calculation methods are not implemented in the added wake calculations. The turbulence at the downstream turbine positions are estimated using only the rotor effective wind speed for both of the wind farms.

Wake Added TI in Lillgrund

The 1-sec turbine data in Lillgrund is extracted from the turbines indicated in Figure 3.6(a). For the calculations of the TI in the wake, Row 8 (D08, C08, B08) with $3.3D$ and Row B (B08, B07, B06) with $4.3D$ turbine spacings are analysed and compared with the met mast data.

Figure 5.2(a) clearly shows the effects of the wake along the wind directions $120\pm 10^{\circ}$ and $300\pm 15^{\circ}$ where the turbine B08, shown in purple, is the most upstream turbine around 120° and the most downstream around 300°. Outside of that interval, the TI is almost identical between the turbines and corresponds to the atmospheric turbulence, as in Figure 5.1. During both of the south-east and north westerly winds, the TI seems to be the highest at the second turbine in the row even though the third turbine is exposed to a double wake. This behaviour is in line with the wake deficit calculations performed as a benchmark case in Section 4.2.2 where the wake deficit at the second turbine is visibly higher than the third and it remains approximately constant among the rest of the turbines in the row.

To understand the relation between the TI and the local wake losses, the standard deviation and the mean wind speed are investigated separately. It can easily be seen in Figures 5.3(a) and 5.2(a) that the standard deviation and the TI have the same pattern

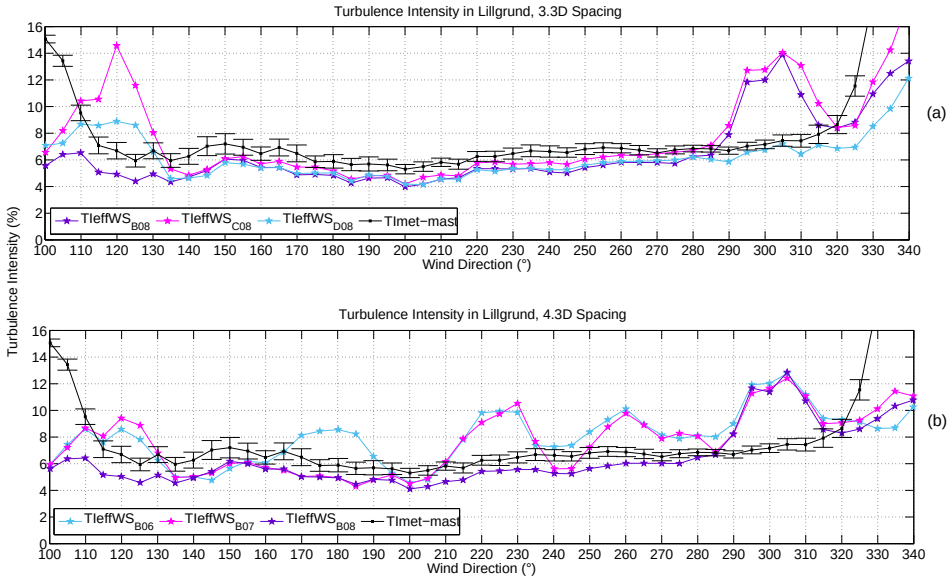

Figure 5.2: Turbulence Intensity in the wake, estimated using the rotor effective wind speed along (a) Row 8 – 3.3D spacing (b) Row B – 4.3D spacing, averaged over 5° wind direction bins, errorbars around the *TImet-mast* indicate 95% normalised confidence intervals

where the wake loss directly affects the difference between the upstream and downstream turbulence levels. In the first wake in Figure 5.3(b), i.e. around 120°, the deficit is much higher than the second wake around 300° due to the difference between the thrust coefficient for upstream wind speed of 9 m/s and 10 m/s, see Figure 3.6(b).

The effects of the wake to the turbulence are observed to be significant such that the difference between the wake and atmospheric TI is up to 7% for the 3.3D spacing case. Also note that the met mast is in the wake of the neighbouring turbines before 115° and after 315° wind directions.

The southernmost three turbines along Row B encounter 5 events where the effects of the wake on the TI are observed for the incoming wind directions between $100-340°$, see Figure 5.2(b). For the first event between $120\pm15°$, both turbines B07 and B06 are exposed to a single wake thus have almost identical values. For the second one between $180\pm15°$ though, both turbine B08 and B07 are upstream and B06 is under the effect of a single wake. The third event is along the perpendicular direction to the row, $222\pm15°$ causing the highest increase in the TI at the location of the second turbine. Interestingly, between $260\pm15°$ turbines B07 and B06 are subjected to the same turbulence where

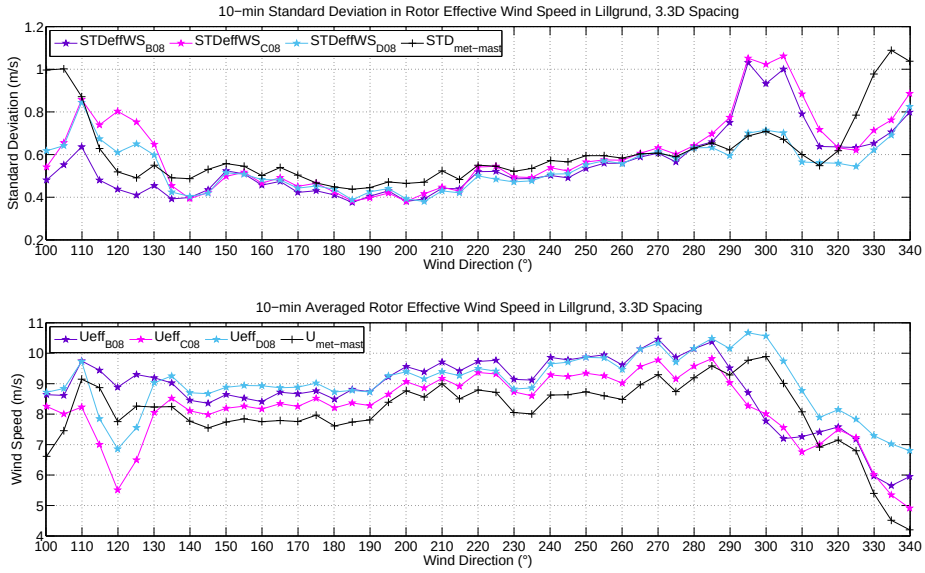

Figure 5.3: The components of the TI in Lillgrund along Row 8 – 3.3D spacing (a) 10-min standard deviation in rotor effective wind speed (b) 10-min mean wind speed, averaged over 5° wind direction bins, errorbars indicating 95% normalised confidence intervals

the former has 4 upstream turbines and the latter has 3 which is also similar to the wake deficit trend in Section 4.2.2. Similarly between $300 \pm 10°$, the estimated TI is almost identical at turbines B06, B07 and B08 where they have 5, 4 and 3 turbines upstream, respectively.

The behaviour of the TI in multiple wakes is presented in Figure 5.5 for the perpendicular direction when turbine – turbine spacing is 3.3D. Figure 5.5 shows that the turbulence level increases significantly at the first upstream turbine and it is higher for a single wake compared to a double wake. Although the number of wake data are limited, it is also seen that the existence of three or four upstream turbines hardly makes any difference which will be discussed utilizing more turbines further upstream with larger spacing for the Horns Rev case, Figure 5.6.

Wake Added TI in Horns Rev-I

For the Horns Rev case, the SCADA signals used to calculate the TI at the turbine locations are not continuous and include the period of 04/10 – 10/10, 14/10 – 21/10, 03/11 – 10/11 and 18/11 – 19/11 in 2013, 21 days in total. Though the number of

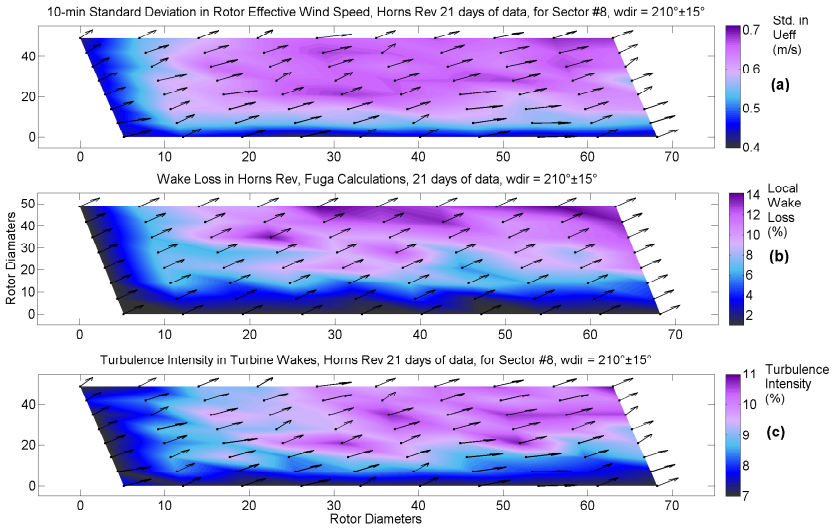

Figure 5.4: (a) 10-min standard deviation in wind speed, (b) The wake loss, calculated using Fuga [78], (c) The turbulence intensity along the Horns Rev I offshore wind farm, arrows indicate the mean wind direction(s) read by the models filtered across $210^\circ \pm 15^\circ$ bin

days considered might not be sufficient enough to come up with long term results, with regards to TI comparison as long as there is enough range in turbulence and wind speed observed in data, the full climatological cycle is not required. Moreover, the analyses are performed to illustrate the wake added turbulence in another wind farm and also to test the model for shorter periods. Similar to the Lillgrund case, the active power, pitch angle, rotational speed, and nacelle anemometer wind speed signals are extracted from all the turbines together with the yaw signals. The main wind direction recorded at the reference turbine WH1105, see Figure 3.1, during the considered period is south-west. Since there are no available met mast data recorded at the same period, the atmospheric TI is not compared to the met mast but instead, the change in the TI through the wind farm is investigated.

Since the data from all the turbines are available for the considered period of 21 days, a 'turbulence map' of the whole wind farm can be constructed. Note that, the TI calculation is in fact limited to individual turbine swept areas and Figure 5.4 is built assuming a linear change between the turbine locations. The observation of the actual behaviour in between the turbines are left as a future work where detailed measurements have to be carried out.

The TI presented in Figure 5.4(a) is calculated using the 10-min standard deviation

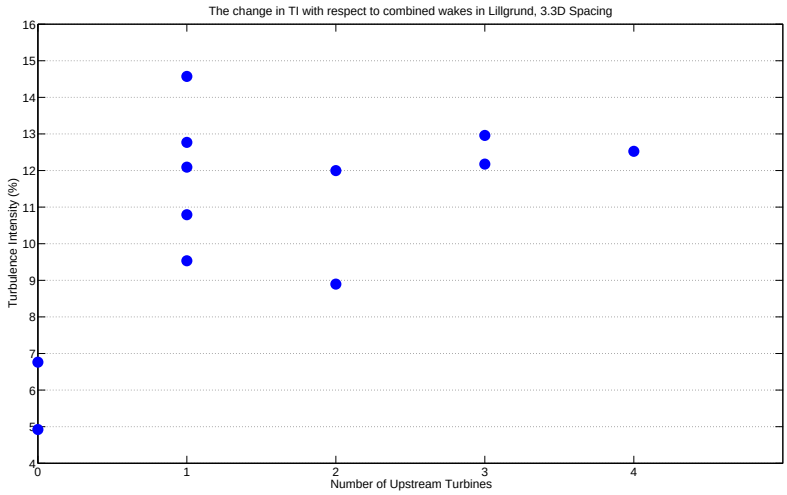

Figure 5.5: The behaviour of TI in Lillgrund with respect to combined wake effects, $3.3D$ spacing along perpendicular 120° and 300° wind directions

and the mean of the 1-sec rotor effective wind speed and averaged over the upstream wind direction bin $210^\circ \pm 15^\circ$. The wake loss in Figure 5.4(b) is calculated using the same dataset with the linearised computational fluid dynamics model Fuga [78] for the same wind direction sector and neutral atmospheric stability. The wind speed and direction from the turbine WH1105 is taken as references where the wake loss is calculated in percentages as $U_{wake}/U = \left(1 - U_{wake}/U_{ref}\right) \cdot 100$.

Figure 5.4(b) and (c) show that the behaviour of the TI follows a very similar trend as the wake deficit such that the turbines with higher loss, thus lower local wind speed, are exposed to higher turbulence. However, their behaviours are not identical due to the simplifications in the employed wake model in which the local wind direction and speed is not taken into account and the calculations are based on the reference wind speed and direction. Still, some of the non-homogeneity is captured inside the wind farm since the directional averaging is applied considering the meandering. Similar to the Lillgrund case, the 10-min standard deviation in wind speed and the added turbulence are not consistently increasing with the superposed wake. Figure 5.6 shows that the turbulence increases the most at the first downstream turbine also, then remains within a certain zone with a slight tendency to increase after the fourth turbine for westerly winds. The pattern of the TI along a single row of turbines is highly analogous to the power deficit measurements in Horns Rev for westerly winds as illustrated by Hansen et al. [36]. Both the TI and the wake loss analyses show that the flow direction at the

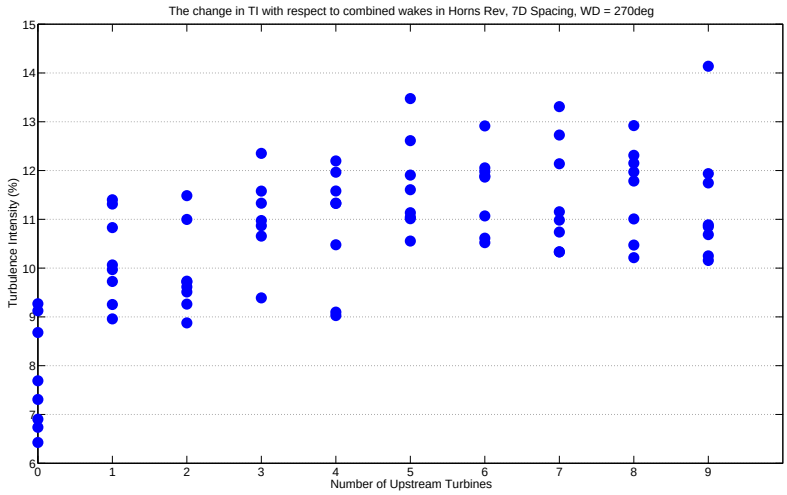

Figure 5.6: The behaviour of TI in Horns Rev with respect to combined wake effects, $7D$ spacing along perpendicular westerly winds, 270°

turbine location plays an important role in defining the trend of the turbulence increases throughout the wind farm, as it sets the direction of the local wake.

5.2 Single Wake Re-calibration

The re-calibration of the Larsen model is performed for a single wake event in Thanet considering the turbines $C01$ and $C02$, see Figure 3.4. The second-wise dataset used in this process are extracted for north – westerly winds, i.e. $317° \pm 20°$). After the wind direction is filtered and the time delay is estimated, the considered data for the re-calibration consist of 24960 seconds which corresponds approximately to 7 hours. The diameter of the Vestas V90 – 3MW offshore turbines are $D = 90m$ and the distance between the turbines for considered wind direction is taken to be $\Delta x = 500m$ in Equation 5.3.

Because the calibration is to be performed using rotor effective wind speed values, the point-wise wake deficit u_x in Equation 4.23 needs to be averaged over the rotor. Gaussian 4-point integration is applied to estimate the wind speed distribution over the rotor using the same Gauss weights and the associated integral variables as in [53]. The integration of Equation 4.23 in this manner gives the effective wake deficit, u_{eff} as;

$$u_{eff} = \frac{-0.2939U_{in}\left(0.0235\left(c_1^2\right)^{2/5}\left(R^2\right)^{3/2} - 0.277\left(c_1^2\right)^{1/5}\left(R^2\right)^{3/4}\sqrt{c_1^2 C_T R^2\left(\Delta x + x_0\right)} + c_1^2 C_T R^2\left(\Delta x + x_0\right)\right)}{\left(c_1^2\right)^{7/5}\left(\frac{\left(C_T R^2\right)}{\left(\Delta x + x_0\right)^2}\right)^{2/3}\left(\Delta x + x_0\right)^3}, \tag{5.3}$$

where U_{in} is the upstream incoming effective wind speed.

5.2.1 Time Delay Concept

Before using the dataset to determine the parameters c_1 and x_0 for the single wake, the time it takes for a particle to move from the most upstream turbine to the turbine in question, namely the time delay t_d, is taken into account by applying a correction to the dataset.

Machefaux et al. [61] studied the advection time in detail, in which the cross-correlation between the measured near wake velocity profiles are investigated. The time lag between the downstream lidar measured patterns is quantified as the specific time shift where the profiles are most correlated. On the other hand, the lack of measurement campaigns in considered wind farms and the framework of this study limit the analysis to be performed only at the turbine locations, using the turbine data. Therefore, the proposed methodology is simply $t_{down} = t_{up} + t_d$ where t_{down} and t_{up} are the time steps of the downstream and upstream locations, respectively and t_d is estimated as; $t_d = \frac{\Delta x}{\left(\overline{U}_{down-data}\right)}$ with $\overline{U}_{down-data}$ being the rotor effective wind speed estimated using the downstream turbine SCADA, averaged up to ten minutes during the re-calibration on Thanet and validation on Horns Rev.

Note that, the distance between the turbine in question and the most upstream turbine is equal to Δx for the single wake re-calibration case. However, the calculations on the wind farm scale are based on the 'instantaneous' upstream distance which is mostly a lot larger depending on the wind direction and the considered downstream turbine location. For both the single and multiple wakes, the average downstream wind speed is updated on every 10-mins if the treated data covers a longer period.

5.2.2 Modelling of the Meandering inside the Wind Farm

The wake velocity field is assumed to be axis-symmetric and self-similar in the Larsen model. However, the wake meandering mechanism is shown to be significant in reducing the wake losses especially for unstable and neutral atmospheric stabilities [4]. Although the effects of meandering on a single wake profile are measured [11] and investigated heavily in the recent years [54, 63, 62], the concept is still under discussion for multiple

wake cases. Although the Dynamic Wake Meandering model (DWM) [54] is validated on the smaller scale Egmond aan Zee wind farm [59], it is not implemented in this study since the location of the wake deficit is modelled by introducing an external 3D turbulence box, rather than calculating the actual TI at the turbine locations using SCADA data. Besides, the DWM model is not able to meet the practical criteria (real-time or online application) of the PossPOW algorithm, as mentioned in the model selection section at the end of the review in Chapter 4.

Since the algorithm reads the individual wind direction signals and the TI estimated at the turbine locations, the changes in the local upstream wind profiles are implicitly taken into consideration in the computations. However, especially for high fidelity calculations in large wind farms, the change in the flow along the distance between the upstream and downstream turbines is also significant. Therefore, Ainslie's correction [4] to the centreline wake deficit by correlating the meandering to the variability in the wind direction is employed as in;

$$\hat{u}_{eff} = u_{eff}\left[1+7.12\left(\frac{\sigma_\theta}{b}\right)^2\right]^{-\frac{1}{2}}, \tag{5.4}$$

where $\hat{u}_{eff}$ is the corrected deficit, σ_θ is the standard deviation in local wind direction fluctuations of timescale of maximum 10-min if the investigated period is longer, and b is the full wake width.

5.2.3 Moving Average of the Time Series

In order to avoid over-fitting and start modelling the noise, both up and downstream effective wind speeds have been filtered using moving window average with Savitzky-Golay convolution coefficients [93]. Since the objective is to model the flow behind the turbine dynamically to achieve the real-time effect, the window size was kept at 60-sec to discard the measurement noise from the SCADA while abstaining from over-smoothing the time series.

5.2.4 Parametrisation and Curve Fitting

As explained earlier, the main variables to adjust inside the wake model are c_1 and x_0 which are highly dependent on C_T and the turbulence intensity, TI (see also Equations 4.27 – 4.30) . They are formulated as in Equation 5.5.

$$\begin{aligned} x_0 &= p_1 C_T^{p_2} + p_3 TI \\ c_1 &= p_4 C_T^{p_5} + p_6 TI \end{aligned} \tag{5.5}$$

The objective function combines Equation 5.3 with Equation 5.1 and together with those 6 parameters, it takes 3 inputs to predict the effective wind speed observed at the

Table 5.1: List of model parameters and goodness of the fit for the Re-calibration of the Larsen model, R^2 is the coefficient of determination and *RMSE* is the root mean square error of the model predictions)

p_1	0.232 (-57.3247, 57.7163)
p_2	74.985 (-147.796, 148.551)
p_3	0.12 (-72.968, 78.098)
p_4	0.763 (-18.052, 41.865)
p_5	17.126 (3.182, 32.874)
p_6	4.459 (4.135, 5.255)
$R^2 = 0.914$	RMSE $= 0.718$ m/s

downstream turbine C02 in Thanet. The first input is the incoming effective wind speed, U_{in}, along the perpendicular direction, pre-processed using moving average. The second is C_T which is tabulated in terms of wind speed as in Figure 3.4(b) and interpolated for changing U_{in} in the algorithm at every second. The turbine specific TI calculated according to Section 5.1 is tabulated in terms of incoming wind speed to be used in 1-sec re-calibration and the rest of the calculations in this study. Note that the ambient TI using the effective wind speed is shown to be consistently lower than the point-wise meteorological mast measurements due to geometrical averaging over the rotor. However, the corresponding correction is automatically embedded in the re-calibration process.

The final parametrised non-linear functions are fitted to data using non-linear least squares approximation (NLSA). Note that this non-linearity results in parameters being highly sensitive to the initial guesses assigned. The concluding parameters together with the 95% confidence intervals are presented in Table 5.1.

The Larsen model with the re-calibrated parameters is implemented in the Horns Rev single wake case for the easterly winds. The wind direction signal extracted from the upstream turbine SCADA system is used when evaluating the re-calibrated parameters. However, the signals indicated a significant bias when compared to the depth of the normalized power between two turbines in the horizontal row. More details about that particular wind direction pre-processing using the turbine data is included in Appendix A.1. The comparison of the original Larsen model and the re-calibrated version for second-wise dataset is presented in Figure 5.7. Note that, for both versions of the model, the inputs, i.e. U_{in}, C_T and TI are the same but the parameters c_1 and x_0 are expressed differently. Although the data is not symmetrically distributed over the wind direction bin, it can easily be seen that the original Larsen model significantly under-predicts the downstream wind speed for the second-wise dataset. Better recovery achieved by the re-calibration is observed especially for $90^\circ \pm 5^\circ$ wind direction bin.

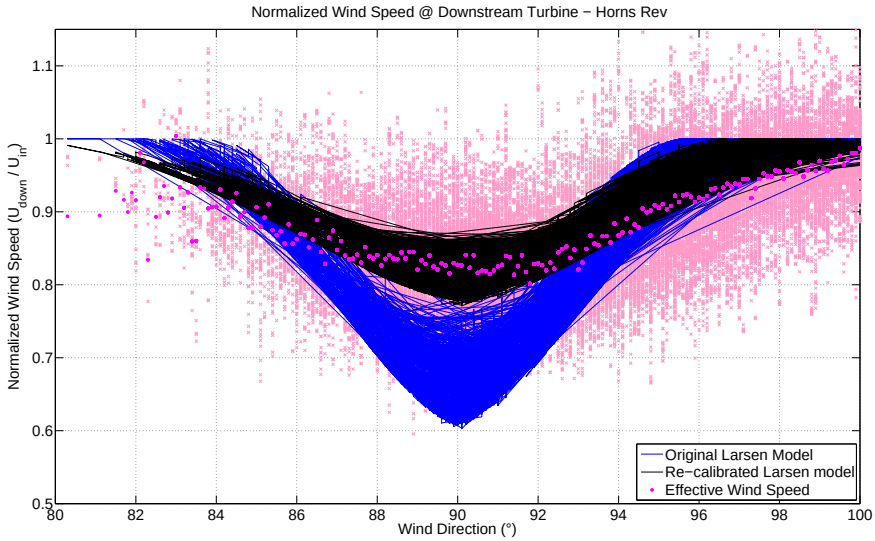

Figure 5.7: Normalised 1-sec wind speed at the downstream turbine, 7D, in Horns Rev - Original and Re-calibrated Larsen model together with the raw data and the moving average

6

PossPOW Algorithm: Wind Farm Scale Available Power Estimation

The local effective wind speed estimated in Chapter 3 was used to estimate the turbulence intensity at the turbine locations in Section 5.1. Both were used to re-calibrate the Larsen wake model for real-time, using single wake events. When it comes to the wind farm scale, the multiple and partial wakes are highly significant in evaluating the available power of the farm. Due to the C_T dependency on the wind speed, see Figures

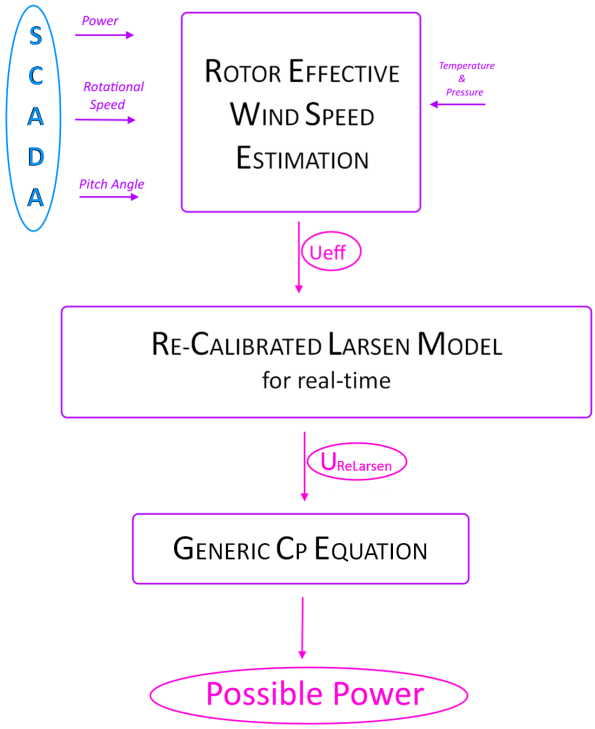

Figure 6.1: PossPOW inputs and workflow

3.4(b) and 3.1(b), two different simplified approaches are applied to superpose the wakes which is a complicated process. For the incoming wind speed below rated, since the C_T is high, only the maximum wake deficit is taken into consideration among contributions from all the upstream turbines at any time. Along the rated region, C_T is much lower so all the dual deficits are weighed via linear summation, as also suggested in [57]. The other wind farm effects, namely the turbulence intensity, time delay and the effect of meandering inside the wind farm, are estimated following the same procedure as the single wake in Section 5.2, using the raw 1 Hz turbine data without the moving average.

Hereby, all the components of the PossPOW algorithm are described and the model is ready to be evaluated. Here in this chapter, the finalized algorithm is implemented in the Thanet and Horns Rev-I wind farms under nominal operation where the available power is equal to the active power of the turbines.

6.1 Local Wind Direction inside the Wind Farm

As seen in Chapter 4, the uncertainty in the wind direction significantly affects the performance of a wake model. Although in the PossPOW algorithm, the standard deviation of the wind direction in 10-minutes intervals, as stated in Gaumond et al. [30], is relatively irrelevant, there is still uncertainty introduced due to the lack of available met-mast data. The removal of the bias in the wind direction signal, as performed before the validation of the re-calibrated parameters for a single wake, is applicable only to the first row of turbines. However, in order to account for the local effects, especially for large offshore wind farms, a more comprehensive pre-processing of the wind direction data is required.

Data observation for relatively larger time periods among the whole wind farm is always a convenient way to point out the off-signals. However, smaller biases can go unnoticed and still affect the results. Furthermore, in all three offshore wind farms studied, there exists a significant number of turbines where the wind direction SCADA signals are not available. The maintenance of the measurement systems and the data acquisition of the yaw, wind direction or nacelle direction signals need to be handled more attentively by the wind farm operators. Although the signals are not fed back to the control system, they are still of vital importance when it comes to operation monitoring including real-time power curve and available power estimation.

Through the analysis of the PossPOW algorithm for multiple turbines cases, the invalid wind direction signals are replaced with the ones extracted from the closest available turbine. That process is repeated at every second. The quantification and propagation of the corresponding uncertainty, together with the other sources of uncertainty, are to be studied as a follow-up project.

6.2 Percentage Error in Wind Speed

The percentage error in wind speed, $\%error_U = \left| \frac{U_{ReLarsen} - U_{eff}}{U_{eff}} \right| \cdot 100$, is estimated using the re-calibrated version of the Larsen model, $U_{ReLarsen}$, together with the meandering correction, and the effective wind speed calculated using the turbine operational data, U_{eff}. Since the wind speed at the downstream turbine is higher during down-regulation, the error is calculated using only the normal operational data. Note that the implementation of the re-calibrated Larsen wake model to the wind farm scale gives the wind power plant level real-time power curve, under all operational conditions. The averaged percentage error in Thanet offshore wind farm over different time intervals is shown in Figure 6.2. Note that the calculations are performed at the turbine locations only and linearly interpolated between the turbines to obtain a continuous error profile inside the farm. The same 7-hours dataset with the indicated filters in the re-calibration process in Section 5.2 is used. The arrows represent the nacelle direction signals, averaged along the same period. As expected, the model prediction error is accumulated going further downstream especially for 10-min or longer averaging time scales. The error distribution remains nearly the same for 10-min and larger bins with a slight flattening. The maximum prediction error is less than 16%, for most of the turbines less than 8%, inside the farm. To illustrate the model error at the individual turbine level, the mean error of every single period (i.e 60s, 300s, 600s, 1800s, 3600s and 7200s; colormaps in Figure 6.2) are averaged among the whole dataset of 7h (indicated in upper left corners in Figure 6.2). The averaging period of interest for the error calculations is 5-min in this study, following the requirements set by Danish TSO Energinet.dk [24].

6.3 Real-Time Wind Speed to Power

While a good agreement is achieved for the single wake and the wind farm wind speed calculations using the re-calibrated Larsen wake model and the meandering correction of Ainslie, the conversion of the wind speed to power production is not straightforward. The manufacturer power curve in Figures 3.4(b) and 3.1(b) are built using 10-min averaged power [1], for higher resolution power curves see [34], and point-wise wind speed measurements and they are standardised for fixed turbulence (typically $TI = 10\%$) and air density [1]. Therefore, the approximated C_P curve using the operational pitch and rotational speed signals together with the calculated $U_{ReLarsen}$ wind speed is implemented to estimate the power production (Equation set 3.2), first at the turbine and then at the wind farm level.

Figures 6.3(a) and 6.4(a) illustrate the comparison of the 5-min averaged model results and the aggregated active power turbine data together with its 5% error band. The nominal operational dataset for the Thanet case covers a period of 12 hours where for the Horns Rev-I analysis 24 hours period is presented. Especially in the Thanet case, the

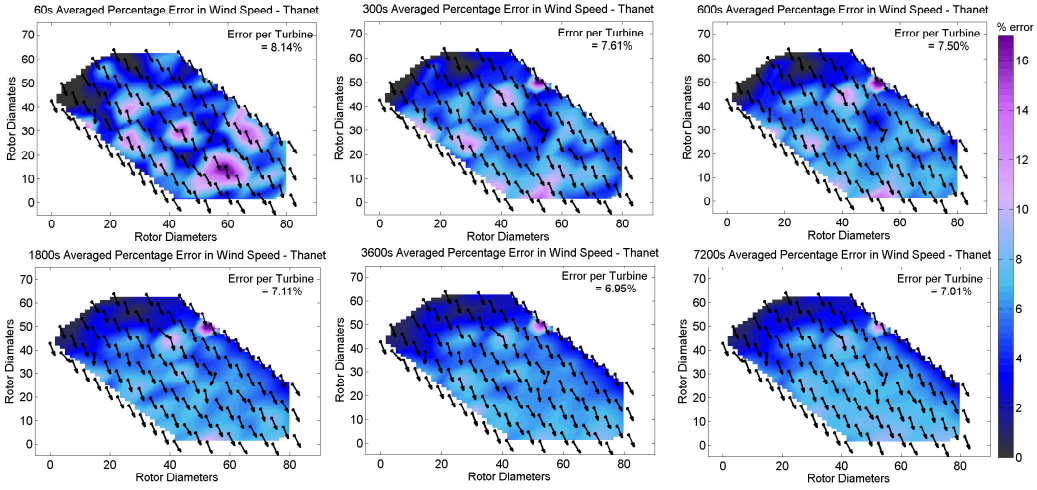

Figure 6.2: Percentage error in wind speed averaged over (a) 60s, (b) 300s, (c) 600s, (d) 1800s, (e) 3000s, (f) 7200s across Thanet offshore wind farm. Error per Turbine values correspond to the average of all the time intervals among the total period of 7-hours (i.e. all 60s intervals in 7-hours, 420 data points in total, etc.)

comparison of the farm level power results with the wind speed and direction inside the wind farm might explain the deviation observed earlier and later in the analysed dataset. The over-estimation in the first part of the dataset is possibly related to the contradictory behaviour of the upstream wind direction signal, Turbine $E03$ (see Figure 3.4(a)) on which the calibration was infeasible due to the lack of data to adjust the center of the wake depth with respect to the wind direction. The same tendency is clearly observed in the Figure 6.3(b) where the distribution of the 5-minutes percentage errors are illustrated. The difference between the active power signal and the algorithm reaches up to 20% during that period when E02 is an upstream turbine. The "hit rate" rate refers to ratio of the points inside and outside of the $\pm 5\%$ error span. Later in the investigated period the wind becomes perpendicular to the long and closely located rows which leads to stronger wakes, as can be perceived clearly in Figure 6.3(c). Towards the end of that region, the wind speed reaches rated where both the C_T and the approximated C_P curves are the most sensitive to the incoming wind speed.

The turbines in the Horns Rev-I case, Figure 6.4, are exposed to north-westerly winds during the investigated period, which corresponds to diagonal wakes with higher upstream turbine distances. The wind speed is slightly lower than the rated with fairly steady wind direction during the most of the dataset. Similar to any other wake model, the PossPOW algorithm is highly sensitive to the wind direction input. Therefore at least

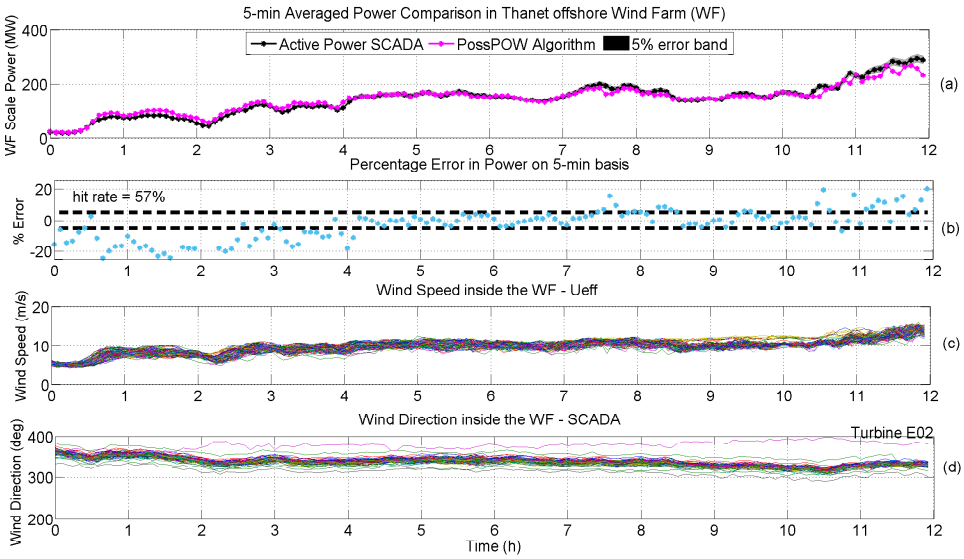

Figure 6.3: (a) 5-minute averaged Active Power (SCADA) and Re-calibrated Larsen model (together with Equation 5.2) results in Thanet, (b) the estimated effective wind speeds and (c) the nacelle direction signals at the turbine locations inside Thanet, 12-hours data.

for the investigated period, the higher hit rate and a better performance is anticipated. It is also seen in Figure 6.4(c) that even for 5-minutes averaged dataset, the bandwidth of the wind speed inside the wind farm is as broad as 4 m/s. This automatically correspond to significant production differences towards downstream, indicating the importance of fast, robust and as accurate as possible wake modelling once again. Despite the highly variable wind speed inside the wind farm, the PossPOW algorithm is seen to be in a good agreement with the dataset in terms of the 5-min averaged produced and predicted power on the wind farm scale.

The performance of the overall PossPOW algorithm for the same wind farm under curtailment is evaluated in the next chapter via a series of dedicated experiments took place in the Horns Rev-I wind farm.

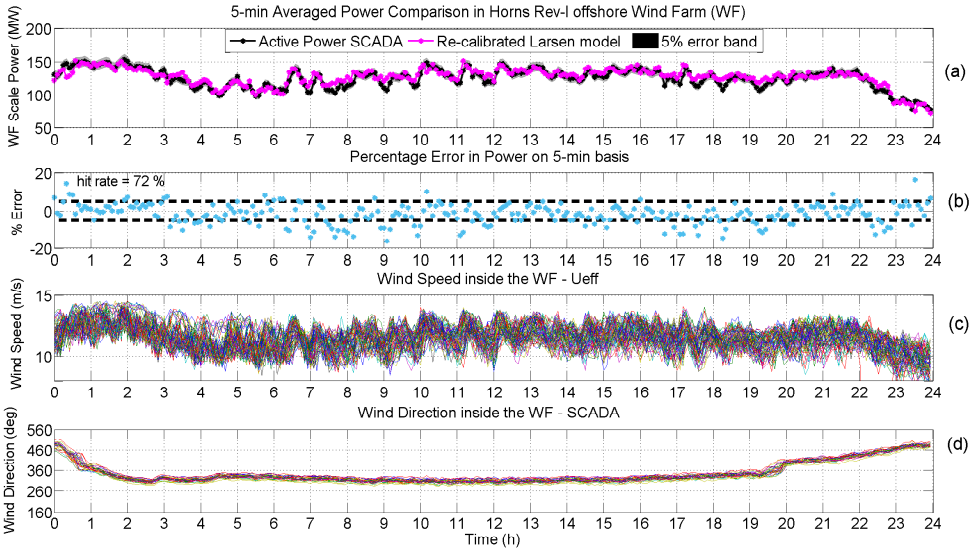

Figure 6.4: (a) 5-minute averaged Active Power (SCADA) and Re-calibrated Larsen model (together with Equation 5.2) results in Horns Rev-I, (b) the estimated effective wind speeds and (c) the wind direction signals at the turbine locations inside Horns Rev, 24-hours data. Wind direction is normalized around 360° due to northerly winds.

7

Full Scale Experiments at Horns Rev-I and Validation of the PossPOW Algorithm

In Chapter 5, we introduced a real-time wake modelling approach and provided an industrially applicable method to estimate the possible (or available) power of a down-regulated wind farm, called PossPOW algorithm, giving the real-time wind farm scale power curve when applied under nominal operation. The algorithm uses free effective wind speeds at the upstream turbine locations as inputs to the real time wake model to obtain the corrected downstream wind. In Chapter 6, the real-time wind farm power curve results together with 5-min averaged error calculated in Thanet and Horns Rev-I offshore wind farms were presented for the normal operation. Here in this chapter, we test the PossPOW algorithm in a series of dedicated experiments in which two of the upstream turbines are curtailed under specific inflow conditions. The idea behind the validation, experimental set-up and the verification results are presented also considering the most advanced legislations put up by the Danish TSO.

7.1 Experimental Setup

The tests took place during the Spring of 2015 in the Horns Rev-I wind farm and they are basically aimed to validate the PossPOW algorithm, under restricted down-regulation conditions. The idea is to down-regulate two separate turbines (test turbines, WH1102 and WH1105) located on two of the inner rows west of the wind farm, see Figure 7.1. In the downstream of the test turbines, the wake losses are reduced due to upstream curtailment, therefore the affected turbines see more wind than usual (turbines WH1112 and WH1115). The assumption is that the available power of the affected turbines is equal to the active power production of the closest neighbouring rows (reference turbines), for perpendicular westerly wind directions. In other words, the active power of the reference turbines with nominal wake deficit is assumed to be identical to the production capacity of the affected turbines. Therefore, the active powers of the turbines WH1111 – WH1113 and WH1114 – WH1116 are taken as the reference available powers for the turbines WH1112 and WH1115, respectively.

The implementation of the down-regulation code will be in such a way that the experiment will be initialized when certain conditions are met and similarly will be finalized when the inflow no longer satisfies certain requirements. The conditions that will trigger the curtailment of the test turbines are conservative in terms of incoming wind direction

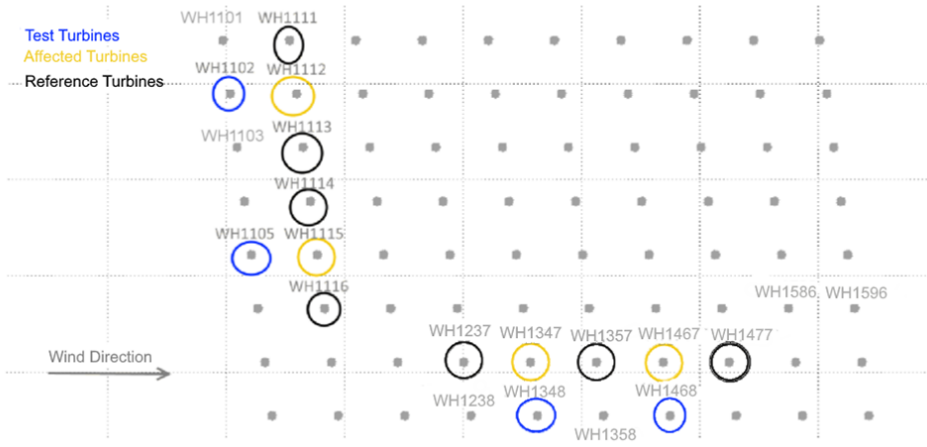

Figure 7.1: The down-regulation experiments for westerly winds in Horns Rev-I offshore wind farm. **Blue:** Curtailed turbines; **Yellow:** Turbines affected by the 'reduced' wake due to curtailment; **Black:** Reference Turbines to correct the 'reduced wake'

and wind speed. On the other hand, the stop trigger is kept relatively broader in order to collect more data including occasional variations to make the most of the experiments.

In order to assure the validity of the similarity assumption, the active power correlation between the turbines in question are investigated using historical 1 Hz data covering a period of 21 days in total. Especially for low-turbulent cases, the clear resemblance between the neighbouring rows is sustained for approximately 20° bin of the incoming wind direction. Therefore this is chosen to be one of the trigger conditions. In Figure 7.2 the active powers of neighbouring rows are compared, and it is seen that the difference in power has a very similar trend to the standard deviation in wind direction. This basically shows that most of the difference is due to atmospheric turbulence. Additionally, Figure 7.2(c) shows the effects of the diagonal wakes clearly, between slightly before day 1 and almost up to day 2. The wakes are also observed clearly, slightly before and after day 2, corresponding to wind direction around 270°, as expected. Note that, both during the analysis of the historical data and the execution of the experiments, the yaw signals from the upstream turbines are calibrated via comparison of the expected wake depth with the upright wind direction (for details, see the re-calibration of the yaw signals in Appendix A).

Another constraint put upon the incoming flow is regarding the wind speed. To test the sensitivity of the PossPOW algorithm and be able to observe a clear difference between the power production during the normal operation and down-regulation, the ex-

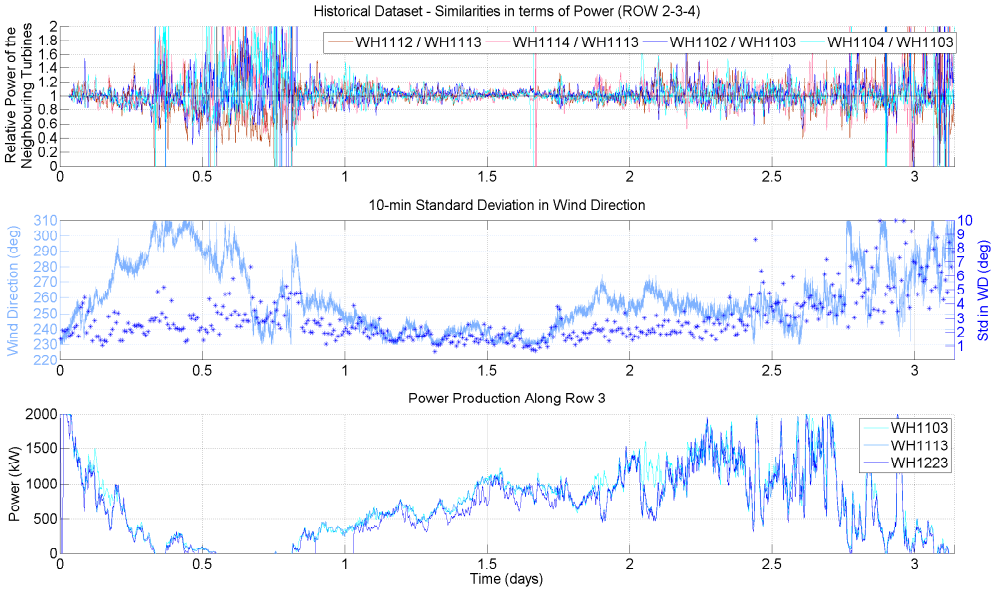

Figure 7.2: Active power SCADA analysis in Horns Rev-I (a) percentage difference in power production between horizontal rows starting with turbines WH1102 – WH1103 and WH1104 – WH1103 (b) 10–minutes standard deviation in wind direction (c) power production along row starting with turbine WH1103

periments are decided to be carried out for wind speeds lower than the rated. This would also ensure a fairly deep wake at the downstream turbines since C_T is significantly higher along that region. However it should also be noted that for lower upstream wind speed values, strong wake effects may cause the downstream turbine to be non-operational (below cut-in), therefore should be avoided.

Since the experiments are to be performed on an operating wind farm, the availability and the accessibility of the SCADA signals are checked, at least for the turbines in question, before executing the curtailment.

Accordingly, the restrictions on the incoming flow are listed below in order to activate (start trigger) and deactivate (stop trigger) the curtailment. Note that in order to activate the down-regulation, all of the conditions in the start trigger have to be satisfied simultaneously. On the other hand, deactivation takes place even only one of the constraints listed in the stop trigger is monitored. A schematic configuration of test, affected and reference turbines is presented in Figure 7.1 for westerly winds in Horns Rev. The colour code is preserved also when presenting the measurements (wind speed and

power) taken from the corresponding turbines.

Start Trigger for curtailment of turbines WH1102 and WH1105

1. 10-min averaged 'Wind Direction' SCADA signal on the turbines WH1102 and WH1105 are inside $260^\circ - 280^\circ$ interval.
2. 10-min averaged 'Wind Speed' SCADA signal (read by the nacelle anemometer) on the turbines WH1102 and WH1105 are inside $8 - 11$m/s interval.

Since the similarity in the neighbouring rows in terms of power production is observed to be more significant for lower ambient turbulence levels, initially it was intended to introduce a relevant constraint in the start trigger. However, it is not implemented due to the absence of a clear corresponding signal in the turbine data. Nevertheless, the effect of turbulence intensity to the similarity of the power production between the rows is discussed later in the results section.

Stop Trigger for curtailment of turbines WH1102 and WH1105

1. 10-min averaged 'Wind Direction' SCADA signal on the turbines WH1102 and WH1105 are outside $255^\circ - 285^\circ$ interval.
2. 10-min averaged 'Wind Speed' SCADA signal (read by the nacelle anemometer) on the turbines WH1102 and WH1105 are outside 7 – 11 m/s interval.
3. Test has been running for 180 minutes.

For all the experiments, the power production of the turbines WH1102 and WH1105 are down-regulated to 500kW regardless of the wind speed. Accordingly, the sensitivity of the PossPOW algorithm to different amounts of percentage-wise down-regulation are aimed to be tested.

7.2 Experimental Results and Validation under Down-regulation

Between mid-February and late May 2015, in total 6 experiments were conducted. The SCADA data are extracted from all the turbines in the Horns Rev-I wind farm covering at least 2 hours before and after WH1102 and WH1105 (or WH1348 and WH1468 for Experiment #1, southerly winds) are curtailed. The duration of the curtailment in each experiment and the mean wind direction and speed at the upstream turbine locations are given in Table 7.1. The collected 1 Hz signals are active power, wind speed (measured by the nacelle mounted anemometer), pitch angle, rotational speed, yaw angle and possible

Table 7.1: The experimental dataset, southerly (Experiment #1) and westerly (Experiment #2 – #6) winds. The effective wind speed (in m/s), U_{mean}, and the pre-processed wind direction (in degrees), WD_{mean}, at the upstream turbines, time averaged over the indicated curtailment period.

	Experiment #1 3000sec (50min)	
	U_{mean}	WD_{mean}
WH1238	10.029	167.4
WH1348	9.803	165.6
WH1358	9.888	168.4
WH1468	9.464	163.2
WH1478	9.945	171.4

	Experiment #2 3000sec (50min)		Experiment #3 3600sec (60min)		Experiment #4 3600sec (60min)		Experiment #5 7200sec (120min)		Experiment #6 7800sec (130min)	
	U_{mean}	WD_{mean}	U_{mean}	WD_{mean}	U_{mean}	WD_{mean}	U_{mean}	WD_{mean}	U_{mean}	WD_{mean}
WH1101	9.005	271.4	9.363	269.8	8.959	269.9	11.084	284.5	10.07	266.5
WH1102	8.916	271.4	9.224	267.9	9.071	269.8	11.086	284.5	9.910	266.4
WH1103	8.906	271.4	9.331	267.5	9.226	269.9	11.097	284.6	10.143	266.3
WH1104	8.865	271.4	9.169	261.5	9.356	270.8	11.052	275.3	10.127	266.3
WH1105	8.875	271.4	8.961	261.7	9.110	270.9	10.889	268.7	9.801	266.3
WH1106	8.682	271.4	9.221	264.2	9.292	274.3	11.102	268.8	9.848	266.4

power at the individual turbine level. For all the experiments, especially for Experiment #2 and #6, the wind direction signals at most of the upstream turbines were undefined. Therefore, they are replaced with the wind direction at the closest available turbine, resulting in almost a single wind direction input to the algorithm in some of the cases. The active and possible power signals are directly employed presenting some of the experimental results while the pitch and rotational speed are used in order to estimate the local wind at the turbine locations as in Chapter 3. Subsequently, the estimated effective wind speeds at the upstream locations, together with the wind direction signals, are fed into the re-calibrated wake model as in Chapter 5, and the overall process is called PossPOW algorithm.

7.2.1 Time series Analysis

The first expectation from the experiments is to be able to clearly observe the reduced wake deficit due to upstream curtailment at the affected turbine, which is used to calculate the individual turbine level possible power SCADA signal. As mentioned earlier, the key challenge in the PossPOW project is to correct that reduced wake deficit and reproduce the wind speed profile at the reference turbine. For the Experiment #2 illustrated in Figure 7.3, the influence of down-regulation to the flow behind the turbine is most clearly seen. During the investigated period, where curtailment is activated between 4100 – 7000 seconds between the grey lines, two explicit wake occurrences are recorded. Along the full depth of the first wake which takes place before the curtailment under nominal operation, the wind speeds at the affected and the reference turbines downstream are seen to be in very good agreement. However during the curtailment

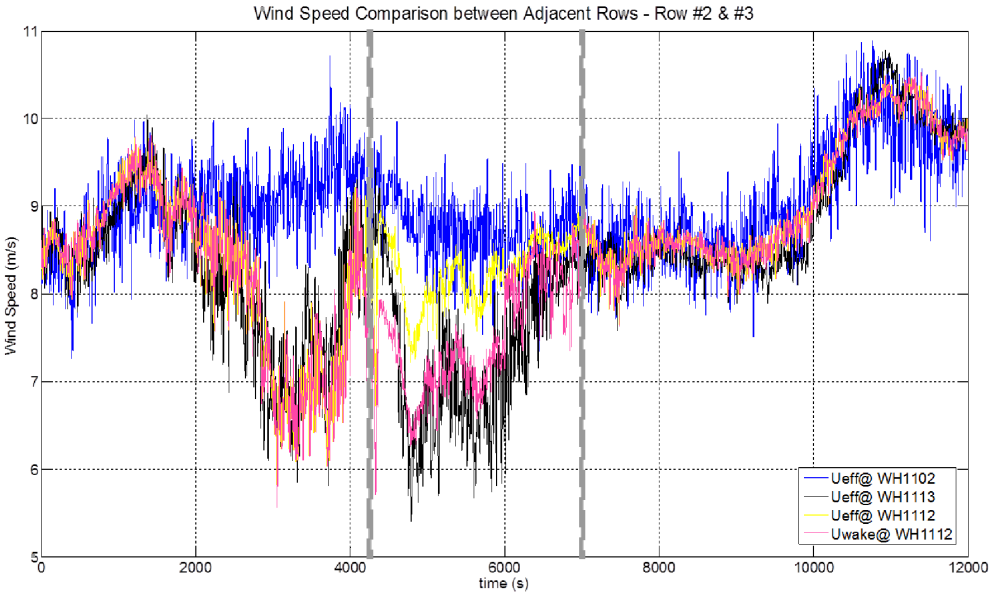

Figure 7.3: Comparison of the effective wind speed at the turbines: **WH1102** – upstream (test) turbine; **WH1113** – reference downstream turbine WH1112 – affected downstream turbine and the **PossPOW** algorithm. Curtailment is activated between 4100–7000sec, Experiment #2

in the second wake event, the affected turbine is exposed to significantly higher wind speeds. The PossPOW algorithm is applied to the whole dataset and seen to maintain a very good agreement with the reference turbine under both nominal and down-regulated operations.

To estimate the available power from the calculated downstream wind speed, the procedure described in Section 6.3 is adjusted so that instead of the variable pitch that occurs during down-regulation, the constant pitch that is followed under nominal conditions is applied. Note that in the particular experimental set-up, the affected turbine is not curtailed hence positioned at a constant pitch (approximately -1° in Horns Rev-I case). The individual possible power SCADA signal and the PossPOW possible power at the affected turbine are compared with the active power of the reference turbine in Figure 7.4. In parallel with the wind speed comparison, the SCADA possible power, **yellow line**, is seen to overestimate the production potential at the affected turbine, **black line**, while the PossPOW algorithm, **pink line**, provides a much better estimation.

Despite missing the opportunity to compare nominal and down-regulated wake as

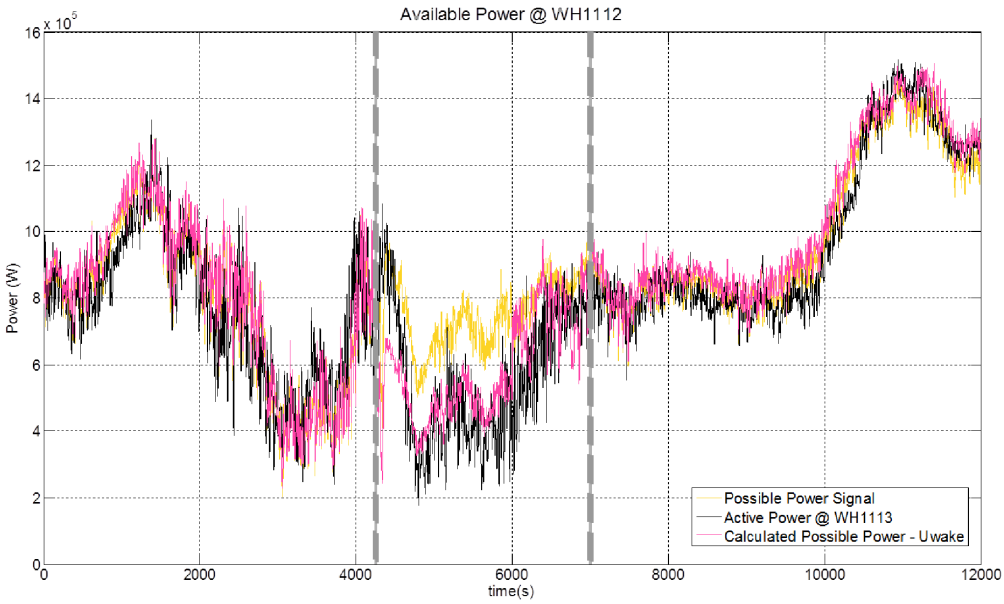

Figure 7.4: Active power, SCADA possible power and estimated power comparison at the downstream turbines, Experiment #2

in Experiment #2, another explicit over-estimation of the SCADA possible power is observed in Experiment #4. The comparison of the current industrial practice and the PossPOW algorithm, together with the reference available power at WH1103 is presented in Figure 7.5. Although the mean wind direction is also approximately perpendicular, see Table 7.1, through the curtailment period between 6000s – 9600s, the difference between the SCADA signal and the reference turbine is not as significant as the Experiment #4. The possible reason might be the higher ambient turbulence level that enhances the wake recovery, partially diminishing the effects of the reduced wake. However note that, the similarity between the neighbouring rows in terms of power production is also sensitive to the ambient turbulence as emphasized earlier. The effects of the atmospheric TI is further discussed in the next section in the frame of active power resemblance between the rows along downstream turbines.

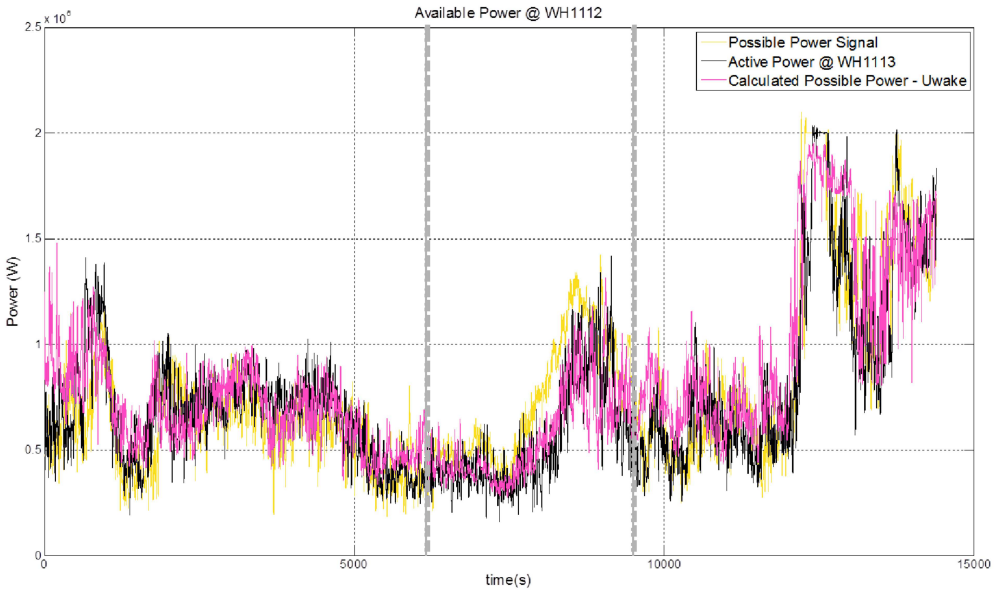

Figure 7.5: Active power, SCADA possible power and estimated power comparison at the downstream turbines, Experiment #4

7.2.2 Effects of Curtailment Further Downstream

Other than contributing to the system stability as ancillary services, curtailment has optimized wind farm operation applications as well. In this context, the principles of modifying the wake effects to increase the energy capture and reduce the fatigue loads have been studied and known for many years [98]. Several studies [5, 43, 67, 85, 72] have predicted between 0,1% and 10% increase in overall power production through down-regulation of the most upstream turbines, even higher reductions in loads. However, the concept has never been tested in an actual operating wind farm. Although during the experiments the effects of a reduced wake on turbine loads are not monitored, the power comparison between two neighbouring rows is presented in Figure 7.6 to investigate the influence of a single upstream turbine curtailment on the capacity and production of the rest of the aligned turbines. In Figure 7.6, the difference between the second and the third horizontal rows, starting with turbines WH1102 and WH1103 respectively, is presented in terms of the individual possible power signal, PPowdiff, and the active power, APowdiff, for the westerly experiments. Note that the difference is averaged over the period of curtailment, and the Experiment #1 is performed for south-north winds where the upstream turbines of the fifth and seventh vertical rows, starting with turbines WH1348

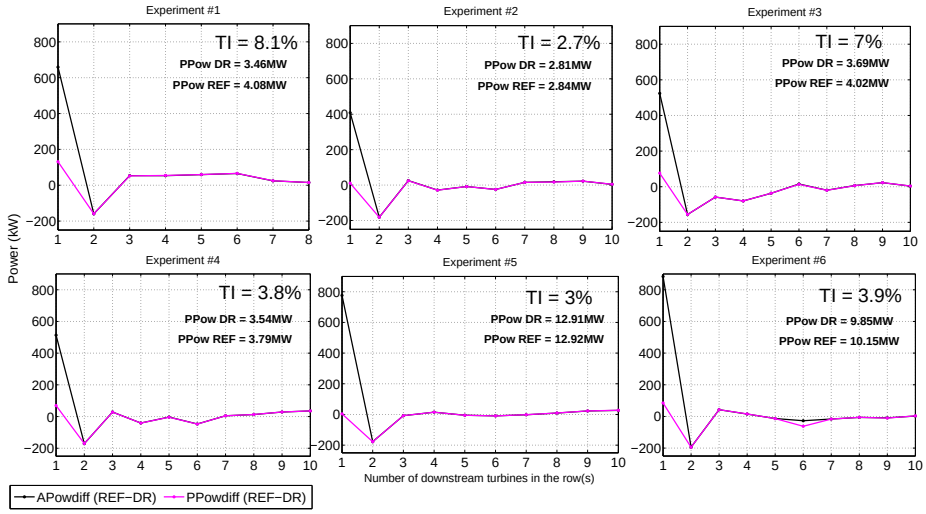

Figure 7.6: The differences between SCADA Possible Power (PPowdiff), and Active Power (APowdiff) between adjacent rows (WH1348 / WH1358 for Experiment #1, WH1102 / WH1103 for Experiment #2 – #6) during the upstream curtailment in Horns Rev-I. The upstream turbulence intensity (TI) and the total SCADA available power along the rows (*PPow REF* and *PPow DR*) are indicated on the upper right corner for each experiment.

and WH1468 respectively, are down-regulated. Consequently, the number of turbines for the first experiment is limited to 8 where the westerly configured experiments enable the analysis to be performed for 10 turbines along the row. In Figure 7.6, the average ambient turbulence intensity during the experiments is calculated using the approach described in Section 5.1.

The difference in the active power between the neighbouring rows, APowdiff, is highly significant on the first turbines due to the curtailment. It is also notable further downstream for Experiment #1, southerly wind, and Experiment #3 which might be related to comparatively high turbulence levels as it is observed to influence the similarity between the rows in the historical data analysis mentioned earlier. It is also supported by the fact that the production capacity of the most upstream turbines are different, i.e. PPowdiff$\neq$0 between the first turbines. Note that in the experiment 6, the difference in the active power signals is due to a SCADA data transformation issue observed at the sixth downstream turbine.

The available powers of those compared turbines in Figure 7.6 are expected to be the same under the described inflow conditions. However, the difference in the individual possible power SCADA signals between two adjacent rows, PPowdiff, is prominent at the second turbine in the rows, namely between the affected and the reference turbines,

in line with the observation presented in Figure 7.4. The effect of the down-regulated wake seem to sustain up until the fifth downstream turbine in the studied experiments, except for the relatively higher turbulent cases in Experiments #1 and #3. Interestingly, regardless of the curtailed amount of the upstream turbines, PPowdiff is approximately 200kW at the second turbines in all the experiments. The concept of total power increase via upstream curtailment is not observed in this experimental campaign but it should be bear in mind that the down-regulation is performed using a fixed set-point for all the tests targeting different inferences.

In addition to down-regulating the turbines for optimized wind farm control, there exist a number of studies that investigate the effects of increasing the yaw angle on the power production and turbine loading [9, 17, 105]. Although the method is found to be promising, it is generally concluded that more experiments are needed to quantify the effects of the deflected wake inside a wind farm.

7.2.3 PossPOW Validation in the frame of the TSO Regulations

The most elaborated constraint on the wind farm scale available power accuracy is framed by Energinet.dk [38] and the signal is checked on 15-minutes averaged basis as described in Section 2.1. It is stated that the BRPs are subjected to a penalty in case of exceeding $>5\%$ of the actual power (produced power). In order to simulate that scenario using the experiments, the PossPOW algorithm and the sum of individual SCADA signals,i.e. the current way of determining the available power, see Chapter 2, at the turbine pairs (i.e. the test turbine and the affected turbine) are compared with the actual power generated by those turbines. The curtailment of the WH1102 and WH1105 turbines (WH1348 and WH1468 for Experiment #1, southerly winds) is considered separately in Figures 7.7 and 7.8.

In Figure 7.7, for the westerly winds, the estimated available powers on WH1102 / WH1112 pair are compared with the active power on turbines WH1101 / WH1111 and WH1103 / WH1113, respectively, corresponding to 2 different data points at each 15-minutes averaging points. In Figure 7.8, on the other hand, the difference in terms of aggregated possible power between the turbine pair WH1105 / WH1115 with WH1104 / WH1114 and WH1106 / WH1116 is presented. Instead of comparing the entire row of turbines as in Figure 7.6, the first and the second turbines are used as a pair to make the most of the similarity assumption and avoid the local turbulence effects. The data points correspond to (Active Power $_{\text{WH1103}}$ + Active Power $_{\text{WH1113}}$) - (Possible Power $_{\text{WH1102}}$ + Possible Power $_{\text{WH1112}}$) and so on where Possible Power represents either the aggregated SCADA signals or the PossPOW calculations. The differences in the power values are not normalized and directly compared with the $\pm 5\%$ of the actual power produced by the test and the affected turbine with the curtailment, e.g. $Active\ Power_{\ WH1102-WH1112}$.

As seen from Figures 7.7 and 7.8, the PossPOW algorithm gives significantly better results compared to the aggregated SCADA possible power signals which is the stan-

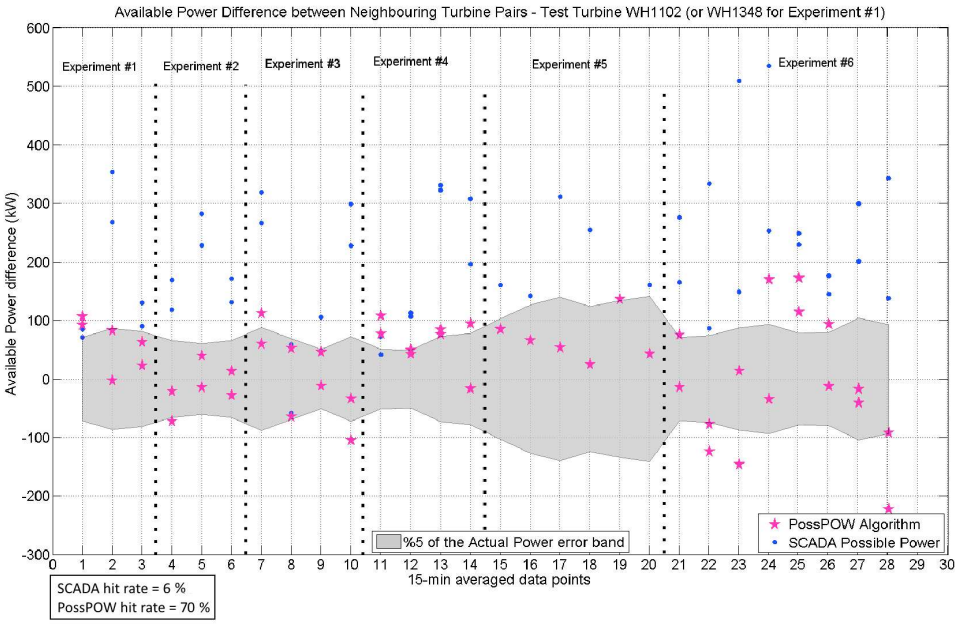

Figure 7.7: The comparison of SCADA Possible Power, and PossPOW algorithm results at turbine pairs WH1102 / WH1112 (or WH1348 / WH1347 for southerly winds in Experiment #1) with the adjacent rows, i.e. WH1101 / WH1111 and WH1103 / WH1113 for westerly winds; WH1238 / WH1237 and WH1358 / WH1357 for southerly winds) in Horns Rev-I experiments. $\pm 5\%$ of *Actual Power* $= \pm 5\%$ of *Active Power* $_{WH1102-WH1112}$

dard industrial practice currently. Note that the 15-minutes averaged data points are collected using all the experiments with different inflow conditions (different upstream wind speed, turbulence intensity, etc.) which provides rather wide scope to evaluate the performance. The current practice is observed to be over-estimating the available power for most of the cases, where the PossPOW results are mostly within the $\pm 5\%$ error band with slight over and under-estimation together. Considering the fact that the turbine pair WH1101 / WH1111 is located on the corner of the wind farm, it is expected that the deviations from the reference available power are more pronounced for the Figure 7.7 compared to the Figure 7.8. It is compatible with the notably lower hit rate of the SCADA possible power signal for the WH1102 events. However, due to availability issues of the signal described in Chapter 6, the processed wind direction signals in Table 7.1 indicate that for most of the experiments, the mean wind direction is below 270°, preventing WH1101 / WH1111 turbine pair to be exposed to free wind in the simulations. Therefore the similarity between WH1101 / WH1111 and WH1102 / WH1112 is rela-

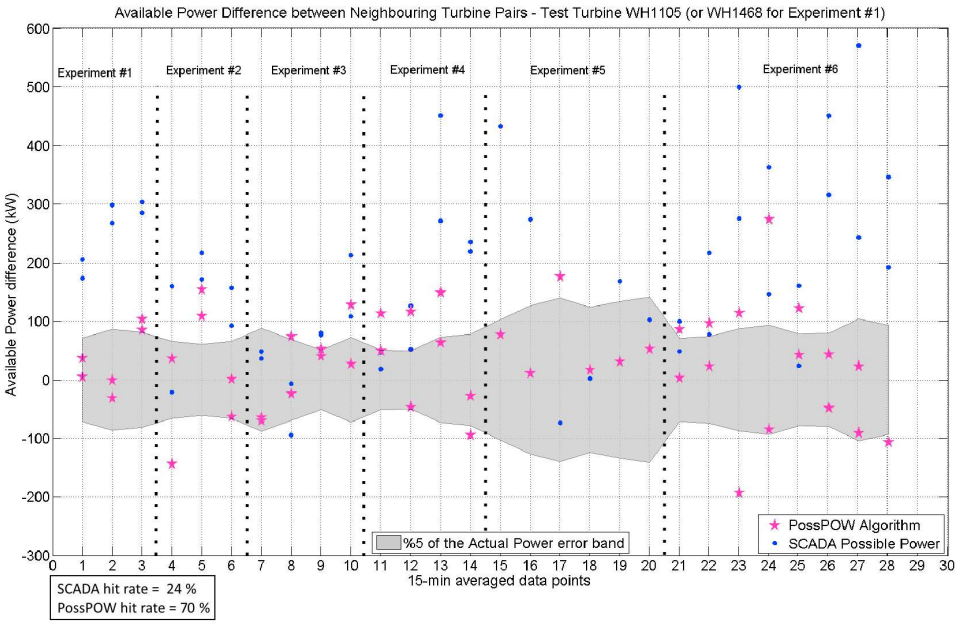

Figure 7.8: The comparison of SCADA Possible Power, and PossPOW algorithm results at turbine pairs WH1105 / WH1115 (or WH1468 / WH1467 for southerly winds in Experiment #1) with the adjacent rows, i.e. WH1104 / WH1114 and WH1106 / WH1116 for westerly winds; WH1358 / WH1357 and WH1478 / WH1477 for southerly winds) in Horns Rev-I experiments. $\pm 5\%$ of *Actual Power* $= \pm 5\%$ of *Active Power* $_{WH1105-WH1115}$

tively conserved and the performance of the PossPOW algorithm remain approximately the same.

Combination of Figures 7.7 and 7.8 collates two affected and four reference turbines for six experiments, in total 24 data points. They can be used to generate a statistical distribution of the percentage error of the possible power estimated at the reference turbine(s), see Equation 7.1 . It is seen from Figure 7.9(a) that the median of the SCADA possible power signal error is approximately 35% where the distribution is also broad indicating higher uncertainty. On the other hand, the PossPOW algorithm seem to reduce that error significantly down to 10% with a considerably narrower distribution. Further discussion on the uncertainty analysis is left as future work in Chapter 8.

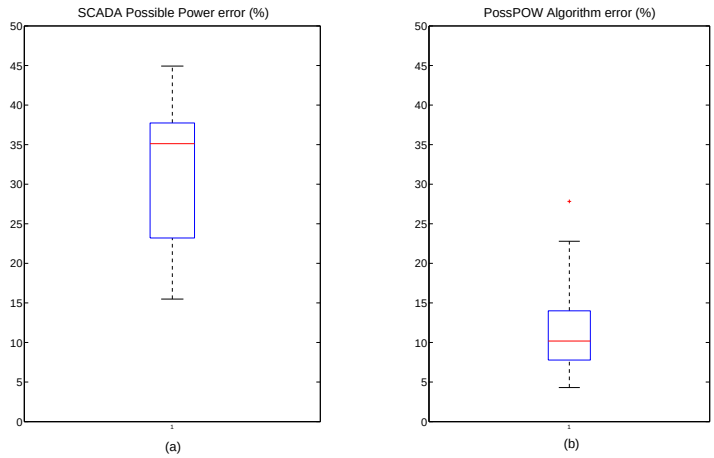

Figure 7.9: Median (red line), 25th and 75th percentiles (edges of the box) of the percentage error of (a) the SCADA Possible Power and, (b) the PossPOW algorithm

$$\text{error}_{\text{ Available Power}} = \left| \frac{\text{Possible Power}_{\text{ Affected Turbine}} - \text{Active Power}_{\text{ Reference Affected Turbine}}}{\text{Active Power}_{\text{ Reference Affected Turbine}}} \right| \tag{7.1}$$

8

Conclusions & Future Work

In order to reach the European climate and energy targets, a future with even more wind power in the grid than the recent record of 140% instantaneous penetration in Denmark [74] is to be expected. Therefore, the wind power plants will have to contribute to the safe operation of the power system through delivery of ancillary services more frequently. One of those ancillary services is reserve power, which is achieved by down-regulating the wind farm from its maximum possible power. The estimation of that maximum possible (or available) active power of a down-regulated wind farm is crucial as it is the amount of the loss production to be compensated during mandated curtailment and the amount of up-regulation potential which can be traded as reserve power on the ancillary services market.

Most of the European TSOs address the quality assessment of the available and / or reserve power calculations. The characteristics of the requested data, either at the turbine or at the wind farm scale, are legislated in terms of time resolution and estimated accuracy as summarized in Section 2.1. As the world leader of the wind energy supply with respect to the electricity consumption, Denmark has the most detailed and advanced legislation applied so far. Therefore throughout this study, available power estimation approaches are evaluated according to the Danish criteria.

Due to change in the wake characteristics during curtailment, the estimation of the available power of a wind farm under down-regulation is a complex process, especially for high resolution data. The state of the art industry practice is to aggregate the possible (or available) power signals from the individual turbine SCADA, which does not take into account the reduction in the wake losses thus over-estimates the production capacity. Here we present and validate the PossPOW Algorithm which corrects the ”down-regulated wake”, and shown to perform significantly better in a series of curtailment experiments in the Horns Rev-I wind farm, compared to the current practice.

The PossPOW project mainly consists of three parts; 1) Chapter 3, to estimate the local wind speed at the upstream locations (as they are not affected by the down-regulated wake), 2) Chapters 4, 5 and 6, to advect the wind speed along the wind farm via a wake model (to replace the reduced wake with the nominal velocity deficit) and calculate the production capacity, and 3) Chapter 7, to test the estimated wind farm scale possible power results and validate the algorithm. The approach is designed to work with 1-second SCADA data aiming to calculate the real-time wind farm power curve as well.

In Chapter 3, the wind speed at the turbine locations are estimated using the pitch, rotational speed and active power from the turbines together with a generic approximation

of the C_P in terms of pitch angle and tip speed ratio. The method is applied and validated on Horns-Rev-I, Thanet and Lillgrund offshore wind farms as well as the NREL 5MW simulations, under both normal and curtailed operations.

For the second part of the project, the existing wake models are reviewed extensively and implemented in several test cases on Sexbierum onshore and Lillgrund offshore wind farms in Chapter 4. The available robust wake models provide comparable results to the advanced, highly detailed models. However, they are tuned for 10-min averaged data to acquire long term, statistical information. Therefore, in order to model the wind speed through the wind farm for higher time resolutions, the Larsen wake model is re-calibrated in Chapter 5. To adjust the parameters in the Larsen wake model, a methodology to estimate the TI across the wind farm based on the rotor effective wind speed is presented. The methodology is implemented in Lillgrund and Horns Rev offshore wind farms and compared with the met mast as well as the nacelle anemometer and standard deviation of the produced power. Second-wise estimated rotor effective wind speed and the tabulated TI at the upstream and downstream turbine locations are used for both the re-calibration in Thanet and the validation in Horns Rev for single wake cases.

The re-calibrated real-time wake model is implemented in the wind farm scale in Chapter 6, considering only the maximum dual wake deficit for the wind speeds lower than the rated; whereas for the wind speeds above, all the wake contributions are taken into account, in accordance with studies performed by Larsen et al. [57]. In order to correct the results in terms of unsteady meandering effects especially for large offshore wind farms, the correlation of the wake deficit and the local wind direction variation introduced by Ainslie [3] is considered. The wake loss calculations are iterated for all the turbines in the wind farm at each second and compared with the data post-processed for localised time delay.

In regard to the Danish TSO requirements on provision of the data for the compensation during mandatory down-regulation, the percentage error was analysed in 5-minutes intervals when evaluating the model performance in wind farm scale power estimation. The applied real-time power curve estimation approach is shown to be in a good agreement with the active power signal, also considering the 5% error band at the power plant level as stated in the same regulation. Then the model is further implemented in the down-regulated state.

To test the performance of the PossPOW algorithm under curtailment, a series of dedicated experiments are conducted and presented in Chapter 7. In view of the fact the available power of a turbine in the wake of a curtailed turbine is not measurable, the idea is to take advantage of a rather simple layout such as Horns Rev-I, using the similarity of the flow along the neighbouring rows. Accordingly, two of the upstream turbines are curtailed for the westerly winds under specific inflow conditions where start and stop triggers are applied considering the incoming wind direction and inflow speed. Six down-regulation events are executed in total, where the inflow conditions satisfy the prerequisite criteria. The results of the experiments show that the PossPOW algorithm

is capable of reproducing the wind speed at the reference turbine, correcting the reduced wake deficit due to down-regulation hence providing the actual possible power with a time resolution of a second. It is also noted that, the effect of down-regulation continues towards approximately five downstream turbines along the row for upright incoming winds. The available power signals obtained from the PossPOW algorithm are compared to the current state of the art industry practice where the individual SCADA signals of the possible power are aggregated. The comparison is presented according to the Danish regulations regarding the quality of the wind farm scale available power signal, where the accuracy is limited to 5% of the actual produced power over 15-minutes intervals. It is seen that the current practice consistently over-estimates the production capacity where the PossPOW algorithm mostly stays within the error band. The mean error of the current practice is observed to be 35% among the six experiments performed, where the PossPOW algorithm is shown to be capable of reducing that error down to 10%. Furthermore, the error range of the current practice and the PossPOW algorithm indicate much narrower distribution for the developed methodology corresponding to lower level of uncertainties.

For further investigation of the model sensitivities, a second wave of experiments in Horns Rev-I are designed. Similar to the presented setup, two of the upstream turbines are to be curtailed for south-westerly winds. The aim is to investigate the effects of the upstream curtailment to the diagonal wake and evaluate the PossPOW algorithm for different turbine spacings.

The next step is to quantify and reduce the uncertainty in the reserve power using the verified PossPOW algorithm together with the state of art forecasting methods. In order to achieve to a more resilient power system, the Concert project has been developed and it is currently being negotiated with the same funding organization. The Concert project aims to quantify and reduce the uncertainty in reserve power, bringing the PossPOW algorithm and the state of the art forecasting methods together. The quantification and propagation of the input uncertainties as well as the parameter uncertainties in the algorithm will be investigated, which is a complex and computationally intensive process for realistic engineering simulations. A variety of methodologies are available in literature, from basic convolution techniques [20] to commonly used Monte Carlo simulations [92], to more sophisticated stochastic spectral Galerkin approaches [40, 106, 32]. After the selection of the most suitable method(s) for the propagation, the uncertainty quantification of the PossPOW algorithm will be finalised. In order to reduce the estimated uncertainty in the available power, the developed approach will be further enhanced by machine learning techniques. Here, the main intention is to provide supplemental information in the regions where the model predictions are the most ambiguous and to improve the confidence in the parameters.

After the available power algorithm is enhanced, a smart spatial distribution of the down-regulation criteria, i.e. set-points, within the turbines in a wind farm or across

several wind farms in a region is possible. Spatially distributing the set-points reduces the correlation between each down-regulation and thereby the correlation of their uncertainties. As independent uncertainties should compensate each-other, that would reduce the combined uncertainty of the wind power plant curtailment. This reduction of uncertainty should allow to optimally minimize the required ”safety factor” in the control, which currently leads to wasted energy. The safety factor is a further down-regulation beyond the envisaged target to be sure that warranted up-regulation capacity is available. So far, this safety factor can be quite sizeable.

As briefly mentioned in Section 7.2.2, the PossPOW algorithm can be implemented to the wind farm control to optimize the power production and the loads in any operational mode as it provides real-time power curve. Therefore, the model complex can be extended to develop control strategies for active load reduction in wind farms and predict the turbine response with respect to the detailed power and load response in time domain for down-regulated turbines operating in wake conditions. Thus, the enhanced PossPOW algorithm can be implemented in active wind farm control approaches considering: 1) the increase in power, 2) longer lifetime and, 3) smaller available power uncertainty via smart distribution of the set points.

List of Abbreviations

BEM Blade Element Momentum (theory)

BRP Balancing Responsible Parties

CFD Computational Fluid Dynamics

DTU Technical University of Denmark

DWM Dynamic Wake Meandering

ENTSO-E European Network of Transmission System Operators for Electricity

IWFBL Infinite Wind Farm Boundary Layer

LES Large Eddy Simulation

PCC Point of Common Coupling

QUICK Quadratic Upstream Interpolation for Convective Kinematics (scheme)

RANS Reynolds Averaged Navier-Stokes Equations

RDT Rapid Distortion Theory

SCADA Supervisory Control and Data Acquisition System

TI Turbulence Intensity

TSO Transmission System Operator

WAsP Wind Atlas Analysis and Application Program

WF Wind Farm

WPP Wind Power Plant

Acknowledgements

I would never have been able to finish my dissertation without the guidance of the PossPOW team, help from colleagues, and support from my family and friends.

Firstly, I do thank the funding agency Energinet.dk for supporting the PossPOW project under the Public Service Obligation (contract number 2012-1-10763).

I would like to express my deepest gratitude to my supervisor, Gregor Giebel, for his excellent guidance, caring, patience, calmness and providing me with an excellent atmosphere for doing research. I would like to thank my co-supervisors Poul Ejnar Sørensen and Niels Kjølstad Poulsen for their help and continuous support during these three years.

I am profoundly grateful to Pierre-Elouan Réthoré for his constant interest and patience; the project would never be the same without our extensive and inspiring discussions on the real-time flow modelling and how to get rid of the curtailed wake.

Furthermore, I would like to thank Mads Rajczyk Skjelmose and Jesper Runge Kristoffersen from Vattenfall for their valuable input to the project and the provision of the data from Horns Rev-I and Thanet wind farms, and also for their supervision and support through the experimental stage. I would also like to thank Michael Støttrup from Siemens Wind Power for all his contributions and for the Lillgrund data.

I would like to thank Olimpo Anaya-Lara for his hospitality and support (and also for his good mood) during my stay in University of Strathclyde in Glasgow.

I am very glad to have worked in such a stimulating environment in DTU Wind Energy, full of inspirational people. My warmest regards go to my beloved colleagues in the Integration and Planning (INP) section.

Lastly, I would like to thank my mum and my brother who were on pins and needles together with me, especially towards the end of the studies. And surely, I want to thank to all my friends here in Denmark, my dear Zhanna Tairova and Alexander Prostejovsky in particular, who persistently remind me that home is the people, not the place...

Appendix A

Calibration of Wind Direction SCADA Signal

Whenever using the 'Wind Direction' or 'Yaw Angle' or even 'Nacelle Direction' signals from the turbines' SCADA, the signals have to be calibrated using the wake depth as there might be misalignment issues.

Before the Validation of the Single Wake case

After re-calibrating the parameters in the Larsen wake model using Thanet data, the model is applied to a single wake case in Horns Rev-I for easterly winds. Before the re-calibrated version is compared with the original version and the dataset, the yaw signals are to be calibrated as a significant bias ranging from 3° to 16.5° is observed across the wind farm. For example, easterly wind specific representation of the yaw angle signal in Figure A.1 indicates a 7.5° shift from the perpendicular 90° flow direction.

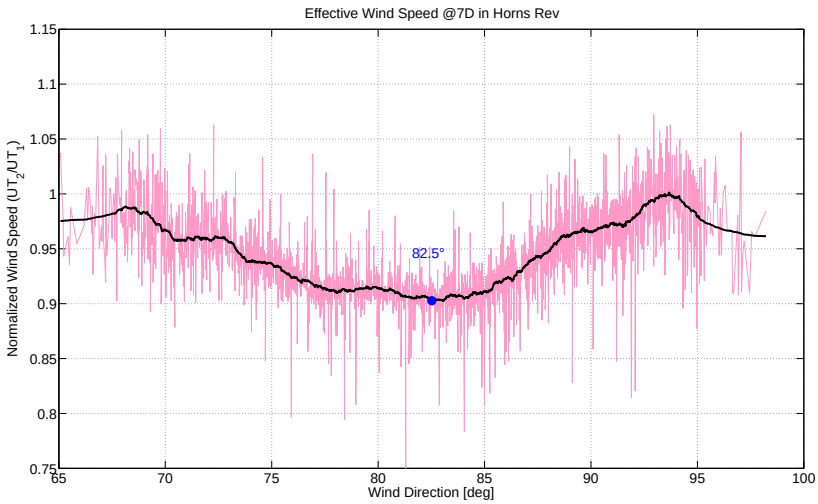

Figure A.1: Horns Rev-I Wind Direction bias in yaw signal, normalized wind speed between WH1586 and WH1596, $\frac{U_{WH1586}}{U_{WH1596}}$, westerly winds

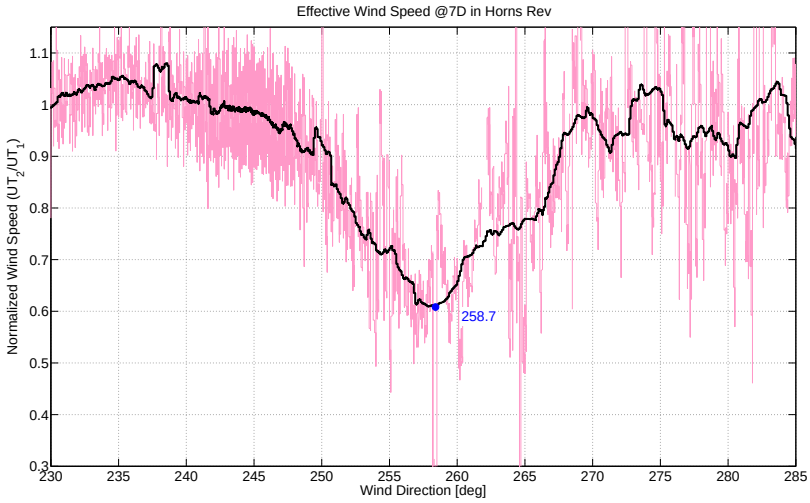

Figure A.2: Horns Rev-I Wind Direction bias in yaw signal, normalized wind speed between WH1103 and WH1113, $\frac{U_{WH1113}}{U_{WH1103}}$, westerly winds

Before the Experiments

The example for turbine WH1103 and WH1113 is given in Figure A.2 for westerly winds. As can be seen from the figure, the wind direction where the wake losses are maximized is located around 259° instead of the perpendicular 270°. This indicates an approximate bias of 11° which would highly change the characteristics of the experimental design. Also note that the bias itself can drift significantly when the turbine restarts, therefore the yaw angle calibration needs to be done shortly before initiating the experiments. The further analysis in the report is performed with the wind direction calibrated accordingly.

Appendix B

Journal Papers

In this chapter, the manuscripts prepared within the frame of the PossPOW project and included in this thesis are presented. The paper entitled "Wind Speed Estimation and Parametrization of Wake Models for Down-regulated Offshore Wind Farms within the scope of PossPOW Project" is attached on page 91, which is peer-reviewed and published in *Journal of Physics: Conference Series (Online)* as an extension of "The Science of Making Torque from Wind 2014 conference".

The subcomponents of wake modelling together with the in-house wake models developed at DTU Wind Energy are described and put to test using an onshore (Sexbierum) and an offshore (Lillgrund) wind farms in paper "Wind Turbine Wake Models Developed at the Technical University of Denmark: A Review". The published version of the article to the journal of *Renewable & Sustainable Energy Reviews* is attached on page 98.

The estimation of the turbulence intensity using the turbine data is submitted as a separate paper, starting from page 116, as it potentially has a broader area of application. It is entitled as "Estimation of Turbulence Intensity Using Rotor Effective Wind Speed in Lillgrund and Horns Rev Offshore Wind Farms" and submitted to *Renewable Energy* journal.

The main body of the PossPOW algorithm, including the re-calibration process of the Larsen wake model for real-time and the wind farm scale applications, is collected in a manuscript. The article is attached on page 133 and planned to be submitted to *Wind Energy* journal in January 2016.

The down-regulation experiments and the validation results of the PossPOW algorithm in Chapter 7 will be extended with the second round of experiments in Horns Rev-I where the reduced wake effect on the diagonal turbines are to be investigated. The final analysis is planned to be submitted to the newly launched *Wind Energy Science – The interactive open-access journal of the European Academy of Wind Energy (EAWE)*, which is in collaboration with Copernicus.

The Science of Making Torque from Wind 2014 (TORQUE 2014) IOP Publishing
Journal of Physics: Conference Series **524** (2014) 012156 doi:10.1088/1742-6596/524/1/012156

Wind Speed Estimation and Parametrization of Wake Models for Downregulated Offshore Wind Farms within the scope of PossPOW Project

Tuhfe Göçmen Bozkurt[1], Gregor Giebel[1], Niels Kjølstad Poulsen[2], Mahmood Mirzaei[2]

Technical University of Denmark: [1]Department of Wind Energy, Risø; [2]Department of Applied Mathematics and Computer Science, Lyngby

E-mail: tuhf@dtu.dk

Abstract. With increasing installed capacity, wind farms are requested to downregulate more frequently, especially in the offshore environment. Determination and verification of possible (or available) power of downregulated offshore wind farms are the aims of the PossPOW project (see PossPOW.dtu.dk). Two main challenges encountered in the project so far are the estimation of wind speed and the recreation of the flow inside the downregulated wind farm as if it is operating ideally. The rotor effective wind speed was estimated using power, pitch angle and rotational speed as inputs combined with a generic C_P model. The results have been compared with Horns Rev-I dataset and NREL 5MW simulations under both downregulation and normal operation states. For the real-time flow recreation, the GCLarsen single wake model was re-calibrated using a 1-s dataset from Horns Rev and tested for the downregulated period. The re-calibrated model has to be further parametrized to include dynamic effects such as wind direction variability and meandering also considering different averaging time scales before implemented in full scale wind farms.

1. Introduction

Wind power plants are important players in the energy market which have the capability to reduce their power supply to the grid, in other words to offer downregulation services to the balancing market. Downregulation of a wind turbine stands for an operational state in which the active power output is curtailed by pitching the blades. At this point, the concept of 'reserve power', i.e. how much the wind farm is downregulated, is substantial. Determination of possible (or available) active power is crucial firstly because the reserve power has considerable market value and also for wind farm developers to be compensated for the loss properly, during mandated downregulation. While the available power calculation is straight-forward and widely known for a single turbine [1], it gets rather complicated for the whole wind farm due to the change in the wake characteristics derived from the downregulated operational conditions. In fact, the wake losses generated by the upstream turbine(s) decrease during downregulation and the downstream turbines see more wind compared to the normal operation case. Currently, the Transmission System Operators (TSOs) have no real way to determine exactly the available power of a whole wind farm which is down-regulated. Therefore, PossPOW project aims to develop a verified and internationally accepted way to determine the possible power of a down-regulated offshore wind

Content from this work may be used under the terms of the Creative Commons Attribution 3.0 licence. Any further distribution of this work must maintain attribution to the author(s) and the title of the work, journal citation and DOI.
Published under licence by IOP Publishing Ltd

The Science of Making Torque from Wind 2014 (TORQUE 2014) IOP Publishing
Journal of Physics: Conference Series **524** (2014) 012156 doi:10.1088/1742-6596/524/1/012156

farm.

The first phase of PossPOW project is to estimate the rotor effective wind speed since the nacelle anemometers are not available on every turbine and known to have high uncertainties. The proposed method is to use power, pitch angle and rotational speed as inputs and combine it with a generic C_P model to estimate the wind speed. The performance of the model has been evaluated for both normal operation and downregulation periods using two different case studies: 1-s data from the Horns Rev-I wind farm and the NREL 5MW single turbine. Those estimated rotor effective wind speeds in the Horns Rev wind farm have been used to re-calibrate the GCLarsen single wake model to simulate the real time wind speed on the downstream turbine(s) which then has to be extended to the wind farm scale to consider dynamic effects inside the farm.

2. Rotor Effective Wind Speed Estimation

Since the nacelle region is exposed to highly distorted flow [2], the anemometers mounted on that region have always been approached with suspicion. Especially for real time calculations, using nacelle wind speed values measured during relatively shorter period, may induce higher uncertainties and can even lead to faults [3]. Therefore, the idea is to use the general power expression given in Eqn.1 with the turbine characteristics and second-wise SCADA signals namely the active power P, pitch angle θ and rotational speed ω.

$$P = \frac{1}{2}\,\rho\, C_P\left(\lambda,\theta\right)\pi R^2 U^3 \tag{1}$$

Since C_P during downregulation does not follow the ideal curve and because generally very limited information is provided by the manufacturers, the generic C_P expression proposed by Heier [4] was used to simulate the pitch angle, θ, and tip speed ratio, λ, dependency of the power coefficient, C_P (Eqn.2).

$$\begin{aligned} C_P\left(\lambda,\theta\right) &= c_1\left(\frac{c_2}{\lambda_i} - c_3\theta - c_4\theta^{c_5} - c_6\right) exp\left(\frac{-c_7}{\lambda_i}\right) \\ \lambda_i &= \left[\left(\frac{1}{\lambda + c_8\theta}\right) - \left(\frac{c_9}{\theta^3+1}\right)\right]^{-1} \end{aligned} \tag{2}$$

The coefficients in Eqn.2 are tabulated in Heier [4] but then modified by Ackermann [5] and Raiambal et al. [6] to fit for variable speed turbines and a specific turbine model, Vestas V-80, respectively. In this study, the latter version of coefficients with slight modifications (maximum change is less than 5 %) is applied where all the modifications are determined by the agreement between the modelled and the provided ideal C_P curves.

2.1. Horns Rev-I Wind Farm Test Case

The Horns Rev-I offshore wind farm is located in western Denmark consists of 80 Vestas V-80, 2MW Offshore wind turbines. The wind speed was calculated for each turbine iteratively using two different dataset sampled at every second extracted from the wind farm. The first dataset presented is recorded under normal operational conditions and covers a 35-hour period where the other dataset is recorded when the wind farm is downregulated and includes 2 hours of information. The provided channels are the active power, blade pitch angle, rotor rpm, averaged temperature, the nacelle anemometer wind speed measurements, wind direction and individual possible power signal for both of the datasets.

In Figure 1, *Rotor Effective Wind Speed* refers to the wind speed calculated iteratively after writing $U^3 = \left(\frac{\Omega R}{\lambda}\right)^3$ and using the C_P model in Eqn.2; the *Nacelle Wind Speed* is the wind speed

The Science of Making Torque from Wind 2014 (TORQUE 2014) IOP Publishing
Journal of Physics: Conference Series **524** (2014) 012156 doi:10.1088/1742-6596/524/1/012156

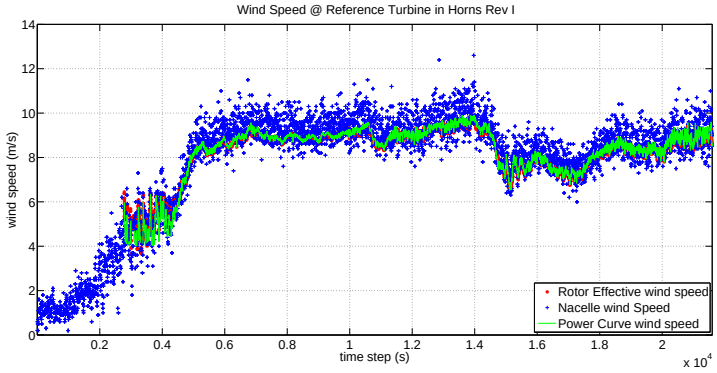

Figure 1. Wind Speed Comparison at the reference turbine located in Horns Rev Wind Farm, during normal (ideal) operation

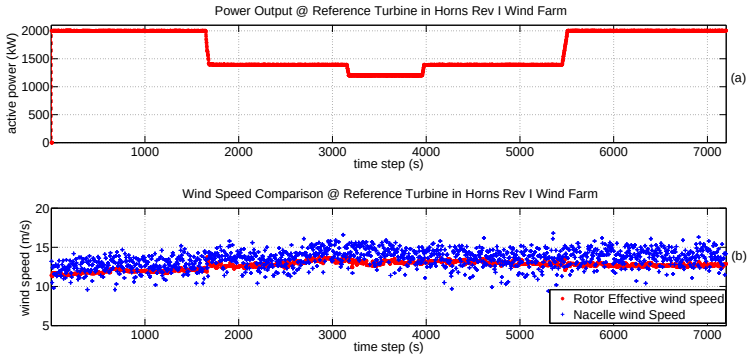

Figure 2. (a) Power Output (b) - Wind Speed Comparison of the reference turbine located in Horns Rev wind farm during downregulation

measured using a nacelle anemometer and *Power Curve wind speed* is the wind speed calculated using the active power signal and the ideal power curve provided by the manufacturer.

It is seen in Figure 1 that the rotor effective wind speed is in a very good agreement with the wind speed calculated using the power curve and also consistent with the nacelle anemometer measurements. Even though the nacelle anemometers are not favoured due to the reasons mentioned earlier, during the periods when the power curve methodology can no longer be applied (i.e. before cut-in and along rated region) the only available information regarding the wind speed is the nacelle anemometer measurements. Figure 2(b) includes a similar comparison this time performed for downregulated conditions. Figure 2(a) schematically represents the active power signal, or in other words the downregulation strategy.

If a comparative analysis is performed between Figure 1 and 2(b), it might be said that the deficit between the wind speed values obtained using the nacelle anemometer measurements and

The Science of Making Torque from Wind 2014 (TORQUE 2014) IOP Publishing
Journal of Physics: Conference Series **524** (2014) 012156 doi:10.1088/1742-6596/524/1/012156

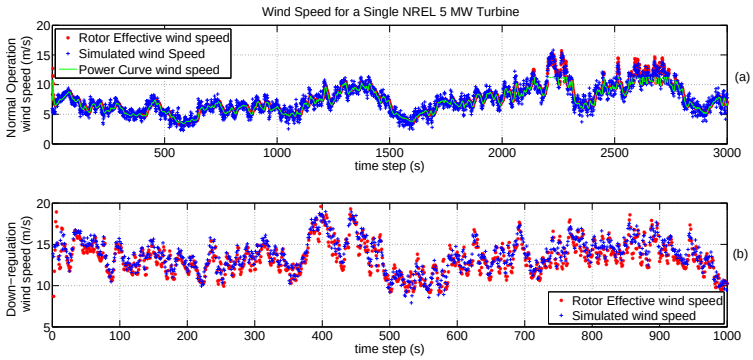

Figure 3. Wind Speed Comparison of a single NREL 5 MW turbine during (a) normal operation (b) 50% downregulation

the Rotor Effective Wind Speed remained approximately the same under standard operation and downregulated conditions. Therefore, assuming the power curve approach in 1 is representative enough for the wind speed, the estimation of the wind speed using the created algorithm for downregulation periods can be justified.

2.2. NREL 5MW Single Turbine Test Case

Since NREL 5MW isw an artificial turbine with public features [7], the developed wind speed algorithm can easily be tested using different scenarios. The simulations performed for NREL 5 MW wind turbine are considered as dataset and they include two different scenarios: normal operation with a mean wind speed of 9 m/s and 50 % downregulation with a mean wind speed of 13 m/s. For the first scenario, the simulated wind speed (dataset) was compared with the power curve and the modelled rotor effective wind speed - see Figure 3(a). The second simulation of wind speed was compared with the model estimation only since the power curve wind speed is not available for downregulation periods - see Figure 3(b).

In Figure 3(a), a very good agreement is observed between the simulated, power curve and effective wind speed values. It is also seen, especially between 2000-2750s time steps, that the power curve method is not applicable where the inflow velocity has exceeded the rated wind speed which is around 12 m/s for NREL 5 MW turbine. Figure 3(b) presents the agreement between the simulated (dataset) and modelled effective wind speed also during downregulation period.

3. Wake Model Recalibration for Real Time

To consider the changing wake effects for normal and downregulated operations, the rotor wind speed values of upstream turbines are to be taken as inputs to the wake model as they are not affected by the wake (downregulated or not). Then we apply the wake model directly to estimate the velocity deficit and calculate the possible power output of the wind farm. However, most of the computationally affordable wake models have only been used to acquire long term, statistical information and verified using 10-min averaged data. Therefore, re-calibration of the GCLarsen wake model [8], which has been implemented in WindPro and shown to perform also well on offshore in Wake Benchmark Work Package in EERA-DTOC [9], is performed and tested

The Science of Making Torque from Wind 2014 (TORQUE 2014) IOP Publishing
Journal of Physics: Conference Series **524** (2014) 012156 doi:10.1088/1742-6596/524/1/012156

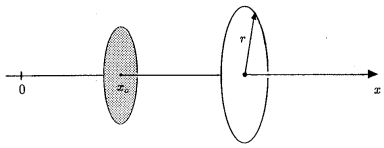

Figure 4. Control Volume considered in GCLarsen model

for single wake case in Horns Rev-I offshore wind farm.

3.1. GCLarsen Wake Model

Larsen has introduced a simple wake calculation procedure [8] and it has been implemented in many engineering applications due to its robustness and simplicity. In the model, the axis-symmetric form of Reynolds Averaged Navier Stokes (RANS) equations with the thin shear layer approximation is used. In GCLarsen model, the upstream turbine is positioned at $x_0 (x_0 > 0)$ and r denotes the radius of the wake (See Figure 4). Where the free stream velocity is indicated by U_∞, the mean velocities in the wake are $U_\infty + u_x$ and u_r along axial and radial direction, respectively.

The final equation for wake deficit, Eqn.3, is obtained after a comprehensive order of magnitude analysis and a series of boundary conditions.

$$u_x(x,r) = \frac{-U_\infty}{9}\left(c_T \pi R^2 x^{-2}\right)^{1/3}\left\{r^{3/2}\left(3c_1^2 c_T \pi R^2 x\right)^{-1/2} - \frac{35}{2\pi}^{3/10}\left(3c_1^2\right)^{-1/5}\right\}^2 \qquad (3)$$

where c_T is the thrust coefficient and R is the rotor radius. The parameters to calibrate are c_1, which is explicitly seen in Eqn.3, and x_0, which is embedded in $x = x_0 + \Delta x$ with Δx being the turbine spacing.

The second-wise dataset used in re-calibration process has been extracted during the normal operational case in Horns Rev-I, when the wind is easterly (i.e. wind direction $= 90° \pm 10°$). Since the model (Eqn3) is nonlinear in x_0, non-linear least squares fitting has been performed to estimate the parameters (c_1 and x_0) - with a convergence criterion of 10^{-6}. Each inside row in Horns Rev wind farm has been used for fitting individually and note that, in each calculation, thrust coefficient, c_T, was taken into account in such a way that the curve, $c_T(U_\infty)$ provided by the manufacturer. This curve was interpolated for each wind speed .

3.2. Time Delay Concept

Before using the dataset to determine the parameters c_1 and x_0, the time step at the downstream velocity has to be adjusted, considering the delay that occurs due to the distance between the turbines. The proposed methodology is to apply $t_{down} = t_{up} + t_d$ where t_{down} and t_{up} are the instants when the considered volume of air passes through the downstream and upstream locations, respectively and t_d is the time delay estimated as; $t_d = \Delta x / mean\left(U_{\infty_{down}}\right)$ with $U_{\infty_{down}}$ being the rotor effective wind speed at the downstream turbine.

3.3. Re-calibration Results

In that process, the rotor effective wind speeds calculated for each turbine was used in pairs, i.e. turbine #94 and #84 in Figure 5, both to calibrate and validate the model. Note that for both processes, the *dataset* term in the legend indicates the rotor effective wind speed values modelled as described in the previous section.

The Science of Making Torque from Wind 2014 (TORQUE 2014) IOP Publishing
Journal of Physics: Conference Series **524** (2014) 012156 doi:10.1088/1742-6596/524/1/012156

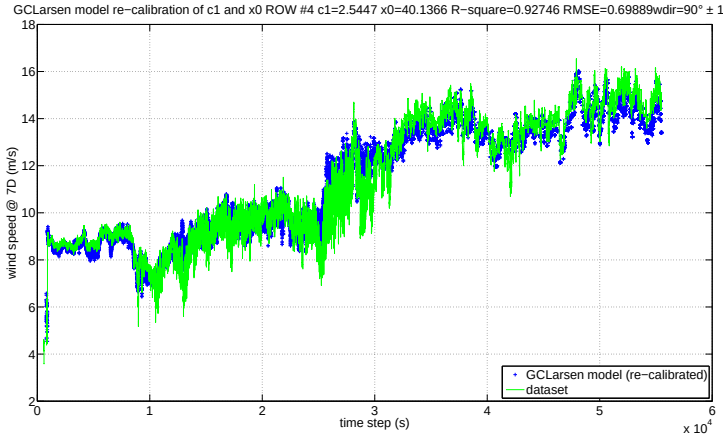

Figure 5. GCLarsen Single Wake model recalibration using Horns Rev, normal operation dataset

As can be seen in Figure 5, the parameters found in the fitting are $c_1 = 2.545$ and $x_0 = 40.137$ while the goodness of fit can be expressed in terms of $R^2 = 0.927$ and $RMSE = 0.699$.

Unfortunately, the validation is performed using the downregulated dataset due to lack of data available during easterly winds (wind direction $= 90° \pm 10°$). The downside of using the downregulated dataset is that the downstream wind speed estimated by the calibrated GCLarsen is expected to be lower than the effective wind speed. The reason is the fact that during downregulation, the wake effects are not as dominant thus leading the wind speed at downstream position to be higher than the standard operation. Because the c_T characteristics of the turbines with respect to the changing pitch angles during downregulation are not publicly available, the re-calibrated GCLarsen model takes into account only the normal operational c_T curve. As a result, the modeled wake effects are stronger therefore the wind speed downstream is lower. Having said that, the modelled, the effective and the measured wind speeds are compared in Figure 6.

First of all, from Figure 6, it can be observed that the variations in the measurements using nacelle anemometer are much higher than the ones in the rotor effective wind speed time series. This is in part due to the smoothing effect of the averaging over the entire rotor. Additionally, as expected, the GCLarsen model results in lower wind speeds at downstream. However, the difference is far from being significant and one of the reasons, maybe the most dominant one, can be the high wind speeds in the dataset, even along the wake since the thrust coefficient, c_T, behaves rather independent of the pitch angle variations (therefore the downregulation) for high wind speeds.

4. Conclusion & Future Work

The PossPOW project aims to develop an internationally accepted way to determine the available power in downregulated offshore wind farms. To be able to do that, the rotor effective wind speeds had to be estimated and the developed methodology has been verified and validated using Horns Rev-I wind farm and NREL 5MW single wake test cases, both during normal operation and downregulation. Using the effective wind speed values calculated second-wise, the

The Science of Making Torque from Wind 2014 (TORQUE 2014) IOP Publishing
Journal of Physics: Conference Series **524** (2014) 012156 doi:10.1088/1742-6596/524/1/012156

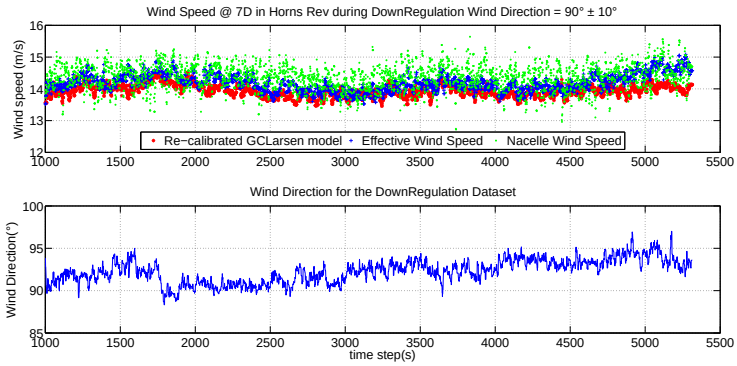

Figure 6. Comparison of Wind Speed values for filtered wind direction in $90° \pm 10°$ bin @ 7 diameters downstream of a turbine in Horns Rev, downregulation dataset

GCLarsen single wake model has been re-calibrated to simulate the real time wake properties. However, the re-defined parameters have been tested using the downregulated dataset which was not fully representative in terms of wake validation cases. Therefore, the first step ahead is to run the re-calibrated GCLarsen model for normal operation and compare the results. When the parameters for the single wake is validated, the model will be extended to the wind farm scale in which the dynamic effects inside the wind farm has to be included; such as the meandering concept, wind direction variability and partial wakes (or wake expansion).

Acknowledgement
The project partners of PossPOW are Vattenfall, Siemens, Vestas, and DONG. PossPOW is financed by Energinet.dk under the Public Service Obligation, ForskEL contract 2012-1-10763. The author would like to thank Mads Rajczyk Skjelmose and Jesper Runge Kristoffersen from Vattenfall for their cooperation and supply of the datasets.

References

[1] Kristoffersen, J. R., "The Horns Rev wind farm and the operational experience with the wind farm main controller," *Revue E-Société Royale Belge des électriciens*, Vol. 122, No. 2, 2006, pp. 26.
[2] Zahle, F. and Sørensen, N. N., "Characterization of the unsteady flow in the nacelle region of a modern wind turbine," *Wind Energy*, Vol. 14, No. 2, 2011, pp. 271–283.
[3] Beltrán, J., Guerrero, J. J., Melero, J. J., and Llombart, A., "Detection of nacelle anemometer faults in a wind farm minimizing the uncertainty," *Wind Energy*, Vol. 16, No. 6, 2013, pp. 939–952.
[4] Heier, S., *Grid Integration of Wind Energy Conversion Systems*, Wiley, Chichester, UK, 1998, p. 446.
[5] Ackermann, T., *Wind Power in Power Systems*, Wiley, 2005, p. 742.
[6] Raiambal, K. and Chellamuthu, C., "Modeling and simulation of grid connected wind electric generating system," *TENCON '02. Proceedings. 2002 IEEE Region 10 Conference on Computers, Communications, Control and Power Engineering*, Vol. 3, Oct 2002, pp. 1847–1852 vol.3.
[7] Scott, G., *Definition of a 5-MW Reference Wind Turbine for Offshore System Development*, Feb 2009.
[8] Larsen, G., *A Simple Wake Calculation Procedure*, rapport Risø-M, 1988.
[9] Hansen, K., "Benchmarking of Lillgrund offshore wind farm scale wake models," 2014, PowerPoint.

Renewable and Sustainable Energy Reviews 60 (2016) 752–769

Contents lists available at ScienceDirect

Renewable and Sustainable Energy Reviews

journal homepage: www.elsevier.com/locate/rser

Wind turbine wake models developed at the technical university of Denmark: A review

Tuhfe Göçmen*, Paul van der Laan, Pierre-Elouan Réthoré, Alfredo Peña Diaz, Gunner Chr. Larsen, Søren Ott

Technical University of Denmark, Department of Wind Energy, Risø campus, Roskilde, Denmark

ARTICLE INFO

Article history:
Received 27 April 2015
Received in revised form
19 December 2015
Accepted 20 January 2016

Keywords:
Wind turbine
Wake modelling
Wake models benchmark

ABSTRACT

Wind turbine wakes are one of the most important aspects in wind power meteorology because they decrease the power production and increase the loading of downstream wind turbines. Therefore, there is a continuous need to find a 'good' wake model to properly plan wind power plant-level control strategies, predict the performance and understand the fatigue loads of turbines. In this paper, six widely used approaches of wake modelling (Jensen, Larsen, Dynamic Wake Meandering, Fuga and, Ellipsys3D LES and RANS together with their interpretations) that were developed at Technical University of Denmark, are described and the model subcomponents are analysed. The models are evaluated using data from the Sexbierum (onshore) and the Lillgrund (offshore) wind farms to understand how to best utilize them.

The paper provides a comprehensive conceptual background to wake modelling combined with the overview of the state-of-the-art models including their implementations on operating wind farms.

© 2016 The Authors. Published by Elsevier Ltd. This is an open access article under the CC BY license (http://creativecommons.org/licenses/by/4.0/).

Contents

1. Introduction . . . 753
2. Governing equations . . . 753
   2.1. RANS . . . 754
   2.2. LES . . . 754
3. Subcomponents of wake modelling . . . 755
   3.1. Inflow generation . . . 755
      3.1.1. Logarithmic (or linear) law . . . 755
      3.1.2. Power law . . . 755
      3.1.3. Atmospheric stability . . . 755
      3.1.4. Precursor turbulence box . . . 755
      3.1.5. Mann turbulence box . . . 755
   3.2. Wake summation . . . 755
   3.3. Rotor wind speed calculations . . . 756
      3.3.1. Elliptic equations . . . 756
      3.3.2. Vortex equations . . . 756
      3.3.3. Parabolic equations . . . 756
   3.4. Wind turbine model . . . 756
      3.4.1. Inverse 1-D momentum theory approach . . . 756
      3.4.2. Induced thrust curve approach . . . 757
      3.4.3. Blade element momentum (BEM) theory and generalized actuator disc model . . . 757
      3.4.4. Sequentially activation method . . . 757
      3.4.5. Aero-elastic model approach . . . 757
   3.5. Wind direction & speed . . . 757

* Corresponding author.
E-mail address: tuhf@dtu.dk (T. Göçmen).

http://dx.doi.org/10.1016/j.rser.2016.01.113
1364-0321/© 2016 The Authors. Published by Elsevier Ltd. This is an open access article under the CC BY license (http://creativecommons.org/licenses/by/4.0/).

4. Wake models . . . 757
4.1. Infinite wind farm boundary layer model . . . 757
4.1.1. Atmospheric stability correction . . . 758
4.2. The Jensen wake model . . . 758
4.2.1. Interpretations of the Jensen model . . . 759
4.3. The Larsen model . . . 759
4.3.1. 1988 (Early) version . . . 759
4.3.2. 2009 (Later) version . . . 759
4.4. Dynamic wake meandering model . . . 760
4.4.1. Velocity deficit . . . 760
4.4.2. Meandering of the wake . . . 760
4.4.3. Rotor induced turbulence . . . 761
4.5. FUGA . . . 761
4.6. EllipSys3D . . . 761
4.6.1. RANS . . . 761
4.6.2. LES . . . 762
5. Benchmarking study . . . 762
5.1. Sexbierum wind farm . . . 762
5.1.1. Introduction . . . 762
5.1.2. Results and discussion . . . 763
5.2. Lillgrund offshore wind farm . . . 764
5.2.1. Introduction . . . 764
5.2.2. Results and discussion . . . 764
6. Application of the models . . . 767
6.1. Typical usage . . . 767
6.2. Accuracy . . . 768
6.3. Complexity and uncertainty of inputs . . . 768
6.4. Computational costs . . . 768
7. Conclusions . . . 768
Acknowledgement . . . 768
References . . . 768

1. Introduction

Wind turbine wake modelling concentrates on characterizing the flow behind wind turbines. There are two main physical phenomena of interest in the wake: (1) the momentum (or velocity) deficit, which causes a reduction in the power output of the downstream turbines, and (2) the increased level of turbulence, which gives rise to unsteady loading on downstream turbines.

The wake-induced power losses and blade loadings are studied in two regions within the wake, referred to as near and far wake. The near wake starts right after the turbine and extends to approximately 2–4 rotor diameters (D) downstream [1,2]. In this region, the flow is highly influenced by the rotor geometry, which leads to the formation of the blade tip vortices. In addition, there are steep gradients of pressure and axial velocity, and wake expansion. In the far wake, the effects of the rotor geometry are limited to the reduced wind speeds and increased turbulence intensities. Further, the turbulence is the dominating physical property in the far wake [3]. In addition to the rotor induced turbulence, the region further downstream is influenced by the large scale (or atmospheric) turbulence. The turbulence mixing accelerates the wake recovery in terms of both the velocity deficit and the turbulence intensity. In the far wake, the velocity deficit approaches a Gaussian profile, which is axisymmetric and self-similar [4]. Moreover, the meandering of the wake might also contribute to the recovery of the velocity deficit although it significantly increases the unsteady loading on the downstream turbine(s). All these elements lead to different approaches for the development of wind turbine wake models. Out of the many, widely used six models and their interpretations developed at the Technical University of Denmark (DTU) are presented here. First, the components of wake modelling are described in order to demonstrate the differences between the modelling approaches better and then the benchmark study for onshore and offshore cases has been performed. The paper is organized as follows: in Section 2, the Navier–Stokes equations are presented with the incorporated turbulence modelling form of Reynolds Averaged Navier–Stokes (RANS) and Large Eddy Simulation (LES), discussed in Sections 2.1 and 2.2, respectively. In Section 3, the sub-components of wake modelling, namely the inflow generation, the wake summation, the calculation of the wind speed at the rotor, the modelling of the wind turbine in the simulations, and the assessment of wind direction and speed are listed. Note that all of these concepts are originally much more comprehensive than their descriptions presented here and are only explained in the frame of wake modelling. The wake models Jensen, Larsen, Dynamic Wake Meandering, Fuga and the flow solver Ellipsys3D (both RANS and LES versions) are described in Section 4 and they are implemented on the onshore Sexbierum and offshore Lillgrund wind farms in Section 5. Accordingly, the models are evaluated in terms of their targets of application in Section 6.

2. Governing equations

It is convenient to say, except for the blade tip region, that the physics of wind turbine wakes can be described by the incompressible Navier–Stokes equations, where the atmospheric flow velocities upstream and downstream of a wind turbine typically range between 4 and 25 m/s. The governing equations in Einstein notation and Cartesian coordinates are:

$$\frac{\partial u_j}{\partial x_j} = 0, \tag{1}$$

$$\frac{\partial u_i}{\partial t} + u_j \frac{\partial u_i}{\partial x_j} = -\frac{1}{\rho}\frac{\partial P}{\partial x_i} + \frac{\partial}{\partial x_j}(2\nu S_{ij}) + f_i, \tag{2}$$

where u is the velocity and x is the position vector, P is the pressure, ρ is the fluid density, ν is the kinematic viscosity, $f_i = \frac{F_i}{\rho}$ are the external body forces, t is the time, i, j are the directional components and S_{ij} is the strain rate tensor defined as

$$S_{ij} = \frac{1}{2}\left(\frac{\partial u_i}{\partial x_j} + \frac{\partial u_j}{\partial x_i}\right). \tag{3}$$

Since Eq. (2) includes a non-linear convective term, $u_j\frac{\partial u_i}{\partial x_j}$, especially in complex turbulent flows, some simplifications in both fluid and blade modelling are needed for computational purposes. There are therefore a large number of turbulence models, and from the computational fluid dynamics (CFD) point of view, we will concentrate in the RANS and LES methodologies.

2.1. RANS

To account for the turbulence effects, which can be of random chaotic nature, the instantaneous Navier–Stokes equations are time-weighted averaged resulting in the well-known RANS equations. The time-weighted average procedure is based on a statistical approach applied to the main variables of the flow and decomposes velocity into an average, $\overline{u}$, and a fluctuation term, u', the so-called Reynolds decomposition [5],

$$u_i(x_i, t) = \overline{u}_i(x_i, t) + u_i'(x_i, t). \tag{4}$$

When applied to the Navier–Stokes equations, the continuity equation becomes

$$\frac{\partial u_j}{\partial x_j} = \frac{\partial\left(\overline{u}_j + u_j'\right)}{\partial x_j} = 0. \tag{5}$$

Note that $\overline{u}_j' = 0$ and both $\overline{u}_j(x_j, t)$ and $u_j'(x_j, t)$ are solenoidal because the flow is assumed to be incompressible which can be written as

$$\frac{\partial \overline{u}_j'}{\partial x_j} = 0 \qquad \frac{\partial \overline{\overline{u}}_j}{\partial x_j} = \frac{\partial \overline{u}_j}{\partial x_j} = 0 \tag{6}$$

the left-hand side of Eq. (2) can be rewritten. Using the continuity relation as,

$$\frac{\partial u_i}{\partial t} + u_j\frac{\partial u_i}{\partial x_j} = \frac{\partial u_i}{\partial t} + \frac{\partial}{\partial x_j}(u_i u_j). \tag{7}$$

The time averaging of Eq. (2), when considering Eq. (7), becomes

$$\frac{\partial \overline{u}_i}{\partial t} + \frac{\partial}{\partial x_j}(\overline{u}_i\overline{u}_j) = -\frac{1}{\rho}\frac{\partial \overline{P}}{\partial x_i} + \nu\frac{\partial^2 \overline{u}_i}{\partial x_i \partial x_j} + \overline{f}_i. \tag{8}$$

The non-linear term $(\overline{u_i u_j})$ can be expanded using Reynolds decomposition.

$$\begin{aligned}\overline{(u_i u_j)} &= \overline{(\overline{u}_i + u_i')(\overline{u}_j + u_j')} \\ &= \overline{(\overline{u}_i\overline{u}_j + u_i'\overline{u}_j + u_j'\overline{u}_i + u_i'u_j')} \\ &= \overline{u}_i\overline{u}_j + \overline{u_i'u_j'}\end{aligned} \tag{9}$$

Substituting Eq. (9) into Eq. (8) results in the final form of RANS equations.

$$\frac{\partial \overline{u}_i}{\partial t} + \overline{u}_j\frac{\partial \overline{u}_i}{\partial x_j} = -\frac{1}{\rho}\frac{\partial \overline{P}}{\partial x_i} + \nu\frac{\partial^2 \overline{u}_i}{\partial x_i \partial x_j} - \frac{\partial(\overline{u_i'u_j'})}{\partial x_j} + \overline{f}_i, \tag{10}$$

where the term $\overline{u_i'u_j'}$ is the Reynolds stress tensor, which is a result of the non-linearity of the convective terms, and represents the averaged momentum transfer caused by turbulent fluctuations. The Reynolds stress tensor contains 6 new additional unknown variables that must be modeled (only 6 additional variables instead of 9 because of the imposed condition of the RANS angular momentum equation). A first approach to model the Reynolds stresses was first proposed by Boussinesq [6] who introduced the concept of turbulent viscosity or eddy viscosity. His idea was to describe turbulent effects as an increased fluid–fluid and fluid–solid viscosity interaction (surface forces). However, the approach assumes turbulence effects to be isotropic. The hypothesis basically relates the Reynolds stresses to the mean rate of deformation and can be simplified as,

$$\overline{u_i'u_j'} = \frac{2}{3}k\delta_{ij} - \nu_T 2\overline{S}_{ij}, \tag{11}$$

where $k \equiv \frac{1}{2}\overline{u_k'u_k'}$ is the turbulent kinetic energy, δ_{ij} is the Kronecker delta, $\overline{S}_{ij}$ is the mean strain rate tensor as defined in Eq. (3), and ν_T is the turbulent eddy viscosity. The Boussinesq hypothesis states that the transfer of the energy mechanism between turbulent eddies is very much like that between molecular formations [7]. However, in contrast to ν, ν_T is not a physical property of the fluid but it represents the turbulent characteristics of the flow. Furthermore, direct numerical simulations (DNS) have indicated that there is no correlation between the terms $\overline{u_i'u_j'}$ and $\overline{S}_{ij}$ [8]. Therefore there is no physical basis for Eq. (11) and the assumptions are not valid for simple shear flows, anisotropic flows or 3D flows [9]. However, because they improve practicality and maintain robustness, the assumptions are applied to a variety of tools that provide solutions within certain accuracy. Several studies [10–12] offer detailed explanations of turbulence modelling and turbulence viscosity models.

2.2. LES

LES is a powerful technique to represent the turbulence characteristics of a flow by decomposing it into large and small scales. The small eddies are filtered out, so that the effect of large structures can be solved using the Navier–Stokes equations directly while small scale turbulent mixing is modelled. Eddies smaller than a certain grid size, Δx, are estimated using a subgrid-scale model. To eliminate the subgrid-scale, a filter with a width of Δx is introduced, which corresponds to the convolution of $u(x, t)$ by the filter function $G_{\Delta x}(\vec{x})$ in the form

$$\tilde{u}\left(\vec{x}, t\right) = \int u\left(\vec{y}, t\right) G_{\Delta x}\left(\vec{x} - \vec{y}\right) d\vec{y} = \int u\left(\vec{y}, t\right) G_{\Delta x}\left(\vec{y}\right) d\vec{y}. \tag{12}$$

Therefore, the subgrid-scale field can be described by the difference between the actual and filtered flow,

$$u' = u - \tilde{u}. \tag{13}$$

When filtering is applied to the combination of Eqs. (2) and (7) we get

$$\frac{\partial \tilde{u}_i}{\partial t} + \frac{\partial}{\partial x_j}(\tilde{u}_i\tilde{u}_j) = -\frac{1}{\rho}\frac{\tilde{P}}{\partial x_i} + \frac{\partial}{\partial x_j}(2\nu S_{ij}) + T_{ij}) + \tilde{f}_i, \tag{14}$$

where T_{ij} is defined as the subgrid stress tensor, is responsible from the momentum exchange between subgrid and filtered scales and is formulated as

$$T_{ij} = \tilde{u}_i\tilde{u}_j - u_i\tilde{u}_j. \tag{15}$$

By using the Boussinesq hypothesis, the subgrid stress tensor can be rewritten in analogy to the RANS equations as;

$$T_{ij} = 2\nu_{SGS}\tilde{S}_{ij}, \tag{16}$$

where $\tilde{S}_{ij}$ is the filtered strain rate tensor and ν_{SGS} is the subgrid-scale eddy viscosity which is most widely used as shown in Smagorinsky et al. [13],

$$\nu_{SGS} = C_s^2\Delta^2|\tilde{S}| \tag{17}$$

where $|\tilde{S}| = \left(2\tilde{S}_{ij}\tilde{S}_{ij}\right)^{1/2}$, C_s is the Smagorinsky constant, which varies between 0.1 and 0.2, depending on the properties of the flow [7], and Δ is defined as $\Delta = (\Delta x\Delta y\Delta z)^{1/3}$. There are other

subgrid-scale models, some of which can be found in the review of Lesieur et al. [14].

Determining Δ, which states the filter width, is crucial in order to represent the physical characteristics of the flow. An example of the accuracy studies performed on LES can be found in Geurts et al. [15].

The major concern regarding LES is the high computational cost for many engineering applications. However, particularly when dealing with flows with a solid wall as a boundary, it is possible to switch to RANS, since Eqs. (16) and (11) have similar characteristics. This is a hybrid approach called detached eddy simulations (DES). Specifically for high Reynolds number flows, where massive detachments may occur, DES has been shown to better represent the flow characteristics than both RANS and LES [16].

3. Subcomponents of wake modelling

After describing the equations for two of the main CFD approaches, RANS and LES, the "initial" and "boundary" conditions of those equations need to be introduced. Furthermore, concerning the analytical models, the approaches to account for multiple wakes and the way the rotor is characterized for wake simulations are described in this section.

3.1. Inflow generation

The characteristics of the atmospheric flow are mainly determined by the orography, the roughness and the roughness changes, together with the atmospheric stability which have been modelled using a variety of approaches. Here, for the description of the vertical velocity profile and turbulence, some fundamental concepts are discussed.

3.1.1. Logarithmic (or linear) law

The logarithmic wind profile can be derived in many ways [17–19] and it is formulated in the meteorological context as

$$U(z) = \frac{u_*}{\kappa} \ln\left(\frac{z}{z_0}\right), \tag{18}$$

where U is the mean wind speed, u_* is the friction velocity, κ is the von Kármán constant (≈ 0.4), z is the elevation above ground level and z_0 is the surface roughness length.

3.1.2. Power law

Another way to characterize the vertical wind profile is the power law, which is widely used in many wind engineering applications due to its practicality. It is given as

$$U(z) = U_{ref}\left(\frac{z}{z_{ref}}\right)^{\alpha}, \tag{19}$$

where U_{ref} is the undisturbed mean wind speed at a reference height, z_{ref}, and α is the power law or shear exponent. In general α is a variable quantity ranging from less than 1/7 during daytime and more than 1/2 during the night [20].

3.1.3. Atmospheric stability

The static stability condition of the atmosphere has an effect on the flow characteristics and is normally taken into account by the Obukhov length, L_S, which represents the ratio of the mechanical to convective turbulence production,

$$L_S = \frac{-u_*^3}{\kappa\left(\frac{g}{T}\right)\left(\frac{H}{C_p\rho}\right)} \tag{20}$$

where g is the gravitational acceleration, T is the air layers mean temperature and H, C_p, and ρ are the kinematic heat flux, specific heat and density of the air, respectively. As $u_* \geq 0$ m/s, an unstable or stable behaviour of the atmosphere is determined by the sign of H. For example when $\frac{dT}{dz} > \left(\frac{dT}{dz}\right)_{adiabatic}$ the atmosphere is considered to be unstable.

In many wind energy applications, the atmosphere is generally assumed neutral. However the atmospheric stability can have a large effect on the atmospheric flow behaviour for the inflow generation for wind turbines [21,22] and therefore it has become a growing research interest [23,24].

Atmospheric stability is taken into account in the log profile by including a correction term Ψ_m,

$$U(z) = \frac{u_*}{\kappa}\left[\ln\left(\frac{z}{z_0}\right) - \Psi_m(z/L_s) + \Psi_m(z_0/L_s)\right] \tag{21}$$

Ψ_m is the integration of ϕ_m which is the dimensionless wind shear $\phi_m = \frac{\kappa z}{u_*}\frac{\partial u}{\partial z}$. The form of ϕ_m and Ψ can be found in [25].

Note that, Eq. (21) is most commonly used in wind energy without the term, $\Psi_m(z_0/L)$, since turbines are deployed in areas with low z_0. However, especially for complex terrain problems (forested areas, complex elevations, etc.) logarithmic law with stability correction should be used as described by Eq. (21).

3.1.4. Precursor turbulence box

A more sophisticated way to generate inflow conditions for wind turbine (or wind farm) simulations is by using a precursor turbulence box, in which a separate simulation without wind turbines under specific boundary conditions and assumptions is performed. In the studies of Bechmann and Sørensen [26], a precursor simulation was run over flat terrain with a set of parabolic equations (the Navier–Stokes equations with a boundary layer approximation), in which the pressure gradient is assumed to be constant, and the Coriolis forces are included.

3.1.5. Mann turbulence box

Mann [27] developed a spectral tensor turbulence model which can be used to simulate wind fields with particular turbulence characteristics [28]. Thus, it is now used for inflow turbulence generation for wake modelling, e.g. Dynamic Wake Meandering model and EllipSys3D, as discussed in Sections 4.4.3 and 4.6.2, respectively.

The Mann model looks at the spectral tensor of atmospheric turbulence at neutral stability state. The spectral tensor contains all information on spectra, cross-spectra and coherences that are required for engineering applications in wind energy. In the model, the Rapid Distortion Theory (RDT) [5] is combined with the "eddy lifetime" to describe the amount of shear, which gives the turbulence an anisotropic character. The model involves three adjustable parameters which can roughly be described as (1) a length scale that defines the size of the turbulent eddies, (2) a non-dimensional parameter to estimate the eddy lifetime, and (3) a parameter related to the energy dissipation.

3.2. Wake summation

One of the subcomponents of wake modelling is the wake superposition concept. In order to include the effects of all the upstream turbines to the total velocity deficit, 4 approaches are mainly used [29]:

Geometric sum $\quad \frac{u_{n+1}}{U_\infty} = \prod_{j=1}^{n} \frac{u_{j+1}}{u_j},$

Linear sum $\quad \left(1 - \frac{u_{n+1}}{U_\infty}\right) = \sum_{j=1}^{n}\left(1 - \frac{u_{j+1}}{u_j}\right),$

Energy balance $\quad \left(U_\infty^2 - u_{n+1}^2\right) = \sum_{j=1}^{n}\left(u_j^2 - u_{j+1}^2\right),$

$$\text{Quadratic sum} \quad \left(1-\frac{u_{n+1}}{U_\infty}\right)^2 = \sum_{j=1}^{n}\left(1-\frac{u_{j+1}}{u_j}\right)^2, \tag{22}$$

where n is to the total number of upstream turbines, therefore u_{n+1} refers to the wind speed at the turbine in question. In addition to these approaches, Van Leuven [30] considers the effects of the closest upstream turbine in the WINDPARK model, which shows a good agreement with the measurements obtained in the Zeebrugge wind farm. Although this approach works fine for onshore conditions, for offshore wind farms where the wake effects are shown to be more dominant, Habenicht [31] underlines the importance of wake superposition methods. He has compared the superposition methods for four different offshore wind farms and showed that the linear and quadratic sums give the best results.

3.3. Rotor wind speed calculations

In this section, the methodologies to model the physical induction of the atmospheric inflow near the rotor disk are discussed.

3.3.1. Elliptic equations

The vortex system created downstream of the turbine induces a velocity component on the rotor axis in the direction opposite to the incoming atmospheric inflow. Characteristically in the elliptic problems, the disturbance signals, or a sudden change of information inside the domain, travel in all directions and affect the solution everywhere else. Hence, the change that occurred downstream of the turbine will naturally affect the modelled flow around the rotor, including the near upstream flow and the rotor itself. Therefore, elliptic solutions techniques for Navier–Stokes equations around wind turbines do not require to introduce any external induction, as it will appear in the flow automatically. However, the major drawback of the elliptic equations is their complexity, corresponding to higher computational cost.

3.3.2. Vortex equations

In the vortex modelling, the blades and the vortices are considered as lifting lines or surfaces. The vortex strength parameter is defined using the circulation which is highly related to the atmospheric inflow. This inflow is induced using the Biot–Savart law, and for a single vortex element of strength Γ the vorticity is given as

$$w = \frac{\Gamma}{4\pi}\oint \frac{r \times ds}{r^3}. \tag{23}$$

where r is the perpendicular distance between the point p and the vortex filament ds, as illustrated in Fig. 1.

3.3.3. Parabolic equations

The parabolic form of the Navier–Stokes equations can be achieved by implementing the boundary-layer or thin shear layer approximation. The latter briefly states that the flow over a surface can be divided into two as the flow inside and outside of the boundary-layer region. Using such approximation, the Navier–Stokes equations can be simplified by omitting the diffusive momentum transport term through the principal direction of the flow. It essentially means neglecting the pressure gradient along the transverse direction, which is assumed to be much smaller than in the principal direction [32]. The solution procedure of the parabolized Navier–Stokes equations is relatively simpler so it is commonly used in many engineering applications [33]. The most common method for induced velocity component in parabolic flows is the actuator disk or 1-D momentum theory.

Actuator disk (1-D momentum theory) approach: This is based on linear momentum theory in which the wind turbine is modelled as an actuator disk, i.e. with an infinite number of blades. The flow before and after the actuator disk is considered to be steady, incompressible, homogeneous, isotropic, asymmetric with constant pressure profile, non-turbulent, inviscid, neutrally stable and non-rotational. Also, the thrust is assumed to be uniformly distributed over the disk area, and the velocity through the disk is considered to be constant. An illustration of the control volume used for the theory is shown in Fig. 2.

The velocity U_1 is induced using an axial induction factor, a, such that [34];

$$U_2 = U_1(1-a). \tag{24}$$

Also, the angular induction is introduced radially by the angular induction factor a' as

$$U_{2rot} = \Omega r(1+a'), \tag{25}$$

where U_{2rot} is the induced tangential velocity at the rotor plane, Ω is the rotational velocity of the rotor, and r is the radial distance from the rotational axis. An example of an iterative calculation procedure for a and a' can be found in Manwell et al. [35].

3.4. Wind turbine model

In this section, some of the methodologies followed throughout the literature to estimate forces applied to the rotor plane are presented.

3.4.1. Inverse 1-D momentum theory approach

The axial force term that appears in Eq. (2) can be modelled using the inverse momentum theory approach, where a general aerodynamic expression for a uniformly loaded actuator disc can be written as

$$f_x = 1/2\rho U_{ref}^2 c_T A, \tag{26}$$

where f_x is the axial force, c_T is the thrust coefficient and A is the rotor swept area.

In Eq. (26), the definition of the reference inflow wind speed, U_{ref}, is not always straightforward for a wake-affected downstream turbine. For the upstream turbines $U_{ref} = U_\infty$, whereas for the

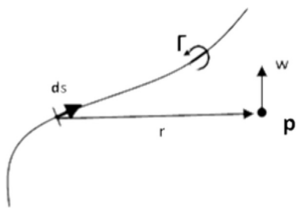

Fig. 1. Single vortex element coordinate system.

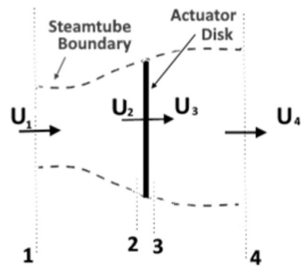

Fig. 2. Actuator disk model of a wind turbine where U_1 is the mean flow speed.

downstream ones, following the studies of Prospathopoulos et al. [36], U_{ref} is defined using the local velocity field and an induction factor as in the 1-D momentum theory so that $U_{ref} = U_{local}/(1-a)$. They proposed an iterative approach by assigning an initial value to U_{ref} and determining the thrust coefficient. The axial induction factor can be approximated accordingly, using the thrust curve of the rotor with $c_T = 4a(1-a)$. The process continues until convergence is achieved for U_{ref}. Finally, that value is used to estimate the axial force applied on the rotor using Eq. (26).

Note that U_{ref} is often over-predicted (2–3%) when estimated using the inverse 1-D momentum theory, leading to 5% and 8% error in total thrust and power, respectively [37].

3.4.2. Induced thrust curve approach

In this approach, the thrust coefficient is defined as a function of the relative or induced velocity, U_{ref} instead of the free stream wind speed (U_∞) where the conventional thrust curves are calculated accordingly i.e. c_T vs. U_∞. In order to create a newly defined thrust curve, a CFD algorithm was created for a relatively simple individual turbine case and run at different wind speeds from which the relative velocity and axial force values can be extracted. As a result, a new thrust curve in terms of induced velocities for that specific wind turbine is constructed and, therefore, can be used in more comprehensive calculations [37].

3.4.3. Blade element momentum (BEM) theory and generalized actuator disc model

BEM theory is one of the first and still the most commonly used methodologies to investigate rotor aerodynamics and it is described in many studies in the literature, e.g. see Hansen [38]. In this section, the application of BEM theory to estimate the forces across the rotor are explained.

The forces on the rotor are calculated using the geometrical components of the aerodynamic sectional lift, L, and drag, D, forces, which strongly depend on the aerodynamic characteristics of the airfoils,

$$(L, D) = 1/2\rho V_{rel}^2 cB(c_L e_L, c_D e_D), \tag{27}$$

where c_L and c_D are the lift and drag coefficients, respectively, e_L and e_D are the unit vectors, c is the chord length of the airfoil, B is the number of blades of the turbine and V_{rel} is the relative velocity. The rotational effects are taken into account in the estimation of the V_{rel} as

$$V_{rel}^2 = (U_\infty - W_z)^2 + (\Omega r_l + W_\theta)^2, \tag{28}$$

where W_z is the induced velocity such that $a = W_z/U_r ef$, r_l is the local radius of the considered annular section, and W_θ is the induced angular velocity.

The axial and tangential forces are determined in terms of the flow angle, ϕ_l defined between the direction of the V_{rel} and the rotor plane,

$$\phi_l = \tan^{-1}\left(\frac{U_\infty - W_z}{\Omega r_l + W_\theta}\right), \tag{29}$$

and the sectional forces become

$$F_{\text{axial}} = L\cos\phi + D\sin\phi_l \quad F_{\text{tangential}} = L\sin\phi_l - D\cos\phi_l \tag{30}$$

In the BEM method, Eqs. (27)–(30) are numerically solved by iterative algorithms (e.g., the Newton–Raphson algorithm) by estimating the axial induction factor using a similar approach as described in Section 3.4.1, whereas in the generalized actuator disc model, the components $V_z = U_\infty - W_z$ and $V_\theta = -W_\theta$ are measured on the disc [39].

3.4.4. Sequentially activation method

In this approach, a CFD simulation is performed for only the upstream turbines in the wind farm, eliminating the induction effect of the downstream turbines. As a result, the incoming velocity, U_∞, at the location of the downstream turbine can be defined and a corresponding c_T can be determined using the conventional thrust curve provided by the manufacturer of the turbine. The procedure is repeated until the whole wind farm is computed and the axial forces are determined accordingly.

3.4.5. Aero-elastic model approach

The axial force or the thrust is known to be the dominant force in relation to bending moments on the wind turbine, which can be measured using e.g. strain gauges. These measured bending moments are used inversely, together with aero-elastic models, e.g. HAWC2 [40], to estimate the thrust, which is spatially integrated over the rotor. Since the thrust is not the only force causing bending on the turbine structures, but those resulting from the interaction between the turbine and the complex atmospheric flow, aero-elastic models are used to estimate the moments that are dominated by the existence of the axial forcing [41].

3.5. Wind direction & speed

Accurate wind direction data is key in wake modelling since the direction defines the path of the wake. Therefore it determines the full and partial wake conditions at the downstream wind turbine positions, which are critical in both wind turbine loading and power production calculations.

Typically in wind-power meteorology, the wind direction is determined either using the measurements from a meteorological mast or the yaw angle extracted from the Supervisory Control And Data Acquisition (SCADA) system of the turbine(s). However, it is well known that the conventional assumptions introduce a considerable amount of uncertainty mainly caused by the physical distance between the meteorological mast and the farm, the sensitivity of yaw measurement techniques also known as “yaw misalignment”.

For example, in the interface of Fuga [42], the model is further described in Section 4.5, the turbine site locations and the wind data are input as done in Wind Atlas Analysis and Application Program (WAsP) [43]. The wind direction measurements can be post-processed by either simple averaging, Gaussian averaging [44], or considering the meandering of the wake in which a spatial correlation is activated to account for the direction uncertainty. In Fuga the meandering is taken into account by creating a curve by joining 10-min averaged wind direction values and considering the probability of the difference between this curve and the instantaneous values.

4. Wake models

In this section, an extensive conceptual review of the wake models developed at the DTU is presented.

4.1. Infinite wind farm boundary layer model

An infinite wind farm boundary layer (IWFBL) model was developed by Frandsen [1]. In the model, around the turbine rotors, i.e. the “rotor layer”, the velocity profile is reduced compared to that above hub height and both profiles are logarithmic as shown in Fig. 3.

Inside the wind farm the turbines are assumed to be evenly spaced at a distance x and a dimensionless separation between the turbines is defined as; $s = x/R$, the term R being the radius of the

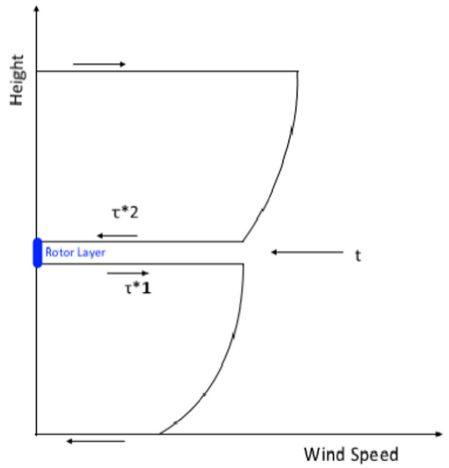

Fig. 3. Illustration of the vertical flow shear, shear forces and external forces in the IWFBL model.

turbine. As shown in Fig. 3, the difference in shear stresses around the turbine hub height is

$$t = -\rho C_T' u_h^2, \tag{31}$$

where u_h is the asymptotic spatial average wind speed at hub height, and t is the simplified thrust term $t = -\rho C_T' u_h^2$ with $C_T' = C_T\pi/(8s^2)$. Therefore the relation between the friction velocities and u_h can be calculated using

$$\rho u_{*2}^2 = \rho u_{*1}^2 + \rho C_T' u_h^2, \tag{32}$$

where u_{*2} is the friction velocity above and u_{*1} below hub height.

Note that, under the rotor layer, the logarithmic wind profile is valid and can be used to relate u_h to u_{*1} using logarithmic law. For the region above that layer, the simplified geostrophic law [45] is applied and the resulting expression is found as;

$$\frac{G-u_h}{u_{*2}} = \frac{1}{\kappa}\ln\left(\frac{G}{hf_p}\right), \tag{33}$$

where h is the hub height, $f_p = f_c \exp(A_*)$ with f_c being the Coriolis parameter, A_* a modified A parameter from the resistance-law constants, and G the geostrophic wind speed. The friction velocities are parametrized as;

$$u_{*1} = \frac{u_h}{K_1}, \quad \text{where } K_1 = \frac{1}{\kappa}\ln\left(\frac{h}{z_0}\right),$$
$$u_{*2} = \frac{G-u_h}{K_2}, \quad \text{where } K_2 = \frac{1}{\kappa}\ln\left(\frac{G}{hf_p}\right). \tag{34}$$

Substituting them into Eq. (32) and solving for u_h yield

$$u_h = \frac{G}{1+K_2\sqrt{K_1^{-2}+C_T'}} \tag{35}$$

After solving for u_h, the friction velocities, u_{*1} and u_{*2}, can also be calculated.

Additionally, Frandsen [1] approximated the wind speed reduction at hub height, $R_u = u_h/u_0$, where u_0 is the undisturbed wind speed at the same height, as

$$R_u \approx \ln\left(\frac{1}{e^{-1/\gamma}+C_T'}\right)^{\gamma}, \tag{36}$$

where $\gamma = 0.025/\ln(h/z_0)^{1/3}$, with z_0 being the surface roughness.

4.1.1. Atmospheric stability correction

Peña and Rathmann [46] added atmospheric stability effects to the IWFBL model extending the logarithmic wind profile to account for atmospheric stability using a correction term depending on the dimensionless wind shear. The wind speed reduction has a similar form as that of Frandsen [1],

$$R_u = \frac{1+K_2(u_{*free})\sqrt{K_1^{-2}}}{1+K_2(u_{*2})\sqrt{K_1^{-2}+C_T'}}, \tag{37}$$

but both K_1 and K_2 are modified to include atmospheric stability by adding/subtracting the stability function, $\Psi_m(z/L_s)$,

$$K_1(u_*) = 1/\kappa\left[\ln\left(\frac{h}{z_0}\right) - \Psi_m(h/L_s)\right], \tag{38}$$

$$K_2(u_*) = 1/\kappa\left[\ln\left(\frac{G}{hf}\right) - A_*(\mu_0) + \psi(h/L_s)\right], \tag{39}$$

where $A_* = \ln\left(\frac{G}{fz_0}\right) - \frac{\kappa G}{u_*}$ and $\mu_0 = \kappa u_*/f_c L_s$, where u_{*2} for the section above rotor layer is formulated as

$$u_{*2} = \frac{u_h\kappa}{\ln(h/z_{00}) - \Psi_m(h/L_s)}. \tag{40}$$

z_{00} is the effective roughness length of the wind farm,

$$z_{00} = \left[\frac{-\kappa}{C_T+K_1^{-2}} - \Psi_m(h/L_s)\right]. \tag{41}$$

4.2. The Jensen wake model

The Jensen wake model is one of the most popular models among engineering applications due to its simplicity, practicality and robustness. The description is based on the studies of Jensen [47] and Katic et al. [48].

Using the control volume presented in Fig. 4, where $D = D_r$ is the rotor diameter, and assuming a top-hat inflow profile the mass balance between the rotor plane and the downstream flow yields,

$$\left(\frac{D_r}{2}\right)^2 u_r + \left[\left(\frac{D_w}{2}\right)^2 - \left(\frac{D_r}{2}\right)^2\right]u_0 = \left(\frac{D_w}{2}\right)^2 u_w, \tag{42}$$

Also, the wake is assumed to be expanded linearly as a function of the downstream distance x at a rate α, $D_w = D_r + 2\alpha x$ and $u_r/u_0 = 1-2a$ using the axial induction factor, the fractional decrease in wind speed, $a = \frac{u_0-u_r}{u_0}$. Putting them into (42), the normalized velocity can be found as

$$\frac{u_w}{u_0} = 1 - \frac{2a}{(1+2\alpha x/D_r)^2}, \tag{43}$$

Assuming ideal axially symmetric flow, no rotation, no turbulence and conic shape wake profile, the axial induction factor can

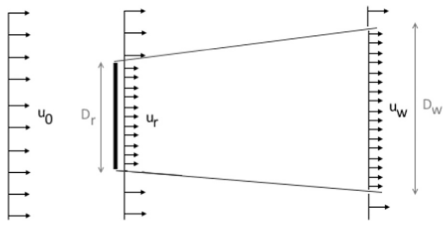

Fig. 4. The control volume of the Jensen wake model.

also be written as

$$a=\frac{1-\sqrt{1-C_T}}{2}. \tag{44}$$

4.2.1. Interpretations of the Jensen model

The Park model: The Park model implemented in WAsP [43] is based on the Jensen wake model and accounts for the effect of multiple wakes on the velocity. In the original version of Katic et al. [48], the ground interaction of the wake is taken into account by assuming an "underground rotor", which is a reflection of the original one. To derive the efficiency of a wind farm, the combination of the effects of four different overlapping mechanisms is considered:

1. Directly upwind rotor wakes.
2. Reflected upwind "underground rotors".
3. Shading upwind rotors, located left or right of the directly upwind rotor.
4. Reflected shading upwind rotors, located left or right of the wind direction.

The local wakes are superposed to estimate the velocity deficit at the nth turbine $\delta_n=\left(\sum_{i=1}^{n}\delta_i^2\right)^{1/2}$ where $\delta_n=1-\frac{u_n}{u_0}$.

Infinite row of turbines: Jensen [47] already estimated a model for the velocity deficit of an infinite row of turbines based on his wake model. If the velocity at the last partition of the infinite row of turbines is defined as u_{inf} then

$$\frac{u_{inf}}{u_0}=1-\left(\frac{2a}{1-2a}\right)\left(\frac{f}{1-f}\right), \tag{45}$$

where

$$f=\left[\frac{1}{1+2\alpha D_r x}\right]^2. \tag{46}$$

Infinite Park Wake model: Considering the effects of four overlapping of wakes in the Park wake model the total wake deficit δ_T is estimated as the quadratic sum of four types of wakes [22],

$$\delta_T^2=\delta_i^2+\delta_{ii}^2+\delta_{iii}^2+\delta_{iv}^2 \tag{47}$$

Rathmann et al. [49] have solved those effects analytically and Peña and Rathmann proposed [46],

$$\begin{aligned}
\delta_i^2&\approx\frac{\delta_0^2}{(1+2\alpha s_r)^3}\left[\frac{1}{2(1+2\alpha s_r)}+\frac{1}{6\alpha s_r}\right],\\
\delta_{ii}^2&\approx\frac{\delta_0^2}{128(h/D)^3}\left[\frac{1}{4(h/D)}+\frac{1}{3\alpha s_r}\right],\\
\delta_{iii}^2&\approx\frac{\delta_0^2}{16s_f^4}\left(1+\frac{s_f/s_r}{\alpha}\right),\\
\delta_{iv}^2&\approx\frac{\delta_0^2}{16s_f^4}\left[\left(1+4\left[(h/D)/s_f\right]^2\right)^{-2}+\left(\frac{s_f/s_r}{\alpha}\right)\left(\frac{1-\left[1+4([h/D]s_f)^2\right]^{-3/2}}{6[(h/D)/s_f]^2}\right)\right],
\end{aligned} \tag{48}$$

where δ_0 is the initial wake deficit, $\delta_0=\left(1-\sqrt{1-C_T}\right)$, s_r is the dimensionless stream-wise separation between turbines, i.e. $s_r=x/D$ and $s_f=y/D$ with y being the cross-wind turbine–turbine distance.

Wake decay coefficient: When using the Park model in WAsP, the wake decay coefficient term α is by default $\alpha=0.075$. In the study of Peña and Rathmann [46], the wake decay coefficient was shown to be a function of height roughness, atmospheric stability and turbulence separation. For practical purposes, the below expression is recommended.

$$\alpha=\alpha\left[\ln(h/z_0)-\Psi_m(h/L_s)\right]^{-1}, \tag{49}$$

which showed very good agreement with data from the Sexbierum [50] and the Horns Rev-I wind farms [51]. Using the similarity theory, α can be related to the turbulence intensity, TI, as $\alpha\approx 0.4TI$.

4.3. The Larsen model

4.3.1. 1988 (Early) version

Larsen [52] has introduced a simple wake calculation procedure which was implemented in the commercial software WindPRO [53]. In the model, the axis-symmetric form of the RANS equations with the thin shear layer approximation is used. The pressure term appearing in the parabolic equations was also neglected and the turbulence closure, ν_T, was represented using Prandtl's mixing-length theory as

$$\nu_T=l^2\sqrt{S_{ij}S_{ij}}, \tag{50}$$

where l is the mixing length and S_{ij} is the strain rate tensor. The problem is assumed to be steady, axisymmetric and self-similar along the perpendicular direction to the flow. Larsen considered the solution of the RANS equations using first and second order approximations. In the first order approximation, the expression to be solved together with continuity equation is simplified as:

$$U_\infty\frac{\partial u_x}{\partial x}=\frac{1}{r}\frac{\partial}{\partial r}\left[l^2 r\left(\frac{\partial u_x}{\partial r}\right)^2\right], \tag{51}$$

u_x is the wake perturbation of the inflow along the axial direction and r is the radial direction and x is the axis of symmetry.

In order to solve Equation (51), two boundary conditions are defined: (1) $u_x=0$ on the boundary of the wake, and (2) $U_\infty \gg u_x$, which is obtained by writing the momentum balance assuming the inflow velocity to be much higher than the axial wake perturbations. Using those conditions, the radius of the wake, r_w, and the axial (u_x) and radial (u_r) wake perturbations are found as:

$$r_w(x,r)=(35/2\pi)^{1/5}(3c_1^2)^{1/5}(C_T A x)^{1/3}, \tag{52}$$

$$u_x(x,r)=-\frac{U_\infty}{9}(C_T A x^{-2})^{1/3}\left\{r^{3/2}(3c_1^2 C_T A x)^{-1/2}-(35/2\pi)^{3/10}(3c_1^2)^{-1/5}\right\}^2, \tag{53}$$

$$u_r(x,r)=-\frac{U_\infty}{3}(C_T A)^{1/3}x^{-5/3}r\left\{r^{3/2}(3c_1^2 C_T A x)^{-1/2}-(35/2\pi)^{3/10}(3c_1^2)^{-1/5}\right\}^2, \tag{54}$$

where C_T is the thrust coefficient, A is the rotor swept area, and c_1 is a constant that is defined empirically [52]. The second order system uses the full form of the RANS equations, which were later found to be negligible for most engineering applications [52].

4.3.2. 2009 (Later) version

The main improvements in the 2009 version of the Larsen model [54] compared to the 1988 one are the boundary condition (s) and the wind farm approach because the early version was derived considering the single wake case only and provided no solution for multiple wake situations. The later version of the model defines the boundary conditions using the results of the analysis of full scale experiments. The first boundary condition is defined at the rotor plane and the second one is defined at a fixed frame of reference placed at a distance 9.6D downstream.

The second order approximation is neglected in the later version as well, and the wake radius and velocity deficit resulting

from the updated boundary conditions are

$$r_w(x,r) = (35/2\pi)^{1/5}(3c_1^2)^{1/5}(C_T A(x+x_0))^{1/3}, \tag{55}$$

$$u_x(x,r) = -\frac{U_\infty}{9}\left(C_T A(x+x_0)^{-2}\right)^{1/3} \left\{r^{3/2}(3c_1^2 C_T A(x+x_0))^{-1/2} - (35/2\pi)^{3/10}(3c_1^2 f)^{-1/5}\right\}^2, \tag{56}$$

where

$$c_1 = (105/2\pi)^{-1/2}\left(\frac{d_1 D}{2}\right)^{5/2}(C_T A x_0)^{-5/6}, \tag{57}$$

$$x_0 = \frac{9.6D}{\left(\frac{2R_{9.6D}}{d_1 D}\right)^3 - 1}, \tag{58}$$

$$d_1 = \sqrt{\frac{1+1/\sqrt{1-C_T}}{2}}, \tag{59}$$

with $R_{9.6D}$ being the wake radius at 9.6D, which is empirically calculated using the analysis performed for the Vindeby offshore wind farm, and expressed using atmospheric turbulence intensity, I_a as,

$$R_{9.6D} = a_1 \exp(a_2 C_T^2 + a_3 C_T + a_4)(b_1 I_a + 1)D, \tag{60}$$

where the constants a_1, a_2, a_3, a_4 and b_1 are defined in Larsen [54].

The wind farm approach is considered using two different methodologies to calculate the inflow speed: the geometric (or linear) averaging and momentum balance, which are respectively,

$$U_\infty = \overline{U} = \frac{1}{A}\int_A U\, dA, \tag{61}$$

$$\overline{U} = \sqrt{\frac{1}{A}\int_A U^2\, dA}, \tag{62}$$

where U is the incoming ambient velocity modelled by logarithmic wind profile. The velocity inside the wind farm is calculated using the linear averaging as:

$$\overline{U}_m = \overline{U} - \sum_{\substack{i=1 \\ R_i \le r_{0_j}+R}}^{M} u_{x_i}, \tag{63}$$

where M is the number of upstream rotors that generate wakes affecting the rotor m.

For the non-linear approach, the decomposition of U_m cannot be performed linearly, thus, the velocity profile imposed on rotor m may be described as;

$$\overline{U}_m = \sqrt{\frac{1}{A}\int_A \left(\overline{U} - \sum_{\substack{i=1 \\ R_i \le r_{0_j}+R}}^{M} u_{x_i}\right)^2 dA}. \tag{64}$$

Eqs. (63) and (64) are solved using a 4-point Gauss integration method, which is explained in detail in Larsen [54]. Additionally, in both of those equations it can be seen that the multiple wake effects are superposed using the linear sum.

4.4. Dynamic wake meandering model

The dynamic wake meandering (DWM) model describes the wake as a passive tracer driven by the large-scale turbulence structures in the atmospheric boundary layer. The model may be further investigated using the studies performed by Larsen et al. [55,56] and Madsen et al. [57]. The recent improvements to the model and the validation cases are presented in [58–61].

The DWM model consists of three elements, which together describe the essential flow characteristics behind a turbine: (1) Velocity or wake deficit; (2) Meandering of the wake; and (3) Rotor added turbulence. Here they will be considered separately.

4.4.1. Velocity deficit

In the DWM model, the velocity deficit is initialized by the pressure gradient and formulated in the meandering frame of reference. The profile behind the turbine is assumed to be axi-symmetric and steady. Parabolic Navier–Stokes equations with neglected pressure terms are used and the resulting equations are

$$U\frac{\partial U}{\partial x} + V_r\frac{\partial U}{\partial r} = \left(\frac{\nu_T}{r}\right)\frac{\partial}{\partial r}\left[r\frac{\partial U}{\partial r}\right], \tag{65}$$

$$\frac{1}{r}\frac{\partial}{\partial r}(rV_r) + \frac{\partial U}{\partial x} = 0, \tag{66}$$

where V_r denote the mean velocity along the radial direction. The eddy viscosity ν_T is mainly described by the methodology proposed by Ainslie [62] and manipulated to include ambient turbulence intensity,

$$\nu_T = F_2 k_2\left(\frac{b}{r}\right)\left(1 - \frac{U_{def,min}}{U_H}\right) + F_1 k_{amb} I_{amb}, \tag{67}$$

where k_2 is an empirical constant for the flow field, b is the instantaneous wake half width, $U_{def,min}$ is the minimum wake wind speed, U_H is the wind speed at hub height, I_{amb} is the ambient turbulence intensity at hub height, k_{amb} is a calibration constant, and F_1 and F_2 are filter functions depending on the downstream distance x only.

4.4.2. Meandering of the wake

As mentioned earlier, the DWM model assumes the wake to behave as a passive tracer transported in a large-scale turbulence field, where eddies larger than two rotor diameters. Therefore, the large-scale transversal and vertical velocities, v and w respectively, are important.

The displacement of the wake is defined by the characteristic velocities,

$$v_c(x^b, y^b, z^b) = \frac{1}{A_f}\iint_{A_f} v(x^b, y^b, z^b)\, dy^b\, dz^b, \tag{68}$$

$$w_c(x^b, y^b, z^b) = \frac{1}{A_f}\iint_{A_f} w(x^b, y^b, z^b)\, dy^b\, dz^b, \tag{69}$$

where (x^b, y^b, z^b) are the inertial coordinate system fixed to the turbulence box introduced, and A_f is the averaging area most logically selected as a circle in which the origin is assigned as (y^b, z^b) with a diameter D_w.

The transversal and vertical wake displacements are described as,

$$\frac{dy^g}{dt} = v_c(U[T-t_i], y^b, z^b), \tag{70}$$

$$\frac{dz^g}{dt} = w_c(U[T-t_i], y^b, z^b), \tag{71}$$

where T is the time interval considered in the "snapshot" associated with the Pseudo-Lagrangian approach formulated by $T = L/U$ with L being the along-width length of the turbulence box considered, and t_i is the time when the velocity deficit is released.

Additionally, the initial conditions at the time t_i are given as,

$$y^g(t_i) = 0; \quad \left.\frac{dy^g}{dt}\right|_{t=t_i} = v_c(U[T-t_i], 0, 0), \tag{72}$$

$$z^g(t_i)=0;\quad \left.\frac{dz^g}{dt}\right|_{t=t_i}=w_c(U[T-t_i],0,0), \tag{73}$$

The solution to Eqs. (68) and (69) together with Eqs. (70)–(73) are presented in detail in Larsen [56] including methodologies for their simplification and a numerical algorithm. Finally, it should be noted that the wake deficit is not affected by the meandering progress.

4.4.3. Rotor induced turbulence

The rotor induced turbulence, or wake added turbulence, in the meandering frame of reference corresponds to the small scale turbulence, namely the tip, root and blade bound vortices, as well as the wake shear layer. In the DWM model, the wake added turbulence at a particular downstream position is modelled using an isotropic Mann turbulence box (Section 3.1.5), with cross sections corresponding to one rotor diameter. Additionally, the added wake turbulence intensity is assumed to be rotationally symmetric and does not influence the meandering or velocity deficit processes.

In summary, the resulting turbulence in the DWM model includes components from meandering, added wake turbulence and ambient turbulence. The resulting velocity field may be expressed as

$$U_{res}=U_m+u_{aw}+u_{amb}, \tag{74}$$

$$v_{res}=v_{aw}+v_{amb}, \tag{75}$$

$$w_{res}=w_{aw}+w_{amb}, \tag{76}$$

where U_{res}, v_{res} and w_{res} are the axial, lateral and vertical velocity components of the resulting velocity field, respectively. The subscript *aw* represents the added wake component, and the subscript *amb* is the ambient contribution. Finally, U_m denotes the unsteady velocity component obtained from the meandering of the velocity deficit, which is determined as

$$U_m=U(x_m,r_m), \tag{77}$$

with x_m and r_m being the downstream axial and radial coordinates, respectively, updated at each time step.

4.5. FUGA

Fuga is a fast engineering tool based on the linearized RANS equations. It uses a system of look-up tables to construct the velocity field behind a turbine, and it uses linear summation to consider multiple wake cases. Due to its simplicity in wake modelling, Fuga is one of the most robust computational fluid dynamics (CFD) based models established for wake effects' calculations. The methodology presented in this study is based on the works by Ott et al. [42].

The Cartesian form of the RANS equations are used with a simple closure, where the eddy viscosity is equal to that usually used within the atmospheric surface layer.

$$\nu_T=\kappa u_* z. \tag{78}$$

Since the equations are not parabolized, there is no need to artificially induce the rotor velocity where the atmospheric inflow is modelled using the logarithmic wind profile including the stability effects. The drag forcing term is modelled using an actuator disk model with a layered control volume as,

$$\overline{f}_i=f_x=-\tfrac{1}{2}\,C_T U_{free}^2\,\delta(x-x_h)\Theta(R^2-(y-y_h)^2-(z-z_h)^2) \tag{79}$$

where δ is the Dirac delta function and Θ is a step function, which is equal to zero for negative and 1 for positive arguments. Due to the fluctuations related to the existence of a step function, the drag calculations are smeared out.

The simplified RANS equations are linearized using Taylor expansion and only the terms with order zero and one are considered. The zeroth order equations correspond to the case without any perturbations to the flow, meaning that there are no turbines. The drag force of order one, f_x^1, is defined by fitting the first order equations to a Chapeau function. The resulting equations are further simplified using Fourier transformation in which two mixed spectral variables are defined along x and y directions. A new numerical scheme is implemented to overcome the difficulties of solving a linearized model for flows over small values of z_0 which is the case for offshore sites with low roughness lengths and where the wakes are more pronounced. The scheme is described in detail in Ott et al. [42] together with the validation of the model for certain test cases.

4.6. EllipSys3D

Ellipsys3D [63,64] is a 3D general purpose CFD solver with a block-structured finite volume approach. Both RANS and LES models are available in EllipSys3D and can be further examined in Sanderse et al. [65].

4.6.1. RANS

In the RANS version of Ellipsys3D, the rotor is modelled as an actuator disk, the elliptic form of the Navier–Stokes equations are used thus no external induction is introduced, and the non-linear terms, $u_j\left(\frac{\partial u_i}{\partial x_j}\right)$, are discretized using the QUICK scheme [66].

Ellipsys3D can use a number of turbulence models. One of the latest developments is the k–ε–f_P model [67], which is a modified version of the widely used k–ε model from Launder and Spalding [68]. Where the standard k–ε model fails to predict the velocity deficit in the near wind turbine wake [67,69–72], the k–ε–f_P model has shown good agreement with LES and measurements for single [67], double wake cases [73], and complete wind farms [74]. In the turbulence models, the turbulent eddy-viscosity is defined as:

$$\nu_T=C_\mu f_P\frac{k^2}{\varepsilon} \tag{80}$$

where C_μ is a constant, k the turbulent kinetic energy, and ε the turbulent dissipation. In the standard k–ε, f_P=1 and the effective eddy-viscosity coefficient $C_\mu f_P$ is a constant. In the k–ε–f_P model, f_P is a scalar function that depends on the local shear parameter $\sigma\equiv\frac{k}{\varepsilon}\sqrt{(u_{ij})^2}$.

The scalar function f_P in the k–ε–f_P model is defined as

$$f_P(\sigma/\tilde{\sigma})=\frac{2f_0}{1+\sqrt{1+4f_0(f_0-1)\left(\frac{\sigma}{\tilde{\sigma}}\right)^2}},\quad f_0=\frac{C_R}{C_R-1}, \tag{81}$$

where $\tilde{\sigma}$ is the shear parameter in an idealized (logarithmic) neutral atmospheric surface layer and C_R is a calibration parameter. In the neutral stability solution, f_P=1 because $\sigma=\tilde{\sigma}$. In regions with a high shear parameter, i.e. $\sigma>\tilde{\sigma}$, $f_P<1$ and the turbulent eddy viscosity from Eq. (80) is decreased.

The near wind turbine wake is characterized by high velocity gradients, where $\sigma\gg\tilde{\sigma}$. As a result, the k–ε–f_P eddy viscosity model delays the wake recovery compared to the standard k–ε. It should be noted that C_R controls the magnitude of the delayed wake recovery. The constant C_R is calibrated against LES for eight different single wind turbine cases [67]. The same transport equations for k and ε are used in both turbulence models,

$$\frac{Dk}{Dt}=\nabla\cdot\left[\left(\nu+\frac{\nu_T}{\sigma_k}\right)\nabla k\right]+\mathcal{P}-\varepsilon, \tag{82}$$

$$\frac{D\varepsilon}{Dt}=\nabla\cdot\left[\left(\nu+\frac{\nu_T}{\sigma_\varepsilon}\right)\nabla\varepsilon\right]+(C_{\varepsilon,1}\mathcal{P}-C_{\varepsilon,2}\varepsilon)\frac{\varepsilon}{k}. \tag{83}$$

Table 1
Model constants.

C_R	C_μ	$C_{\varepsilon,1}$	$C_{\varepsilon,2}$	σ_k	σ_ε	κ
4.5	0.03	1.21	1.92	1.00	1.30	0.40

where $\mathcal{P} \equiv \overline{u_i' u_j'} U_{i,j}$ is the turbulent production, ν is the kinematic molecular viscosity and $C_{\varepsilon,1}$, $C_{\varepsilon,2}$, σ_k, σ_ε are constants. The values of the constants are listed in Table 1.

When the standard k–ε is applied to atmospheric flows, it is common to control the ambient turbulence intensity at a reference height $I_{H,\infty}$ with C_μ using

$$I_{H,\infty} \equiv \frac{\sqrt{\frac{2}{3}k}}{U_\infty} = \frac{\kappa\sqrt{\frac{2}{3}}}{\ln\left(\frac{z_{ref}}{z_0}\right)\sqrt[4]{C_\mu}}, \tag{84}$$

Subsequently, one of the model constants from Table 1 is adjusted to maintain the logarithmic solution [75]

$$\sqrt{C_\mu}\sigma_\varepsilon(C_{\varepsilon,1} - C_{\varepsilon,2}) + \kappa^2 = 0. \tag{85}$$

However, the behaviour of the f_P function changes when C_μ is altered, which is not desired. Therefore, the ambient turbulence intensity is set with z_0, and the friction velocity u_* is adapted to set the free-stream velocity. As a result, the velocity inflow profile differs from the measured profile, although the difference in the rotor area is only in the order of a few percent.

4.6.2. LES

In the EllipSys3D LES, a combination of Eqs. (14)–(16) is performed. The non-linear terms are discretized using a hybrid scheme formed of QUICK and fourth order central differencing schemes and the empirical constants are chosen based on the studies of Troldborg related with the actuator line [76]. There, the rotor is modelled as an actuator line, and the axial force is defined using BEM, which requires sectional aerodynamic characteristics of the blades but increases the efficiency of the calculations. The inflow velocity profile is defined using the logarithmic wind profile (see Section 3.1.1), and the Mann Turbulence box (see Section 3.1.5) is used as inflow turbulence, where neutral atmospheric conditions are assumed.

5. Benchmarking study

5.1. Sexbierum wind farm

5.1.1. Introduction

Sexbierum is an onshore wind farm located in the Northern part of the Netherlands at approximately 4 km from the shore on homogeneous flat terrain, mainly grassland. It consists of 18 turbines with a total installed capacity of 5.4 MW. The layout of the wind farm is presented in Fig. 5.

The turbines in the farm are HOLEC WPS 30-3 [77] with a rated power of 310 kW, a rotor diameter of 30.1 m and 35 m hub height. These turbines are pitch regulated with a cut-in wind speed of 5 m/s, a rated wind speed of 14 m/s, and a cut-out wind speed of 20 m/s.

For Sexbierum case, two benchmarks were defined; the single and double wake cases by Cleijne [78,79].

B1 - single wake: In the single wake test case, the comparison between the simulations and the measurements is performed in the wake of the turbine T18. The met masts are placed 2.5, 5.5 and 8 diameters downstream of T18, and the wind speed measurements during 6 months provided in Cleijne [78] are considered in the benchmark. The observed wind speeds are between 5 and

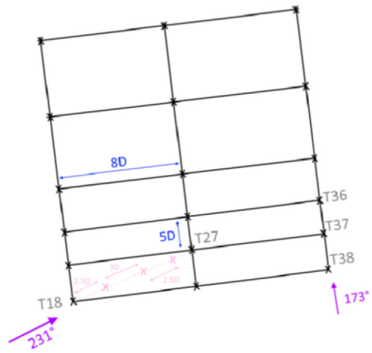

Fig. 5. Sexbierum Wind Farm Layout.

10 m/s, where for the simulations 8 ± 1 m/s incoming wind speed is considered as this is the most frequent wind speed bin observed. The roughness length and the turbulence intensity at hub height are estimated to be 0.049 m and 9.5%, respectively. Neutral atmospheric stability is assumed for the wake computations but discussed afterwards.

In this benchmark, the results of the Jensen model, Larsen model, Fuga, and Ellipsys3D RANS and LES solvers are presented. Two RANS turbulence models are tested: the standard k–ε model and the k–ε–f_P model. The RANS computations are performed with a domain size of $25D \times 16D \times 8D$. The inlet is defined at $5D$ upstream of T18 and the refinement of the mesh in the wake region is performed in such a way that there are 10 cells per rotor diameter as proposed by van der Laan et al. [67] to obtain good resolution in the near wake region with Ellipsys3D RANS. The high resolution area starts at $3D$ downstream from the inlet with a width and length of $4D$ and $14D$, respectively. Vertically, it starts from $0.5D$ below hub height and goes up to $1.5D$ above the rotor. The mesh has a maximum expansion ratio of 1.2 with an initial height of z_0 on the ground. The computational domain for Ellipsys3D RANS includes 1.57 million cells, and the boundary conditions for that domain are: (1) rough wall condition at the ground surface, (2) symmetric boundary conditions on the sides, (3) inlet velocity condition at the inlet and top, and (4) far field outlet boundary conditions.

The time required to run Ellipsys3D RANS for the single wake case with a convergence criterion of 10^{-5}, i.e. the iteration is terminated when the difference between two calculation steps falls below 10^{-5}, is 3-min and 3-s with a time step of 0.008-s and 48 CPUs.

The computational domain used for Ellipsys3D LES is the same for both the single and double wake cases and its dimensions are $15D \times 15D \times 23.25D$. The inlet boundary is located at $7.35D$ from the first upstream turbine (T18 for single wake, T38 for double wake case). The grid points are distributed uniformly in such a way that there are 30 points corresponding to each rotor, and two refined regions to resolve the inflow and wake turbulence. The first high resolution region is located at $0.35D$ upstream of the first turbine and extends to $10.3D$ downstream with a height and width of $1.8D$. The second highly resolved area is located at $1.8D$ upstream of the first turbine where the inflow turbulence is introduced. It has the same height and width of $1.8D$ and it extends to $1.9D$. The computational domain has 19.7 million grid points and the boundary conditions for that domain are: (1) no slip condition at the ground surface, (2) periodic boundary conditions on the sides, (3) far-field velocity on the top, (4) inlet

velocity and turbulence as described in Section 4.6.1, and (5) unsteady convective outlet conditions.

The computational time required to run the single wake case using the Ellipsys3D LES for 12-min real-time with a time step of 0.008-s and 150 CPUs is approximately 4 days and 4 h. However, it should be noted that the computational domain used for the single wake case was actually optimized for the double wake case. Therefore it should be expected that the performance of the simulation in terms of the computational costs can be enhanced by simplifying the mesh according to the single wake requirements.

B2 - double wake: In this benchmark, the power measurements of turbine T36 in the wake of T38 and T37 (see Fig. 5), covering a period of 3 months are studied. Similar to the single wake case, the wind speed interval is 5–10 m/s for the dataset. The model simulations are performed at 8 m/s and the roughness length and turbulence intensity are 0.045 m and 9.5%, respectively, as recommended by Cleijne [79].

For the double wake case, the results of the Jensen model, Larsen model, Fuga, and Ellipsys3D RANS (using the same two turbulence models) and LES solvers are presented. Four relative different wind directions [0°, +7°, +14°, +21°] are simulated in LES, and 22 min of data with a time step of 0.008-s and 150 CPUs took over a week to run, which corresponds to approximately 27 500 CPU hours.

5.1.2. Results and discussion

B1 - single wake: In the Sexbierum single wake case two different wind direction averaging techniques are applied to both the Jensen (with wake decay coefficient, α=0.04) and the Larsen results; a wind direction sectoral averaging (BinAve) and a Gaussian averaging considering the wind direction uncertainty [44] (GauAve). For these two models, the bin averaging is performed for a 30° wind direction span where 2.5° simulations are run and averaged over 5° bins. The Gaussian averaging method was applied with a standard deviation of 5° in the wind direction, although no information about the wind direction uncertainty is provided in the corresponding report [78]. Note that, the free stream wind direction is measured via the meteorological mast and given relative to the line connecting turbines *T*18 and *T*27, denoted as 0°.

The wake model performance in the near wake region is compared in Fig. 6. All the model and solver results, independent of the post-processing method, considerably deviate from the measurements. The data were collected approximately for only 43 h, therefore they are not statistically representative.

The deviation might be due to the atmospheric conditions. However, the atmosphere is very likely to be stable during the measured period [50]. With a low turbulent mixing of the stable atmosphere, the wake takes longer to recover, which explains the depth of the measured wake together with the under-estimation of the models, which are valid for neutral conditions, especially in the near wake region – see Fig. 6(a).

Looking at the performance of the models, Fuga, the Larsen and the standard k–ε RANS underestimate the velocity deficit, and the k–ε–f_P compares well with the LES (note that the LES results are not Gaussian averaged though). The Jensen model, the simplest of all, with Gaussian averaging provides very similar results to those of LES at 2.5*D* and 5.5*D* downstream distances. The Jensen model outperforms the others because of the wake decay coefficient used in the simulations. For onshore sites the recommended value is α=0.075, whereas in our case α=0.04 but as shown in Peña et al. [50] α could be even lower.

B2 - double wake: Fig. 7 is a combination of the results of the Jensen (with a wake decay coefficient of α=0.04), the Larsen and Fuga models, EllipSys3D RANS k–ε–f_P and Ellipsys3D LES solvers where the runs were performed in a similar manner as in the single wake case using a 5° bin and a wind direction step size of 2.5°.

Similar to the single wake case, the models generally underpredict the wake losses which might be due to the stable atmospheric conditions (9.5% turbulence intensity for a 0.045 m roughness length).

Apart from the performance of the Jensen model, especially the bin averaged version, the Larsen model with bin average seems to perform very well compared to the LES results. This might be due to the turbine spacing for the double wake case (10*D*) which is very close to the distance that the model is calibrated (9.6*D*). On the other hand, the Gaussian averaged version of the Larsen, Fuga and RANS k–ε–f_P turbulence model results seem to deviate from the measurements. Note that the Gaussian averaging takes into account the wind directions that might highly differ from the

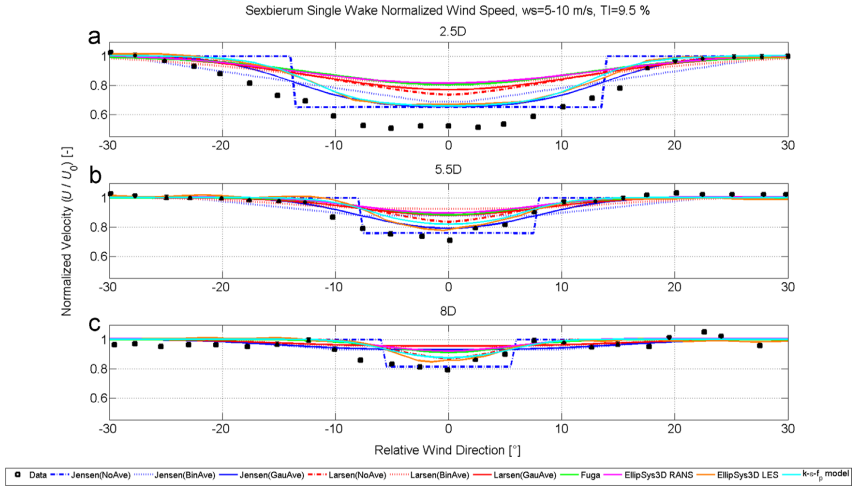

Fig. 6. Sexbierum single wake normalized wind speed at (a) 2.5D downstream, (b) 5.5D downstream, and (c) at 8D downstream.

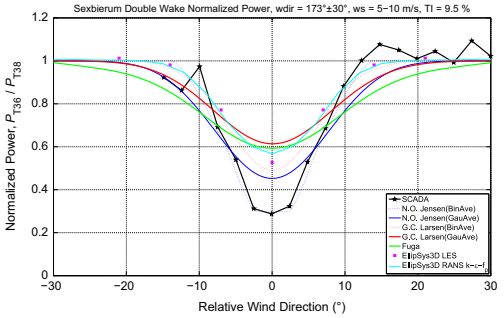

Fig. 7. Sexbierum Double Wake Normalized Power flow direction = 173° ± 30°.

mean value during the averaging time period. However, for less turbulent cases, the deviation of the wind direction from the mean value is small. In that case, the wake deficit profile is over-smeared and the details are lost.

Notes and remarks about the Sexbierum wind farm case: The benchmarks included in the Sexbierum case were constructed using the reports of Cleijne [78,79] and all the models except for DWM were used for the simulations. In general, the models seem to deviate from the measurements significantly, which may be a consequence of the probable stable characteristic of the atmosphere. The Jensen model with a low wake decay seems to provide very good results although it is the simplest model used. It is concluded that the post-processing approach for stable cases should be revised and differ from the one developed for the neutral atmospheric conditions.

Note that in all the cases, the measured wake deficit profile is far from being symmetric which may occur due to the onshore effects such as terrain complexity, etc. However, it is not easy to tell since the dataset covers only a short period of time and the observations might be biased in terms of the atmospheric stability by the seasonal variation of the atmospheric stability. The wind farm wake modelling, especially for onshore sites, requires more inputs to model the inflow and the Sexbierum case is another example of data issues encountered in wind farm simulations.

5.2. Lillgrund offshore wind farm

5.2.1. Introduction

The Lillgrund wind farm is located in Øresund, 6–8 km from the Swedish west coast and south of Malmø. It consists of 48 SWT-2.3-93 wind turbines with a total rated capacity of 110 MW. The Lillgrund wind farm has an irregular layout with a gap in between, and the internal spacing of the turbines is 3.3 and 4.3D rotor diameters, as shown in Fig. 8. In the EERA-DTOC report for the Lillgrund wind farm test case [80], four benchmarks were specified as listed below.

The benchmark consists of 4 main cases:

B1 - sector variation: The power deficit along complete rows with internal spacing of 3.3D and 4.3D is simulated to test the sensitivity of the models to the flow direction. The roughness length is 0.0001 m, the inflow mean velocity at hub height is 9 m/s and the inflow turbulence intensity at hub height is 6%, which is estimated based on sector wise-long term measurements of the met mast.

Two different rows that do not have a missing turbine are used and for the 3.3D case the wind direction is in the interval $120 \pm 15°$, whereas for the 4.3D case it is $222 \pm 15°$. Note that, the runs are performed at every 2.5° step for both arrays.

B2 - speed recovery: The power deficit along a row with missing turbine(s) and internal spacing of 3.3D and 4.3D are observed. In addition, the sensitivity of the models to the flow direction together with the speed recovery due to the missing turbines is tested. The input data and the characteristics of the runs to be performed are the same as in the previous benchmark, B1.

B3 - power deficit as a function of turbulence intensity: The calculations are performed for different inflow turbulence intensity levels at hub height (2–12%) with the same inflow conditions as in the previous benchmarks. Two different runs are performed for both 3.3D and 4.3D spacings using only the first two turbines in the row and the wind direction sectors are $120 \pm 2.5°$ and $222 \pm 2.5°$, respectively.

B4 - park efficiency: The wind farm park efficiency is defined as the ratio between the wind farm total output power and the power of the wind farm assuming undisturbed inflow for each turbine. Similar input data as in the previous benchmarks is considered and the inflow sector is taken as 0–360° with a span of 3°.

5.2.2. Results and discussion

We use a wake decay coefficient of 0.04 for the Jensen model with a quadratic sum for the wake summation, whereas for the Larsen model a linear summation is applied. Additionally, the thrust coefficients in both models are those provided by the turbine manufacturer.

B1 - sector variation: In Fig. 9, two different wind direction averaging techniques with 3 different models are run for this case with 3.3D and 4.3D spacings. The simulations are run at 2.5° step wind directions and averaged over 5° bins. The Gaussian averaging is applied for a 5° standard deviation in wind direction. Additionally, the same technique is applied to Fuga where the uncertainties in wind direction are taken into account using a Gaussian distribution of 4.9°. The Larsen model and Fuga under predict the wake losses for the second turbine placed at 3.3D and 4.3D. Both models are however designed to simulate the flow behaviour at much larger downstream distances. On the other hand, as shown in Fig. 10(a), the wake deficit under-prediction is compensated with a good prediction for the following rows, especially for the Larsen model.

The models are shown to perform better for wider wind direction sectors in Lillgrund by Gaumond et al. [82]. In our case, the EllipSys3D RANS k–ε–f_P model over-performs to estimate the power deficit at the second wind turbine, because the f_P function delays the wake recovery compared to the standard k–ε model.

B2 - speed recovery: In Fig. 11, the recovery point is clearly seen at 16.5D for $120 \pm 2.5°$ and 17.2D for $222 \pm 2.5°$. All the models capture the recovery and for this particular case the Larsen and the k–ε–f_P model seem to estimate the power production reasonably well, especially after the second turbine. Both the Jensen and the Larsen models produce better results with the post processing of the wind direction uncertainty using a Gaussian distribution, which was also the case in previous benchmark, B1. Fuga seems to over-predict the power production for the first downstream turbine and then under-predicts the power production for the following turbines including the recovery point in the 3.3D spacing case. However, for the 4.3D spacing case, and similar to the previous benchmark, agreement between Fuga and the measurements is improved.

B3 - power deficit as a function of turbulence intensity: The standard uncertainty of the power deficit for the turbulence case is represented by the error bars in Fig. 12 with a confidence level of 68% for the SCADA results [83].

Since the original Jensen model does not consider the variations in turbulence, it remains constant. Both the Larsen model and Fuga significantly deviate from the measurements, especially for high turbulence levels. Increasing turbulence intensity levels

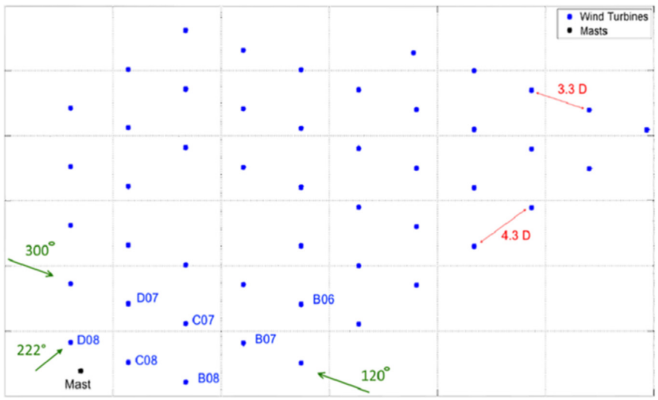

Fig. 8. Layout of the Lillgrund offshore wind farm [81].

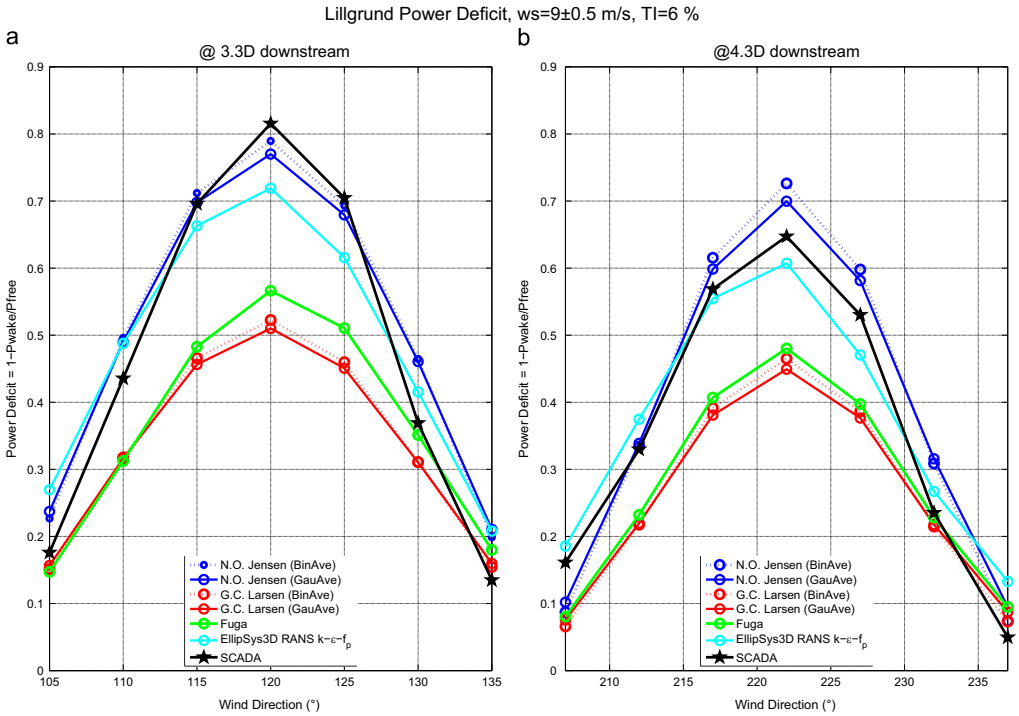

Fig. 9. Lillgrund power deficit at (a) 3.3*D* for 120° ± 15° and (b) 4.3*D* for 222° ± 15°.

show larger lateral wind components. That results in greater wind direction variations. Due to those large variations and narrow sectors, both models might fail to reproduce the observations well. The necessity to use the local turbulence intensity in simulations is addressed later in this study. Furthermore, a pragmatic approach to introduce dynamic effects to the engineering wake model is developed and presented in the following chapter.

B4 - park efficiency: The error bars indicated in Fig. 13 correspond to the uncertainty of power deficit with a 68% confidence level for the SCADA results [83]. The improvement of the model results by post-processing the wind direction uncertainty using a Gaussian distribution is considerable. Those Gaussian averaged versions of the Jensen and the Larsen model show a fair agreement with measurements. However, significant differences around

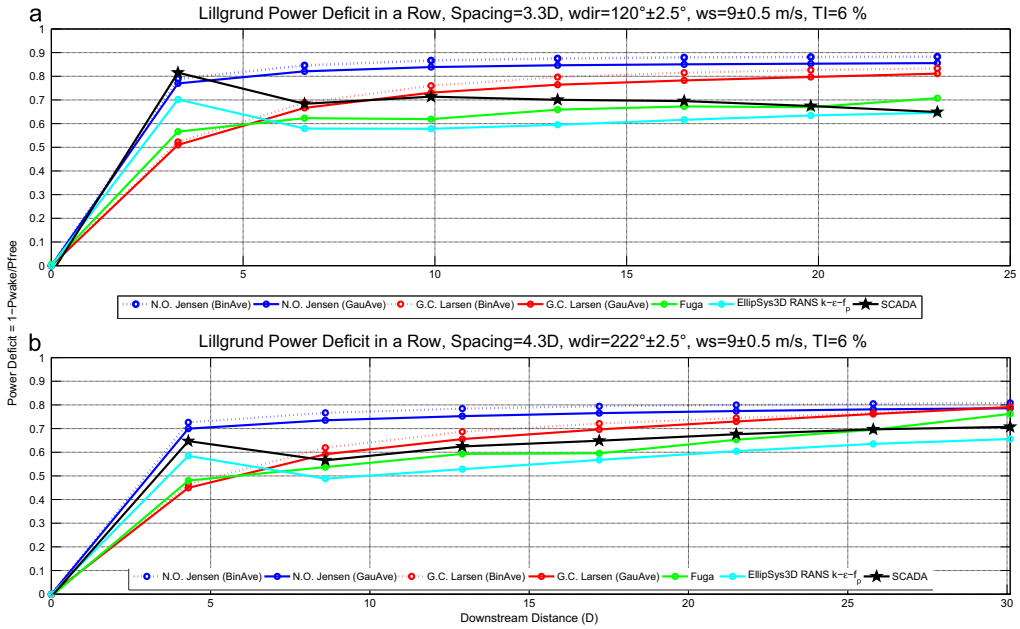

Fig. 10. Lillgrund power deficit in a row with (a) 3.3*D* spacing and 120° ± 2.5° and (b) 4.3*D* spacing and 222° ± 2.5°.

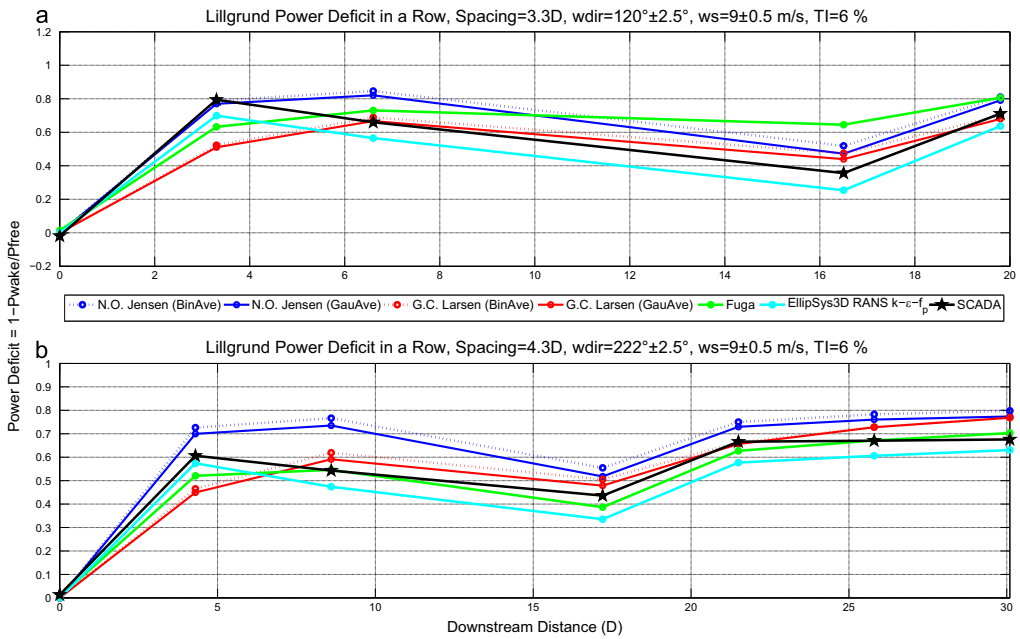

Fig. 11. Lillgrund power deficit in a row with (a) 3.3*D* spacing, 2 missing turbines and 120° ± 2.5° and (b) 4.3*D* spacing, 1 missing turbine and 222° ± 2.5°.

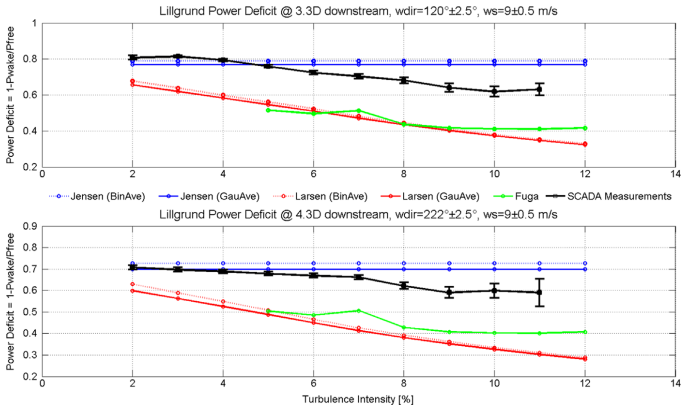

Fig. 12. Lillgrund power deficit in a row at (a) 3.3*D* with $120^\circ \pm 2.5^\circ$ and (b) 4.3*D* with $222^\circ \pm 2.5^\circ$.

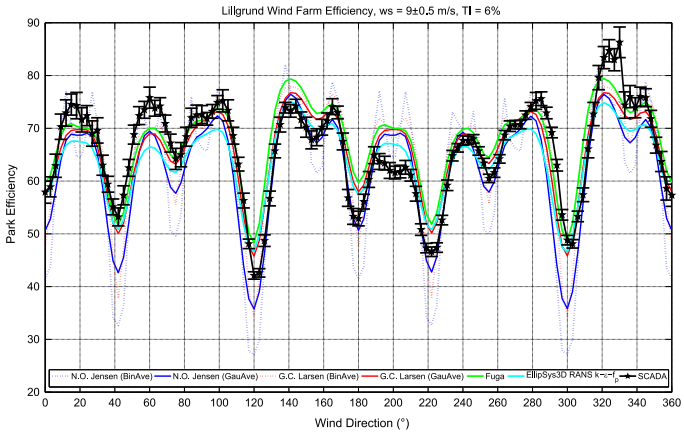

Fig. 13. Lillgrund wind farm efficiency for inflow sector 0–360° with 3° increment and 1.5° sector.

maxima and minima, which are critical wind direction sectors are observed.

Remarks about Lillgrund wind farm case: Especially for the first three benchmark cases, the narrow wind sector of 5° ($\pm 2.5^\circ$) is the major source of uncertainty since the data is 10-min averaged and most probably includes wind directions outside of that range.

Overall, the Larsen model and Fuga performed in a similar manner when considering a Gaussian distribution for the direction uncertainty, in agreement with the results obtained for Horns Rev Wind Farm [44]. In such a layout with small turbine spacings, the k–ε–f_P closure of the Ellipsys3D RANS is seen to capture well the wind speed at the closest turbines through downstream. It can be said that even though the direction bins are narrow ($\pm 2.5^\circ$) for 10-min averaged data, the performances of all the models were considerably good in all benchmarks in general.

6. Application of the models

In this section, the application of the wake models developed in DTU will be discussed in terms of their typical usage, validity, accuracy, complexity, the uncertainty of the required inputs and computational costs.

6.1. Typical usage

The WAsP version of the Park model based on the Jensen model is targeted for wind farm planning and annual energy production (AEP) estimates. Due to its simplicity and practicality, it is often used to perform preliminary studies which are then improved with more sophisticated models.

Similarly, the Larsen model, also implemented in WindPro, is used for both single wind turbine and wind farm design and development stages. Fuga is a relatively new model. However, its robustness, speed, and promising results have already made it popular in the wind energy industry, and it is recently implemented in WAsP. The results showed that especially for the Lillgrund offshore wind farm case, Fuga and the Larsen model provide good results and are comparable to those of the more sophisticated models in offshore.

The DWM model is not only developed to be able to estimate the power production losses due to wake effects but it can also

calculate the loading caused by the wake effects. It is implemented in the aeroelastic code HAWC2 and calibrated accordingly but unfortunately it was not available for the present work.

The LES version of Ellipsys3D, due to its complexity and computational cost, is run by a limited number of users and mainly for academic purposes. Additionally, both RANS and LES simulations are conventionally performed for small number of turbines rather than large scale wind farms for the same practicality reasons.

6.2. Accuracy

Most of the models proposed show a fair agreement with the observations especially when they are post-processed to take into account the wind direction uncertainty or the atmospheric stability conditions. Physically, the models with more realistic considerations, or in other words less simplifying assumptions are more successful in simulating wake characteristics in detail. Thus, in general, the more complicated models are more likely to be more accurate. However, the Sexbierum test case in Section 5.1 showed that even the most sophisticated models can fail to reproduce the flow characteristics when the inputs are erroneous or deficient.

6.3. Complexity and uncertainty of inputs

The quantity and quality of the modelling inputs are crucial for wakes. In general, all models regarding their complexity require measurements of the turbulence level and the atmospheric stability condition. Additionally the wind speed and direction should contain information about their distribution so that a proper post-processing can be performed and the results are fairly compared with the observations. Particularly for Ellipsys3D LES, when modelling the wind turbine, the tabulated values of the airfoil aerodynamic properties are required, which are calculated using the airfoil geometry. Such information is hard to obtain from the manufacturers. In addition, the methodologies used to obtain the lift and drag coefficients of a given geometry have their own inaccuracies and limitations.

6.4. Computational costs

In general, the computational expenses of the wake models increase with the complexity of the model. Therefore, the Jensen model is the fastest to produce results, followed by the Larsen model and Fuga. The DWM model needs a relatively highly resolved turbulence field to feed back the aeroelastic code in the current version, but yet the computational cost is not implied as a main issue. Ellipsys3D, on the other hand, suffers a lot from high CPU usage especially for the LES version, which eventually limits its application to the super-computers or clusters. There are a lot of studies regarding the hybrid RANS and LES methods which are more accurate and representative than RANS simulations but still more affordable than LES alone. A comprehensive review of various approaches to couple RANS with LES may be found in the study of Fröhlich and von Terzi [84].

7. Conclusions

Six of the wake models developed at DTU are investigated. The models have different levels of complexity, and overall they represent the wide range of wake models available for the wind energy industry and research community. The models are described and inter-compared using the Sexbierum onshore and Lillgrund offshore wind farms. Both benchmark cases have provided valuable insights in terms of the effects of the turbine spacing (or wind farm layout in general), wind direction averaging sector variations, turbulence intensity and possible atmospheric stability conditions. Finally, the models are briefly evaluated in terms of their application.

The benchmark cases show that the analytical and linearized models of DTU (the Jensen model, the Larsen model and Fuga) are convenient for large wind farm calculations as they are robust and computationally affordable. They provide good results both onshore and offshore implementations as long as the far wake region is considered and the atmospheric conditions are well defined.

The more sophisticated CFD solvers (Ellipsys3D RANS with k–ε and k–ε–f_P turbulence closures and LES) are used in the benchmark cases. The k–ε–f_P and LES in particular are observed to be in a very good agreement with the measurements. Because of their computational cost however, they are very rarely implemented on large wind farms and their applications are generally limited to the near wake region or highly complex flows.

The benchmarking study also shows that introduction of the wind direction uncertainty significantly improves the accuracy of the power predictions of the Jensen model, Larsen model and Fuga, for the Lillgrund case. For the Sexbierum case, however, even the state-of-the-art model Ellipsys3D LES fails to reproduce the depth of the wake deficit. The limited period of the investigated data and lack of information regarding the characteristics of the inflow are considered to be the reason of the model deficiencies, as they led to erroneous assumptions. Accordingly, the significance of the data set quality, as well as the quantity, for the wind turbine wake model benchmarking has to be underlined.

Acknowledgement

The author would like to thank Kurt Schaldemose Hansen from DTU for the pre-processing of the dataset and the construction of the benchmark cases, to José Francisco Herbert Acero from Instituto Tecnológico y de Estudios Superiores de Monterrey (ITESM) for his theoretical contribution and overall review.

This work was partially supported by the International Collaborative Energy Technology R&D Program of the Korea Institute of Energy Technology Evaluation and Planning (KETEP), granted financial resource from the Ministry of Trade, Industry & Energy, Republic of Korea. (No. 20138520021140).

References

[1] Frandsen S. On the wind speed reduction in the center of large clusters of wind turbines. J Wind Eng Ind Aerodyn 1992;39(1):251–65.
[2] Magnusson M, Smedman A-S. Air flow behind wind turbines. J Wind Eng Ind Aerodyn 1999;80(1–2):169–89.
[3] Crespo A, Hernandez J. Turbulence characteristics in wind-turbine wakes. J Wind Eng Ind Aerodyn 1996;61(1):71–85.
[4] Barthelmie R, Folkerts L, Larsen G, Rados K, Pryor S, Frandsen S, et al. Comparison of wake model simulations with offshore wind turbine wake profiles measured by sodar. J Atmos Ocean Technol 2006;23:888–901.
[5] Pope SB. Turbulent flows. Cambridge, UK: Cambridge University Press; 2000. Cambridge Books Online.
[6] Boussinesq JV. Théorie générale des mouvements qui sont propagés dans un canal rectangulaire horizontal. CR Acad Sci Paris 1871;73:256–60.
[7] Garnier E, Adams N, Sagaut P. Large eddy simulation for compressible flows. New York: Springer Science & Business Media; 2009.
[8] Schmitt FG. About Boussinesq's turbulent viscosity hypothesis: historical remarks and a direct evaluation of its validity. C R-Méc. 2007;335(9–10):617–27.
[9] Rodi W, Fueyo N. Engineering turbulence modelling and experiments, vol. 5. Amsterdam: Elsevier; 2002.
[10] Germano M, Piomelli U, Moin P, Cabot WH. A dynamic subgrid-scale eddy viscosity model (1989–1993). Phys Fluids A: Fluid Dyn 1991;3(7):1760–5.
[11] Shih T-H, Liou WW, Shabbir A, Yang Z, Zhu J. A new $k-\varepsilon$ eddy viscosity model for high Reynolds number turbulent flows. Comput Fluids 1995;24(3):227–38.
[12] Piquet J. Turbulent flows: models and physics. Berlin: Springer-Verlag; 2001.

[13] Smagorinsky J. General circulation experiments with the primitive equations: I. the basic experiment*. Mon Weather Rev 1963;91(3):99–164.
[14] Lesieur M, Metais O. New trends in large-eddy simulations of turbulence. Annu Rev Fluid Mech 1996;28(1):45–82.
[15] Geurts BJ, Fröhlich J. A framework for predicting accuracy limitations in large-eddy simulation. Phys Fluids 2002;14(6).
[16] Spalart PR. Detached-eddy simulation. Annu Rev Fluid Mech 2009;41:181–202.
[17] Plate EJ. Aerodynamic characteristics of atmospheric boundary layers. Technical report, Argonne National Lab., Ill. Karlsruhe Univ., West Germany; 1971.
[18] Panofsky HA, Dutton JA. Atmospheric turbulence: models and methods for engineering aplications. In: Atmospheric turbulence: models and methods for engineering applications. New York: John Wiley & Sons; 1984.
[19] Haugen DA, Busch N. Workshop on micrometeorology. Boston: American Meteorological Society; 1973.
[20] Hasager CB, Stein D, Courtney M, Peña A, Mikkelsen T, Stickland M, et al. Hub height ocean winds over the north sea observed by the norsewind lidar array: measuring techniques, quality control and data management. Remote Sens 2013;5(9):4280–303.
[21] Peña A, Gryning S-E, Mann J. On the length-scale of the wind profile. Q J R Meteorol Soc 2010;136(653):2119–31.
[22] Peña A, Rathmann O. Atmospheric stability-dependent infinite wind-farm models and the wake-decay coefficient. Wind Energy 2014;17(8):1269–85.
[23] Rozenn W, Michael C, Torben L, Uwe P. Simulation of shear and turbulence impact on wind turbine performance. Risø National Laboratory for Sustainable Energy, Roskilde.
[24] Sumner J, Masson C. Influence of atmospheric stability on wind turbine power performance curves. J Solar Energy Eng 2006;128(4):531–8.
[25] Peña A. Sensing the wind profile, vol. 1000; 2008.
[26] Bechmann A, Sørensen NN. Hybrid rans/les method for wind flow over complex terrain. Wind Energy 2010;13(1):36–50.
[27] Mann J. The spatial structure of neutral atmospheric surface-layer turbulence. J Fluid Mech 1994;273:141–68.
[28] Mann J. Wind field simulation. Probab Eng Mech 1998;13(4):269–82.
[29] Renkema DJ. Validation of wind turbine wake models [Master of Science Thesis]. Delft University of Technology.
[30] Van Leuven J. The energetic effectiveness of a cluster of wind turbines. Louvain-la-Neuve, Belgium: Universite Catholique de Louvain; 1992.
[31] Habenicht G. Offshore wake modelling. Renewable UK Offshore Wind, RES.
[32] Ferziger JH, Perić M. Computational methods for fluid dynamics, vol. 3. Berlin: Springer; 2002.
[33] Ainslie JF. Calculating the flowfield in the wake of wind turbines. J Wind Eng Ind Aerodyn 1988;27(1):213–24.
[34] Burton T, Jenkins N, Sharpe D, Bossanyi E. Wind energy handbook. Chichester: Wiley; 2011.
[35] Manwell JF, McGowan JG, Rogers AL. Wind energy explained: theory, design and application. Chichester: John Wiley & Sons; 2010.
[36] Prospathopoulos J, Politis E, Rados K, Chaviaropoulos P. Enhanced cfd modelling of wind turbine wakes. In: Extended abstracts for euromech colloquium, vol. 508; 2009.
[37] van der Laan MP, Sørensen NN, Réthoré P-E, Mann J, Kelly MC, Troldborg N. The $k-\varepsilon-f_P$ model applied to double wind turbine wakes using different actuator disk force methods. Wind Energy 2015;18:2223–40. http://dx.doi.org/10.1002/we.1816.
[38] Hansen MO. Aerodynamics of wind turbines. London: Routledge; 2013.
[39] Mikkelsen R. Actuator disc methods applied to wind turbines [Ph.D. thesis]. Technical University of Denmark; 2003.
[40] Larsen TJ, Hansen AM. How 2 HAWC2, the user's manual. Risø National Laboratory; 2007.
[41] Réthoré PE. Thrust and wake of a wind turbine: relationship and measurements [Master's thesis]. Denmark: Technical University of Denmark, DTU; September 2006.
[42] Ott S. Linearised CFD models for wakes. Danmarks Tekniske Universitet, Risø Nationallaboratoriet for Bæredygtig Energi; 2011.
[43] Mortensen NG, Landberg L, Troen I, Lundtang Petersen E. Wind Atlas Analysis and Application program (WAsP): vol. 3: Utility programs. Risø National Laboratory; 1997. 46 p. (Risø-I; No. 666(v.3)(ed.3)(EN)).
[44] Gaumond M, Réthoré P-E, Ott S, Peña A, Bechmann A, Hansen KS. Evaluation of the wind direction uncertainty and its impact on wake modeling at the Horns Rev offshore wind farm. Wind Energy 2014;17(8):1169–78.
[45] Jensen NO. Change of surface roughness and the planetary boundary layer. Q J R Meteorol Soc 1978;104(440):351–6.
[46] Peña A, Rathmann O. Atmospheric stability-dependent infinite wind-farm models and the wake-decay coefficient. Wind Energy 2014;17(8):1269–85.
[47] Jensen NO. A note on wind generator interaction; 1983.
[48] Katic I, Højstrup J, Jensen N. A simple model for cluster efficiency. In: European wind energy association conference and exhibition; 1986. p. 407–10.
[49] Rathmann O, Frandsen S, Nielsen M. Wake decay constant for the infinite wind turbine array. In: Proceedings of the European wind energy association conference & exhibition; 2010.
[50] Peña A, Réthoré P-E, van der Laan MP. On the application of the Jensen wake model using a turbulence-dependent wake decay coefficient: the Sexbierum case. Wind Energy 2015. http://dx.doi.org/10.1002/we.1863.
[51] Peña A, Réthoré P-E, Rathmann O. Modeling large offshore wind farms under different atmospheric stability regimes with the Park wake model. Renew Energy 2014;70:164–71.
[52] Larsen GC. A simple wake calculation procedure; 1988.
[53] Nielsen P, Villadsen J, Kobberup J, Thørgersen ML, Sørensen MV, Sørensen T, et al. Windpro: Software and manual. EMD International A/S, Aalborg, Denmark, 2005; 2003.
[54] Larsen G. A simple stationary semi-analytical wake model. Technical report. Technical Report Risø; 2009.
[55] Larsen GC, Madsen Aagaard H, Bingöl F, Mann J, Ott S, Sørensen JN, et al. Dynamic wake meandering modeling. Roskilde: Risø National Laboratory; 2007.
[56] Larsen GC, Madsen HA, Thomsen K, Larsen TJ. Wake meandering: a pragmatic approach. Wind Energy 2008;11(4):377–95.
[57] Madsen HA, Larsen GC, Larsen TJ, Troldborg N, Mikkelsen R. Calibration and validation of the dynamic wake meandering model for implementation in an aeroelastic code. J Solar Energy Eng 2010;132(4):041014.
[58] Larsen TJ, Madsen HA, Larsen GC, Hansen KS. Validation of the dynamic wake meander model for loads and power production in the egmond aan zee wind farm. Wind Energy 2013;16(4):605–24. http://dx.doi.org/10.1002/we.1563.
[59] Keck R-E, de Maré M, Churchfield MJ, Lee S, Larsen G, Aagaard Madsen H. On atmospheric stability in the dynamic wake meandering model. Wind Energy 2014;17(11):1689–710. http://dx.doi.org/10.1002/we.1662.
[60] Keck R-E, de Maré M, Churchfield MJ, Lee S, Larsen G, Madsen HA. Two improvements to the dynamic wake meandering model: including the effects of atmospheric shear on wake turbulence and incorporating turbulence build-up in a row of wind turbines. Wind Energy 2015;18(1):111–32. http://dx.doi.org/10.1002/we.1686.
[61] Keck R-E, Veldkamp D, Madsen HA, Larsen G. Implementation of a mixing length turbulence formulation into the dynamic wake meandering model. J Solar Energy Eng 2012;134(2):021012.
[62] Ainslie J. Wake modelling and the prediction of turbulence properties. In: Proceedings of the 8th British wind energy association conference, Cambridge; 1986. p. 19–21.
[63] Michelsen J. Basis3d-a platform for development of multiblock pde solvers. Report AFM 92–05; 1992.
[64] Sørensen NN. General purpose flow solver applied to flow over hills [Ph.D. thesis]. Technical University of Denmark; 1995.
[65] Sanderse B, Pijl S, Koren B. Review of computational fluid dynamics for wind turbine wake aerodynamics. Wind Energy 2011;14(7):799–819.
[66] Versteeg HK, Malalasekera W. An introduction to computational fluid dynamics: the finite volume method. Essex: Pearson Education; 2007.
[67] van der Laan MP, Sørensen NN, Réthoré P-E, Mann J, Kelly MC, Troldborg N, et al. An improved $k-\varepsilon$ model applied to a wind turbine wake in atmospheric turbulence. Wind Energy 2015;18:889–907. http://dx.doi.org/10.1002/we.1736.
[68] Launder BE, Spalding D. The numerical computation of turbulent flows. Comput Methods Appl Mech Eng 1974;3(2):269–89.
[69] Cabezón D, Migoya E, Crespo A. Comparison of turbulence models for the computational fluid dynamics simulation of wind turbine wakes in the atmospheric boundary layer. Wind Energy 2011;14:909–21.
[70] Réthoré P-E. Wind turbine wake in atmospheric turbulence [Ph.D. thesis]. Roskilde, Denmark: Aalborg University, Risø DTU; 2009.
[71] El Kasmi A, Masson C. An extended k–ε model for turbulent flow through horizontal-axis wind turbines. J Wind Eng Ind Aerodyn 2008;96:103–22.
[72] Prospathopoulos JM, Politis ES, Rados KG, Chaviaropoulos PK. Evaluation of the effects of turbulence model enhancements on wind turbine wake predictions. Wind Energy 2011;14:285–300.
[73] van der Laan MP, Sørensen NN, Réthoré P-E, Mann J, Kelly MC, Troldborg N. The k–ε–f_p model applied to double wind turbine wakes using different actuator disk force methods. Wind Energy. Published online: http://dx.doi.org/10.1002/we.1816.
[74] van der Laan MP, Sørensen NN, Réthoré P-E, Mann J, Kelly MC, Troldborg N, et al. The $k-\varepsilon-f_P$ model applied to wind farms. Wind Energy 2015;18:2065–84. http://dx.doi.org/10.1002/we.1804.
[75] Richards PJ, Hoxey RP. Appropriate boundary conditions for computational wind engineering models using the k–ε turbulence model. J Wind Eng Ind Aerodyn 1993;46(47):145–53.
[76] Troldborg N. Actuator line modeling of wind turbine wakes [Ph.D. thesis]. Technical University of Denmark; 2008.
[77] Flint I, Johann GT. Ten features which make the holec wind turbine wps 30-3 unique in the world. J Wind Eng Ind Aerodyn 1988;27(1):15–25.
[78] Cleijne J. Results of sexbierum wind farm: single wake measurements. Technical report. TNO Environmental and Energy Research; 1993.
[79] Cleijne J. Results of sexbierum wind farm: double wake measurements. Technical report. TNO Environmental and Energy Research; 1992.
[80] Hansen KS. Benchmarking of Lillgrund offshore wind farm scale wake models; 2014.
[81] Dahlberg J-A. Assessment of the Lillgrund wind farm: power performance wake effects. Vattenfall Vindkraft AB, 6_1 LG Pilot Report. ⟨http://www.vattenfall.se/sv/file/15_Assessment_of_the_Lillgrund_W.pdf_16596737.pdf⟩ [cited March 30, 2012].
[82] Gaumond M, Réthoré P-E, Bechmann A, Ott S, Larsen GC, Peña A, et al. Benchmarking of wind turbine wake models in large offshore wind farms. In: Proceedings of the science of making torque from wind conference; 2012.
[83] Hansen KS. Benchmarking of Lillgrund offshore wind farm scale wake models; 2014.
[84] Fröhlich J, von Terzi D. Hybrid les/rans methods for the simulation of turbulent flows. Prog Aerosp Sci 2008;44(5):349–77.

Estimation of Turbulence Intensity Using Rotor Effective Wind Speed in Lillgrund and Horns Rev-I Offshore Wind Farms

Tuhfe Göçmen, Gregor Giebel

Technical University of Denmark: Department of Wind Energy, Risø Campus, Roskilde Denmark

Abstract

Turbulence characteristics of the wind farm inflow have a significant impact on the energy production and the lifetime of a wind farm. The common approach is to use the meteorological mast measurements to estimate the turbulence intensity (TI) but they are not always available and the turbulence varies over the extent of the wind farm. This paper describes a method to estimate the TI at individual turbine locations by using the rotor effective wind speed calculated via high frequency turbine data.

The method is applied to Lillgrund and Horns Rev-I offshore wind farms and the results are compared with TI derived from the meteorological mast, nacelle mounted anemometer on the turbines and estimation based on the standard deviation of power. The results show that the proposed TI estimation method is in the best agreement with the meteorological mast. Therefore, the rotor effective wind speed is shown to be applicable for the TI assessment in real-time wind farm calculations under different operational conditions. Furthermore, the TI in the wake is seen to follow the same trend with the estimated wake deficit which enables to quantify the turbulence in terms of the wake loss locally inside the wind farm.

Keywords: turbulence intensity, rotor effective wind speed, real-time wind farm calculations

1. Introduction

The turbulence characteristics in a wind farm are important in estimating the power production and the loads on the wind turbines. As the wind farms increase in size, particularly offshore, a good description of the wakes becomes crucial for an accurate performance prediction of the wind farm. The atmospheric turbulence enhances the wake recovery while together with the wake-induced turbulence, they are the major source of fatigue loading on the wind turbines [1]. Both the atmospheric and the wake added turbulence are parametrised in various wake models in terms of Turbulence Intensity (TI) [2, 3, 4, 5, 6] which is defined by

$$TI = \frac{\sigma_U}{U}, \tag{1}$$

where U is the wind speed and σ_U is the standard deviation of the wind speed.

In wind farm calculations, the best possible way to estimate the TI is to use the standard deviation and the mean of the wind speed over 10 minute intervals measured by a meteorological mast (met mast). However, those measurements do not provide the accurate TI at the turbine position since they are located elsewhere and, depending on the wind direction, the measurements might be in the wake of the wind farm or any other obstacle. Also in some cases, often after the turbines started operating, the met mast measurements are not available or they can not be used due to data issues [7, 8]. On the other hand, to estimate the turbulence in the wake either advanced, computationally expensive numerical simulations or parametrised correlations fitted to the experimental data are in use, depending on the distance from the upstream turbine [9]. Here we propose another method to estimate the TI using the turbine data which is applied to the Lillgrund and Horns Rev I offshore wind farms. The results are compared with the TI derived from the met mast measurements as well as the standard deviation of the nacelle anemometer wind speed and the power fluctuations. Both the atmospheric and wake added TI are calculated using the rotor effective wind speed algorithm which was developed to estimate the wind speed using operational supervisory control and data acquisition (SCADA) system. It was designed to be used in real-time wind farm calculations that are required to perform control strategies and follow the balancing market regulations. The effective wind speed algorithm was validated on Horns Rev and Thanet wind farms for both normal operation and down-regulation conditions [6].

For the Lillgrund test case, an additional Siemens turbine SCADA signal called "WindEstimate" is considered as the wind speed to estimate the TI at the turbine locations. The "WindEstimate" was introduced to have a signal with smaller fluctuations, and one that is less sensitive to turbine curtailments than the anemometer signal. The signal is calculated by generating a look-up table for the produced power in terms of the rotor averaged wind speed, rotational speed and pitch angle together with the original rotor geometry. The look-up table is then used considering the operational power, rotational speed and pitch to interpolate the wind speed when the turbine is online.

2. Sites and Data

2.1. Lillgrund Offshore Wind Farm

The Lillgrund wind farm is located in Øresund area, between Sweden and Denmark, 6 – 8 km from the Swedish west coast; south of Malmø. It consists of 48 Siemens SWT-2.3-93 wind turbines with a total rated capacity of 110 MW. The turbine diameters are 93 m and the hub is located at 65 m height. The layout of the Lillgrund is rather unusual due to a gap in the middle of the

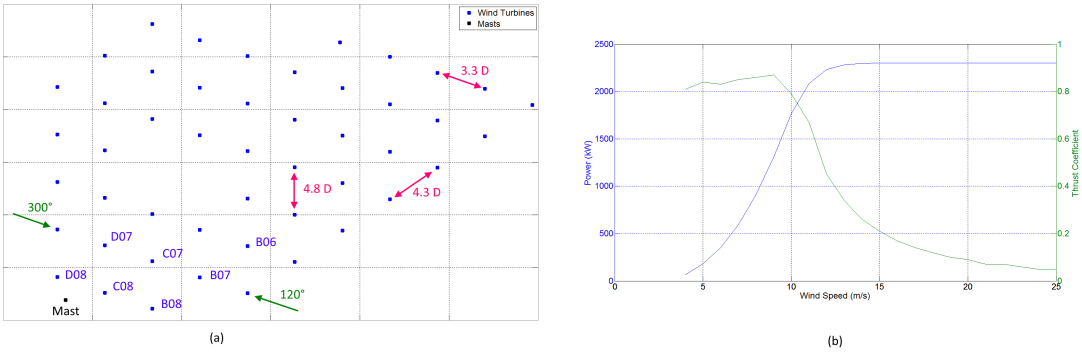

Figure 1: (a) Layout of the Lillgrund offshore wind farm and (b) Siemens SWT-2.3-93 turbine power, P, and thrust, c_T, curve

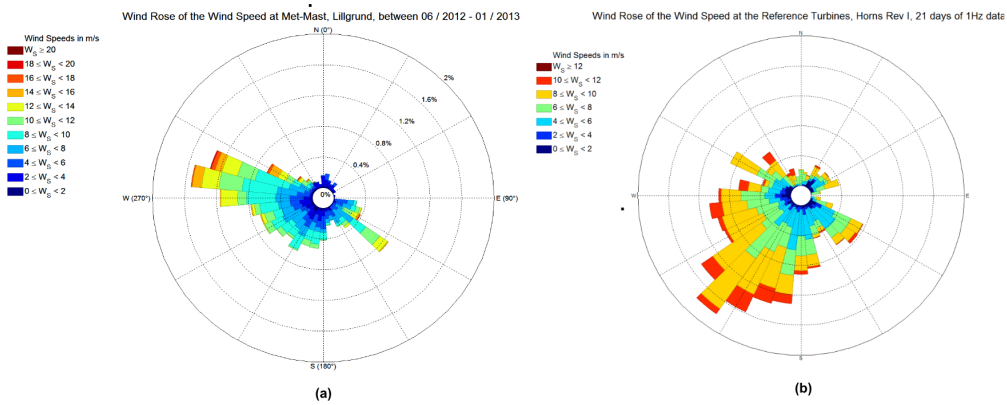

Figure 2: Wind rose of the offshore sites, wind speed observed at (a) Lillgrund – the met mast location at 61 m from 06/2012 to 01/2013, 7 months in total (b) Horns Rev I – the upstream reference turbine(s), covering a period of 21 days in total

farm, and the quite small internal spacings of the turbines of 3.3 and 4.3 rotor diameters, D, as shown in Figure 1(a). The power and thrust curves of the Simens turbines on the site are shown in Figure 1(b)).

The data used in the calculations cover a period of 7 months, from 06/2012 to 01/2013, with a sampling rate of 1 Hz. On the met mast, the closest sensors to the hub height of the turbines are taken into account therefore the second-wise wind speed measurements are taken at 65 m while the wind direction and temperature are observed at 61 m. The wind rose in Figure 2(a) of the met mast data shows the pattern of the prevailing winds, mainly westerly during the considered period. The second-wise extracted signals from the SCADA system are active power, pitch angle, rotational speed, and nacelle anemometer wind speed, where the first three are used to calculate the rotor effective wind speed. Additionally, the Siemens "WindEstimate" signal (SiemensWS) is received from the turbines in question and it is first used in the estimated wind speed comparison and then in the TI calculations.

2.2. Horns Rev I Offshore Wind Farm

The Horns Rev wind farm is located 14 km away from the west coast of Denmark and consists of 80 Vestas V80 turbines with a total capacity of 160 MW. The layout of the wind farm together with the locations of the 2 of the surrounding met masts ($M2, M6$) is shown in Figure 3(a).

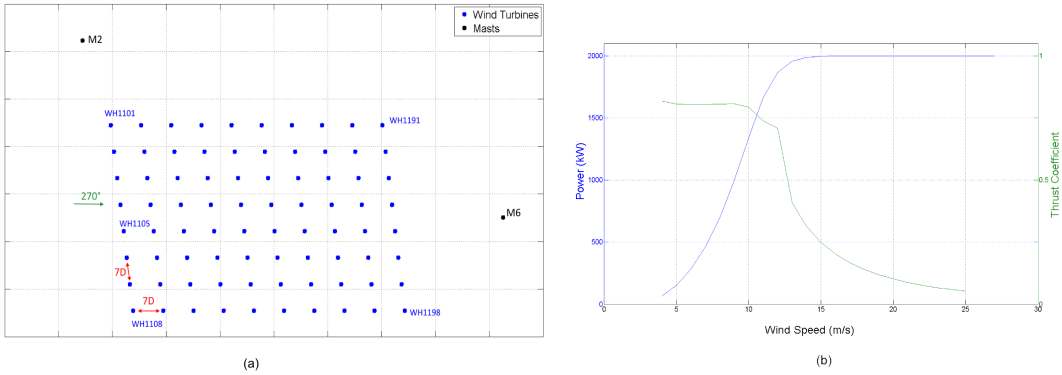

Figure 3: (a) Layout of the Horns Rev I offshore wind farm and (b) Vestas V80-2MW offshore turbine power, P, and thrust, c_T, curve

For the Horns Rev case, the SCADA signals used to calculate the TI at the turbine locations are not continuous and include the period of 04/10 – 10/10, 14/10 – 21/10, 03/11 – 10/11 and 18/11 – 19/11 in 2013, 21 days in total.

The implementation of the TI estimation algorithms on short-term data might provide insight on the operational wind characteristics in the area as emphasized in the studies of Longley et al. [10] and Chan [11]. In order to assess if the 21 days of data in question is adequate to evaluate the model performance in estimating the turbulence levels, the uncertainty of the variances among the time series are quantified using approximations proposed by Lenschow et al. [12, 13]. The relative systematic and random errors of the second order moment of the rotor effective wind speed, which is described in Section 3, are calculated at the turbine positions for the 21 days period, as shown in equations 2 and 3, respectively.

$$\frac{F - \langle F(T) \rangle}{F} \approx 2\frac{\tau}{T} \tag{2}$$

$$\frac{\sigma_F(T)}{|F|} \approx 2\sqrt{\frac{\tau}{T}} \tag{3}$$

where F is the second order moment, or the flux, of the rotor effective wind speed, T is the length of the time series in question, σ_F is the standard deviation of the random error of the flux and τ is the integral time scale defined as in equation 4.

$$\tau = \int_0^T \rho(t)dt \tag{4}$$

$\rho(t)$ being the autocorrelation function. Note that the approximations are derived in [12] where $T \gg \tau$, which is clearly satisfied where $0.506 \leq \tau \leq 15.651$ among the turbine locations.

Along the wind farm, the systematic error differs from 0.0335% to 1.035% for the investigated time interval, thus considered negligible. On the other hand, the relative random error of the second order moment of the rotor effective wind speed is estimated to be between 1.829% – 10.174% throughout the wind farm, which is significantly larger than the systematic error but still $\leq$10% level. Therefore, the considered 21 days period is found adequate to estimate the turbulence levels at the turbine locations inside Horns Rev-I.

Similar to the Lillgrund case, the active power, pitch angle, rotational speed, and nacelle anemometer wind speed signals are extracted from all the turbines together with the yaw signals. It can be seen from Figure 2(b) that the main wind direction recorded at turbine WH1105 during the considered period is south-west. Since there are no available met mast data recorded at the same period, the atmospheric TI is not compared to the met mast but instead, the change in the TI through the wind farm is investigated.

3. High Frequency Rotor Effective Wind Speed

The common approaches to estimate the wind speed at the turbine location(s) are either to use the power production together with the power curve (power curve wind speed) [14] or the nacelle anemometer (nacelle wind speed) [15]. The power curve wind speed is not applicable outside the region between cut-in and rated wind speed as well as for different operational conditions, e.g. down-regulation, where the optimal power curve is no longer valid. The nacelle wind speed can induce unacceptable uncertainties especially for real-time calculations during shorter periods [16]. In order to estimate the wind speed at the turbine locations, the proposed methodology considers power, P, pitch angle, θ, and rotational speed, ω , together with the general power expression, which is

$$P = \frac{1}{2}\rho C_P\left(\lambda, \theta\right)\pi R^2 U^3, \tag{5}$$

where ρ is the air density, λ is the tip speed ratio, R is the rotor radius, and U is the incoming wind speed.

Since C_P does not follow the optimal curve during off-performance conditions and the look-up tables are a matter of confidentiality, the generic pitch angle and tip speed ratio dependence of power coefficient proposed by Heier [17] is applied to simulate the $C_P(\theta, \lambda)$, see equation set 6. In Göçmen et al. [6], the rotor effective wind speed estimation approach is described in detail and applied to data from Horns Rev-I wind farm and NREL 5 MW turbine simulations, under different operational conditions. In Figure 4, the rotor effective wind speed is implemented in Lillgrund and compared with the power curve, nacelle wind speed and Siemens estimated wind speed as well as the high frequency (1 Hz) met mast wind speed observations.

$$\begin{aligned} C_P\left(\lambda, \theta\right) &= c_1\left(\frac{c_2}{\lambda_i} - c_3\theta - c_4\theta^{c_5} - c_6\right) exp\left(\frac{-c_7}{\lambda_i}\right) \\ \lambda_i &= \left[\left(\frac{1}{\lambda + c_8\theta}\right) - \left(\frac{c_9}{\theta^3 + 1}\right)\right]^{-1} \end{aligned} \tag{6}$$

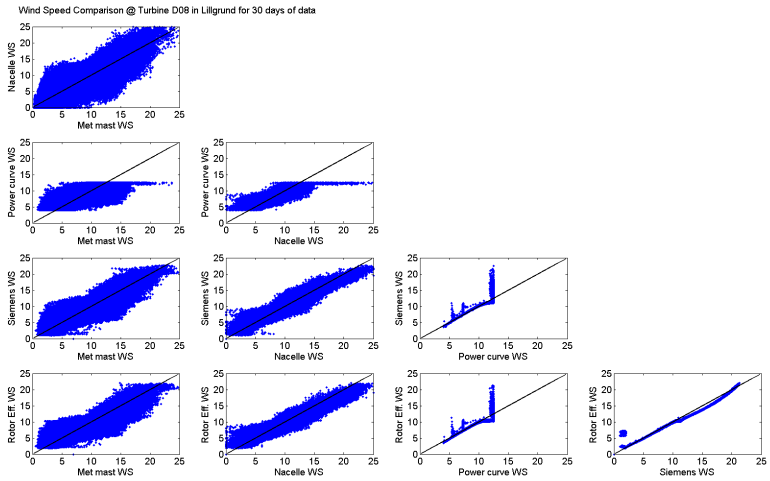

Figure 4: Second-wise Wind speed comparison of the measurements taken at the met mast (Met mast WS) and the nacelle anemometer (Nacelle WS) with the estimations using the turbine power curve (Power curve WS), using the manufacturer $C_P(\lambda, \theta)$ (Siemens WS) and using the approximated $C_P(\lambda, \theta)$ [6] (Rotor eff. WS)

Figure 4 shows that the fluctuations in point measurements (i.e. the nacelle and met mast wind speed) are a lot larger than the others. Due to the geometrical (or volume) averaging embedded in the power curve wind speed, Siemens estimated wind speed and rotor effective wind speed, the scatter is smaller. Moreover, since those rotor averaged wind speeds use active power as an input, they seem inefficient to simulate lower range wind speeds around the cut-in. It is also seen that the power curve wind speed is not applicable for the wind speeds in the rated region, i.e. above 13 m/s. The geometrical average also explains the better agreement seen between the three local wind speed estimation methods. The developed rotor effective algorithm is seen to successively reproduce the wind speed estimated using the authentic $C_P(\lambda, \theta)$ table of the Siemens SWT – 2.3 – 93 turbine with a slight underestimation around the rated wind speed where the pitch peaks. The only significant deviation between those two outputs occurs where the pitch is around $\theta = -1°$, due to the sensitivity in the developed algorithm, see equation set 6. It should be noted that the Siemens wind speed data is filtered for the turbine operational state.

4. Atmospheric Turbulence Intensity

The atmospheric turbulence levels are generally lower offshore than over land and the typical TI values offshore are 6 – 8% [8]. Low atmospheric turbulence, together with stable conditions, tends to delay the wake recovery and does not necessarily mean less structural loading on the turbines since the wake added turbulence plays an important role. Therefore, also in the offshore wind farm calculations the TI is considered to be an important parameter [18].

The TI calculated using the 1 Hz met mast measurements for a period of 7 months is compared to the upstream turbine data in Lillgrund. Using 1 Hz SCADA data, the atmospheric TI is computed using; 1) the nacelle anemometer measurements, 2) Siemens estimated wind speed, 3) rotor effective wind speed, and 4) the standard deviation of the active power signal from the most upstream turbine(s) in equation 1. The implementation of the first three methods is fairly straight-forward. In the last approach, the standard deviation of the active power is correlated to the standard deviation of the wind speed using the method developed by Jørgensen et al. [19] based on Thomsen and Petersen [20], as

$$\sigma_P = B\sigma_U \left(\frac{dP}{dU}\right)_{U_{pow}}, \tag{7}$$

where σ_P is the 10-min standard deviation of the active power signal sampled at 1 Hz, B is a constant typically ranges between $0.8 - 0.9$, depending on the mean wind speed, P is the active power and U is the wind speed. The slope $\left(\frac{dP}{dU}\right)_U$ is calculated using the manufacturer's power curve and the mean power curve wind speed. Therefore, it is important to note that the difference between the operational power curve and the manufacturer's power curve affects the results. Additionally, the method is only applicable where the slope, $\left(\frac{dP}{dU}\right)_{U_{pow}}$ is other than zero and the turbine is operational, i.e. between the cut-in and rated wind speeds, 4 – 13 m/s for SWT – 2.3 – 93 offshore wind turbine.

In order to approximate the constant B, the methodology proposed by Barthelmie et al. [21] is implemented as

$$B = \frac{\sigma_P}{\left(\frac{dP}{dU}\right)_{U_{pow}} U_{pow} TI_{metmast}}, \tag{8}$$

where the TI calculated by the power fluctuations (TI_{pow}) is assumed to be equal to the TI calculated using the met mast measurements ($TI_{metmast}$). Averaging results between 5 and 12 m/s, using another dataset from Lillgrund covering 3 years period (from 01/2012 to 01/2015), gives $B = 0.744$ which is considered in both the atmospheric and the wake induced turbulence calculations.

In Figure 5, the ambient TI is calculated using the met mast together with the power measurements, nacelle anemometer (TI_{nws}), Siemens estimated wind

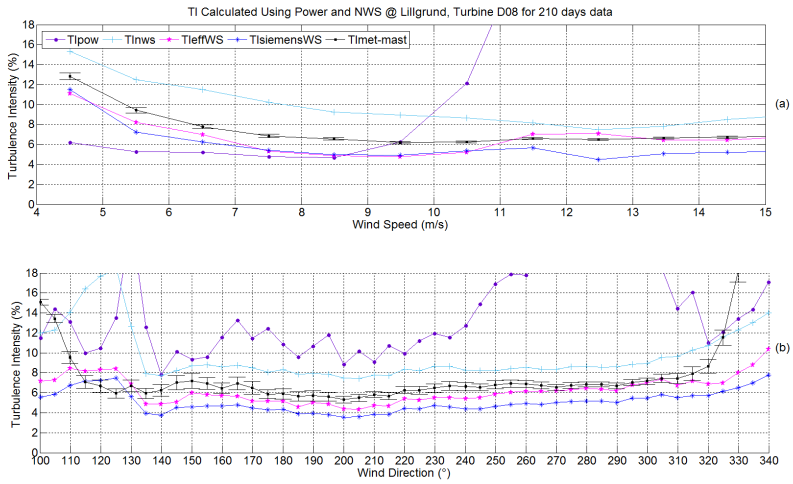

Figure 5: Ambient Turbulence Intensity in Lillgrund, presented in terms of (a) the wind speed (b) the wind direction, errorbars indicating 95% normalized confidence intervals

speed ($TI_{SiemensWS}$), and rotor effective wind speed (TI_{effWS}) at turbine $D08$. The results are averaged over 1 m/s bins between 4.5 - 15.5 m/s for all the wind directions in the top figure and; over 5° wind direction bins for all the wind speeds in the bottom figure where $TI_{metmast}$ is presented with 95% confidence level normalized with respect to the number of data points in the interval.

It can be seen from both Figure 5(a) and (b) that the TI is over-estimated by the nacelle anemometer wind speed. Although the TI_{pow} is in a good agreement with the met mast for low speed flows, around the rated wind speed it rapidly increases due to the behaviour of the power curve. The TI_{effWS} on the other hand, seems to be successfully representing the characteristics of the $TI_{metmast}$ with a consistent under-estimation similar to the Siemens estimated wind speed. That difference can be explained by the fact that the $TI_{metmast}$ is calculated using the point measurements whereas the TI_{effWS} and $TI_{SiemensWS}$ are considering the wind speed seen by the whole rotor. That automatically includes the geometrical averaging between 21.5 m – 114.5 m, which smooths out the fluctuations in wind speed. Where the wind direction is between $100 - 120°$ and $320 - 340°$ in Figure 5(b), the results of the TI_{effWS} and $TI_{metmast}$ are diverse due to the location of the turbine $D08$ and the met mast, where the met mast is affected by the wake - see Figure 1. Note that the TI measured by the met mast in the wake is much higher than the atmospheric TI which will be discussed later in detail.

5. Turbulence Intensity in Wind Turbine Wakes

Downstream of a turbine, in addition to the atmospheric turbulence the wake induced turbulence should also be taken into account. While increasing TI corresponds to higher mixing and therefore reduced wake losses, its impact on the fatigue loading of the downstream turbine(s) is significant mainly due to the partial wakes [22].

Since the atmospheric TI calculations show that the rotor estimated wind speed gives the best TI estimate, the other TI calculation methods are not implemented in the added wake calculations. The turbulence at the downstream turbine positions are estimated using only the rotor effective wind speed for both of the wind farms.

5.1. Wake added TI in Lillgrund

The 1-sec turbine data in Lillgrund is extracted from the turbines indicated in Figure 1(a). For the calculations of the TI in the wake, Row 8 (D08, C08, B08) with $3.3D$ and Row B (B08, B07, B06) with $4.3D$ turbine spacings are analysed and compared with the met mast data.

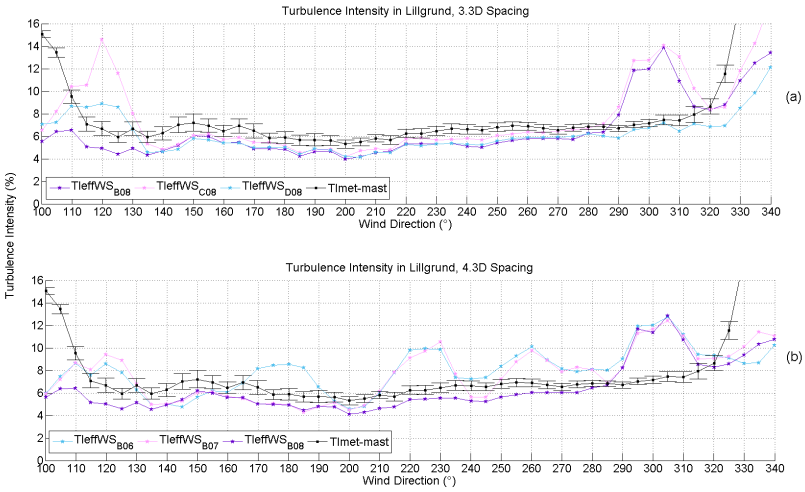

Figure 6: Turbulence Intensity in the wake, estimated using the rotor effective wind speed along (a) Row 8 – $3.3D$ spacing (b) Row B – $4.3D$ spacing, averaged over 5° wind direction bins, errorbars indicating 95% normalised confidence intervals

Figure 6(a) clearly shows the effects of the wake along the wind directions $120 \pm 10°$ and $300 \pm 15°$ where the turbine B08 is the most upstream turbine

around 120° and the most downstream around 300°. Outside of that interval, the TI is almost identical between the turbines and corresponds to the atmospheric turbulence, as in Figure 5. During both of the south-east and north westerly winds, the TI seems to be the highest at the second turbine in the row even though the third turbine is exposed to a double wake. This behaviour is in line with the wake deficit calculations performed as a benchmark case in [23] where the wake deficit at the second turbine is visibly higher than the third and it remains approximately constant among the rest of the turbines in the row. To understand the relation between the TI and the local wake losses, the standard deviation and the mean wind speed are investigated separately. It can easily be seen in Figures 7(a) and 6(a) that the standard deviation and the TI have the same pattern where the wake loss directly affects the difference between the upstream and downstream turbulence levels. In the first wake in Figure 7(b), i.e. around 120°, the deficit is much higher than the second wake around 300° due to the difference between the thrust coefficient for upstream wind speed of $9m/s$ and $10m/s$, see Figure 1(b).

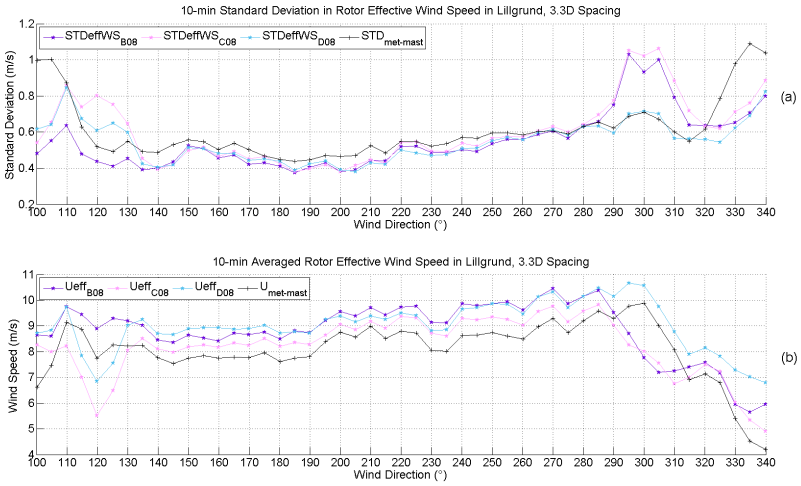

Figure 7: The components of the TI in Lillgrund along Row 8 – $3.3D$ spacing (a) 10-min standard deviation in rotor effective wind speed (b) 10-min mean wind speed, averaged over 5° wind direction bins, errorbars indicating 95% normalised confidence intervals

The effects of the wake to the turbulence is observed to be significant such that the difference between the wake and atmospheric TI is up to 7% for the $3.3D$ spacing case. Also note that the met mast is in the wake of the neighbouring turbines before 115° and after 315° wind directions.

The southernmost three turbines along Row B encounter 5 events where the effects of the wake on the TI are observed for the incoming wind directions between $100-340°$, see Figure 6(b). For the first event between $120\pm15°$, both turbines B07 and B06 are exposed to a single wake thus have almost identical values. For the second one between $180\pm15°$ though, both turbine B08 and B07 are upstream and B06 is under the effect of a single wake. The third event is along the perpendicular direction to the row, $222\pm15°$ causing the highest increase in the TI at the location of the second turbine. Interestingly, between $260\pm15°$ turbines B07 and B06 are subjected to the same turbulence where the former has 4 upstream turbines and the latter has 3 which is also similar to the wake deficit trend in [23]. Similarly between $300\pm10°$, the estimated TI is almost identical at turbines B06, B07 and B08 where they have 5, 4 and 3 turbines upstream, respectively. The behaviour of the TI in multiple wakes is presented in Figure 8 for the perpendicular direction when turbine – turbine spacing is $3.3D$. Figure 8 shows that the turbulence level increases significantly at the first upstream turbine and it is much higher for a single wake compared to a double wake. Although the number of wake data are limited, it is also seen that the existence of three or four upstream turbines hardly makes any difference which will be discussed utilizing more turbines further upstream with larger spacing for the Horns Rev case, Figure 9.

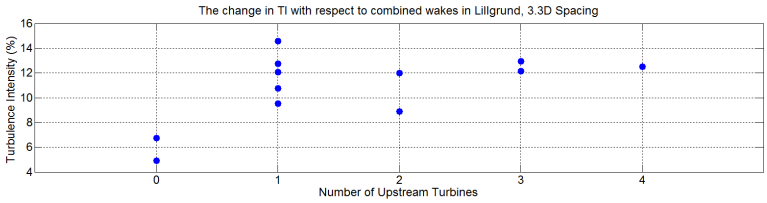

Figure 8: The behaviour of TI in Lillgrund with respect to combined wake effects, $3.3D$ spacing along perpendicular 120° and 300° wind directions

5.2. Wake added TI in Horns Rev I

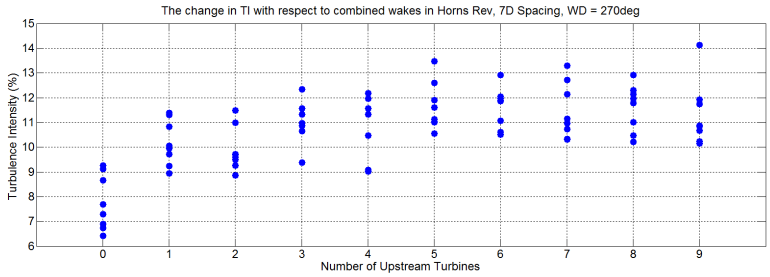

Figure 9: The behaviour of TI in Horns Rev with respect to combined wake effects, $7D$ spacing along perpendicular westerly winds, 270°

In Horns Rev, the data from all the turbines are available for the considered period of 21 days therefore a 'turbulence map' of the whole wind farm can be constructed. Note that, Figure 10 is built based on the linearity assumption between the turbine locations where the information is in fact limited to individual turbine swept areas. The observation of the actual behaviour in between the turbines are left as a future work where detailed measurements have to be carried out.

The TI presented in Figure 10(a) is calculated using the 10-min standard deviation and the mean of the 1-sec rotor effective wind speed and averaged over the upstream wind direction bin $210° \pm 15°$. The wake loss in Figure 10(b) is calculated using the same dataset with the linearised computational fluid dynamics model Fuga [24] for the same wind direction sector and neutral atmospheric stability. The wind speed and direction from the turbine WH1105 is taken as references where the wake loss is calculated in percentages as $U_{wake}/U = (2 - U_{wake}/U_{ref}) \cdot 100$.

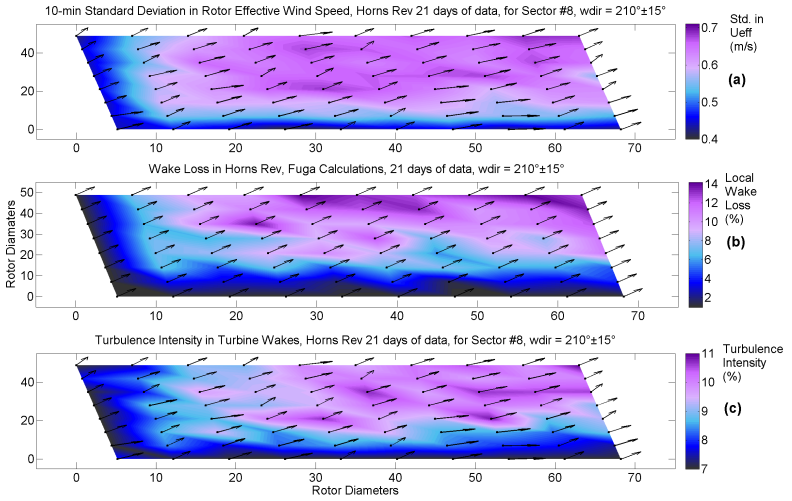

Figure 10: (a) 10-min standard deviation in wind speed, (b) The wake loss, calculated using Fuga [24], (c) The turbulence intensity along the Horns Rev I offshore wind farm, arrows indicate the mean wind direction(s) read by the models filtered across 210° ± 15° bin (see 2(b))

Figure 10(b) and (c) show that the behaviour of the TI follows a very similar trend as the wake deficit such that the turbines with higher loss, thus lower local wind speed, are exposed to higher turbulence. However, their behaviours are not identical due to the simplifications in the employed wake model in which the local wind direction and speed is not taken into account and the calculations are based on the reference wind speed and direction. Still, some of the non-homogeneity is captured inside the wind farm since the directional averaging is applied considering the meandering. Similar to the Lillgrund case, the 10-min standard deviation in wind speed and the added turbulence are not consistently increasing with the superposed wake. Figure 9 shows that the turbulence increases the most at the first downstream turbine also, then remains within a certain zone with a slight tendency to increase after the fourth turbine for westerly winds. The pattern of the TI along a single row of turbines is highly analogous to the power deficit measurements in Horns Rev for westerly winds as illustrated by Hansen et al. [7]. Both the TI and the wake loss analyses show that the flow direction at the turbine location plays an important role in defining the trend of the turbulence increases throughout the wind farm, as it sets the direction of the local wake.

6. Conclusions

To comprehend the atmospheric and wake induced turbulence is crucial for wind farm calculations to estimate the power production and the structural loading on wind turbines. Therefore, here we present a methodology to estimate the TI across the wind farm based on the rotor effective wind speed calculated using the turbine data. The methodology is implemented in Lillgrund and Horns Rev-I offshore wind farms and compared with the met mast as well as the nacelle anemometer and standard deviation of the produced power.

In Lillgrund, the proposed method estimates the atmospheric TI consistently lower than the met mast, by 1.6% for the analysed data with an averaged wind speed 7.7 m/s. Such discrepancy is to be expected since the met mast provides point measurements and the proposed method characteristically includes geometrical averaging over the rotor. Nevertheless, it is shown to produce closer results to the met mast TI compared to the TI derived from the Siemens "WindEstimate" SCADA signal and unlike the one derived using the standard deviation of power, it is applicable also at rated region or under curtailment. The nacelle wind speed measurements on the other hand, over-estimate the atmospheric TI by up to 3.7% compared to the met mast, depending on the wind speed. The performance of the method to approximate the TI in the wake is evaluated using two different rows of 3 turbines with $3.3D$ and $4.3D$ spacings where a higher increase in TI is perceived along the first downstream turbine(s). The results show that in both cases, during perpendicular flows the second turbine is exposed to the highest TI whereas the turbulence levels in the wake of 4 and 5 turbines are very similar. The increase in the TI along the rows is found to be highly correlated to the wake deficit trend observed in the same wind farm.

The TI behaviour across Horns Rev is investigated using the rotor effective wind speeds and compared to the wake loss calculated using linearized CFD model Fuga. The south-westerly wind direction bin averaged results clearly show that the local TI is directly proportional to the wake loss, as observed in the Lillgrund case. The parametrisation of the added wake TI in terms of the local wake loss in offshore wind farms is left as a future work.

Acknowledgements

The author would like to thank Michael Støttrup from Siemens Wind Power, Brande, Denmark for provision of the 1 Hz data in Lillgrund offshore wind farm, clarifications of Siemens SCADA system and the revision of this work which is a part of the PossPOW Project: Possible Power of Offshore Wind power plants, funded by Energinet.dk under the Public Service Obligation (contract number 2012-1-10763).

References

[1] S. T. Frandsen, Turbulence and turbulence-generated structural loading in wind turbine clusters, Risø-R-1188(EN), Risø National Laboratory, 2007.

[2] M. P. van der Laan, N. N. Sørensen, P.-E. Réthoré, J. Mann, M. C. Kelly, N. Troldborg, J. G. Schepers, E. Machefaux, An improved $k-\varepsilon$ model applied to a wind turbine wake in atmospheric turbulence, Wind Energy 18 (5) (2015) 889–907.

[3] G. C. Larsen, A simple stationary semi-analytical wake model, risø-r-171, Tech. rep., Risø, Denmark (2009).

[4] G. C. Larsen, H. Madsen Aagaard, F. Bingöl, J. Mann, S. Ott, J. N. Sørensen, V. Okulov, N. Troldborg, N. M. Nielsen, K. Thomsen, Dynamic wake meandering modeling, Risø-R-1607(EN), Risø National Laboratory, 2007.

[5] J. F. Ainslie, Calculating the flowfield in the wake of wind turbines, Journal of Wind Engineering and Industrial Aerodynamics 27 (1) (1988) 213–224.

[6] T. Göçmen Bozkurt, G. Giebel, N. K. Poulsen, M. Mirzaei, Wind speed estimation and parametrization of wake models for downregulated offshore wind farms within the scope of PossPOW project, in: Journal of Physics: Conference Series, Vol. 524, IOP Publishing, 2014, pp. 12156–12162.

[7] K. S. Hansen, R. J. Barthelmie, L. E. Jensen, A. Sommer, The impact of turbulence intensity and atmospheric stability on power deficits due to wind turbine wakes at Horns Rev wind farm, Wind Energy 15 (1) (2012) 183–196.

[8] R. Barthelmie, O. F. Hansen, K. Enevoldsen, J. Højstrup, S. Frandsen, S. Pryor, S. Larsen, M. Motta, P. Sanderhoff, Ten years of meteorological measurements for offshore wind farms, Journal of Solar Energy Engineering 127 (2) (2005) 170–176.

[9] L. Vermeer, J. N. Sørensen, A. Crespo, Wind turbine wake aerodynamics, Progress in aerospace sciences 39 (6) (2003) 467–510.

[10] I. Longley, M. Gallagher, J. Dorsey, M. Flynn, J. Barlow, Short-term measurements of airflow and turbulence in two street canyons in manchester, Atmospheric Environment 38 (1) (2004) 69–79.

[11] P. Chan, Atmospheric turbulence in complex terrain: verifying numerical model results with observations by remote-sensing instruments, Meteorology and Atmospheric Physics 103 (1-4) (2009) 145–157.

[12] D. Lenschow, J. Mann, L. Kristensen, How long is long enough when measuring fluxes and other turbulence statistics?, Journal of Atmospheric and Oceanic Technology 11 (3) (1994) 661–673.

[13] D. H. Lenschow, L. Kristensen, Uncorrelated noise in turbulence measurements, Journal of Atmospheric and Oceanic Technology 2 (1) (1985) 68–81.

[14] P. Moriarty, J. S. Rodrigo, P. Gancarski, M. Chuchfield, J. W. Naughton, K. S. Hansen, E. Machefaux, E. Maguire, F. Castellani, L. Terzi, IEA-task 31 wakebench: Towards a protocol for wind farm flow model evaluation. part 2: Wind farm wake models, in: Journal of Physics: Conference Series, Vol. 524, IOP Publishing, 2014, p. 012185.

[15] A. Albers, H. Klug, D. Westermann, Power performance verification, in: EWEC-CONFERENCE 1-5 March, Nice, France, 1999, pp. 657–660.

[16] F. Zahle, N. N. Sørensen, Characterization of the unsteady flow in the nacelle region of a modern wind turbine, Wind Energy 14 (2) (2011) 271–283.

[17] S. Heier, Grid integration of wind energy conversion systems, Publisher: John Wiley & Sons, ISBN X 47197143 (1998) 35–36.

[18] A. Sempreviva, R. Barthelmie, S. Pryor, Review of methodologies for offshore wind resource assessment in European seas, Surveys in Geophysics 29 (6) (2008) 471–497.

[19] H. Jørgensen, S. Frandsen, P. Vølund, Analyses of wake effects on Middelgrunden wind farm, risø-r-1403, Tech. rep., Risø National Laboratory (2003).

[20] S. Markkilde Petersen, Experimental investigation of gear box duration loadings on stall and pitch controlled wind turbines, Technical University of Denmark. Department of Fluid Mechanics, 1995, pp. 97–108.

[21] R. J. Barthelmie, S. T. Frandsen, M. Nielsen, S. Pryor, P.-E. Rethore, H. Jørgensen, Modelling and measurements of power losses and turbulence intensity in wind turbine wakes at Middelgrunden offshore wind farm, Wind Energy 10 (6) (2007) 517–528.

[22] M. J. Churchfield, S. Lee, J. Michalakes, P. J. Moriarty, A numerical study of the effects of atmospheric and wake turbulence on wind turbine dynamics, Journal of Turbulence (13).

[23] T. Göçmen Bozkurt, P. van der Laan, P.-E. Réthoré, A. Peña Diaz, G. C. Larsen, S. Ott, Wind turbine wake models developed at the Technical University of Denmark: A review, in Review (2015).

[24] S. Ott, Linearised CFD Models for Wakes, Denmark. Forskningscenter Risoe. Risoe-R, Danmarks Tekniske Universitet, Risø Nationallaboratoriet for Bæredygtig Energi, 2011.

Possible (Available) Power of Down-regulated Offshore Wind Power Plants: The PossPOW Algorithm

Tuhfe Göçmen[1], Gregor Giebel[1], Niels Kjølstad Poulsen[2], and Poul Ejnar Sørensen[1]

[1]Technical University of Denmark: Department of Wind Energy, Risø Campus, Roskilde Denmark
[2]Technical University of Denmark: Department of Applied Mathematics and Computer Science, Kgs. Lyngby Denmark

Abstract

Available (or Possible) Power is the power that a turbine or a wind power plant would produce if it had not been down-regulated (or curtailed). In the modern offshore wind power plants, possible power estimation is becoming more of an issue due to increasing shares in wind and operating reserve calculations. Additionally, to establish wind farm scale dynamic control scenarios a real-time power curve assessment is essential. Currently, there is no regulated approach to assess the available power of a curtailed wind farm agreed by the Transmission System Operators (TSOs) worldwide. Therefore, the PossPOW project proposes to develop an industry standard method for the real-time estimation of the available power of an offshore wind farm. Although the modern wind turbines have a possible power signal at individual turbine level, summation of these signals is simply an over-estimation for the wind power plant level since the wake losses significantly decrease during curtailment. Therefore, to calculate the real-time wind farm available power, high frequency free wind speed at turbine locations has to be estimated and input to the wake model calibrated for the same resolution. As Part I of this two-part series, in this paper the estimation algorithm is elaborated where the main focus is given to the real-time wake modelling. The algorithm is tested on the Thanet and Horns Rev-I offshore wind farms, using the maximum production (or optimum) operational state.

1 Introduction

Offshore wind farms are designed as wind power plants required to contribute to the stability of the grid by offering grid services (also called ancillary services). One of those services is reserve power, which is achieved by down-regulating the wind farm from its maximum available power [10, 27, 7]. The modern wind turbines have a supervisory control and data acquisition system (SCADA) signal called available [18] or possible power [19]. However, the sum of those individual signals is a clear over-estimation of the available power of a down-regulated wind farm simply because the wind speed is higher at the downstream turbine location(s) due to the decrease in wake losses under curtailment. Therefore, the key to the wind farm scale available power estimation is to correct these reduced wake effects during down-regulation. In order to do that, here we introduce a real-time wake modelling approach and provide an industrially applicable method to estimate the available power of a wind farm in the frame of PossPOW project [1, 12]. When applied during the nominal operation, the algorithm clearly provides a real-time wind farm power curve which can then be fed into the control system.

First the 1-sec upstream wind speed is estimated as it is not affected by the reduced wake, in the PossPOW algorithm. Then the upstream wind is introduced into the wake model, adjusted for the same resolution, to simulate the power losses that would occur under nominal operation.

At every second, the effective wind speed is calculated at the curtailed upstream turbines which are not affected by the reduced (or also "down-regulated") wake. The wind speed estimation approach takes power, pitch angle, and rotational speed as inputs. It was developed and validated during both down-regulation and normal operation using 1 Hz met mast and SCADA data from the Horns Rev-I, Lillgrund and Thanet offshore wind farms, together with NREL 5MW simulations [14, 13]. In order to replace the down-regulated wake, the upstream wind should be read by the wake model to estimate the velocity deficit for normal operation. However, most of the robust wake models are tuned and verified for 10-min averaged data and used to acquire long term, statistical information [9, 30, 16]. Therefore, the analytical model proposed by Larsen [20, 21] is re-calibrated for the single wake case in Thanet offshore wind farm, validated in Horns Rev and then implemented in both of the wind farms on farm scale considering the time delay and the local turbulence.

The test and validation of the algorithm is rather challenging since there is no actual measure of the available power on the wind farm scale. However, we can benefit from the similarity in power production between the neighbouring rows in a simple layout like the Horns Rev-I wind farm. The idea behind the validation, experimental set-up and the verification results are presented in the follow-up paper, PossPOW Part II: Down-regulation

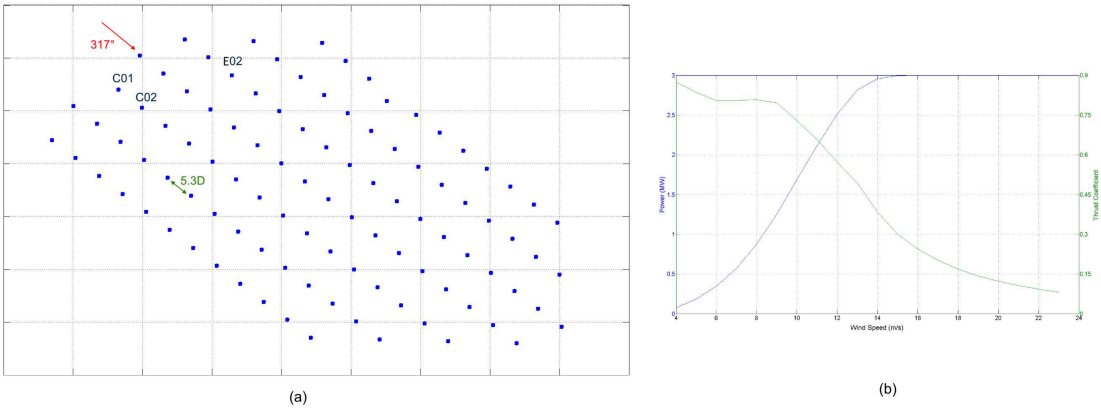

Figure 1: (a) Layout of the Thanet offshore wind farm and (b) Vestas – V90 3MW offshore turbine power, P, and thrust, c_T, curve

experiments in Horns Rev I and model validation.

2 Sites and Data

2.1 Thanet Offshore Wind Farm

The Thanet offshore wind farm is located in the eastern UK, approximately 15 km away from the nearest shore. The wind farm consists of 100 Vestas – V90 3MW offshore turbines. The turbine diameters are 90 m and the hub is located at 70 m height. The distance between the turbines is 500 m corresponding to 5.3 diameters, D, for the perpendicular wind direction, 317°. The layout of the wind farm, together with the manufacturer's power and thrust curve is presented in Figure 1.

The second-wise dataset used in this process are extracted for north – westerly winds, i.e. $317° \pm 20°$). The provided 1 Hz SCADA signals are Active Power, P, Rotational Speed, ω, Pitch Angle, θ, Nacelle Wind Speed (measured by nacelle anemometers), NWS, averaged temperature, Wind Direction (yaw angles) and Possible Power (turbine level). After the wind direction filter and the time delay concept explained further in the paper is applied, the considered data for the re-calibration consist of 24960 seconds which corresponds approximately to 7 hours.

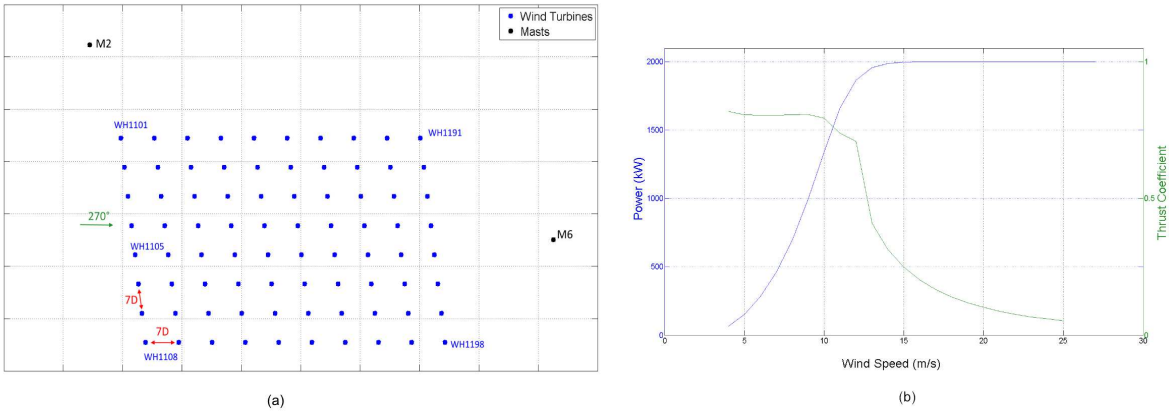

Figure 2: (a) Layout of the Horns Rev-I offshore wind farm and (b) Vestas – V80 2MW offshore turbine power, P, and thrust, c_T, curve

2.2 Horns Rev-I Offshore Wind Farm

The Horns Rev wind farm is located on western Denmark, approximately 14 km away from the coast, and consists of 80 Vestas-V80 2MW turbines. The hub height of the installed turbines are 70 m where the diameter is 80 m. Horns Rev I is a commonly studied wind farm with a regular, slightly inclined layout as shown in Figure 2.

The same 1 Hz SCADA signals as in the Thanet case are extracted from Horns Rev. The single wake validation dataset in Horns Rev consist of easterly winds, i.e. $90° \pm 20°$ covering a period of 77950 seconds, approximately 21.5 hours. For the wind farm scale calculations, a consecutive 24 hours data is presented in terms of 5-min averaged values to enhance the visualisation. Note that, the upstream wind direction signals in Horns Rev are corrected from the bias using the maximum wake depth along the perpendicular incoming flows.

3 Real-time Wake Modelling

Accurate prediction of wake effects has been a key focus area in wind energy research from the individual turbine level [4], to a group of turbines [28] and wind farms level [8]. Most of the existing computationally affordable wake models are tuned and validated for 10-mins data to simulate steady-state, long term behaviour. However, in order to observe the wind farm operations on-line and develop active control strategies accordingly, dynamic

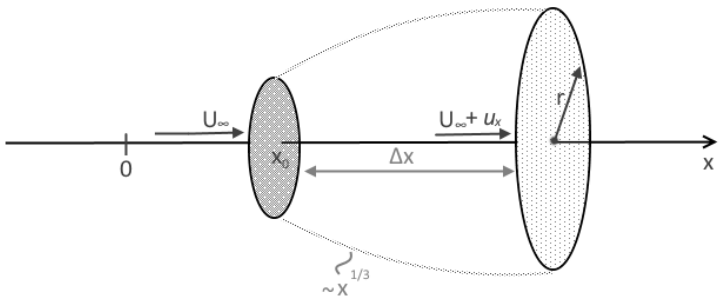

Figure 3: The Larsen wake model (adapted from [20])

simulations that are capable to represent short term performance are required. Instead of developing yet another wake model, here we choose to re-calibrate the Larsen wake model [20, 21] as it is robust and shown to perform relatively well also on offshore [16, 11].

The Larsen wake model has been implemented in many engineering applications due to its practicality and simplicity. In the model, the axis-symmetric form of Reynolds Averaged Navier Stokes (RANS) equations with thin shear layer approximation is used; the control volume considered in the equations is illustrated in Figure 3. The turbulence closure was represented using Prandtl's mixing-length theory. After performing an order of magnitude analysis, Larsen has considered the solution in two parts; first and second order approximations. The second order approximation was found to be negligible for most engineering applications. The final version of the axial velocity deficit equation is obtained as;

$$u_x(x,r) = -\frac{U_\infty}{9}(c_T A x^{-2})^{1/3}\left\{r^{3/2}(3c_1^2 c_T A x)^{-1/2} - (35/2\pi)^{3/10}(3c_1^2)^{-1/5}\right\}^2, \tag{1}$$

where U_∞ is the free-stream inflow velocity, u_x is the wake perturbation of the inflow in the axial direction, r is the radial direction, c_T is the thrust coefficient and $A = \pi R^2$ is the rotor swept area, R being the rotor radius. The parameters to calibrate using 1 Hz field data are; c_1, which is explicitly seen in Equation 1, and x_0, which is embedded in $x = x_0 + \Delta x$ where Δx is the axial distance between the turbines. The term x_0 stands for the position of the rotor in the coordinate system where $x_0 > 0$.

3.1 Local Wind at Upstream Turbine(s)

The anemometers mounted on the nacelle are exposed to highly distorted flow [31]. Particularly for real-time calculations, using nacelle wind speed

Table 1: The coefficients used in the effective wind speed estimation

c_1	c_2	c_3	c_4	c_5	c_6	c_7	c_8	c_9
0.47	101	0.4	0.01	1.95	5	16.5	0.089	0.02

measured during relatively shorter periods may induce higher uncertainties [5]. Therefore, the rotor effective wind speed [14, 13] at turbine locations are used for re-calibration and validation. As well as the rotor geometry, the wind speed estimation procedure, Equation set 2, takes active power, pitch angle and rotational speed signals of the turbine to iteratively estimate the effective wind speed.

$$\begin{aligned} P &= \frac{1}{2}\rho\, C_P\left(\lambda,\theta\right)\pi R^2 U^3, \text{with} \\ C_P\left(\lambda,\theta\right) &= c_1\left(\frac{c_2}{\lambda_i} - c_3\theta - c_4\theta^{c_5} - c_6\right) exp\left(\frac{-c_7}{\lambda_i}\right), \text{and} \\ \lambda_i &= \left[\left(\frac{1}{\lambda + c_8\theta}\right) - \left(\frac{c_9}{\theta^3+1}\right)\right]^{-1} \end{aligned} \tag{2}$$

where ρ is the air density, λ is the tip speed ratio, R is the rotor radius, and U is the incoming effective wind speed. The constants fitted in [14], Table 1, are used to approximate the C_P and estimate the effective wind speed. The methodology is applied to both the upstream and the downstream turbine(s).

After the wind speed is estimated at the upstream turbine locations, a real-time integrated wake model can be applied to remove the reduced wake effects and simulate the nominal operation of the wind farm.

3.2 Re-calibration of the Larsen Wake Model

Because the calibration is to be performed using rotor effective wind speed values, the point-wise wake deficit u_x in Equation 1 needs to be averaged over the rotor. Gaussian 4-point integration is applied to estimate the wind speed distribution over the rotor using the same Gauss weights and the associated integral variables as in [21]. The integration of Equation 1 in this manner gives the effective wake deficit, u_{eff} as;

$$u_{eff} = \frac{-0.2939U_{in}\left(0.0235\left(c_1^2\right)^{2/5}\left(R^2\right)^{3/2} - 0.277\left(c_1^2\right)^{1/5}\left(R^2\right)^{3/4}\sqrt{c_1^2 c_T R^2\left(\Delta x + x_0\right)} + c_1^2 c_T R^2\left(\Delta x + x_0\right)\right)}{\left(c_1^2\right)^{7/5}\left(\frac{\left(c_T R^2\right)}{\left(\Delta x + x_0\right)^2}\right)^{2/3}\left(\Delta x + x_0\right)^3}, \tag{3}$$

where U_{in} is the upstream incoming effective wind speed.

The re-calibration of the Larsen model is performed for a single wake event in Thanet considering the turbines $C01$ and $C02$ for $317° \pm 15°$ incoming wind direction, see Figure 1. The radius of the Vestas V90 – 3MW offshore turbines are $R = 90m$ and the distance between the turbines for considered wind direction is taken to be $\Delta x = 500m$ in Equation 3.

3.2.1 Time Delay Concept

Before using the dataset to determine the parameters c_1 and x_0 for the single wake, the time it takes for a particle to move from the most upstream turbine to the turbine in question, namely the time delay t_d, is taken into account by applying a correction to the dataset.

Machefaux et al. [24] studied the advection time in detail, in which the cross-correlation between the measured near wake velocity profiles are investigated. The time lag between the downstream lidar measured patterns is quantified as the specific time shift where the profiles are most correlated. On the other hand, the lack of measurement campaigns in considered wind farms and the framework of this study limit the analysis to be performed only at the turbine locations, using the turbine data. Therefore, the proposed methodology is simply $t_{down} = t_{up} + t_d$ where t_{down} and t_{up} are the time steps of the downstream and upstream locations, respectively and t_d is estimated as; $t_d = \frac{\Delta x}{\left(\overline{U}_{down-data}\right)}$ with $\overline{U}_{down-data}$ being the rotor effective wind speed estimated using the downstream turbine SCADA, averaged up to ten minutes during the re-calibration on Thanet and validation on Horns Rev.

Note that, the distance between the turbine in question and the most upstream turbine is equal to Δx for the single wake re-calibration case. However, the calculations on the wind farm scale are based on the 'instantaneous' upstream distance which is mostly a lot larger depending on the wind direction and the considered downstream turbine location. For both the single and multiple wakes, the average downstream wind speed is updated on every 10-mins if the treated data covers a longer period.

3.2.2 Moving Average of the Time Series

In order to avoid over-fitting and start modelling the noise, both up and downstream effective wind speeds have been filtered using moving window average with Savitzky-Golay convolution coefficients [29]. Since the objective is to model the flow behind the turbine dynamically to achieve the real-time effect, the window size was kept at 60-sec to discard the measurement noise from the SCADA while abstaining from over-smoothing the time series.

3.2.3 Modelling of the Meandering inside the wind farm

The wake velocity field is assumed to be axis-symmetric and self-similar in the Larsen model. However, the wake meandering mechanism is shown to be significant in reducing the wake losses especially for unstable and neutral atmospheric stabilities [2]. Although the effects of meandering on a single wake profile are measured [6] and investigated heavily in the recent years [22, 26, 25], the concept is still under discussion for multiple wake cases. Although the Dynamic Wake Meandering model (DWM) [22] is validated on the smaller scale Egmond aan Zee wind farm [23], it is not implemented to the PossPOW algorithm since the location of the wake deficit is modelled by introducing an external 3D turbulence box, rather than calculating the actual TI at the turbine locations using SCADA data.

Since the algorithm reads the individual wind direction signals and the TI estimated at the turbine locations, the changes in the local upstream wind profiles are implicitly taken into consideration in the computations. However, especially for high fidelity calculations in large wind farms, the change in the flow along the distance between the upstream and downstream turbines is also significant. Therefore, Ainslie's correction [2] to the centreline wake deficit by correlating the meandering to the variability in the wind direction, Equation 4, is implemented in this study for both Thanet and Horns Rev-I offshore wind farm applications. Therefore,

$$\hat{u}_{eff} = u_{eff}\left[1 + 7.12\left(\frac{\sigma_\theta}{b}\right)^2\right]^{-\frac{1}{2}}, \tag{4}$$

where $\hat{u}_{eff}$ is the corrected deficit, σ_θ is the standard deviation in local wind direction fluctuations of timescale of maximum 10-min if the investigated period is longer, and b is the full wake width.

3.2.4 Parametrisation and Curve Fitting

As explained earlier, the main variables to adjust inside the wake model are c_1 and x_0 which are highly dependent on c_T and the turbulence intensity, TI. They are formulated as in Equation 5.

$$\begin{aligned} x_0 &= p_1 c_T^{p_2} + p_3 TI \\ c_1 &= p_4 c_T^{p_5} + p_6 TI \end{aligned} \tag{5}$$

The objective function combines Equation 3 with Equation 5 and together with those 6 parameters, it takes 3 inputs to predict the effective wind speed observed at the downstream turbine C02 in Thanet. The first input is the incoming effective wind speed, U_{in}, along the perpendicular direction, pre-processed using moving average. The second is c_T which is tabulated in terms of wind speed as in Figure 1(b) and interpolated for changing U_{in} in the algorithm at every second. On the other hand, estimation of

Table 2: List of model parameters and goodness of the fit for the Re-calibration of the Larsen model, R^2 is the coefficient of determination and $RMSE$ is the root mean square error of the model predictions)

p_1	0.232 (-57.3247, 57.7163)
p_2	74.985 (-147.796, 148.551)
p_3	0.12 (-72.968, 78.098)
p_4	0.763 (-18.052, 41.865)
p_5	17.126 (3.182, 32.874)
p_6	40.459 (40.135, 50.255)
$R^2 = 0.914$	RMSE = 0.718 m/s

the third input, TI is not as straightforward, especially when it comes to the wind farm scale. For that reason, the methodology proposed by Göçmen et al.[13] that employs 10-min averages of 1 Hz rotor effective wind speed using only the turbine data is implemented in both of the Thanet and Horns Rev dataset. The turbine specific TI that is calculated accordingly is tabulated in terms of incoming wind speed to be used in 1-sec re-calibration and the rest of the calculations in this study. Note that the ambient TI using the effective wind speed is shown to be consistently lower than the point-wise meteorological mast measurements due to geometrical averaging over the rotor. However, the corresponding correction is automatically embedded in the re-calibration process.

The final parametrised non-linear functions are fitted to data using non-linear least squares approximation (NLSA). Note that this non-linearity results in parameters being highly sensitive to the initial guesses assigned. The concluding parameters together with the 95% confidence intervals are presented in Table 2.

The Larsen model with the re-calibrated parameters is implemented in the Horns Rev single wake case for the easterly winds. The comparison of the original Larsen model and the re-calibrated version for second-wise dataset is presented in Figure 4. Note that, for both versions of the model, the inputs, i.e. U_{in}, c_T and TI are the same but the parameters c_1 and x_0 are expressed differently. Although the data is not symmetrically distributed over the wind direction bin, it can easily be seen that the original Larsen model significantly under-predicts the downstream wind speed for the second-wise dataset. Better recovery achieved by the re-calibration is observed especially for $90^\circ \pm 5^\circ$ wind direction bin.

4 Wind Farm Scale Available Power Estimation

The re-calibrated Larsen model is implemented to the wind farm scale where multiple and partial wakes are highly significant in evaluating the available

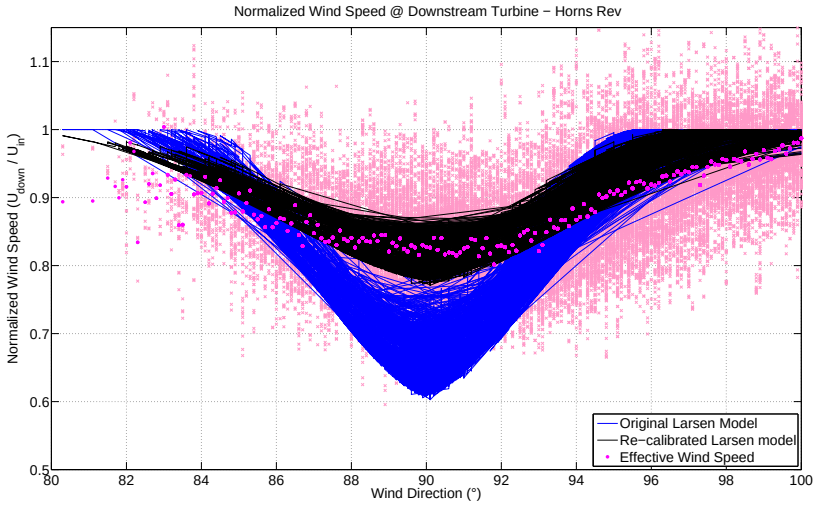

Figure 4: Normalised 1-sec wind speed at the downstream turbine, $7D$, in Horns Rev - Original and Re-calibrated Larsen model together with the raw data and the moving average

power of the farm. Due to the dependency on c_T to the wind speed, see Figures 1 and 2, two different simplified approaches are applied to superpose the wakes which is a complicated process. For the incoming wind speed below rated, since the c_T is high, only the maximum wake deficit is taken into consideration among contributions from all the upstream turbines at any time. Along the rated region, c_T is much lower so all the dual deficits are weighed via linear summation.

The time delay and the TI inside the wind farm is estimated following the same procedure as the single wake case using the raw 1 Hz turbine data without the moving average. However, while implementing the model to the wind farm scale, the effect from wake meandering is to be taken into account as comprehensive as possible.

4.1 Percentage Error in Wind Speed

The percentage error in wind speed, $\%error_U = \left| \frac{U_{ReLarsen} - U_{eff}}{U_{eff}} \right| \cdot 100$, is estimated using the re-calibrated version of the Larsen model, $U_{ReLarsen}$, together with the meandering correction, and the effective wind speed calculated using the turbine operational data, U_{eff}. Since the wind speed at the downstream turbine is higher during down-regulation, the error is calculated

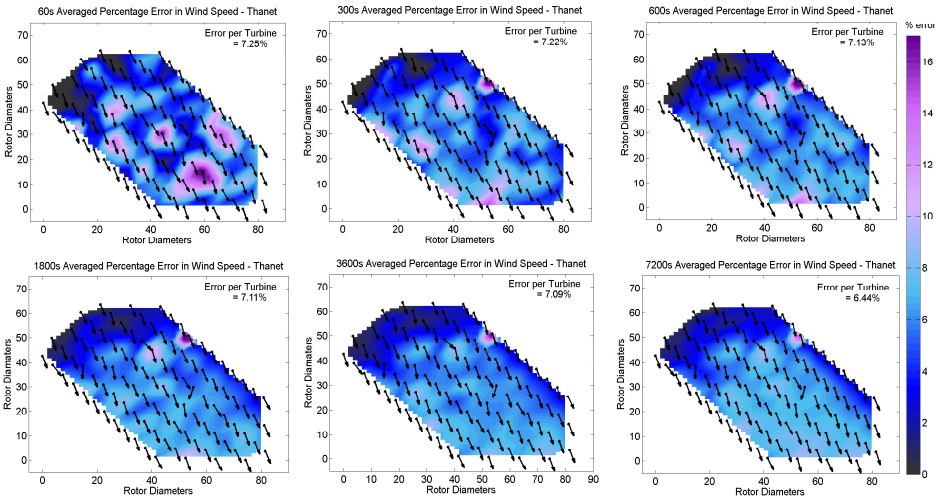

Figure 5: Percentage error $\left(\%error_U = \left|\frac{U_{ReLarsen} - U_{eff}}{U_{eff}}\right| \cdot 100\right)$ in wind speed averaged over (a) 60s, (b) 300s, (c) 600s, (d) 1800s, (e) 3000s, (f) 7200s across Thanet offshore wind farm.Error per Turbine values correspond to the average of all the time intervals among the total period of 7-hours (i.e. all 60s intervals in 7-hours, 420 data points in total, etc.)

using only the normal operational data. Note that the implementation of the re-calibrated Larsen wake model to the wind farm scale gives the wind power plant level real-time power curve, under all operational conditions. The averaged percentage error in Thanet offshore wind farm over different time intervals is shown in Figure 5. The arrows represent the nacelle direction signals, averaged along the same period. As expected, the model prediction error is accumulated going further downstream especially for 10-min or longer averaging time scales. The error distribution remains nearly the same for 10-min and larger bins with a slight flattening. The maximum prediction error is less than 16%, for most of the turbines less than 8%, inside the farm. To illustrate the model error at the individual turbine level, the mean error of every single period (i.e 60s, 300s, 600s, 1800s, 3600s and 7200s; colormaps in Figure 5) are averaged among the whole dataset of 7h (indicated in upper left corners in Figure 5). The averaging period of interest for the error calculations is 5-min in this study, following the requirements set by Danish TSO Energinet.dk [10].

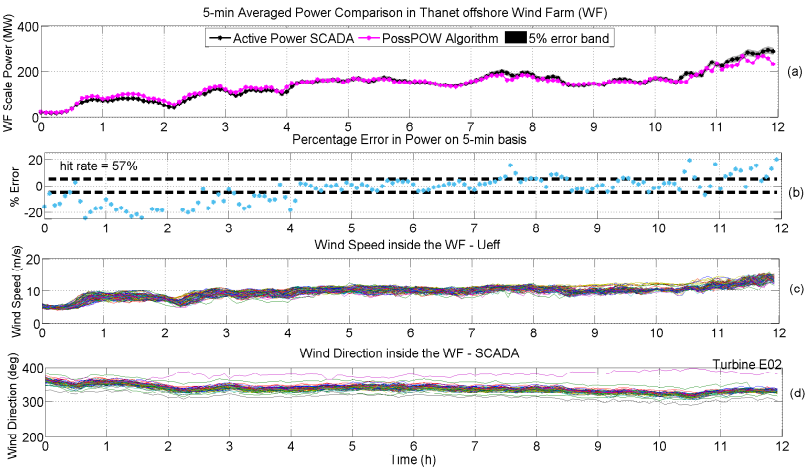

Figure 6: (a) 5-minute averaged Active Power (SCADA) and Re-calibrated Larsen model (together with Equation 2) results in Thanet, (b) the estimated effective wind speeds and (c) the nacelle direction signals at the turbine locations inside Thanet, 12-hours data.

4.2 Real-Time Wind Speed to Power

While a good agreement is achieved for the single wake and the wind farm wind speed calculations using the re-calibrated Larsen wake model and the meandering correction of Ainslie, the conversion of the wind speed to power production is not straightforward. The manufacturer power curve in Figures 1(b) and 2(b) are built using 10-min averaged power [3], for higher resolution power curves see [17], and point-wise wind speed measurements and they are standardised for fixed turbulence (typically $TI = 10\%$) and air density [3]. Therefore, the approximated C_P curve using the operational pitch and rotational speed signals together with the calculated $U_{ReLarsen}$ wind speed is implemented to estimate the power production (Equation set 2), first at the turbine and then at the wind farm level.

Figures 6(a) and 7(a) illustrate the comparison of the 5-min averaged model results and the aggregated active power turbine data together with its 5% error band. The nominal operational dataset for the Thanet case covers a period of 12 hours where for the Horns Rev-I analysis 24 hours period is presented. Especially in the Thanet case, the comparison of the farm level power results with the wind speed and direction inside the wind farm might explain the deviation observed earlier and later in the analysed dataset. The over-estimation in the first part of the dataset is possibly related to the contradictory behaviour of the upstream wind direction signal,

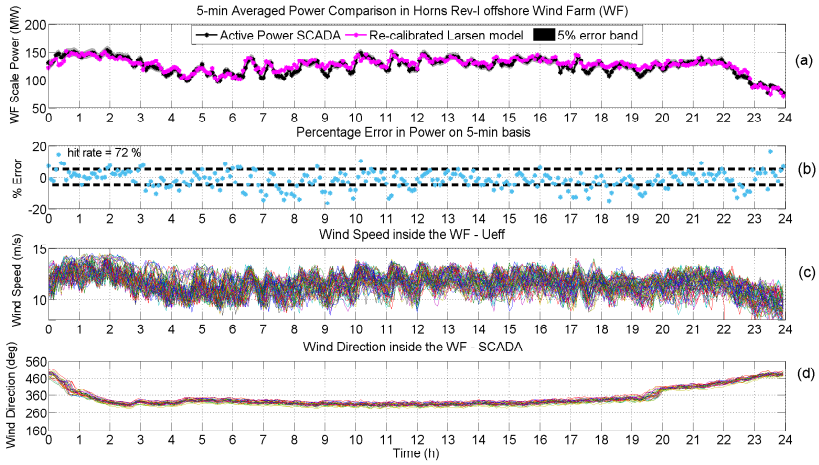

Figure 7: (a) 5-minute averaged Active Power (SCADA) and Re-calibrated Larsen model (together with Equation 2) results in Horns Rev-I, (b) the estimated effective wind speeds and (c) the wind direction signals at the turbine locations inside Horns Rev, 24-hours data. Wind direction is normalized by 360° due to northerly winds.

Turbine $E02$ (see Figure 1(a)) on which the calibration was infeasible due to the lack of data to adjust the center of the wake depth with respect to the wind direction. The same tendency is clearly observed in the Figure 6(b) where the distribution of the 5-minutes percentage errors are illustrated. The difference between the active power signal and the algorithm reaches up to 20% during that period when E02 is an upstream turbine. The "hit rate" rate refers to ratio of the points inside and outside of the $\pm 5\%$ error span. Later in the investigated period the wind becomes perpendicular to the long and closely located rows which leads to stronger wakes, as can be perceived clearly in Figure 6(c). Towards the end of that region, the wind speed reaches rated where both the C_T and the approximated C_P curves are the most sensitive to the incoming wind speed.

The turbines in the Horns Rev-I case, Figure 7, are exposed to northwesterly winds during the investigated period, which corresponds to diagonal wakes with higher upstream turbine distances. The wind speed is slightly lower than the rated with fairly steady wind direction during the most of the dataset. Similar to any other wake model, the PossPOW algorithm is highly sensitive to the wind direction input. Therefore at least for the investigated period, the higher hit rate and a better performance is anticipated. It is also seen in Figure 7(c) that even for 5-minutes averaged dataset, the bandwidth of the wind speed inside the wind farm is as broad as 4 m/s. This automat-

ically correspond to significant production differences towards downstream, indicating the importance of fast, robust and as accurate as possible wake modelling once again. Despite the highly variable wind speed inside the wind farm, the PossPOW algorithm is seen to be in a good agreement with the dataset in terms of the 5-min averaged produced and predicted power on the wind farm scale. Note that the performance of the overall PossPOW algorithm for the same wind farm under curtailment is evaluated in the second part of this study, PossPOW Part II: Large scale down-regulation experiments in Horns Rev-I and model validation.

5 Conclusions

Due to change in the wake characteristics during curtailment, the estimation of the available power of a wind farm under down-regulation is a complex process, especially for high resolution data. Here we present and validate a re-calibrated real-time wake model as well as an approximated dynamic power curve approach which draws upon the pitch and the rotational speed data together with the wind speed at the turbine location(s), valid for all the operational conditions. Combination of those two procedures gives real-time available power during down-regulation and under nominal conditions it estimates the real-time power curve of the wind power plant. In this study, the algorithm is implemented in the Thanet and Horns Rev-I offshore wind farms for the case of normal operation. The model evaluation under down-regulation via a series of experiments conducted in Horns Rev-I wind farm is presented as a follow-up paper [15].

The available robust wake models are tuned for 10-min averaged data to acquire long term, statistical information. Therefore, in order to model the wind speed through the wind farm for higher time resolutions, the Larsen wake model is re-calibrated. Second-wise estimated rotor effective wind speed at the upstream and downstream turbine locations are used for both the re-calibration in Thanet and the validation in Horns Rev for single wake cases.

The re-calibrated real-time wake model is implemented in the wind farm scale considering only maximum dual wake deficit for the wind speeds lower than the rated whereas for the wind speeds above all the wake contributions are taken into account. In order to correct the results in terms of unsteady meandering effects especially for large offshore wind farms, the correlation of the wake deficit and the local wind direction variation introduced by Ainslie is considered. The wake loss calculations are iterated for all the turbines in the wind farm at each second and compared with the data post-processed for localised time delay. The percentage error in wind speed is calculated for different time averaging bins in Thanet and for shorter intervals, it is observed to be less than 8% for most of the turbines where the maximum is

around 16%.

In regard to the Danish TSO requirements for the compensation during mandatory down-regulation, 5-minutes averaged percentage error was analysed when evaluating the model performance in wind farm scale power estimation. The applied real-time power curve estimation approach is shown to be in a good agreement with the active power signal, also considering the 5% error band at the power plant level as stated in the same regulation. The model is to be further implemented in the down-regulated state.

Acknowledgements

The authors would like to thank Mads Rajczyk Skjelmose and Jesper Runge Kristoffersen from Vattenfall Wind Power A/S Kolding, Denmark together with Michael Støttrup from Siemens Wind Power, Brande, Denmark for provision of the 1 Hz data in both Thanet and Horns Rev offshore wind farms, consultancy especially during data processing and overall revision of this work which is a part of the PossPOW Project: Possible Power of Offshore Wind power plants, funded by Energinet.dk under the Public Service Obligation (contract number 2012-1-10763).

References

[1] PossPOW: Possible Power of Offshore Wind power plants. `http://www.posspow.vindenergi.dtu.dk`.

[2] *Wake modelling and prediction of turbulence properties*, volume 8 of *Lecture Notes in Computer Science*, UK, 1986. Cambridge.

[3] IEC International Standard, IEC 61400-12-1, Wind Turbines – Part 12-1 : Power performance measurements of electricity producing wind turbines, 2005.

[4] R. J. Barthelmie, G. C. Larsen, S. T. Frandsen, L. Folkerts, K. Rados, S. C. Pryor, B. Lange, and G. Schepers. Comparison of Wake Model Simulations with Offshore Wind Turbine Wake Profiles Measured by Sodar. *Journal of Atmospheric and Oceanic Technology*, 23(7):888–901, July 2006.

[5] J. Beltrán, J. J. Guerrero, J. J. Melero, and A. Llombart. Detection of nacelle anemometer faults in a wind farm minimizing the uncertainty. *Wind Energy*, 16(6):939–952, 2013.

[6] Ferhat Bingöl, Jakob Mann, and Gunner C Larsen. Light detection and ranging measurements of wake dynamics Part I: One-dimensional scanning. *Wind energy*, 13(1):51–61, 2010.

[7] Bundesnetzagentur. Leitfaden zum EEG-Einspeisemanagement – abschaltrangfolge, berechnung von entschädigungszahlungen und auswirkungen auf die Netzentgelte, version 2.1, 2014.

[8] Merete Bruun Christiansen and Charlotte B Hasager. Wake effects of large offshore wind farms identified from satellite sar. *Remote Sensing of Environment*, 98(2):251–268, 2005.

[9] Antonio Crespo, J. Hernández, and Sten T. Frandsen. Survey of modelling methods for wind turbine wakes and wind farms. *Wind Energy*, 2(1):1–24, January 1999.

[10] Energinet.dk. Technical regulation 3.2.5 for wind power plants with a power output above 11 kW, 2015.

[11] M Gaumond, Pierre-Elouan Réthoré, Andreas Bechmann, Søren Ott, Gunner Chr Larsen, Alfredo Pena Diaz, and KS Kurt. Benchmarking of wind turbine wake models in large offshore windfarms. *Proceedings of the Science of Making Torque From Wind*, 2012.

[12] Gregor Giebel, Tuhfe Göçmen, Poul Ejnar Sørensen, Niels Kjølstad Poulsen, and Jesper Runge Kristoffersen. Posspow: Possible power of offshore wind power plants. In *Proceedings of EWEA 2013*. European Wind Energy Association (EWEA), 2013.

[13] Tuhfe Göçmen and Gregor Giebel. Estimation of turbulence intensity using rotor effective wind speed in Lillgrund and Horns Rev offshore wind farms. Under Review, 2015.

[14] Tuhfe Göçmen, Gregor Giebel, Niels Kjølstad Poulsen, and Mahmood Mirzaei. Wind speed estimation and parametrization of wake models for downregulated offshore wind farms within the scope of PossPOW project. *Journal of Physics: Conference Series (Online)*, 524(1), 2014.

[15] Tuhfe Göçmen, Gregor Giebel, and Mads Rajczyk Skjelmose. Possible (available) power of offshore wind power plants, PossPOW Part II: Down-regulation experiments in Horns Rev-I and model validation. Submitted, 2015.

[16] Tuhfe Göçmen, Paul van der Laan, Pierre-Elouan Réthoré, Alfredo Peña Diaz, Gunner Chr Larsen, and Søren Ott. Wind turbine wake models developed at the technical university of denmark: A review. *Renewable and Sustainable Energy Reviews*, 60:752–769, 2016.

[17] Julia Gottschall and Joachim Peinke. How to improve the estimation of power curves for wind turbines. *Environmental Research Letters*, 3(1):015005, 2008.

[18] R. Krishna. Available power estimator, March 29 2012. US Patent App. 13/321,932.

[19] Jesper Runge Kristoffersen. The horns rev wind farm and the operational experience with the wind farm main controller. *Revue E-Société Royale Belge des électriciens*, 122(2):26, 2006.

[20] Gunner C. Larsen. A simple wake calculation procedure. Technical report, risø-m-2760(en), RisøDTU, 1988.

[21] Gunner C. Larsen. A simple stationary semi-analytical wake model. Technical Report, Risø-R-1713(EN) August, RisøDTU, 2009.

[22] Gunner C Larsen, Helge Aa Madsen, Kenneth Thomsen, and Torben J Larsen. Wake meandering: a pragmatic approach. *Wind energy*, 11(4):377–395, 2008.

[23] Torben J Larsen, Helge Aa Madsen, Gunner C Larsen, and Kurt S Hansen. Validation of the dynamic wake meander model for loads and power production in the Egmond aan Zee wind farm. *Wind Energy*, 16(4):605–624, 2013.

[24] Ewan Machefaux, Gunner Chr Larsen, Niels Troldborg, Mac Gaunaa, and Andreas Rettenmeier. Empirical modeling of single-wake advection and expansion using full-scale pulsed lidar-based measurements. *Wind Energy*, 2014.

[25] Ewan Machefaux, Gunner Chr. Larsen, Niels Troldborg, Mac Gaunaa, and Andreas Rettenmeier. Empirical modeling of single-wake advection and expansion using full-scale pulsed lidar-based measurements. *Wind Energy*, 2014.

[26] H Aa Madsen, Gunner Chr Larsen, Torben J Larsen, Niels Troldborg, and R Mikkelsen. Calibration and validation of the dynamic wake meandering model for implementation in an aeroelastic code. *Journal of Solar Energy Engineering*, 132(4):041014, 2010.

[27] Office of Gas and Electricity Markets, UK. Grid code GC0063: Power Available, 2015.

[28] B. Sanderse, S. P. Van Der Pijl, and B. Koren. Review of computational fluid dynamics for wind turbine wake aerodynamics. *Wind Energy*, 14(7):799–819, 2011.

[29] Abraham Savitzky and Marcel JE Golay. Smoothing and differentiation of data by simplified least squares procedures. *Analytical chemistry*, 36(8):1627–1639, 1964.

[30] L. J. Vermeer, Jens Nørkæ r Sø rensen, and Antonio Crespo. Wind turbine wake aerodynamics. *Progress in aerospace sciences*, 39(6-7):467–510, October 2003.

[31] Frederik Zahle and Niels N. Sø rensen. Characterization of the unsteady flow in the nacelle region of a modern wind turbine. *Wind Energy*, 14(2):271–283, 2011.

Appendix C

Conference Proceedings

Giebel, Gregor; Göçmen, Tuhfe; Sørensen, Poul Ejnar; Poulsen, Niels Kjølstad; Runge Kristoffersen, Jesper / POSSPOW: Possible Power of Offshore Wind Power Plants. Proceedings of EWEA 2013. European Wind Energy Association (EWEA), 2013.

Göçmen, Tuhfe; Giebel, Gregor; Sørensen, Poul Ejnar; Mirzaei, Mahmood / PossPOW: Possible Power of Downregulated Offshore Wind Power Plants. 2013. Poster session presented at EWEA Offshore 2013, Frankfurt, Germany.

Göçmen, Tuhfe; Giebel, Gregor; Sørensen, Poul Ejnar; Poulsen, Niels Kjølstad; Réthoré, Pierre-Elouan; Mirzaei, Mahmood / PossPOW: possible Power of Downregulated Offshore Wind Power Plants. Conference proceedings - EWEA Offshore 2013. European Wind Energy Association (EWEA), 2013.

Göçmen, Tuhfe; Giebel, Gregor; Poulsen, Niels Kjølstad; Mirzaei, Mahmood / Wind Speed Estimation and Parameterization of Wake Models for Downregulated Offshore Wind Farms. 2014. Poster session presented at European Wind Energy Conference & Exhibition 2014, Barcelona, Spain.

Göçmen, Tuhfe / PossPOW. Estimation of Possible Power in Offshore Wind Farms during Downregulation. 2014. EERA DeepWind 2014 - 11th Deep Sea Offshore Wind R&D Conference, Trondheim, Norway, 22/01/2014.

Mirzaei, Mahmood; Göçmen, Tuhfe; Giebel, Gregor; Sørensen, Poul Ejnar; Poulsen, Niels Kjølstad / Estimation of the Possible Power of a Wind Farm. In: I F A C Workshop Series, Vol. 19, 2014, p. 6782-6787.

Hasager, Charlotte Bay ; Hansen, Kurt Schaldemose ; Réthoré, Pierre-Elouan ; Volker, Patrick ; Palomares, Ana ; Prospathopoulos, John ; Chaviaropoulos, Takis ; Sieros, Giorgos ; Schepers, Gerard ; Ott, Søren ; Peña, Alfredo ; Cantero, Elena ; Palma, Jose ; Pryor, Sara ; Barthelmie, Rebecca Jane ; Mouche, Alexis ; Giebel, Gregor ; Badger, Merete ; Lozano, Sergio ; Correia, Pedro Fernandes ; Rathmann, Ole ; Göçmen, Tuhfe ; Young, Tom ; Rodrigo, Javier ; Madsen, Peter Hauge ; Maguire, E. / EERA DTOC wake results offshore. 2014. European Wind Energy Association (EWEA).European Wind Energy Conference & Exhibition 2014, Barcelona, Spain, 10/03/2014.

Göçmen, Tuhfe; Giebel, Gregor; Kjølstad Poulsen, Niels; Réthoré, Pierre-Elouan; Mirzaei, Mahmood / Wind Speed Estimation and Wake model Re – calibration for Downregulated Offshore Wind Farms, EGU General Assembly Conference Abstracts, Vol.16, p.9366, 2014.

Mirzaei, Mahmood; Göçmen, Tuhfe; Giebel, Gregor; Sørensen, Poul Ejnar; Poulsen, Niels Kjølstad / Turbine Control Strategies for Wind Farm Power Optimization. Proceedings of 2015 American Control Conference. IEEE, 2015. p. 1709 - 1714.

Göçmen, Tuhfe; Giebel, Gregor; Sørensen, Poul Ejnar; Réthoré, Pierre-Elouan; Mirzaei, Mahmood; Poulsen, Niels Kjølstad; Skjelmose, Mads Rajczyk; Kristoffersen, Jesper Runge / Real-time available power estimation for offshore wind power plants. 2015. Poster session presented at EWEA Offshore 2015 Conference, Copenhagen, Denmark.

Giebel, Gregor; Göçmen, Tuhfe; Sørensen, Poul Ejnar; Réthoré, Pierre-Elouan; Poulsen, Niels Kjølstad; Mirzaei, Mahmood; Skjelmose, Mads Rajczyk ; Kristoffersen, Jesper Runge / Experimental verification of a real-time power curve for down-regulated offshore wind power plants. 2015. Poster session presented at EWEA Offshore 2015 Conference, Copenhagen, Denmark.

Bibliography

[1] IEC International Standard, IEC 61400-12-1, Wind Turbines – Part 12-1 : Power performance measurements of electricity producing wind turbines, 2005.

[2] Thomas Ackermann. *Wind Power in Power Systems*, page 742. Wiley, 2005.

[3] JF Ainslie. Wake modelling and the prediction of turbulence properties. In *Proceedings of the 8th British Wind energy Association Conference, Cambridge*, pages 19–21, 1986.

[4] John F Ainslie. Wake modelling and prediction of turbulence properties. In *Wind Energy Conversion, 1986: Proceedings of the 8th British Wind Energy Association Conference*, volume 8 of *Lecture Notes in Computer Science*, UK, 1986. Cambridge.

[5] Jennifer Annoni, Patrick Seiler, Kenneth Johnson, Paul Fleming, and Pieter Gebraad. Evaluating wake models for wind farm control. In *American Control Conference (ACC), 2014*, pages 2517–2523. IEEE, 2014.

[6] Rebecca Barthelmie, Ole Frost Hansen, Karen Enevoldsen, Jørgen Højstrup, Sten Frandsen, Sara Pryor, Søren Larsen, Maurizio Motta, and Peter Sanderhoff. Ten years of meteorological measurements for offshore wind farms. *Journal of Solar Energy Engineering*, 127(2):170–176, 2005.

[7] Rebecca Jane Barthelmie, Sten Tronæs Frandsen, MN Nielsen, SC Pryor, P-E Rethore, and HE Jørgensen. Modelling and measurements of power losses and turbulence intensity in wind turbine wakes at Middelgrunden offshore wind farm. *Wind Energy*, 10(6):517–528, 2007.

[8] R.J. Barthelmie, L. Folkerts, Gunner Chr. Larsen, K. Rados, S.C. Pryor, Sten Tronæs Frandsen, B. Lange, and G. Schepers. Comparison of wake model simulations with offshore wind turbine wake profiles measured by sodar. *J. Atmos. Ocean. Technol.*, 23:888–901, 2006.

[9] Majid Bastankhah and Fernando Porté-Agel. A wind-tunnel investigation of wind-turbine wakes in yawed conditions. In *Journal of Physics: Conference Series*, volume 625, page 012014. IOP Publishing, 2015.

[10] J. Beltrán, J. J. Guerrero, J. J. Melero, and A. Llombart. Detection of nacelle anemometer faults in a wind farm minimizing the uncertainty. *Wind Energy*, 16(6):939–952, 2013.

[11] Ferhat Bingöl, Jakob Mann, and Gunner C Larsen. Light detection and ranging measurements of wake dynamics Part I: One-dimensional scanning. *Wind energy*, 13(1):51–61, 2010.

[12] Bundesnetzagentur. Leitfaden zum EEG-Einspeisemanagement – abschaltrangfolge, berechnung von entschädigungszahlungen und auswirkungen auf die Netzentgelte, version 2.1, 2014.

[13] D. Cabezón, E. Migoya, and A. Crespo. Comparison of turbulence models for the computational fluid dynamics simulation of wind turbine wakes in the atmospheric boundary layer. *Wind Energy*, 14:909–921, 2011.

[14] Matthew J Churchfield, Sang Lee, John Michalakes, and Patrick J Moriarty. A numerical study of the effects of atmospheric and wake turbulence on wind turbine dynamics. *Journal of Turbulence*, (13), 2012.

[15] JW Cleijne. Results of sexbierum wind farm: double wake measurements. Technical report, TNO Environmental and Energy Research, 1992.

[16] JW Cleijne. Results of sexbierum wind farm: single wake measurements. Technical report, TNO Environmental and Energy Research, 1993.

[17] Gustave Paul Corten, Koert Lindenburg, and Pieter Schaak. Assembly of energy flow collectors, such as windpark, and method of operation, November 27 2007. US Patent 7,299,627.

[18] A. Crespo and J. Hernandez. Turbulence characteristics in wind-turbine wakes. *Journal of Wind Engineering and Industrial Aerodynamics*, 61(1):71 – 85, 1996.

[19] Antonio Crespo, J. Hernández, and Sten T. Frandsen. Survey of modelling methods for wind turbine wakes and wind farms. *Wind Energy*, 2(1):1–24, January 1999.

[20] Cornelius Frank Dietrich. *Uncertainty, calibration and probability: the statistics of scientific and industrial measurement*. CRC Press, 1991.

[21] EirGrid. Quality Standard for Wind Farm Power Station Available Active Power (AAP) Signal, version 2.0, 2010.

[22] A. El Kasmi and C. Masson. An extended k-ε model for turbulent flow through horizontal-axis wind turbines. *Journal of Wind Engineering and Industrial Aerodynamics*, 96:103–122, 2008.

[23] Elia, Belgium. Delivery of downward aFRR by wind farms, 2015.

[24] Energinet.dk. Compensation for offshore wind farms ordered to perform downward regulation, 2009.

[25] Energinet.dk. Technical regulation 3.2.5 for wind power plants with a power output above 11 kW, 2015.

[26] European Commission. COMMUNICATION FROM THE COMMISSION TO THE EUROPEAN PARLIAMENT, THE COUNCIL, THE EUROPEAN ECONOMIC AND SOCIAL COMMITTEE AND THE COMMITTEE OF THE REGIONS A policy framework for climate and energy in the period from 2020 to 2030, 2014.

[27] Ir Flint and G Th Johann. Ten features which make the holec wind turbine wps 30-3 unique in the world. *Journal of Wind Engineering and Industrial Aerodynamics*, 27(1):15–25, 1988.

[28] Sten Frandsen. On the wind speed reduction in the center of large clusters of wind turbines. *Journal of Wind Engineering and Industrial Aerodynamics*, 39(1):251–265, 1992.

[29] Jochen Fröhlich and Dominic von Terzi. Hybrid les/rans methods for the simulation of turbulent flows. *Progress in Aerospace Sciences*, 44(5):349–377, 2008.

[30] M Gaumond, P-E Réthoré, Søren Ott, Alfredo Peña, Andreas Bechmann, and Kurt Schaldemose Hansen. Evaluation of the wind direction uncertainty and its impact on wake modeling at the Horns Rev offshore wind farm. *Wind Energy*, 17(8):1169–1178, 2014.

[31] M Gaumond, Pierre-Elouan Réthoré, Andreas Bechmann, Søren Ott, Gunner Chr Larsen, A Peña, and Kurt Schaldemose Hansen. Benchmarking of wind turbine wake models in large offshore wind farms. In *Proceedings of the Science of Making Torque from Wind Conference*, 2012.

[32] Roger G Ghanem and Pol D Spanos. *Stochastic finite elements: a spectral approach*. Courier Corporation, 2003.

[33] GWEC Global Wind Energy Council. Global Wind Report - annual market update, 2014.

[34] Julia Gottschall and Joachim Peinke. How to improve the estimation of power curves for wind turbines. *Environmental Research Letters*, 3(1):015005, 2008.

[35] Kurt S Hansen. Benchmarking of Lillgrund offshore wind farm scale wake models, 2014.

[36] Kurt S. Hansen, Rebecca J. Barthelmie, Leo E. Jensen, and Anders Sommer. The impact of turbulence intensity and atmospheric stability on power deficits due to wind turbine wakes at Horns Rev wind farm. *Wind Energy*, 15(1):183–196, 2012.

[37] Kurt Schaldemose Hansen. Benchmarking of lillgrund offshore wind farm scale wake models, 2014. PowerPoint.

[38] Lars Henrik Hansen. Dealing with TSO requirements to available power estimates, 2015. Presented at WIND ENERGY DENMARK Annual Event 2015.

[39] Siegfried Heier. *Grid Integration of Wind Energy Conversion Systems*, page 35. Wiley, Chichester, UK, 1998.

[40] Jon C Helton, Jay Dean Johnson, Cedric J Sallaberry, and Curt B Storlie. Survey of sampling-based methods for uncertainty and sensitivity analysis. *Reliability Engineering & System Safety*, 91(10):1175–1209, 2006.

[41] Niels Otto Jensen. Change of surface roughness and the planetary boundary layer. *Quarterly Journal of the Royal Meteorological Society*, 104(440):351–356, 1978.

[42] Niels Otto Jensen. *A note on wind generator interaction*. 1983.

[43] Kathryn Johnson and Geraldine Fritsch. Assessment of extremum seeking control for wind farm energy production. *Wind Engineering*, 36(6):701–716, 2012.

[44] H Jørgensen, S Frandsen, and P Vølund. Analyses of wake effects on Middelgrunden wind farm, risø-r-1403. Technical report, Risø National Laboratory, 2003.

[45] I Katic, J Højstrup, and NO Jensen. A simple model for cluster efficiency. In *European Wind Energy Association Conference and Exhibition*, pages 407–410, 1986.

[46] Rolf-Erik Keck, Martin de Maré, Matthew J Churchfield, Sang Lee, Gunner Larsen, and Helge Aagaard Madsen. On atmospheric stability in the dynamic wake meandering model. *Wind Energy*, 17(11):1689–1710, 2014.

[47] Rolf-Erik Keck, Martin de Maré, Matthew J Churchfield, Sang Lee, Gunner Larsen, and Helge Aagaard Madsen. Two improvements to the dynamic wake meandering model: including the effects of atmospheric shear on wake turbulence and incorporating turbulence build-up in a row of wind turbines. *Wind Energy*, 18(1):111–132, 2015.

[48] Rolf-Erik Keck, Dick Veldkamp, Helge Aagaard Madsen, and Gunner Larsen. Implementation of a mixing length turbulence formulation into the dynamic wake meandering model. *Journal of Solar Energy Engineering*, 134(2):021012, 2012.

[49] R. Krishna. Available power estimator, 2012. US Patent App. 13/321,932.

[50] Jesper Runge Kristoffersen. The horns rev wind farm and the operational experience with the wind farm main controller. *Revue E-Société Royale Belge des électriciens*, 122(2):26, 2006.

[51] M Paul Laan, Niels N Sørensen, Pierre-Elouan Réthoré, Jakob Mann, Mark C Kelly, Niels Troldborg, J Gerard Schepers, and Ewan Machefaux. An improved k-ε model applied to a wind turbine wake in atmospheric turbulence. *Wind Energy*, 2014.

[52] Paul Maarten Laan, van der, Niels N Sørensen, Pierre-Elouan Réthoré, Jakob Mann, Mark C Kelly, Niels Troldborg, Kurt Schaldemose Hansen, and Juan Pablo Murcia Leon. The k-ε-f p model applied to wind farms. *Wind Energy*, 2014.

[53] Gunner C. Larsen. A simple stationary semi-analytical wake model. Technical Report, Risø-R-1713(EN) August, RisøDTU, 2009.

[54] Gunner C Larsen, Helge Aa Madsen, Kenneth Thomsen, and Torben J Larsen. Wake meandering: a pragmatic approach. *Wind energy*, 11(4):377–395, 2008.

[55] Gunner Chr. Larsen. *A Simple Wake Calculation Procedure*. rapport Risø-M. 1988.

[56] Gunner Chr Larsen, Helge Madsen Aagaard, Ferhat Bingöl, Jakob Mann, Søren Ott, Jens N Sørensen, Valery Okulov, Niels Troldborg, Niels Morten Nielsen, Kenneth Thomsen, et al. *Dynamic wake meandering modeling*. Risø National Laboratory, 2007.

[57] Torben J. Larsen, Gunner Chr. Larsen, Helge Aagaard Madsen, and Søren Markilde Pedersen. Wake effects above rated wind speed. - an overlooked contributor to high loads in wind farms, 2015. PowerPoint.

[58] Torben J. Larsen, Helge Aa. Madsen, Gunner C. Larsen, and Kurt S. Hansen. Validation of the dynamic wake meander model for loads and power production in the egmond aan zee wind farm. *Wind Energy*, 16(4):605–624, 2013.

[59] Torben J Larsen, Helge Aa Madsen, Gunner C Larsen, and Kurt S Hansen. Validation of the dynamic wake meander model for loads and power production in the Egmond aan Zee wind farm. *Wind Energy*, 16(4):605–624, 2013.

[60] Brian Edward Launder and DB Spalding. The numerical computation of turbulent flows. *Computer methods in applied mechanics and engineering*, 3(2):269–289, 1974.

[61] Ewan Machefaux, Gunner Chr Larsen, Niels Troldborg, Mac Gaunaa, and Andreas Rettenmeier. Empirical modeling of single-wake advection and expansion using full-scale pulsed lidar-based measurements. *Wind Energy*, 2014.

[62] Ewan Machefaux, Gunner Chr. Larsen, Niels Troldborg, Mac Gaunaa, and Andreas Rettenmeier. Empirical modeling of single-wake advection and expansion using full-scale pulsed lidar-based measurements. *Wind Energy*, 2014.

[63] H Aa Madsen, Gunner Chr Larsen, Torben J Larsen, Niels Troldborg, and R Mikkelsen. Calibration and validation of the dynamic wake meandering model for implementation in an aeroelastic code. *Journal of Solar Energy Engineering*, 132(4):041014, 2010.

[64] M. Magnusson and A.-S. Smedman. Air flow behind wind turbines. *Journal of Wind Engineering and Industrial Aerodynamics*, 80(1–2):169 – 189, 1999.

[65] Jakob Mann. The spatial structure of neutral atmospheric surface-layer turbulence. *Journal of Fluid Mechanics*, 273:141–168, 1994.

[66] Jakob Mann. Wind field simulation. *Probabilistic engineering mechanics*, 13(4):269–282, 1998.

[67] Jason R Marden, Shalom D Ruben, and Lucy Y Pao. A model-free approach to wind farm control using game theoretic methods. *Control Systems Technology, IEEE Transactions on*, 21(4):1207–1214, 2013.

[68] S. Markkilde Petersen. *Experimental investigation of gear box duration loadings on stall and pitch controlled wind turbines*, pages 97–108. Technical University of Denmark. Department of Fluid Mechanics, 1995.

[69] JA Michelsen. Basis3d-a platform for development of multiblock pde solvers. *Report AFM*, pages 92–05, 1992.

[70] MINISTERE DES AFFAIRES ECONOMIQUES. Federal Grid Code Ed. 2, Art. 157, Belgium, 2002.

[71] Mahmood Mirzaei, Tuhfe Göçmen, Gregor Giebel, Poul Ejnar Sørensen, and Niels Kjølstad Poulsen. Estimation of the possible power of a wind farm. *I F A C Workshop Series*, 19:6782–6787, 2014.

[72] Mahmood Mirzaei, Tuhfe Göçmen, Gregor Giebel, Poul Ejnar Sørensen, and Niels Kjølstad Poulsen. *Turbine Control Strategies for Wind Farm Power Optimization*, pages 1709 – 1714. IEEE, 2015.

[73] N Gylling Mortensen, Lars Landberg, Ib Troen, and Erik Lundtang Petersen. Wind Atlas Analysis and Application Program (WAsP). 1993.

[74] Arthur Neslen. Wind power generates 140% of Denmark's electricity demand. *The Guardian*, 2015.

[75] Per Nielsen et al. Windpro: Software and manual, 2003.

[76] Nicolai Gayle Nygaard. Wakes in very large wind farms and the effect of neighbouring wind farms. In *Journal of Physics: Conference Series*, volume 524, page 012162. IOP Publishing, 2014.

[77] Office of Gas and Electricity Markets, UK. Grid code GC0063: Power Available, 2015.

[78] Søren Ott. *Linearised CFD Models for Wakes, Risø-R-1772, Risø-R-1772(EN)*. Denmark. Fo. Danmarks Tekniske Universitet, Risø Nationallaboratoriet for Bæredygtig Energi, 2011.

[79] Alfredo Peña and Ole Rathmann. Atmospheric stability-dependent infinite wind-farm models and the wake-decay coefficient. *Wind Energy*, 17(8):1269–1285, 2014.

[80] Alfredo Peña, Pierre-Elouan Réthoré, and Paul van der Laan. On the application of the Jensen wake model using a turbulence-dependent wake decay coefficient: the Sexbierum case. in Review.

[81] Alfredo Peña and Ole Rathmann. Atmospheric stability-dependent infinite wind-farm models and the wake-decay coefficient. *Wind Energy*, 17(8):1269–1285, 2014.

[82] Alfredo Peña, Pierre-Elouan Réthoré, and Ole Rathmann. Modeling large offshore wind farms under different atmospheric stability regimes with the park wake model. *Renewable Energy*, 70:164–171, 2014.

[83] Erich J Plate. P1 – Policy 1: Load-Frequency Control and Performance [C] . Technical report, European Network of Transmission System Operators for Electricity (ENTSO-E), March 2009.

[84] Stephen B. Pope. *Turbulent flows*. Cambridge University Press, 2000. Cambridge Books Online.

[85] Mikel de Prada Gil et al. Design, operation and control of novel electrical concepts for offshore wind power plants. 2014.

[86] J. M. Prospathopoulos, E. S. Politis, K. G. Rados, and P. K. Chaviaropoulos. Evaluation of the effects of turbulence model enhancements on wind turbine wake predictions. *Wind Energy*, 14:285–300, 2011.

[87] K. Raiambal and C. Chellamuthu. Modeling and simulation of grid connected wind electric generating system. In *TENCON '02. Proceedings. 2002 IEEE Region 10 Conference on Computers, Communications, Control and Power Engineering*, volume 3, pages 1847–1852 vol.3, 2002.

[88] OS Rathmann, S Frandsen, and M Nielsen. Wake decay constant for the infinite wind turbine array. In *Proceedings of the European Wind Energy Association Conference & Exhibition*, 2010.

[89] P.-E. Réthoré. *Wind Turbine Wake in Atmospheric Turbulence*. PhD thesis, Aalborg University, Risø DTU, Roskilde, Denmark, 2009.

[90] P. J. Richards and R. P. Hoxey. Appropriate boundary conditions for computational wind engineering models using the k-ε turbulence model. *Journal of Wind Engineering and Industrial Aerodynamics*, 46,47:145–153, 1993.

[91] B Sanderse, SP Pijl, and B Koren. Review of computational fluid dynamics for wind turbine wake aerodynamics. *Wind Energy*, 14(7):799–819, 2011.

[92] Zsolt Sándor and Péter András. Alternative sampling methods for estimating multivariate normal probabilities. *Journal of Econometrics*, 120(2):207–234, 2004.

[93] Abraham Savitzky and Marcel JE Golay. Smoothing and differentiation of data by simplified least squares procedures. *Analytical chemistry*, 36(8):1627–1639, 1964.

[94] G. Scott. *Definition of a 5-MW Reference Wind Turbine for Offshore System Development*. 2009.

[95] A.M. Sempreviva, R.J. Barthelmie, and S.C. Pryor. Review of methodologies for offshore wind resource assessment in European seas. *Surveys in Geophysics*, 29(6):471–497, 2008.

[96] Niels N Sørensen. *General purpose flow solver applied to flow over hills*. PhD thesis, Technical University of Denmark, 1995.

[97] Peter Sorknæs, Anders N Andersen, Jens Tang, and Sune Strøm. Market integration of wind power in electricity system balancing. *Energy Strategy Reviews*, 1(3):174–180, 2013.

[98] Christopher John Spruce. *Simulation and control of windfarms*. PhD thesis, University of Oxford, 1993.

[99] Jesper Starn and Weixin Zha. Germany Pays to Halt Danish Wind Power to Protect Own Output. *Bloomberg*, December 2015.

[100] Niels Troldborg. *Actuator line modeling of wind turbine wakes*. PhD thesis, Technical University of Denmark, 2008.

[101] National Grid UK. Grid code GC0063 – Power Available, Stage 03: Report to the Authority, 2014.

[102] M. P. van der Laan, N. N. Sørensen, P.-E. Réthoré, J. Mann, M. C. Kelly, and N. Troldborg. The k-ε-f_p model applied to double wind turbine wakes using different actuator disk force methods. *Wind Energy*, 2014. Published online: DOI: 10.1002/we.1816.

[103] LJ Vermeer, Jens Nørkær Sørensen, and A Crespo. Wind turbine wake aerodynamics. *Progress in aerospace sciences*, 39(6):467–510, 2003.

[104] Henk Kaarle Versteeg and Weeratunge Malalasekera. *An introduction to computational fluid dynamics: the finite volume method*. Pearson Education, 2007.

[105] JW Wagenaar, LAH Machielse, and JG Schepers. Controlling wind in ecn's scaled wind farm. *Proc. Europe Premier Wind Energy Event*, pages 685–694, 2012.

[106] Norbert Wiener. The homogeneous chaos. *American Journal of Mathematics*, pages 897–936, 1938.

[107] Frederik Zahle and Niels N. Sørensen. Characterization of the unsteady flow in the nacelle region of a modern wind turbine. *Wind Energy*, 14(2):271–283, 2011.